THE SIMPLICITY AND COMPLEXITY OF THE HIGGS BOSON

Couplings, Simplified Template Cross Sections, and CP properties in the H→WW decay channel

Federica Pasquali

The simplicity and complexity of the Higgs boson

Couplings, Simplified Template Cross Sections and CP properties in the H→WW decay channel

Federica Pasquali

Cover design: Malwina Chabocka (2022)
Printed by: Proefschriftenprinten.nl
ISBN: 978-90-833743-9-0
DOI: 10.5281/zenodo.10245035

The research presented in this thesis was carried out at the Nationaal Instituut voor Subatomaire Fysica (Nikhef) in Amsterdam, which is financially supported by the Nederlandse organisatie voor Wetenschappelijk Onderzoek (NWO), and at the European Organization for Nuclear Research (CERN) in Geneva. The author was financially supported by NWO.

The simplicity and complexity of the Higgs boson

Couplings, Simplified Template Cross Sections and CP properties in the H-WW decay channel

ACADEMISCH PROEFSCHRIFT

ter verkrijging van de graad van doctor
aan de Universiteit van Amsterdam
op gezag van de Rector Magnificus
prof. dr. ir. P.P.C.C. Verbeek
ten overstaan van een door het College voor Promoties ingestelde commissie,
in het openbaar te verdedigen in de Agnietenkapel
op dinsdag 5 maart 2024, te 13.00 uur

door Federica Pasquali
geboren te Alessandria

Promotiecommissie

Promotores:	prof. dr. W. Verkerke	Universiteit van Amsterdam
	prof. dr. ing. B. van Eijk	Universiteit Twente
Copromotores:	prof. dr. P. Ferrari	Radboud Universiteit
Overige leden:	prof. dr. M.P. Decowski	Universiteit van Amsterdam
	prof. dr. A.P. Colijn	Universiteit van Amsterdam
	prof. dr. ir. P.J. de Jong	Universiteit van Amsterdam
	prof. dr. R. Fleischer	Vrije Universiteit Amsterdam
	dr. A. Nisati	Sapienza Università di Roma

Faculteit der Natuurwetenschappen, Wiskunde en Informatica

The simplicity and complexity of the Higgs boson

Couplings, Simplified Template Cross Sections and CP properties in the H→WW decay channel

Short abstract:
The main objective of this thesis is exploiting the main caratheristics of the Higgs decay into two W boson and consequently in a pair of opposite sign leptons and two neutrinos by using the ATLAS detector at the Large Hadron Collider.

Keywords: Higgs, $H \to WW^* \to \ell\nu\ell\nu$, Semplified Template Cross Sections 1.2

List of Publications

[I] G. Aad et al. "Constraints on Higgs boson properties using $WW^*(\to e\nu\mu\nu)jj$ production in 36.1 fb^{-1} of $\sqrt{s}$=13 TeV pp collisions with the ATLAS detector". In: *The European Physical Journal C* 82.7 (2022), p. 622.

[II] ATLAS Collaboration. *Observation of vector-boson-fusion production of Higgs bosons in the $H \to WW^* \to e\nu\mu\nu$ decay channel in pp collisions at $\sqrt{s} = 13$ TeV with the ATLAS detector*. ATLAS-CONF-2020-045. 2020.

[III] ATLAS Collaboration. "Measurements of Higgs boson production by gluon−gluon fusion and vector-boson fusion using $H \to WW^* \to e$ decays in pp collisions at $\sqrt{s} = 13$ TeV with the ATLAS detector". In: (2022). DOI: 10.48550/ARXIV.2207.00338.

Contribution report

Papers I, II, and III are mainly the work of the author.

Contents

Abstract:

This thesis aims to draw a clear picture of the Higgs boson (H) when decaying in two W bosons. The specific decay $H \to W^{\pm}W^{\mp *} \to l^{-}\bar{\nu}_{l}l'^{+}\nu_{l'}$, where the two W bosons decay in a pair of different flavor leptons, is chosen as the target decay mode. This decay is particularly powerful in testing the Standard Model of particle physics (SM) given its large branching fraction (BF) and the possibility of investigating the WW scattering through its vector-boson fusion (VBF) production mode.

The first analysis presented in this thesis uses the kinematics of the gluon-fusion (ggF) process with two additional jets to constrain the charge conjugation-parity (CP) properties of the effective Higgs–gluon interaction. The CP of the Higgs is performed through the analysis of the top-Yukawa coupling, whose CP properties are propagated into the angular correlation between the two outgoing jets. The azimuthal difference among the 2 leading jets is a particularly sensitive quantity to set constraints of CP properties, the effects of new non-SM particles in the loop in the ggF effective vertex, or a combination of both these effects. For this measurement, a dataset corresponding to 36.1 fb^{-1} of $\sqrt{s} = 13$ TeV proton–proton collisions recorded by the ATLAS experiment at the LHC is used. Parametrizing with α the mixing angle between CP-even and CP-odd distribution, a value of $\tan\alpha = 0.0 \pm 0.4$ (stat.) ± 0.3 (syst.) is obtained. This result is consistent with SM prediction and complements existing studies of the CP properties of the Higgs boson. The signal strength parameter for the ggF production of the Higgs boson in addition with 2 jets is also determined and it is found to be $\mu_{\text{ggF+2jets}} = 0.5 \pm 0.4\,(\text{stat.})^{+0.7}_{-0.6}$ (syst.).

The second study, with a larger dataset of 139 fb^{-1}, derives the Higgs boson production cross-section for ggF and VBF. The measurement is performed by combining 4 different, separately optimized, and orthogonal sub-analyses. The products of the total ggF and VBF cross sections times the $H \to WW^*$ BF are respectively measured to be 12.0 ± 1.4 pb and $0.75^{+0.19}_{-0.16}$ pb, in agreement with SM predictions. Additionally, the first observation of the VBF production in the $H \to WW^*$ channel is obtained with a significance of 5.8 standard deviations. On top of this, the cross sections in specific phase space regions are extracted according to the 'Simplified Template Cross Section' scheme, for which 11 categories are defined. The results are in agreement with SM predictions with a p-value of 53%.

Testa alta
un passo alla volta
e sii coraggiosa.

I

Introduction

After almost 10 years after its discovery, the Higgs boson is still the holy grail of particle physics.

Developed in the second half of the 20th century, the *Standard Model of particle physics* (SM) had the aim of describing coherently and inclusively the fundamental particles discovered and their interactions. Despite the effort, a problem needed to be solved: according to the theory, the particles were supposed to be massless, which was in direct contradiction with the results from experiments. With the use of a mathematical technique, the *spontaneous symmetry breaking*, already used to explain superconductivity in solid-state physics, the issue was resolved, and as a side product, the Higgs boson was predicted. After years of futile searches using the Large Electron Positron Collider at *Conseil Européen pour la Recherche Nucléaire*, and the TeVatron at Fermilab, its observation was finally announced on July 4th, 2012 using the Large Hadron Collider, a newer and more powerful accelerator built for this purpose.

The Higgs boson is the *simplest* particle in the Standard model scenario: as far as we know, it has no spin, no charge, and no internal structure. This simplicity paradoxically generates a rich palette of interactions: it can easily couple to every known massive particle, and maybe—who knows—also to the particles that have not been discovered yet. After the decay into a b and anti-b quark pair, the decay into two W bosons has the largest branching ratio, which allows to collect enough data to probe (the $H \to WW^*$ characteristics) with high precision. In this thesis, the $H \to WW^*$ decay mode is studied for the case in which the two W bosons decay leptonically. Different production modes are investigated and their cross-sections are measured. But it is not the full story: also searches beyond the Standard Model can be performed. By looking at the top-Yukawa coupling, for example, constraints can be set on the charge conjugation-parity (CP) properties.

"Why is there a *complex* in the title of this thesis?", one might ask. A major challenge is found in the analyzed decay channel: the two neutrinos in the final state are not directly detectable by the ATLAS experiment. This translates into the impossibility of fully reconstructing the mass of the WW^* system. Fortunately, a successful optimization of the analysis strategies and the use of multivariate analysis techniques, made the extraction of the results smoother.

Organization of the manuscript and own contribution

Chapter 1 introduces quantum field theory and illustrates the key features of the Standard Model of particle physics. This Chapter also contains a description of the physics related to the Higgs boson, as well as models to characterize it.

I

Chapter 2 describes the experimental setup including the LHC accelerator complex and the ATLAS detector. Details on the used algorithms to reconstruct the proton-proton collisions follow.

Chapter 3 summarizes the statistical methods for the interpretation of the results discussed in this thesis.

Chapter 4 illustrates the basic concepts of $H \to WW^*$ events, from the signal topology to the background modeling that will be used in the following Chapters. A list of useful variables for discrimination is also provided after the definition of the physics objects used in the analyses.

Chapter 5 consists of the trigger requirements for selecting data for the $H \to WW^*$ analyses and illustrates the Monte Carlo generators for the modeling of the used samples and their uncertainties.

Chapter 6 focuses on the CP properties of the Higgs boson produced via gluon-fusion (ggF) in association with two jets in the $H \to WW^*$ decay. I had a strong involvement in the statistical analysis of the results.

Chapters 7 and 8 present the measurement of the ggF and vector-boson fusion (VBF) cross-section in the $H \to WW^*$ decay channel, as well as the 'Simplified Template Cross Section' (STXS). I contributed to the improvement of the analysis in two ways: I re-trained the boosted decision tree used in the previous publication for the VBF production mode to have a reference to compare the new neural network machine and I optimised the binning for the STXS measurement. On top of this, I assumed a leading role in the development of the fitting strategies and the combination of the results. They were further provided as input for a combined interpretation of various Higgs boson productions and decays.

A list of acronyms is in Chapter L.

1

Why: the Higgs boson and the theoretical framework

In the second half of the 20th century, a huge effort was made to describe three of the four known fundamental forces, as well as classifying all known elementary particles, in a single theory: the *Standard Model of particle physics (SM).* This theory is described in Section 1.1, with a focus on the physics of the Higgs boson following in Section 1.2. Despite the effort, some phenomena still lack a complete explanation, and Section 1.3 gives a brief description of them. The Chapter closes with Section 1.4, dedicated to the effective field theories and models useful to explain the analyses presented in this thesis.

Contents

1.1 The Standard Model of particles physics

1

The SM is the framework that captures our current understanding of the laws of nature. Developed in the second half of the twentieth century, it describes the fundamental building blocks of the universe, the elementary particles, and their interactions.
Figure 1.1 shows a representation of the particle content of the SM based on [4], where the main characteristics of the particles, such as electric charge, color charge, mass, and spin, are listed. According to the theory, all matter consists of 12 types of fermions, and their anti-particles, in addition to 5 types of force carriers, and 1 Goldstone boson. Fermions, which are half-integer spin particles, can be distinguished in leptons, with integer electric charge, and quarks with -1/3 or +2/3 electrical charge and equipped with a color charge. The anti-fermions have identical masses and opposite quantum numbers. While leptons can be observed as isolated particles, quarks are always bound to form colorless particles with integer electric charge, called *hadrons*. If hadrons are built-up from three quarks they are called *baryons* and have half-integer spin, instead, a quark/anti-quark pair forms a *meson* with integer spin.
The interaction among the fermions is mediated by bosons, elementary particles with integer spin. The gluon, g, mediates the strong force between color-charged quarks. It also carries a color charge itself and therefore it can self-interact. The photon, γ, mediates the electric force and thus couples with particles with a non-zero electric charge. The weak bosons, W^+, W^- and Z, mediate the weak force among all fermions. Lastly, the Higgs boson, H, is responsible for providing mass to bosons through a mechanism called *Electroweak symmetry breaking*.

The interactions between particles are not described by the SM as collisions of rigid objects but as *fields* coupling to matter particles mediating their interactions. This interpretation and the underlying mathematical formulation are commonly referred to as *quantum field theory (QFT)* [5]. The dynamic of these fields is described through the Lagrangian density, $\mathscr{L}$, which is commonly called the *Lagrangian*.
The Lagrangian $\mathscr{L}$ is function of the fields $\phi_j(x)$ (where x is the four-vector with components $(t, \mathbf{x})$) and their spatial and temporal derivatives $\frac{\partial \phi_j(x)}{\partial x^\mu} \equiv \partial_\mu \phi_j(x)$:

$$\mathscr{L}(t, \mathbf{x}) = \mathscr{L}(\phi_j(x), \partial_\mu \phi_j(x)),$$

where $\mu = 0$ identifies the temporal component and $\mu = 1, 2, 3$ the spatial ones.
By integrating $\mathscr{L}(x)$ over the spatial coordinates, the integrated Lagrangian L is obtained:

$$L(t) = \int \mathrm{d}^3 x \mathscr{L}(x),$$

while the integration of $\mathscr{L}(x)$ over the spatial and temporal coordinates gives the action S:

$$S = \int L(x) dt = \int \mathrm{d}^4 x \mathscr{L}(\phi_j(x), \partial_\mu \phi_j(x)).$$

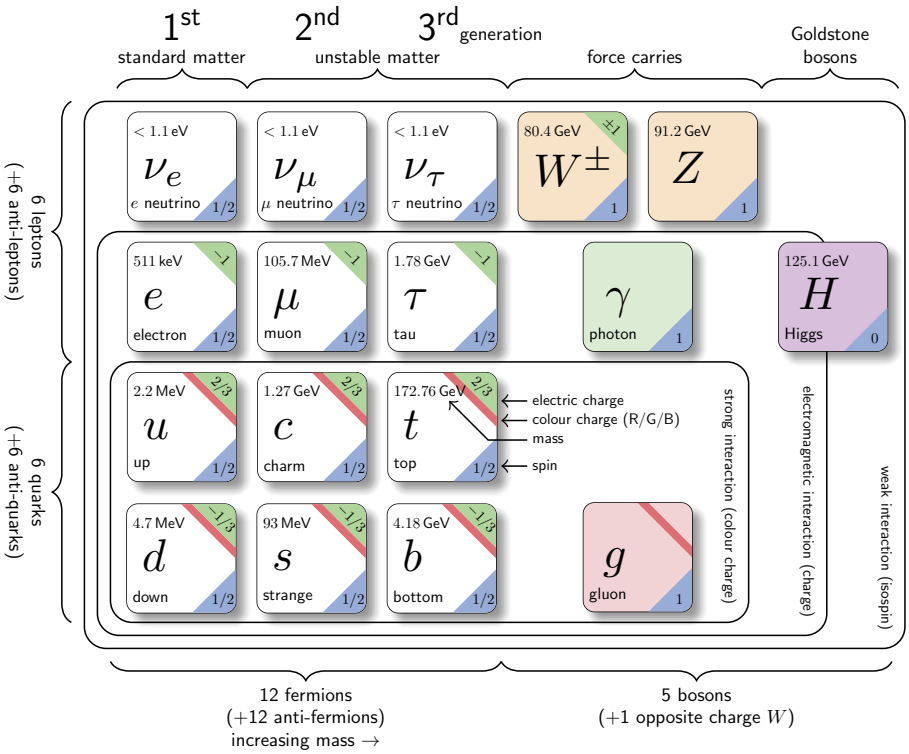

Figure 1.1: Custom-made depiction of the particle content of the SM including the respective quantum numbers as well as mass measurements and limits, based on [4]. The first three columns show the three generations of fermions with leptons, where in two columns in the top leptons are described, and the quarks in the last two ones. On the right-hand side of the figure, the force carriers and the Higgs boson have their place.

The equations of the motion are obtained from the equation of Euler-Lagrange:

$$\frac{\partial \mathscr{L}}{\partial \phi_j} - \frac{\partial}{\partial x^\mu}\left(\frac{\partial \mathscr{L}}{\partial \partial_\mu \phi_j(x)}\right) = 0 \tag{1.1}$$

which derive from the principle of Least Action[1]:

$$\delta \int_{t_1}^{t_2} L(t)dt = 0,$$

where t_1 and t_2 are arbitrary and the variation of fields in $t = t_1$ and $t = t_2$ are set to 0. Deriving the equations of motion by applying the Equation (1.1) is not always possible, sometimes the differential equations cannot be solved exactly. In this case, a common approach consists in first assuming that the dominant influence is the only factor and then making small corrections for

[1] The path taken by the system between times t_1 and t_2 is the one for which the action is stationary (no change) to first order.

additional factors. Considering for example the Lagrangian of the ϕ^4 theory:

$$\mathscr{L} = \frac{1}{2}(\partial\phi)^2 - \frac{1}{2}m^2\phi^2 + \frac{\lambda}{4!}\phi^4 \tag{1.2}$$

1

where ϕ is a scalar field with mass m, self-interacting with a coupling strength λ. Under the assumption that λ is small enough, the interacting Green function[2] solution of Equation (1.2) can be expanded in a power series of λ. Since the individual contributions may yield infinite results the original field can be rescaled through a number $Z \in \mathbb{C}$ as

$$\phi \to \sqrt{Z}\phi_R.$$

Equation (1.2) then becomes

$$\mathscr{L} = \frac{1}{2}Z(\partial\phi)^2 - \frac{1}{2}Zm^2\phi^2 + \frac{Z^2\lambda}{4!}\phi^4$$

with the *bare* parameters Z, m and g, which can be infinite. These parameters can be rewritten as *normalized* parameters as

$$Z = 1 + \delta_Z, \quad m^2Z = m_R^2 + \delta_m, \text{and} \quad Z^2g = g_R + \delta_\lambda$$

in order to obtain the *renormalized* Lagrangian

$$\mathscr{L} = \frac{1}{2}(\partial\phi_R)^2 - \frac{1}{2}m^2\phi_R^2 + \frac{\lambda}{4!}\phi_R^4 + \frac{1}{2}\delta_Z(\partial\phi_R)^2 - \frac{1}{2}m^2\delta_m^2 + \frac{\delta_\lambda}{4!}\phi_R^4.$$

The *counter terms* δ can be used to absorb the divergence. In the case of a theory in which they are sufficient to absorb all the infinities appearing, the theory is called *renormalizable*. In order to resolve the ambiguities, a *renormalization scale* is chosen, and this introduces an unphysical constant for the subtraction scheme and which vanishes as more terms of the power series are included. Renormalizability is not just an artifact to get rid of infinities but is also a criterion that defines universality in a theory: theories, where the physics at long distances do not depend on the microscopic detail, are renormalizable.

1.1.1 Symmetries of the SM

In the context of the SM, symmetries have a big relevance: according to Noether's theorem, [6], for each interaction presenting a symmetry there are corresponding conserved quantities whose values are conserved in time.
A theory is symmetric under a group if the Lagrangian is left invariant when a transformation belonging to that group is applied. What distinguishes a global transformation from a local one is that the transformation is the same for each point of space-time for the first case, and can differ between points in the latter case. The Lagrangian described by Equation (1.2) without the ϕ^4 term

[2] The Green function G(x,s) of a linear differential operator L(x) is defined as $LG(x,s) = \delta(x-s)$.

is indeed invariant under any global phase transformation

$$\phi(x) \to U(\alpha)\phi(x) \tag{1.3}$$

where the transformation

$$U(\alpha) = e^{i\alpha} \tag{1.4}$$

is from the abelian Lie group U(1). The field ϕ thus transforms as $\phi(x) \to (1 + i\alpha)\phi(x)$. The invariance requires the Lagrangian to stay unchanged, so

$$\begin{aligned} 0 &= \delta\mathscr{L} \\ &= \frac{\partial\mathscr{L}}{\partial\phi} + \frac{\partial\mathscr{L}}{\partial(\partial_\mu\phi)}\delta(\partial_\mu\phi) + \text{h.c.} \\ &= i\alpha\left[\frac{\partial\mathscr{L}}{\partial\phi} - \partial_\mu\left(\frac{\partial\mathscr{L}}{\partial\partial_\mu}\phi\right)\right]\phi + i\alpha\partial_\mu\left(\frac{\partial\mathscr{L}}{\partial\partial_\mu}\phi\right) + \text{h.c.} \end{aligned} \tag{1.5}$$

where the first term vanishes thanks to the Euler-Lagrange described in equation (1.1), and the following relation has been used:

$$\partial_\mu\left(\frac{\partial\mathscr{L}}{\partial\partial_\mu}\delta\phi\right) = \partial_\mu\frac{\partial\mathscr{L}}{\partial\partial_\mu}\cdot\delta\phi + \frac{\partial\mathscr{L}}{\partial\partial_\mu}\cdot\partial_\mu\delta\phi.$$

Equation (1.5) reduces to the form of $\partial_\mu j^\mu = 0$ where, thanks to the Noether theorem [6] a current j^μ is conserved.
In the case of local symmetries, the parameter α in equation (1.3) is a function of x: $\alpha \to \alpha(x)$, and it may happen that the Lagrangian of a specific process is no longer invariant under this type of local U(1) gauge transformation. In order to enforce the local invariance a covariant derivative can be defined to replace ∂_μ:

$$\mathcal{D}_\mu \equiv \partial_\mu + igA_\mu(x) \tag{1.6}$$

where $A_\mu(x)$ is an additional gauge field and g is the coupling constant of the Lagrangian to transform. The local phase transformations become:

$$\begin{aligned} \mathcal{D}_\mu \to \mathcal{D}_\mu\phi(x)' &= e^{ig\alpha(x)}\mathcal{D}_\mu\phi(x) \\ A_\mu(x) \to A_\mu(x)' &= A_\mu(x) - \partial_\mu\alpha(x). \end{aligned}$$

With reference to equation (1.4), a Lie group is a continuous group and a differentiable ($\mathbb{C}^\infty$) manifold, *i.e*, locally it is similar enough to linear space for the operation of the group to allow for differential calculus. Given this property, each group element can be written as

$$U = e^{i\theta^a T^a}\mathbb{1}$$

where θ^a are the parameters the group elements, $\mathbb{1}$ the identity matrix and T^a the group generators. These generators satisfy the commutation relation through the structure constants f^{abc}

$$[T^a, T^b] = if^{abc}T^c.$$

If $f^{abc} = 0 \quad \forall a, b, c$ the group is called *abelian*, it is non-abelian otherwise.

The SM is a non-abelian gauge theory with a gauge group

$$SU(3)_C \times SU(2)_L \times SU(1)_Y.$$

The internal symmetries of the SM are the strong interaction ($SU(3)_C$, acting on colour charge), the weak interaction ($SU(2)_L$, acting on left handed fermions) and the electromagnetic (EM) ($SU(1)_Y$, acting on hypercharge). The local $SU(2)_L \times SU(1)_Y$ symmetry is called electroweak (EW). The single symmetries are described in Sections 1.1.2, 1.1.3, 1.1.4.

1.1.2 Quantum electrodynamics

Quantum electrodynamics (QED) is the QFT that describes the phenomena involving charged particles interacting through the EM force. It is an Abelian gauge field theory with a gauge group U(1). The Lagrangian for the electron-positron interaction mediated by photons is

$$\mathscr{L} = \bar{\psi}(i\hbar\gamma_\mu D^\mu - m^2)\psi - \frac{1}{4}F_{\mu\nu}F^{\mu\nu}$$

where

ψ ($\bar{\psi}$) is the spinor (anti-spinor) of Dirac representing the charged particles ($\bar{\psi} = \psi^\dagger\gamma^0$),

$\mathcal{D}_\mu$ is the covariant derivative introduced in equation (1.6) with $g = -e$ (being e the electric charge) and A_μ the potential vector covariant of the EM field,

$F_{\mu\nu}$ is the tensor of the EM field defined as

$$F_{\mu\nu} = \partial_\mu A_\nu - \partial_\nu A_\mu$$

representing the kinetic term of the photon,

γ_μ are the Dirac matrices, defined as

$$\gamma^0 = \begin{pmatrix} 1&0&0&0\\0&1&0&0\\0&0&-1&0\\0&0&0&-1\end{pmatrix}, \quad \gamma^1 = \begin{pmatrix} 0&0&0&1\\0&0&1&0\\0&-1&0&0\\-1&0&0&0\end{pmatrix}, \quad \gamma^2 = \begin{pmatrix} 0&0&0&-i\\0&0&i&0\\0&i&0&0\\-i&0&0&0\end{pmatrix}, \quad \gamma^3 = \begin{pmatrix} 0&0&1&0\\0&0&0&-1\\-1&0&0&0\\0&1&0&0\end{pmatrix}$$

satisfying the following relations with $k \in 1, 2, 3$

$$(\gamma^0)^2 = I, \quad (\gamma^k)^2 = -I, \quad \gamma^{0\dagger} = \gamma^0, \quad \gamma^{k\dagger} = -\gamma^k, \quad \{\gamma^\mu, \gamma^\nu\} \equiv \gamma^\mu\gamma^\nu + \gamma^\nu\gamma^\mu 2\eta^{\mu\nu} I_4$$

with η the Minkowski metric with signature (+- - -) and I_4 the 4×4 identity matrix.

It is not possible to introduce a mass term for the EM field as it would break the gauge invariance. This implies that the photon, as mediator of the EM interaction, must be massless.

1.1.3 Electroweak theory

The EW theory is a *chiral* theory since it distinguishes between left- and right-handed fermions field defined as

$$\psi_L = P_L\psi = \frac{1}{2}(1-\gamma^5)\psi$$
$$\psi_R = P_R\psi = \frac{1}{2}(1+\gamma^5)\psi,$$

where $P_{L,R}$ assumes the name of *projector operator* and it is defined through the Dirac matrices. γ^5 is defined as

$$\gamma^5 \equiv i\gamma^0\gamma^1\gamma^2\gamma^3 = \begin{pmatrix} 0 & 0 & 1 & 0 \\ 0 & 0 & 0 & 1 \\ 1 & 0 & 0 & 0 \\ 0 & 1 & 0 & 0 \end{pmatrix},$$

satisfying

$$(\gamma^5)^2 = 1, \quad \gamma^{5\dagger} = \gamma^5, \quad \gamma^5\gamma^\mu = -\gamma^\mu\gamma^5.$$

The operators P_L and P_R have the opposite effect when acting on anti-fermions. The left-chiral fermions are combined into doublets of isospin I in $SU(2)_L$ space, whereas right-chiral fermions are iso-singlets; this template is shown in Table 1.1.

	Quarks	Leptons
left-handed	$\begin{pmatrix} u \\ d \end{pmatrix}_L \begin{pmatrix} c \\ s \end{pmatrix}_L \begin{pmatrix} t \\ b \end{pmatrix}_L$	$\begin{pmatrix} \nu_e \\ e \end{pmatrix}_L \begin{pmatrix} \nu_\mu \\ \mu \end{pmatrix}_L \begin{pmatrix} \nu_\tau \\ \tau \end{pmatrix}_L$
right-handed	$u_R, c_R, t_R, d_R, s_R, b_R, t_R$	e_R, μ_R, τ_R

Table 1.1: Arrangement of quarks and leptons in weak iso-doublets and iso-singlets.

The symmetry of this interaction (also called the Glashow-Salam-Weinberg interaction, [7]) is a local gauge transformation of the form

$$U(x) = \exp\left(i\frac{Y}{2}\alpha(x) + iI\sum_i \sigma_i\beta_i(x)\right),$$

where α and β are local functions and σ_i are the Pauli matrices defined as

$$\sigma_1 = \begin{pmatrix} 0 & 1 \\ 1 & 0 \end{pmatrix}, \quad \sigma_2 = \begin{pmatrix} 0 & -i \\ i & 0 \end{pmatrix}, \quad \sigma_3 = \begin{pmatrix} 1 & 0 \\ 0 & -1 \end{pmatrix},$$

I the weak isospin (equal to $1/2$ for left-handed fermions and 0 for right-handed fermions) and where Y is the hypercharge defined as

$$Y = 2(Q - I_3),$$

where the electric charge Q and the third component of the weak isospin are combined. The covariant derivative $\mathcal{D}_\mu$ that preserves the local invariance $SU(2)_L \times U(1)_Y$ on left-chiral spinors and $U(1)_Y$ on right-chiral spinor is of the form

$$\mathcal{D}_\mu = \partial_\mu - i\frac{g}{2}\sigma_i W_\mu^i(x) - i\frac{g'}{2}YB_\mu(x), \tag{1.7}$$

where g and g' are the coupling strength of $SU(2)_L$ and $U(1)_Y$ respectively, $W_\mu^i (i = 1, 2, 3)$ are the $SU(2)_L$ gauge boson fields, and B_μ is the $U(1)_Y$ one. The full Lagrangian consists of a fermionic term ($\mathscr{L}_\psi$) and a term only involving gauge boson ($\mathscr{L}_{\text{gauge}}$):

$$\begin{aligned}\mathscr{L}_\psi &= -\frac{1}{4}(W_{\mu\nu}^i)^2 - \frac{1}{4}B_{\mu\nu}^2 \\ \mathscr{L}_{\text{gauge}} &= i\bar{\psi}\gamma_\mu\partial^\mu\psi - \frac{g}{2}\bar{\psi}\gamma^\mu\sigma_i W_\mu^i - \frac{g'}{2}Y\bar{\psi}\gamma^\mu B_\mu\psi,\end{aligned}$$

where $B_{\mu\nu}$ and $W_{\mu\nu}^i$ represents the field tensor of the form

$$\begin{aligned}B_{\mu\nu} &= \partial_\mu B_\nu - \partial_\nu B_\mu \\ W_{\mu\nu}^i &= \partial_\mu W_\nu^i - \partial_\nu W_\mu^i - g\varepsilon^{ijk}W_\mu^j W_\mu^k,\end{aligned}$$

with the totally antisymmetric tensor[3] ε^{ijk}. The unphysical fields W_μ^i and B_μ relate to the charged boson W as follows:

$$W^\pm = \frac{1}{2}(W_\mu^1 \mp iW_\mu^2)$$

and the neutral Z boson and the field associated with the photon γ relate as

$$\begin{pmatrix}\gamma \\ Z\end{pmatrix} = \begin{pmatrix}\cos\theta_W & \sin\theta_W \\ -\sin\theta_W & \cos\theta_W\end{pmatrix}\begin{pmatrix}B \\ W^3\end{pmatrix},$$

where θ_W is the *weak mixing angle* or Weinberg angle defined as

$$\cos\theta_W = \frac{g}{\sqrt{g^2+g'^2}} \quad \text{and} \quad \sin\theta_W = \frac{g'}{\sqrt{g^2+g'^2}}. \tag{1.8}$$

1.1.4 Quantum chromodynamics

Quantum chromodynamics (QCD) is the QFT that describes the phenomena involving quarks, which are arranged in colour triplets. It is a non-abelian gauge theory of the $SU(3)$ gauge group with transformation

$$U(x) = \exp\left\{i\sum_{j=1}^{8}\alpha(x)\frac{\lambda_j}{2}\right\}, \tag{1.9}$$

[3] A tensor is antisymmetric if it alternates sign when any two indices of the subset are interchanged.

with arbitrary gauge function $\alpha(x)$ acting on the triplets. The generators of this $SU(3)$ are the eight 3×3 λ^j matrices, called *Gell-Mann matrices*:

$$\lambda^1 = \begin{pmatrix} 0 & 1 & 0 \\ 1 & 0 & 0 \\ 0 & 0 & 0 \end{pmatrix}, \quad \lambda^2 = \begin{pmatrix} 0 & -i & 0 \\ i & 0 & 0 \\ 0 & 0 & 0 \end{pmatrix}, \quad \lambda^3 = \begin{pmatrix} 1 & 0 & 0 \\ 0 & -1 & 0 \\ 0 & 0 & 0 \end{pmatrix}$$
$$\lambda^4 = \begin{pmatrix} 0 & 0 & 1 \\ 0 & 0 & 0 \\ 1 & 0 & 0 \end{pmatrix}, \quad \lambda^5 = \begin{pmatrix} 0 & 0 & 0-i \\ 0 & 0 & 0 \\ i & 0 & 0 \end{pmatrix}, \quad \lambda^6 = \begin{pmatrix} 0 & 0 & 0 \\ 0 & 0 & 1 \\ 0 & 1 & 0 \end{pmatrix}$$
$$\lambda^7 = \begin{pmatrix} 0 & 0 & 0 \\ 0 & 0 & -i \\ 0 & i & 0 \end{pmatrix}, \quad \lambda^8 = \frac{1}{\sqrt{3}} \begin{pmatrix} 1 & 0 & 0 \\ 0 & 1 & 0 \\ 0 & 0 & -2 \end{pmatrix},$$

which respect the following relations

$$\begin{aligned} \operatorname{tr}(\lambda_i \lambda_j) &= 2\delta_{ij}, \\ [\lambda_i, \lambda_j] &= 2i \sum_k f^{ijk} \lambda_k, \\ \{\lambda_i, \lambda_j\} &= \frac{4}{3}\delta_{ij} I + 2 \sum_j d^{ijk} \lambda_c, \end{aligned}$$

with structure constants

$$f^{ijk} = -\frac{1}{4} \operatorname{tr}(\lambda_i [\lambda_j, \lambda_k]) \text{ and } d^{ijk} = -\frac{1}{4} \operatorname{tr}(\lambda_i \{\lambda_j, \lambda_k\}). \tag{1.10}$$

The covariant derivative $\mathcal{D}_\mu$ which preserves the local gauge symmetry this time is of the form

$$\mathcal{D}_\mu = \partial_\mu + i g_C \sum_{j=1}^{8} \frac{\lambda^j}{2} G_\mu^j(x),$$

with the gluon fields $G_\mu^j(x)$ and the strong coupling constant g_C. The index j runs over each type of gluon identified by a specific colour-anticolour combination. The QCD Lagrangian is

$$\mathscr{L} = -\frac{1}{4} G_i^{\mu\nu} G^i_{\mu\nu},$$

where the gluon field strength tensor is defined as

$$G^i_{\mu\nu} = \partial_\mu G^i_\nu - \partial_\nu G^i_\mu - g_C \sum_{j,k=1}^{8} f^{ijk} G^j_\mu G^k_\nu$$

with the structure constant f^{ijk} introduced in equation (1.10); also here, no mass term is present in order not to break the symmetry.

Running coupling strength α_s
The coupling constant for the QCD interaction appearing Equation (1.9) can be expressed as a function of the transferred energy in the interaction Q

$$\alpha_s(Q^2) = \frac{g_C}{4\pi} = \frac{12\pi}{(11n_c - 2n_f)\ln\frac{Q^2}{\Lambda^2_{\text{QCD}}}}$$

with n_c and n_f the number of colour and quark flavour respectively, and Λ^2_{QCD} is the energy scale at which the perturbative QCD coupling diverges ($\sim 200\,\text{MeV}$). This perturbative approach works only when the energy scale Q^2 is much larger than Λ_{QCD}. The divergence of the coupling at low energy causes the quarks and gluons to form hadronic color singlets (a QCD property also known as *confinement*), while the dependency of α_s on Q^2 leads to the fact that at $Q^2 \to \infty$ quarks behave as free particles.

1.1.5 Symmetry breaking and Brout-Englert-Higgs mechanism

So far, no mass term has been added for either the fermions or the gauge fields since they would make the Lagrangian not invariant anymore under the respective gauge transformation. Experimental evidence instead suggests that fermions and gauge bosons have mass. The introduction of an additional complex scalar field can resolve this inconsistency between the theory presented here and the experimental results:

Symmetry breaking in scalar field
Introducing a mass term *by hand* in the Lagrangian often breaks the global or local symmetry of the theory. An alternative mechanism that can be introduced to *give* mass to the fields of a theory is called *symmetry breaking*. This method consists of introducing a potential of the scalar ϕ of the form

$$V(\phi) = \mu^2\phi\phi - \frac{\lambda}{4}\phi^2\phi^2 \tag{1.11}$$

to a kinetic Lagrangian for ϕ: $\mathscr{L} = \frac{1}{2}(\partial_\mu\phi)(\partial^\mu\phi)$. The resulting Lagrangian is invariant under any transformation of the type

$$\phi \to \phi e^{i\alpha}.$$

The potential of equation (1.11) has its minimum at

$$|\phi| = \sqrt{\frac{2\mu^2}{\lambda}} \equiv v.$$

The excitation of the field ϕ can be obtained by considering perturbations around v, called also the vacuum state, by defining

$$\phi(x) = v + \eta(x).$$

Given that $\partial_\mu \phi = \partial_\mu \eta$, the Lagrangian expressed in terms of η is of the form:

$$\begin{aligned}\mathscr{L} &= \frac{1}{2}(\partial_\mu \eta)(\partial^\mu \eta) - V(\eta) \\ &= \frac{1}{2}(\partial_\mu \eta)(\partial^\mu \eta) - \frac{1}{2}\mu^2(v+\eta)^2 - \frac{1}{4}\lambda(v+\eta)^4 \\ \text{(using } \mu^2 = \lambda v^2) &= \frac{1}{2}(\partial_\mu \eta)(\partial^\mu \eta) + \lambda v^2 \eta^2 + \lambda v \eta^3 - \frac{1}{4}\lambda \eta^4 + \frac{1}{4}\lambda v^4.\end{aligned}$$

By comparison, with the free scalar-field Lagrangian described in equation (1.2), the term proportional to η^2 can be interpreted as a mass $m = -\sqrt{-2\lambda v^2} = \sqrt{2\mu^2}$ where the terms proportional to η^3 and η^4 can be identified as triple and quartic interaction terms and the term $\lambda v^4/4$ as constant. By performing these substitutions, the Lagrangian can be written as

$$\mathscr{L}(\eta) = \frac{1}{2}(\partial_\mu \eta)(\partial^\mu \eta) - \frac{1}{2}m_\eta^2 \eta^2 - V(\eta) \quad \text{with } V(\eta) = \lambda v \eta^3 + \frac{1}{4}\lambda \eta^4. \tag{1.12}$$

Equation (1.12) is identical to equation (1.2), re-expressed as excitation around the minimum.

Symmetry breaking in a complex scalar field

The idea can be extended to a complex scalar field

$$\phi = \frac{1}{\sqrt{2}}(\phi_1 + i\phi_2)$$

with a corresponding Lagrangian

$$\mathscr{L}(\eta) = \frac{1}{2}(\partial_\mu \phi)^*(\partial^\mu \phi) - V(\phi) \quad \text{with } V(\phi) = \mu^2(\phi^*\phi) - \lambda(\phi^*\phi)^2.$$

The shape of the potential depends on the sign of μ^2. If $\mu^2 < 0$, the minimum occurs when $\phi_1 = \phi_2 = 0$, while for $\mu^2 > 0$, the potential has an infinite set of minima defined by

$$\phi_1 + \phi_2 = \frac{\mu^2}{\lambda} = v.$$

Without loss of generality, the vacuum state can be chosen at $\phi_2 = 0$ and $\phi_1 = v$, so that the field ϕ can be expanded around the vacuum state as

$$\phi = \frac{1}{\sqrt{2}}(\eta + v + i\varepsilon)$$

where

$$\begin{aligned}\phi_1(x) &= \eta(x) + v \\ \phi_2(x) &= \varepsilon(x).\end{aligned}$$

By following the same steps as for the case of a real scalar field, the Lagrangian can be written as

$$\mathscr{L}(\eta) = \frac{1}{2}(\partial_\mu \eta)(\partial^\mu \eta) - \frac{1}{2}m_\eta^2 - \eta^2 \frac{1}{2}(\partial_\mu \varepsilon)(\partial^\mu \varepsilon) - V_{\text{int}}(\eta, \varepsilon)$$

with $m_\eta = \sqrt{-2\lambda v}$ and the interaction potential given by

$$V_{\text{int}}(\eta, \varepsilon) = \lambda v \eta^3 + \frac{1}{4}\lambda\eta^4 + \frac{1}{4}\lambda\varepsilon^4 \lambda v \eta\varepsilon^2 + \frac{1}{2}\lambda\eta^2\varepsilon^2.$$

1

The excitation of the massive field η produces the appearance of a massless particle ε by virtue of spontaneously breaking a continuous symmetry. This result is known as Goldstone's theorem, and the massless scalar particle is called a Goldstone boson [8].

Brout-Englert-Higgs mechanism

The Brout-Englert-Higgs mechanism [9, 10] predicts in their simplest model a complex scalar field with four degrees of freedom. In fact, three Goldstone bosons are required in order to provide the longitudinal degree of freedom of the W^+, W^-, and Z bosons with in addition one massive scalar particle corresponding to the chosen field excitation. Since the mass of the neutral Z boson is created with this mechanism, one of the fields must be neutral and the other one must be charged, ϕ^+ and $(\phi^+)^\dagger = \phi^-$, in order to produce the masses of the W^+ and the W^-.
The minimal Higgs model predicts a scalar field of the form

$$\phi = \begin{pmatrix} \phi^+ \\ \phi^0 \end{pmatrix} = \frac{1}{\sqrt{2}} \begin{pmatrix} \phi_1 + i\phi_2 \\ \phi_3 + i\phi_4 \end{pmatrix}, \tag{1.13}$$

and the associated Lagrangian is of the form

$$\mathscr{L}(\eta) = \frac{1}{2}(\partial_\mu \phi)^\dagger (\partial^\mu \phi) - V(\phi) \quad \text{with } V(\phi) = \mu^2(\phi^\dagger\phi) - \lambda(\phi^\dagger\phi)^2. \tag{1.14}$$

The fields can be expanded around the the minimum satisfying $\phi^\dagger\phi = 1/2(\phi_1^2+\phi_2^2+\phi_3^2+\phi_4^2) = \frac{\mu^2}{\lambda}$ as

$$\phi(x) = \frac{1}{\sqrt{2}} \begin{pmatrix} \phi_1(x) + i\phi_2(x) \\ v + \eta(x) + i\phi_4 \end{pmatrix}. \tag{1.15}$$

By breaking the symmetry as described in Section 1.1.5, the Higgs doublet can be expressed as

$$\phi(x) = \frac{1}{\sqrt{2}} \begin{pmatrix} 0 \\ v + h(x) \end{pmatrix}. \tag{1.16}$$

Gauge bosons mass

Applying the covariant derivative of the EW interaction (Equation (1.7))[4] to the Higgs field, the kinetic term $(\mathcal{D}_\mu\phi)^\dagger)(\mathcal{D}^\mu\phi))$ of the EW interaction can be derived as

$$\begin{aligned} \mathcal{D}_\mu\phi &= \frac{1}{2\sqrt{2}} \begin{pmatrix} 2\partial_\mu + igW_\mu^{(3)} + ig'B_\mu & ig(W_\mu^{(1)} - iW_\mu^{(2)}) \\ ig(W_\mu^{(1)} + iW_\mu^{(2)}) & 2\partial_\mu - igW_\mu^{(3)} + ig'B_\mu \end{pmatrix} \begin{pmatrix} 0 \\ v + h(x) \end{pmatrix} \\ &= \frac{1}{2\sqrt{2}} \begin{pmatrix} ig(W_\mu^{(1)} - iW_\mu^{(2)})(v+h) \\ (2\partial_\mu - igW_\mu^{(3)} + ig'B_\mu)(v+h) \end{pmatrix}. \end{aligned}$$

[4] where $Y = 1$ since the lower component of the Higgs doublet is neutral and it has thus $I_W^{(3)} = -\frac{1}{2}$.

When calculating $(\mathcal{D}_\mu\phi^\dagger)(\mathcal{D}^\mu\phi)$, the following is obtained:

$$\begin{aligned}(\mathcal{D}_\mu\phi^\dagger)(\mathcal{D}^\mu\phi) =&\frac{1}{2}(\partial_\mu h)(\partial^\mu h) + \frac{1}{8}g^2(W_\mu^{(1)} + iW_\mu^{(2)})(W^{(1)\mu} - iW^{(2)\mu})(v+h)^2 \\ &+ \frac{1}{8}(gW_\mu^{(3)} - g'B_\mu)(gW^{(3)\mu} - g'B^\mu)(v+h)^2.\end{aligned}$$

The gauge bosons masses are determined by the quadratic terms in the equation

$$\frac{1}{8}v^2g^2(W_\mu^{(1)}W^{(1)\mu} + W_\mu^{(2)}W^{(2)\mu}) + \frac{1}{8}v^2(gW_\mu^{(3)} - g'B_\mu)(gW^{(3)\mu} - g'B_\mu) \tag{1.17}$$

as

$$\frac{1}{2}m_W^2W_\mu^{(1)}W^{(1)\mu} \quad \text{and} \frac{1}{2}m_W^2W_\mu^{(2)}W^{(2)\mu},$$

therefore the mass of the W boson is

$$m_W = \frac{1}{2}gv. \tag{1.18}$$

For the mass of the Z boson, the terms quadratic in the neutral $W^{(3)}$ and B fields need to be considered:

$$\frac{v^2}{8}(gW_\mu^{(3)} - g'B_\mu)(gW^{(3)\mu} - g'B^\mu) = \frac{v^2}{8}\begin{pmatrix}W_\mu^{(3)} & B_\mu\end{pmatrix}\begin{pmatrix}g^2 & -gg' \\ -gg' & g'^2\end{pmatrix}\begin{pmatrix}W_\mu^{(3)} \\ B_\mu\end{pmatrix}.$$

Here, the central matrix needs to be diagonal in order to retrieve the *physical* boson fields[5]

$$\frac{v^2}{8}\begin{pmatrix}A_\mu & Z^\mu\end{pmatrix} = \begin{pmatrix}0 & 0 \\ 0 & g'^2 + g^2\end{pmatrix}\begin{pmatrix}A_\mu \\ Z^\mu\end{pmatrix},$$

from which the mass of the photon and the Z can be obtained

$$m_\gamma = 0 \quad \text{and} \; m_Z = \frac{1}{2}v\sqrt{g^2 + g'^2}. \tag{1.19}$$

Moreover, by combining equation (1.8), equation (1.19) and equation (1.18), the following relation can be obtained

$$\frac{m_W}{m_Z} = \cos\theta_W.$$

Last but not least, the value of v can be extracted from equation (1.18) and it is found that the vacuum expectation value of the Higgs field is $246\,\text{GeV}$.

[5]The physical boson fields propagate as eigenstates if the free particle Hamiltonian, where the mass matrix is diagonal: $\begin{pmatrix}A_\mu & Z^\mu\end{pmatrix} = \begin{pmatrix}m_A^2 & 0 \\ 0 & m_Z^2\end{pmatrix}\begin{pmatrix}A_\mu \\ Z^\mu\end{pmatrix}$.

1

Coupling to the W bosons

The second term of equation (1.17) can be written in terms of the physical $W^{\pm}$ fields

$$\frac{1}{4}g^2W_\mu^-W^{+\mu}(v+h)^2 = \frac{1}{4}g^2v^2W_\mu^-W^{+\mu} + \frac{1}{2}g^2vW_\mu^-W^{+\mu}h + \frac{1}{4}g^2W_\mu^-W^{+\mu}hh,$$

where the first term gives the mass of the $W^{\pm}$, while the hW^+W^- and hhW^+W^- are the triple and quartic couplings of Higgs boson to W bosons. In particular, the coupling strength at the hW^+W^- vertex is

$$g_{H\to W^-W^+} = \frac{1}{2}g^2v \equiv gm_W,$$

where equation (1.18) is used.

Fermions mass and Yukawa couplings

The mass of the fermions can be obtained by using the same mechanism used with the bosons while paying attention that the left- and right-chiral components respect different symmetries, since they are placed in $SU(2)$ doublets and $SU(2)$ singlets. In the covariant derivative of the EW interaction (equation (1.7)), the $SU(2)$ infinitesimal transformation acting on an $SU(2)$ doublet ϕ as the Higgs field, has the form

$$\phi \to \phi' = (I + g\varepsilon(x)\cdot\mathbb{T})\phi$$

with $\mathbb{T}$ being generators of the group transformation. The same transformation is applied on a left-handed L and on $\bar{L} = L^\dagger\gamma^0$, where it assumes the form $\bar{L} \to \bar{L}' = \bar{L}(I + g\varepsilon(x)\cdot\mathbb{T})$. This construct implies that $\bar{L}\phi$ is invariant under the $SU(2)_L$ transformation. In order to have an invariance under $SU(2)\otimes U(1)_Y$ a Lagrangian of the form $-g(\bar{L}\phi R + \bar{R}\phi^\dagger L)$ is chosen. Taking a fermion l and the associated neutrino ν_l, the corresponding Lagrangian follows

$$\mathscr{L}_l = -g\left[\begin{pmatrix}\bar{\nu}_l & \bar{l}\end{pmatrix}_L\begin{pmatrix}\phi^+\\ \phi^0\end{pmatrix}l_R + \bar{l}_R\begin{pmatrix}\phi^{+*} & \phi^{0*}\end{pmatrix}\begin{pmatrix}\nu_l\\ l\end{pmatrix}_L\right]$$

which becomes, after plugging in the Higgs doublet in the unitary gauge (equation (1.16)),

$$\mathscr{L}_l = -\frac{g}{\sqrt{2}}v(\bar{l}_Ll_R + \bar{l}_Rl_L) - \frac{g}{\sqrt{2}}h(\bar{l}_Ll_R + \bar{l}_Rl_L). \tag{1.20}$$

By comparing the first term of equation (1.20) with the Dirac Lagrangian, it is clear that this has the form of a mass term for the lepton. The parameter g is not predicted by the Higgs mechanism but it can be chosen to be consistent with the observation of the lepton mass, i.e.

$$g = \sqrt{2}\frac{m_l}{v}.$$

The parameter g is called *Yukawa coupling*. The described mechanism confers mass to the lower component of the doublets only, so it is not directly applicable to derive the mass of the quarks. Instead of using the Higgs doublet in the unitary gauge, the conjugated doublet (described in

Section 1.1.6) ϕ_c of the Higgs field expressed in equation (1.13), can be constructed as

$$\phi_c = -i\sigma_2\phi^* = \begin{pmatrix} -\phi^{0*} + \\ \phi^- \end{pmatrix} = \frac{1}{\sqrt{2}} \begin{pmatrix} -\phi_3 + i\phi_4 \\ \phi_1 - i\phi_2 \end{pmatrix},$$

and transforms exactly as ϕ (Section 1.1.6). The gauge invariant mass term for the up-type quarks is constructed then from the invariant as $-g(\bar{L}\phi_c R + \bar{R}\phi_c^\dagger L)$ and after symmetry breaking the Lagrangian has the form

$$\mathscr{L}_{\text{up-type}} = -\frac{g}{\sqrt{2}} v(\bar{u}_L u_R + \bar{u}_R u_L) - \frac{g}{\sqrt{2}} h(\bar{u}_L u_R + \bar{u}_R u_L),$$

with the Yukawa coupling given by $g = \sqrt{2}\frac{m_u}{v}$. Generalizing to all fermion types the Yukawa coupling g_f is

$$g = \sqrt{2}\frac{m_f}{v}. \tag{1.21}$$

With a top quark mass that has experimentally been measured to have a mass of (172.76 ± 0.30) GeV [4], its couplings with the Higgs is notably almost exactly unity.

1.1.6 Charge conjugation, parity and time transformations

It is interesting to consider the effect of three discrete symmetries the SM:

Charge conjugation is a discrete symmetry transformation that replaces particles with the corresponding anti-particles. The charge conjugation operator $\hat{C}$ acts on a wave function ψ as it follows $\hat{C}\psi = i\gamma^2\psi^*$. If ψ is a Dirac spinor, $\hat{C}\psi$ still satisfies the Dirac equation.

Parity symmetry is a discrete symmetry transformation that corresponds to spatial inversion through the origin

$$x' = -x \quad y' = -y \quad z' = -z \quad \text{and} \quad t' = t.$$

The parity operator is acting on ψ as $\hat{P}\psi = \gamma^0\psi$. If ψ is a Dirac spinor, $\hat{P}\psi$ still satisfies the Dirac equation.

Time symmetry is a discrete symmetry transformation that corresponds to time inversion through the origin

$$x' = x \quad y' = y \quad z' = z \quad \text{and} \quad t' = -t.$$

The product of these three symmetries, CPT, is believed to be an exact symmetry of the universe.

1.2 Standard Model Higgs boson physics

1

The SM Higgs boson is a massive, chargeless elementary particle with spin 0, positive charge conjugation-parity (CP), with a measured mass of $m_H = 125.25 \pm 0.17$GeV [4].

Since the Higgs Lagrangian is quadratic in its field h (equation (1.14)), it remains invariant under CP conjugation, where the following three scenarios can be considered

$$\begin{aligned} \hat{CP}(h) = h &\Rightarrow h \text{ is a } \hat{CP} \text{ even scalar} \\ \hat{CP}(h) = -h &\Rightarrow h \text{ is a } \hat{CP} \text{ odd pseudo-scalar} \\ \hat{CP}(h) = c_1 h_{even} + c_2 h_{odd} &\Rightarrow h \text{ is a } \hat{CP} \text{ mixed state,} \end{aligned}$$

where $\hat{C}$ and $\hat{P}$ are the operators described in Section 1.1.6 and the ratio c_2/c_1 is the mixing angle of the two eigenstates.

In order to confirm that the Higgs boson observed is the one described by the SM, alternative options on spin and CP properties have to be experimentally excluded. A study providing evidence for the spin-0 nature of the Higgs boson, with positive parity being strongly preferred, can be found in [11], from which Figure 1.2 has been extracted. The Figure shows a column per investigated J^P scenario, where the expected and observed confidence levels (CLs)[6] are shown, favoring a J^P in agreement with the SM.

Experimental results on the CP properties will be shown in Section 1.4.4, where the for such measurement is introduced.

1.2.1 Higgs production modes

For a process $xy \to jk$, the *cross section* σ is defined as the probability that a particle j and k are produced by the interaction of particles x and y; the cross-section has a dimension of an area and it is usually measured in units of barn (1 b=10^{-24} cm^2). There are four major mechanisms that produce a Higgs boson in a proton-proton collision (pp$\to H + X$) and their leading order (LO) Feynman diagrams are depicted in Figure 1.3[7]. Feynman diagrams are a useful graphical representation of a perturbative contribution to the transition amplitude. In these diagrams, each interaction vertex is associated with a factor depending on the strength of the interaction, internal lines correspond to a factor of the virtual particle's propagator[8] and incoming and outgoing lines carry energy, momentum and spin.

[6] The confidence level is a way of expressing the probability of obtaining the same result if repeating the experiment. A 0% confidence level means that there is no faith that the same result can be obtained if repeating the experiment, while 100% means that the same result will be obtained in a new experiment with no doubt.

[7] The relative contribution of each production mode, as a function of center-of-mass energy, are displayed in Figure 1.5.

[8] It is a function that specifies the probability amplitude for a particle to travel from one place to another in a given period of time, or to travel with a certain energy and momentum.

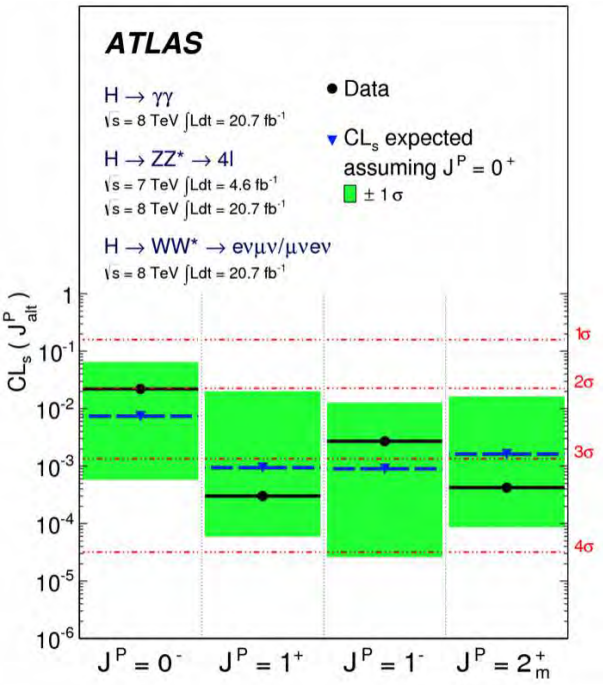

(a)

Figure 1.2: Different J^P scenarios of the Higgs boson. The simulated scenario according to the SM (expected) (blue triangles/dashed lines) and observed (black circles/solid lines) confidence level CLs for alternative spin-parity hypotheses assuming a $J^P = 0^+$ signal. The green band represents the 68% CLs expected exclusion range for a signal with assumed $J^P = 0^+$ [11].

The cross-section values introduced below refer to a SM Higgs boson with a mass of m_H =125.0 GeV.

Gluon-fusion (ggF) via quark loop is the leading mechanism for Higgs boson production at the LHC. It is initiated by gluons that couple to the Higgs via a fermion loop. Since the couplings with the Higgs depend on the mass of the fermion (equation (1.21)) the largest contribution comes from quarks, in particular from the top quark. In the approximation of infinite mass for the top quark, the cross-section can be calculated at next to next to next to leading order (NNNLO) [12] and is

$$\sigma_{\text{ggF}} = 48.58\,\text{pb}^{+4.56\%}_{-6.72\%}\,(\text{theory}) \pm 3.20\%\ (\text{PDF} + \alpha_s),$$

where the uncertainty depends on theory prediction, the parton distribution function (PDF) and the uncertainty on α_s. In this process no initial-state radiation is present, which results in the Higgs boson not having significant transverse momentum.

Vector-boson fusion (VBF) is the second largest production cross section. Two quarks from the protons radiate vector bosons, which initiate the process by fusing and producing the Higgs boson. The cross section has been calculated to next to next to leading order (NNLO) in QCD

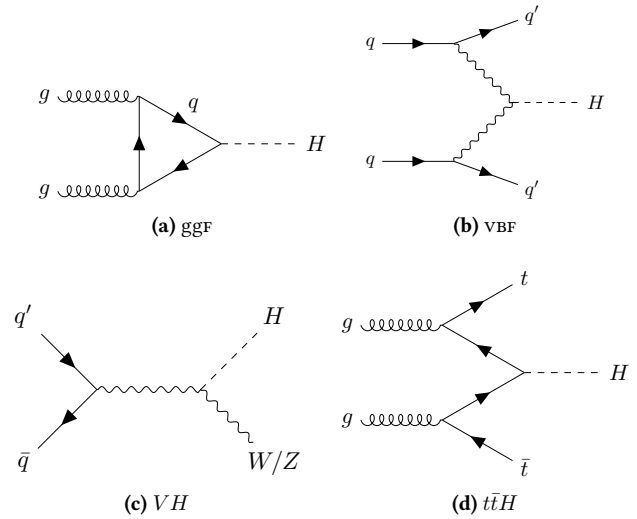

(a) ggF **(b)** VBF **(c)** VH **(d)** $t\bar{t}H$

Figure 1.3: Feynman diagrams of leading order Higgs boson production.

and includes next to leading order (NLO) EW corrections [12], and corresponds to

$$\sigma_{\text{VBF}} = 3.78\,\text{pb}^{+0.43\%}_{-0.33\%}\,(\text{scale}) \pm 2.1\%\,(\text{PDF} + \alpha_s).$$

In this process, the initial state radiation involves only vector bosons, therefore the quarks retain their longitudinal momentum. This process produces jets close to the beamline, so-called *forward jets*, and results in large values of the di-jet invariant mass m_{jj}.

Higgs strahlung (VH) produces a Higgs boson in association with a W or a Z vector boson. The cross-section has been calculated at NNLO QCD with NLO EW corrections, where the calculation has been split into Drell-Yan induced, top-loop induced, photon-induced corrections:

$$\begin{aligned}
\sigma_{W^+H\,(W^+\to l^+\nu)} &= 94.26\,\text{fb}^{+0.5\%}_{-0.7\%}\,(\text{scale}) \pm 1.8\%\,(\text{PDF} + \alpha_s)\\
\sigma_{W^-H\,(W^+\to l^-\bar{\nu})} &= 59.83\,\text{fb}^{+0.4\%}_{-0.7\%}\,(\text{scale}) \pm 2.0\%\,(\text{PDF} + \alpha_s)\\
\sigma_{ZH\,(Z\to l^+l^-)} &= 29.82\,\text{fb}^{+3.8\%}_{-3.1\%}\,(\text{scale}) \pm 1.6\%\,(\text{PDF} + \alpha_s)\\
\sigma_{ZH\,(Z\to \nu+\bar{\nu})} &= 177.62\,\text{fb}^{+3.8\%}_{-3.3\%}\,(\text{scale}) \pm 1.6\%\,(\text{PDF} + \alpha_s).
\end{aligned}$$

Quark associated production ($t\bar{t}H$) , where a top quark pair is produced in association with the Higgs boson, has been calculated at NLO QCD with NLO EW corrections

$$\sigma_{t\bar{t}H} = 507.1\,\text{fb}^{+5.8\%}_{-9.2\%}\,(\text{scale}) \pm 3.6\%\,(\text{PDF} + \alpha_s).$$

All Higgs cross sections presented are summarized in a more compact way in Table 1.2, where a percentage expresses how often a Higgs boson is produced via each decay mode is also given. In

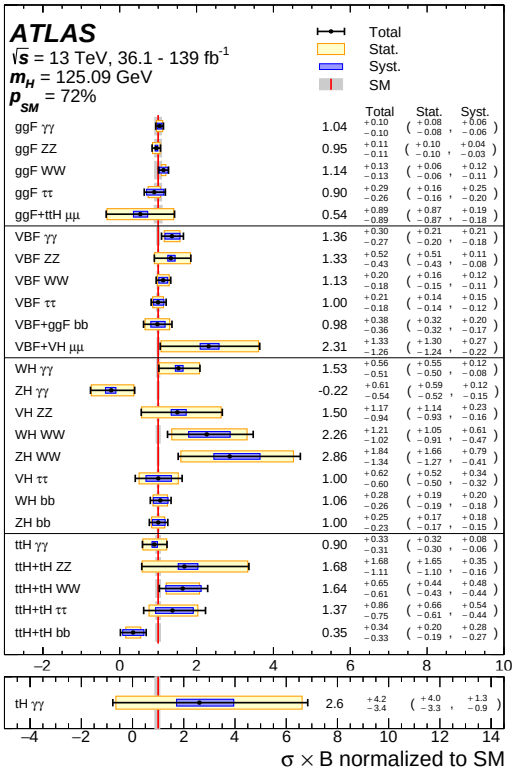

Figure 1.4: Cross sections (fixed to their SM predictions) times BF for ggF, VBF, VH and $t\bar{t}H + tH$ production in each relevant decay mode, normalized to their SM predictions. The values are obtained from a simultaneous fit to all channels [13].

the table, the total quoted uncertainties are estimated assuming no correlations between α_s and PDF uncertainties.

	ggF	VBF	WH	ZH	$t\bar{t}H$	total
σ (pb)	$48.6^{+4.6\%}_{-6.7\%}$	$3.78^{+2.2\%}_{-2.2\%}$	$1.37^{+2.6\%}_{-2.6\%}$	$0.88^{4.1\%}_{-3.5\%}$	$0.5^{+6.8\%}_{-9.9\%}$	55.1
%	88.20	6.86	2.49	1.60	0.91	

Table 1.2: Production cross section (in pb) for an Higgs boson with m_H=125 GeV at $\sqrt{s}$=13 TeV [4].

The cross section values in Table 1.2 have been tested against the SM in multiple mesurements. Figure 1.4 shows the combined measurements in terms of cross sections times branching fraction (BF) for all production and decay modes. The level of compatibility between the measurement and the SM prediction corresponds to a p-value of p_{SM} = 72% [13].

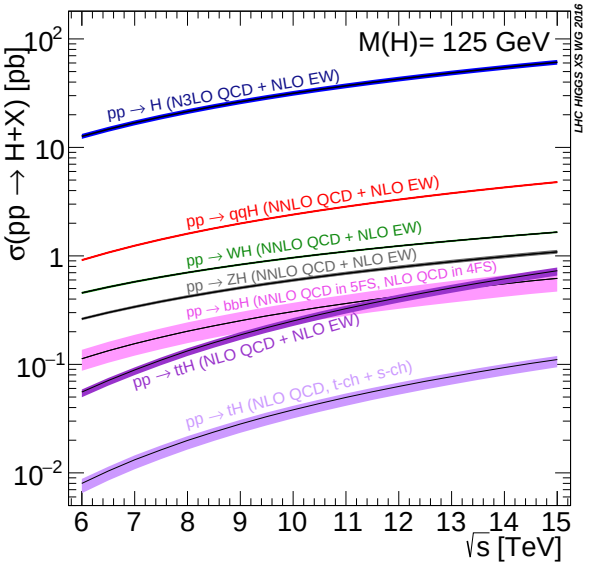

Figure 1.5: Higgs boson production cross sections as a function of the centre-of-mass-energies. The width of the lines encode the respective theory uncertainties [14].

1.2.2 Decay modes

Very shortly after the Higgs boson is produced, it decays into a pair of bosons fermions. The BF of each final state X_i is defined as

$$BR(H \to X_i) = \frac{\Gamma(H \to X_i)}{\sum_i \Gamma(H \to X_i)}$$

where $\sum_i \Gamma(H \to X_i)$ corresponds to the sum of the relative widths of all the possible Higgs boson decay modes, is depicted for a Higgs boson with $m_{\mathrm{H}=125\,\mathrm{GeV}}$ in Figure 1.6(a), where the explicit percentages are shown in Figure 1.6(b), and it is

Contributions from electrons, first generation quarks and neutrinos are assumed negligible.

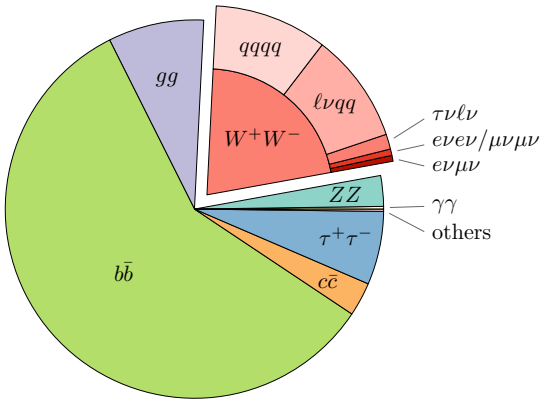

(a)

Decay mode	%
$b\bar{b}$	58.24
W^+W^-	21.37
gg	8.187
$\tau^+\tau^-$	6.272
$c\bar{c}$	2.891
ZZ	2.619
$\gamma\gamma$	0.227
$Z\gamma$	0.153
$\mu\mu$	0.022
$W^+W^- \to qqqq$	9.636
$W^+W^- \to l\nu qq$	9.396
$W^+W^- \to \tau\nu l\nu$	1.283
$W^+W^- \to e\nu e\nu/\mu\nu\mu\nu$	0.551
$W^+W^- \to e\nu\mu\nu$	0.504

(b)

Figure 1.6: Branching fraction of the Higgs boson with $m_{\mathrm{H}=125\,\mathrm{GeV}}$. The decay into W bosons is further subdivided based on the W boson decay mode [4].

1.3 Beyond the SM

The SM described in Section 1.1 is a self-consistent theory offering a precise description of all physical phenomena in its domain. A section of open issues is described below.

Hierarchy problem if the SM were a complete description of the nature, no large energy gaps would present in the explored scales, for example between the EW scale ($\mathcal{O}(10^2\,\mathrm{GeV})$) and the scale of new physics. Moreover, at the Plank scale ($\mathcal{O}(10^{19}\,\mathrm{GeV})$) the laws of physics appear not valid anymore.

Gravity the description of gravity is not included in the SM. Quantum gravity theories hypothesize a similar field behavior for gravity, with a mediator called graviton that has not been observed so far.

Dark matter and energy astrophysical studies show that 95% of the universe is made up of matter and energy that do not interact via EM force, but that are subject to gravity. Even if there are no direct measurements of this form of energy and matter, its existence has been hypothized to explain why galaxies hold together, evolve and move in the way they do.

Neutrino masses are zero according to the SM, however, the observation of neutrino flavour oscillation implies a non-zero mass for neutrinos [15].

The world in which we live is made of matter, and although the violation of CP in the SM can account for some of the **asymmetry between matter and antimatter**, it does not explain why this thesis is not annihilating within your hands.

Many theories beyond the SM (BSM) have been built over the years in order to provide answers to these questions, ranging from extending the SM (*Additional Electroweak Singlet*, *Composite Higgs model*, *SuperSymmetry*), to entirely rebuilding it (*String theory*).

1

1.4 Effective field theories and effective frameworks

Several theories and models can be used to interpret the data and compare them with the theoretical predictions. In this Section, some of them are described.

An effective field theory (EFT) is a theory based on the assumption that one can describe deviations from a known theory at a lower energy scale that are due to the presence of new physics at a higher energy scale. An EFT is based on the idea that physics at low energies (long distances) does not depend on details of physics at high energy (short distances). In order to model this effect a cut-off energy scale,Λ, that separates low and high energy, is introduced. The description of the observed physics with an EFT is thus valid up to Λ. An example of EFT is the Fermi theory of β decay [16] which can be seen as an EFT of the SM.

Searches for physics beyond SM assume that the Lagrangian of the theory can be written as the sum of the SM Lagrangian and contributions from scales above an energy cut scale Λ as

$$\mathscr{L} = \mathscr{L}_{SM} + \sum_k \frac{1}{\Lambda^k} g_{ik}(\Lambda)\mathscr{O}_{ik}$$

where $\mathscr{O}_{ik}$ are the operators constructed from combination of SM fields and g_{ik} are the corresponding coupling constants, also referred to as *Wilson coefficients*.

1.4.1 Kappa framework

Describing the nature through EFTs is not the only method to search effect of new physics. A new parametrization, which introduces new degrees of freedom in which to observe possible deviations, can be built without the need of constructing a Lagrangian. A common example of this approach is the parametrization of the presence or the absence of a new particle X by using a *signal strength* parameter μ, defined in terms of the observed cross-section σ_{obs} and predicted one σ_{theo} of X for specific decay/measurement:

$$\mu_X = \frac{\sigma_{obs,X}}{\sigma_{theo,X}}. \tag{1.22}$$

If a new scaling factor, for each coupling is introduced to the SM as a degree of freedom, the framework is called the Kappa framework [17]. These scaling factors are scalars, which implies that no differences in the shape of kinematic distributions can be observed unless a factor is given per sub-region of the analyzed quantity; this latter case is treated in Section 1.4.2.

The Kappa framework has been mainly set up to measure Higgs couplings deviation from the SM and is based on the following assumptions:

- The signals observed in different searches originated from a **single** resonance with a mass of 125 GeV.
- The resonance has a **narrow width** so that the zero-width approximation can be used to decompose the cross section as

$$\sigma \times BR(i \to H \to f) = \frac{\sigma_i \cdot \Gamma_f}{\Gamma_H}$$

  where σ_i is the production cross section of the initial state i, Γ_f the partial decay width into the final state f and Γ_H is the total width of the Higgs boson.
- The only modification is in the coupling strength, **the tensor structure of the SM stays is always assumed**.

As the κ parameters scale amplitude, they appear quadratically in all cross-section expressions:

$$\sigma \times BR(i \to H \to f) = \frac{\sigma_i^{SM}\kappa_i^2 \cdot \Gamma_f^{SM}\kappa_f^2}{\Gamma_H^{SM}k_H^2} \quad \to \quad \mu_i^f \equiv \frac{\sigma \cdot BR}{\sigma_{SM} \cdot BR_{SM}} = \frac{\kappa_i^2 \cdot \kappa_f^2}{\kappa_H^2}$$

where μ is the predicted rate relative to the SM expectation, and κ_H^2 expresses the Higgs width modification introduced by the κ factors:

$$\kappa_H^2 \equiv \sum_j \frac{\Gamma_j^{SM}}{\Gamma_H^{SM}} = \frac{\Gamma_H}{\Gamma_H^{SM}},$$

with j enumerating the decay modes of the Higgs boson listed in Figure 1.6. Equation 1.4.1 is derived under the assumption that no additional BSM Higgs decay modes (into either invisible or undetectable final states ($i \to H \to inv$)) contribute to the total width. Contributions from electrons, first-generation quarks, and neutrinos are assumed to have a negligible effect on the total width. In case of invisible (or undetectable) final states, contributing to the total width, the following relation can be used instead:

$$\Gamma_H = \frac{\kappa_H^2 \Gamma_H^{SM}}{1 - (BF_{inv} + BF_{undet})}.$$

The coupling strength of the Higgs boson to individual particles, expressed through coupling modifiers κ, has been tested against the SM, showing no significant deviation from the SM. Figure 1.7 shows the result of this model in terms of absolute coupling strength, where the measured scale factor κ_F multiplies the SM predicted coupling strength $\frac{m_F}{\nu}$ for fermions as a function of the particle mass m_F, assuming a SM Higgs boson with a mass of 125.09 GeV, ν=246 GeV vacuum expectation value of the Higgs field and the square root of the bosonic coupling scale factors scales the SM predictions for the coupling strength to W and Z bosons.

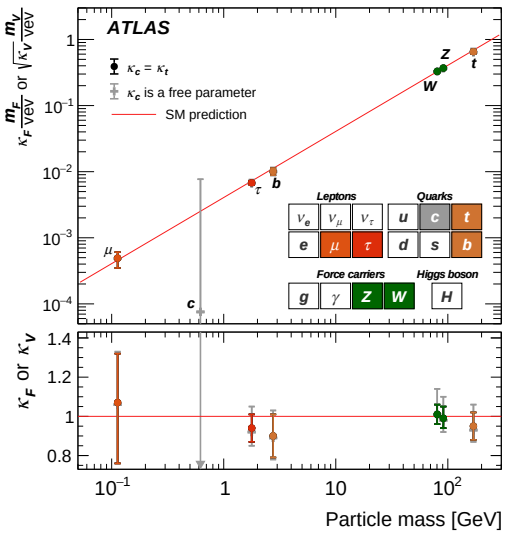

Figure 1.7: Reduced coupling strength modifiers for fermions $\kappa_F \frac{m_F}{\nu}$ and for weak gauge boson $\sqrt{\kappa_V}\frac{m_V}{\nu}$ as a function of their masses m_F and m_V, respectively, and the vacuum expectation value of the Higgs field $\nu = 246\,\text{GeV}$. The SM prediction for both cases is also shown with a red line [13].

1.4.2 Simplified Template Cross Sections

The simplified template cross sections (STXS) framework [12, 18, 19] aims to model not only scalar changes of the Higgs signal strength but also the shape of differential distributions by introducing individual scale factors for separated kinematic regions of these data. These subsets can be defined for example by Higgs production mode, jet multiplicity, transverse momentum of the Higgs boson, or mass of the di-jet system if present. The data measurement is performed in simplified fiducial volumes to maximize the measurement's sensitivity while minimizing the theory dependence. The fiducial space is divided into exclusive regions of phase space called *bins* which are specific to the different production modes. Their definitions are motivated by

- minimizing the dependence on theoretical uncertainties that are directly folded into the measurements
- maximizing the experimental sensitivity
- isolation of possible BSM effects
- minimizing the number of bins without loss of experimental sensitivity.

The number of separately measured bins evolved with time, increasing with the increase of the integrated luminosity. The current adopted scheme, called *Stage 1.2* will be described in detail in Section 7.

1.4.3 Higgs characterization framework

The Higgs Characterization (HC) [20] framework is an effective parametrization of the SM: the Lagrangian of the SM is taken after symmetry breaking, but without the Higgs sector $\mathscr{L}_{SM-H}$ while adding a new term with energy cut-off scale $\Lambda = 1$ TeV for a generic spin 0 Higgs boson X_0 (like in equation (1.15)):

$$\mathscr{L}_{HC} = \mathscr{L}_{SM-H} + \mathscr{L}_{X_0}$$

where $\mathscr{L}_{X_0}$ contains the kinematic and the interaction term of X_0 with SM particles and possibly BSM particles. The operators of $\mathscr{L}_{X_0}$ are gauge invariant under local transformation of $SU(2)_L \times U(1)_Y$. $\mathscr{L}_{X_0}$ allows mixing between CP-even states and CP-odd ones, with the parameter α parametrizing the degree of mixing. Defining $c_\alpha \equiv \cos\alpha$ and $s_\alpha \equiv \sin\alpha$ and restricting only to the third fermion generations for simplicity, the $\mathscr{L}_{X_0}$ is of the form

$$\mathscr{L}^f_{X_0} = -\sum_{f=t,b\tau} \bar{\psi}_f (c_\alpha \kappa_{Hff} g_{Hff} + i s_\alpha \kappa_{Aff} g_{Aff} \gamma^5) \psi_f X_0$$

where ϕ_f is the fermionic field, g_{Hff} is the scalar SM Higgs coupling ($g_{Hff} = m_f/v$), g_{Aff} is the pseudoscalar Higgs coupling to the fermion ($g_{Aff} = m_f/v$) and κ_i real scalar variables as introduced in Section 1.4.1.
The Higgs interaction with the vector bosons is described by

$$\begin{aligned}
\mathscr{L}^V_{X_0} = [&c_\alpha \kappa_{SM} (\frac{1}{2} g_{HZZ} Z_\mu Z^\mu + g_{HWW} W^+_\mu W^{-\mu}) && (1.23)\\
&- \frac{1}{4}(c_\alpha \kappa_{H\gamma\gamma} g_{H\gamma\gamma} A_{\mu\nu} A^{\mu\nu} + s_\alpha \kappa_{A\gamma\gamma} g_{A\gamma\gamma} A_{\mu\nu} \tilde{A}^{\mu\nu})\\
&- \frac{1}{2}(c_\alpha \kappa_{HZ\gamma} g_{HZ\gamma} Z_{\mu\nu} A^{\mu\nu} + s_\alpha \kappa_{AZ\gamma} g_{AZ\gamma} Z_{\mu\nu} \tilde{A}^{\mu\nu})\\
&- \frac{1}{4}(c_\alpha \kappa_{Hgg} g_{Hgg} G_{\mu\nu} G^{\mu\nu} + s_\alpha \kappa_{Agg} g_{Agg} G^a_{\mu\nu} \tilde{G}^{a,\mu\nu}) && (1.24)\\
&- \frac{1}{4}\frac{1}{\Lambda}(c_\alpha \kappa_{HZZ} Z_{\mu\nu} Z^{\mu\nu} + s_\alpha \kappa_{AZZ} Z_{\mu\nu} \tilde{Z}^{\mu\nu}) && (1.25)\\
&- \frac{1}{2}\frac{1}{\Lambda}(c_\alpha \kappa_{HWW} W^+_{\mu\nu} W^{-,\mu\nu} + s_\alpha \kappa_{AWW} W^+_{\mu\nu} \tilde{W}^{-,\mu\nu}) && (1.26)\\
&- \frac{1}{\Lambda} c_\alpha (\kappa_{H\partial\gamma} Z_\nu \partial_\mu A^{\mu\nu} + \kappa_{H\partial Z} Z_\nu \partial_\mu Z^{\mu\nu} + (\kappa_{H\partial W} W^+_\nu \partial_\mu W^{-,\mu\nu} + h.c.)] X_0,
\end{aligned}$$

where the $V = A, Z, W^+, W^-$ and G fields are implemented as

$$\begin{aligned}
V_{\mu\nu} &= \partial_\mu V_\nu - \partial_\nu V_\mu\\
G^a_{\mu\nu} &= \partial_\mu G^a_\nu - \partial_\nu G^a_\mu - g_C f^{abc} G^b G^c\\
\tilde{V}_{\mu\nu} &= \varepsilon_{\mu\nu\rho\sigma} V^{\rho\sigma}\\
\tilde{G}^a_{\mu\nu} &= \varepsilon_{\mu\nu\rho\sigma} G^{a,\rho\sigma}.
\end{aligned}$$

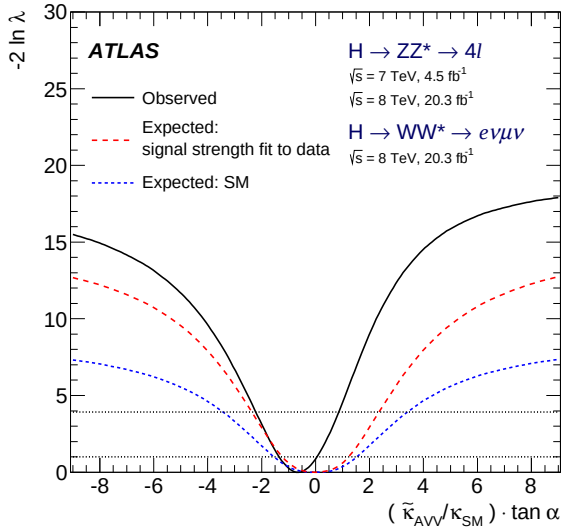

Figure 1.8: Simulated according to the SM (expected) and observed distributions of the test statistic for the combination of the $H\to WW^*\to e\nu\mu\nu$ and the $H\to ZZ^*\to 4l$ analyses. The distributions are shown as a function of the BSM coupling ratio $(\tilde{\kappa}_{AVV}/\kappa_{SM})\cdot\tan\alpha$. The 68% and 95% CL exclusion regions are indicated as lying above the corresponding horizontal lines. The expected distributions are simulated for the SM signal strength μ = 1 and presented for the signal strengths obtained from the fit to data [21].

The generic X_0 Higgs boson coincides with the SM one for $c_\alpha = 1$ and $\kappa_{Hff} = 1$ (which leads to $s_\alpha = 0$), while a completely CP odd pseudoscalar X_0 is obtained for $s_\alpha = 1$ and $\kappa_{Aff} = 1$ (which leads to $c_\alpha = 0$).

1.4.4 Testing the CP properties of the Higgs boson

The HC framework can be used to test the CP properties of the Higgs boson, and the study in the decay channel in two W bosons in this framework is presented in Section 6. Figure 1.8[21] presents the results of an earlier study, using both $H\to WW^*$ and $H\to ZZ^*$ decays, using only terms ((1.23),(1.25),(1.26)) to quantify the presence of BSM contribution.

The parameter analysed was BSM coupling ratio, $(\tilde{\kappa}_{AVV}/\kappa_{SM})\cdot\tan\alpha$, where $\tilde{\kappa}_{AVV} = \frac{1}{4}\frac{1}{\Lambda}\kappa_{AVV}$ with v the vacuum expectation value of the SM field, and here was assumed that the BSM coupling ratio has the same value for the two decay modes. Figure 1.8 shows the distribution of the test statistics, which will be described more in detail in Section 3.1, for the combination of the $H\to WW^*\to e\nu\mu\nu$ and the $H\to ZZ^*\to 4l$ analyses. The plot shows that the pure CP odd scenario is excluded, while a CP mixed scenario is possible with a CP odd contribution up to ∼30%.

1.5 References

[4] P.A. Zyla et al. "Review of Particle Physics". In: *PTEP* 2020.8 (2020), p. 083C01. DOI: 10.1093/ptep/ptaa104 (cit. on pp. 4, 5, 17, 18, 21, 23, 36, 71, 72, 86, 89, 92).

[5] Mark Thomson. *Modern particle physics*. New York: Cambridge University Press, 2013 (cit. on p. 4).

[6] Emmy Noether. "Invariant variation problems". In: *Transport Theory and Statistical Physics* 1.3 (1971), pp. 186–207 (cit. on pp. 6, 7).

[7] S.M. Bilenky and J. Hošek. "Glashow-Weinberg-Salam theory of electroweak interactions and the neutral currents". In: *Physics Reports* 90.2 (1982), pp. 73–157 (cit. on p. 9).

[8] Ian Low and Aneesh V. Manohar. "Spontaneously Broken Spacetime Symmetries and Goldstone's Theorem". In: *Physical Review Letters* 88.10 (Feb. 2002). DOI: 10.1103/physrevlett.88.101602 (cit. on p. 14).

[9] F. Englert and R. Brout. "Broken Symmetry and the Mass of Gauge Vector Mesons". In: *Phys. Rev. Lett.* 13 (9 Aug. 1964), pp. 321–323. DOI: 10.1103/PhysRevLett.13.321 (cit. on p. 14).

[10] Peter W. Higgs. "Broken Symmetries and the Masses of Gauge Bosons". In: *Phys. Rev. Lett.* 13 (16 Oct. 1964), pp. 508–509. DOI: 10.1103/PhysRevLett.13.508 (cit. on p. 14).

[11] ATLAS Collaboration. "Evidence for the spin-0 nature of the Higgs boson using ATLAS data". In: *Phys. Lett. B* 726 (2013), p. 120. DOI: 10.1016/j.physletb.2013.08.026. arXiv: 1307.1432 [hep-ex] (cit. on pp. 18, 19).

[12] D. de Florian et al. *Handbook of LHC Higgs Cross Sections: 4. Deciphering the Nature of the Higgs Sector*. CERN Yellow Reports: Monographs. 869 pages, 295 figures, 248 tables and 1645 citations. Working Group web page: https://twiki.cern.ch/twiki/bin/view/LHCPhysics/LHCHXSWG. Geneva: CERN, Oct. 2016. DOI: 10.23731/CYRM-2017-002 (cit. on pp. 19, 20, 26).

[13] Nicolas Morange et al. *Ten years with the Higgs boson: a detailed picture of its interactions from the ATLAS experiment*. Tech. rep. Geneva: CERN, Feb. 2022 (cit. on pp. 21, 26).

[14] *LHC Higgs Cross Section WG Picture Gallery*. URL: https://twiki.cern.ch/twiki/bin/view/LHCPhysics/LHCHWGCrossSectionsFigures?redirectedfrom=LHCPhysics.LHCHXSWGCrossSectionsFigures (cit. on p. 22).

[15] Douglas Clowe et al. "A Direct Empirical Proof of the Existence of Dark Matter". In: *The Astrophysical Journal* 648.2 (Aug. 2006), pp. L109–L113. DOI: 10.1086/508162 (cit. on p. 23).

[16] E. Fermi. "Versuch einer Theorie der β-Strahlen. I". In: *Zeitschrift für Physik* 88.3 (1934), pp. 161–177 (cit. on p. 24).

[17] S Heinemeyer et al. *Handbook of LHC Higgs Cross Sections: 3. Higgs Properties: Report of the LHC Higgs Cross Section Working Group*. Ed. by S Heinemeyer. CERN Yellow Reports: Monographs. Comments: 404 pages, 139 figures, to be submitted to CERN Report. Working Group web page: https://twiki.cern.ch/twiki/bin/view/LHCPhysics/CrossSections. Geneva: CERN, July 2013. DOI: 10.5170/CERN-2013-004 (cit. on p. 24).

[18] Frank Tackmann et al. "Simplified template cross sections". In: (Mar. 2016) (cit. on p. 26).

[19] S. Badger et al. *Les Houches 2015: Physics at TeV Colliders Standard Model Working Group Report*. 2016. arXiv: 1605.04692 [hep-ph] (cit. on p. 26).

[20] P. Artoisenet et al. "A framework for Higgs characterisation". In: *Journal of High Energy Physics* 2013.11 (Nov. 2013). DOI: 10.1007/jhep11(2013)043 (cit. on p. 27).

[21] ATLAS Collaboration. "Study of the spin and parity of the Higgs boson in diboson decays with the ATLAS detector". In: *Eur. Phys. J. C* 75 (2015), p. 476. DOI: 10.1140/epjc/s10052-015-3685-1. arXiv: 1506.05669 [hep-ex] (cit. on pp. 28, 114). Erratum: in: *Eur. Phys. J. C* 76 (2016), p. 152. DOI: 10.1140/epjc/s10052-016-3934-y.

2

Where: the ATLAS experiment at the LHC

Proton-proton collisions are fertile ground to test the SM prediction illustrated in Chapter 1. A description of the accelerator complex of CERN is described in section 2.1, while in Section 2.2 the ATLAS detector is illustrated, which is responsible for collecting the data used in this thesis. The data need to be processed in order to reconstruct the physical objects that will be used in the various analyses. The procedures are described in Section 2.3. The Chapter closes with an overview of the scheduled upgrades of the LHC and the ATLAS detector, with a focus on the Inner Tracker one.

Contents

2.1 The Large Hadron Collider

The Large Hadron Collider (LHC) [22] is a circular superconducting hadron accelerator and collider that is built, maintained and operated by *Conseil Européen pour la Recherche Nucléaire* (CERN). Installed in a 26.7 km tunnel constructed for the former Large Electron Positron Collider (LEP) [23], LHC is the largest and most powerful particle accelerator built to date.

LHC has been designed to collide protons at a centre-of-mass energy[1] of 14 TeV with an instantaneous luminosity of $10^{34}\,\mathrm{cm}^{-2}\,\mathrm{s}^{-1}$. The machine is also able to accelerate and collide heavy ions (Pb) with an energy of 2.8 TeV per nucleon with a peak luminosity of $10^{27}\,\mathrm{cm}^{-2}\,\mathrm{s}^{-1}$.
Among the main purposes of LHC are the intensive study of the Higgs boson, the exploration of the TeV mass scale and precise tests of the SM.

2.1.1 From LEP to LHC

At the first phase of LEP, electrons and positions were accelerated to an energy of 45 GeV per beam, sufficient for the production and the extensive study of the Z boson. During the second phase, the energy of the beams was increased to study the WWZ couplings. During the final phase, the energy of the beams was pushed to its limit in an attempt to discover the Higgs boson. The LEP collider, like other electron-positron machines, was excellent for precision physics (no substructure of the collided components results in clean events, and complete annihilation results in the precise knowledge of the collision energy). Unfortunately, the downside of accelerating low-mass particles is the loss of energy due to synchrotron radiation. Reaching higher energy, thus, was extremely complicated at LEP. Indeed, when a charged particle with energy E and mass m is accelerated in a circular trajectory of radius R, it radiates power according to Larmor's law [24]:

$$P = \frac{2}{3}\frac{e^2 c}{R^2}\left(\frac{E}{mc^2}\right)^4 .$$

Comparing the emitted power of an accelerated electron (e) and proton (p)

$$\frac{P_e}{P_p} = \left(\frac{m_p}{m_e}\right)^4 = 1.13 \cdot 10^{13}$$

it is evident that accelerating protons for a given radius leads to a smaller loss of energy.

The choice of going from LEP to LHC was driven not only by the will to explore new energy scales, which were impossible to achieve with the technology available during the LEP time, but also to investigate the substructure of the particles involved in the interactions. At the LHC, the acceleration power is not limited by synchrotron radiation but by the peak field of the dipoles in the storage ring. The nominal field is 8.33 T, corresponding to an energy of 7 TeV per beam.

[1] The centre-of-mass energy of a system is defined as the energy measured in the centre-of-mass frame. This energy corresponds to all the energy available to create new particles or to explore the internal structure of particles.

2.1.2 How the beams are created and accelerated

The CERN accelerator complex consists of a series of linear and circular machines. A sketch of the accelerator chain is present in Figure 2.1, and a description follows.

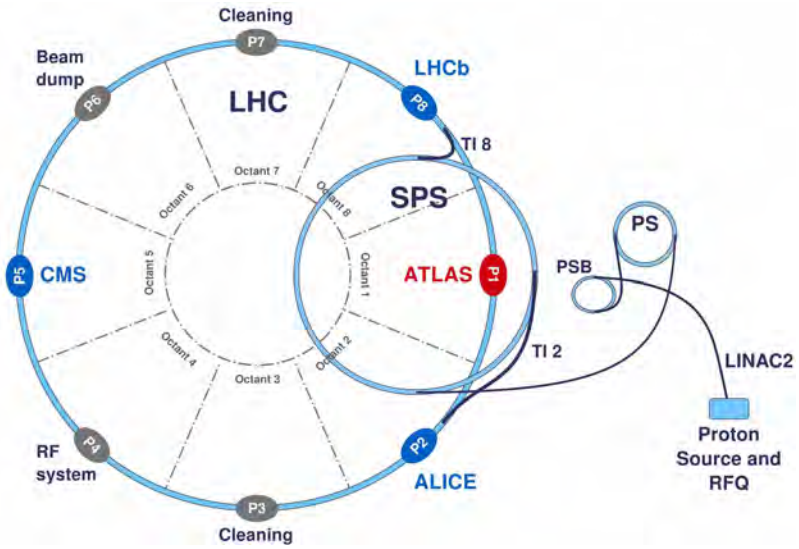

Figure 2.1: Simplified view of the acceleration chain for the LHC and its main detectors.

Protons are delivered by a duoplasmatron source [25], depicted in the bottom right hand side of Figure 2.1. A sketch of the duoplasmatron is shown in Figure 2.2. The working principle of this device is to generate a discharge that releases the electrons from the protons through a process of the type:

$$\begin{aligned} H_2 + e^- &\rightarrow H_2^+ + 2e^- \\ H_2^+ + e^- &\rightarrow H^+ + H + e^- \\ H + e^- &\rightarrow H^+ + 2e^- \\ \hline H_2 &\rightarrow 2H^+ + 2e^- \end{aligned}$$

The protons are accelerated by a 90 keV potential difference and leave the duoplasmatron with 1.4% speed of light.

The pre-accelerated protons are further accelerated up to 50 MeV in the LINAC2. The LINAC2 is a linear accelerator consisting of a series of coaxial metallic tubes connected by metallic chambers. These chambers, known as radio frequency (RF) cavities, are modeled to a specific size and shape so that electromagnetic waves become resonant and build up inside the cavity. Charged particles passing through the cavity feel the overall force and direction of the resulting electromagnetic field, which transfers energy to push them forwards along the accelerator. Figure 2.3 shows a schematic view of a linear accelerating structure. The lengths of the tube segments are chosen such that the particles reach the gap between two successive tubes only when the RF field is

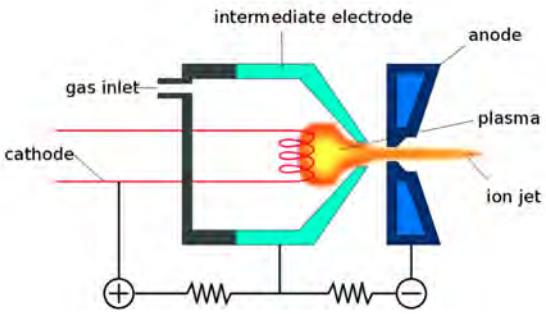

Figure 2.2: Sketch of the duoplasmatron that serves the LINAC2. Proton gas is injected in a chamber that is ionized in order to extract proton beams.

accelerating. The acceleration is most efficient when the distance between the centre of two adjacent gaps is equal to the travel time of the particles from one gap to the next.

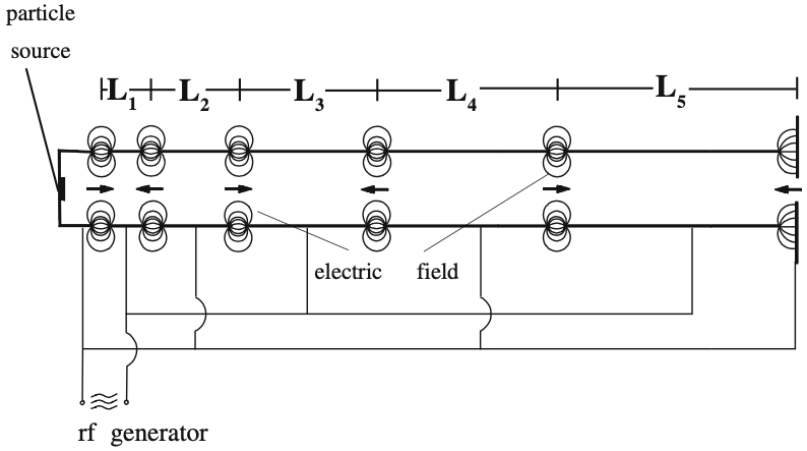

Figure 2.3: Scheme of an accelerating linear structure [26]. A variable electric field is responsible for the acceleration of the particles.

The protons are then accelerated up to 1.4 GeV in the Proton Synchrotron Booster (PSB). This accelerator is composed of four separate synchrotron pipes, stacked on top of each other, with a 25 m radius. From here, the protons are injected into the Proton Synchrotron (PS), where they reach an energy of 25 GeV. Following that is the Super Proton Synchrotron (SPS), which brings the energy of the protons up to 450 GeV, before injecting them into the LHC. The last acceleration step, which accelerates the protons to their final energy, is performed by the LHC, where the protons are injected in a clockwise and anticlockwise direction.

The LHC is equipped with 10000 superconducting magnets [27], including 1232 superconducting main dipole magnets, which provide a magnetic field up to 8.3 T responsible for keeping the particles on a circular trajectory. The LHC is divided into eight sections called *octants*.

One octant houses the acceleration system: eight superconducting radio-frequency cavities for each beam are responsible for the increase of the particle energy and for the reduction of the energy differences among the particles of the same beam. In two octants the beams are monitored: any particle straying from the ideal beam trajectory is absorbed by devices known as collimators. One octant is connected to the LHC main dump used as end of the road of particles: blocks of graphite, are used to absorb the beams when a LHC run needs to be stopped. The remaining four octants accommodate interaction points where the beams can collide, and where the experiments are located. This octant structure, as well as the four of the main experiments that are described in Section 2.1.4 is shown in Figure 2.1.

2.1.3 LHC luminosity and pileup

The accelerated beam consists of bunches of protons organized in small cylinders a few cm long and with a diameter of the order of a mm. Each proton bunch is squeezed at the interaction point down to a transverse size of a few μm. The number of protons contained in each bunch (N_p) decreases over time, due to beam loss and pp collisions in the following way

$$N_p(t) = \frac{N_p(0)}{(1 + t/\tau_{bunch}(\mathcal{L}))^2},$$

where $N_p(0)$ is the initial amount of protons and $\tau_{bunch}(\mathcal{L})$ is a parameter that depends from the structure of the bunch and the beam and how two bunches interact.

The parameter $\mathcal{L}$ is called instantaneous luminosity and it is defined as the number of particles colliding per second and per effective unit area of the overlapping beams in a Gaussian approximation, in other words:

$$\mathcal{L}(t) = f_{rev}\frac{n_1 n_2 n_b \gamma}{4\pi\varepsilon_n\beta^*}F \quad [\mathrm{cm}^{-2}\,\mathrm{s}^{-1}]$$

where

f_{rev} is the revolution frequency of the beam

n_1, n_2 are the protons contained in each colliding bunches

n_b is the number of bunches per beam

γ is the relativistic factor

ε_n is the normalized beam emittance which measures the average spread of particle coordinates in the position-momentum phase space

β^* is the beta focusing function at the collision point indicating what is the transverse size of the particle beam in the nominal beam trajectory

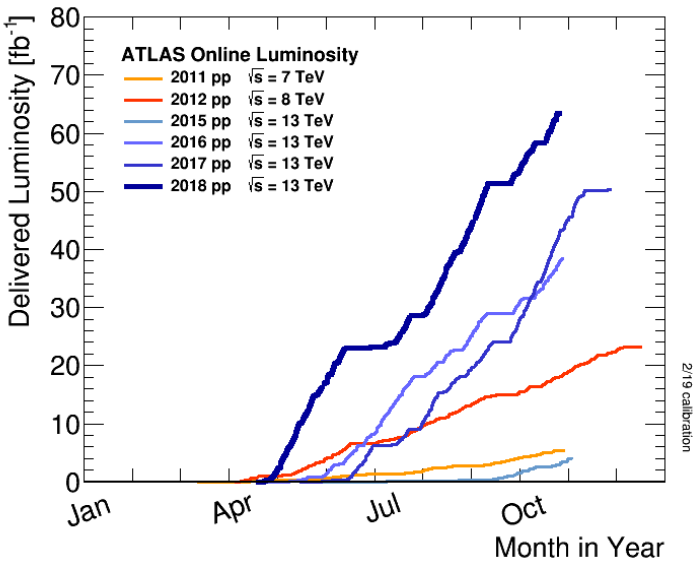

Figure 2.4: Integrated luminosity versus time delivered by the LHC to ATLAS, during stable beam conditions for pp collisions for the period 2011-2012 and 2015-2018 [28].

F is a factor that reduces the luminosity by taking into account the fact that the bunches may not cross head-to-head.

The design values of the parameters described above and their operational values for the period 2015-2018 can be found in [4].

The luminosity integrated over time (*integrated luminosity*) is the final figure of merit because it relates directly to the number of total observed events for a specific process $x \to jk$:

$$\mathcal{L}_{int} = \int_0^T \mathcal{L}(t')\mathrm{d}t', \quad \mathcal{L}_{int} \cdot \sigma_{x\to jk} = \text{number of } x \to jk \text{ events.}$$

The cumulative integrated luminosity delivered to ATLAS at in the periods[2] 2011-2012 and 2015-2018 is shown in Figure 2.4.

If multiple collisions happen in the same readout window, with a resulting high occupancy of the detector, this is called *pile-up*. Two types of pile-up are possible:

- *in-time pile-up* which refers to the inelastic pp collisions per bunch crossing. Following a Poissonian distribution, its mean value μ depends on the instantaneous luminosity as follows:

$$\mu = \frac{\mathcal{L}\sigma_{ie}}{n_b f_{rev}}$$

[2]The first period of data taking of the ATLAS experiment is called *Run 1* and it covers the years 2011 and 2012. A second *Run* took place from 2015-2018, known by the name of *Run 2*.

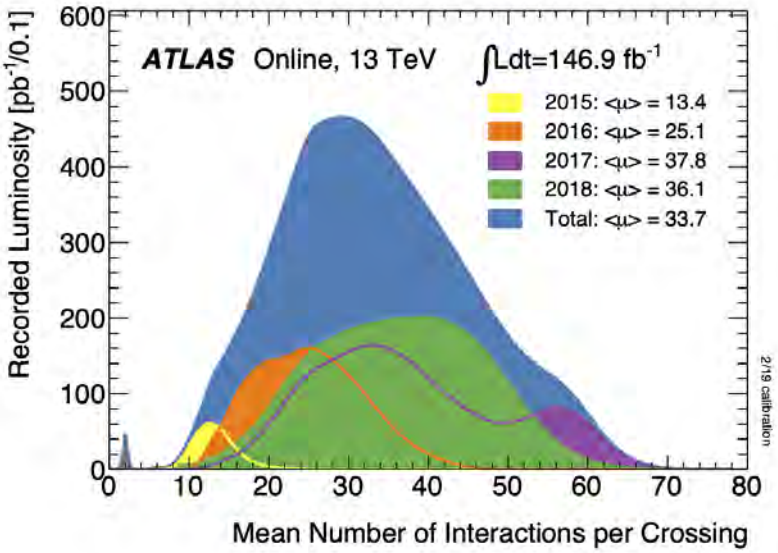

Figure 2.5: The luminosity weighted distribution of the mean number of interactions for the period 2015-2018 recorded by the ATLAS experiment. The mean number of interactions per crossing corresponds to the mean of the Poisson distribution of the number of interactions per crossing calculated for each bunch [28].

where σ_{ie} is the total inelastic cross-section of the pp collisions, n_b is the number of bunches per beam which has f_{rev} as revolution frequency;

- *out of time pile-up* which refers to additional collisions coming from neighboring bunch crossing.

Figure 2.5 shows the luminosity-weighted distribution of the mean number of interactions for the period 2015-2018 by the ATLAS collaboration.

Since the two proton bunches have a Gaussian density and do not have an infinitesimal length, the collisions will not happen all in the same place but instead will be spread out in space (along the beamline). Figure 2.6 shows a candidate Z boson event when an additional 24 reconstructed pile-up interactions are found. The bottom panel shows the longitudinal view of the 25 reconstructed vertices and how they are spread over a length of $\sim$5 cm.

2.1.4 Experiments at LHC

Around the four interaction points (octants 1, 2, 5, 8 depicted in Figure 2.1) different experiments are located: TOTal Elastic and diffractive cross section Measurement (TOTEM) [30] focusing on measuring the total pp cross section, as well as elastic and diffractive scattering processes; Large Hadron Collider forward (LHCF) [31] dedicated to the measurement of neutral particles emitted in the forward region; Monopole and Exotics Detector at the LHC (MOEDAL) [32] searching for

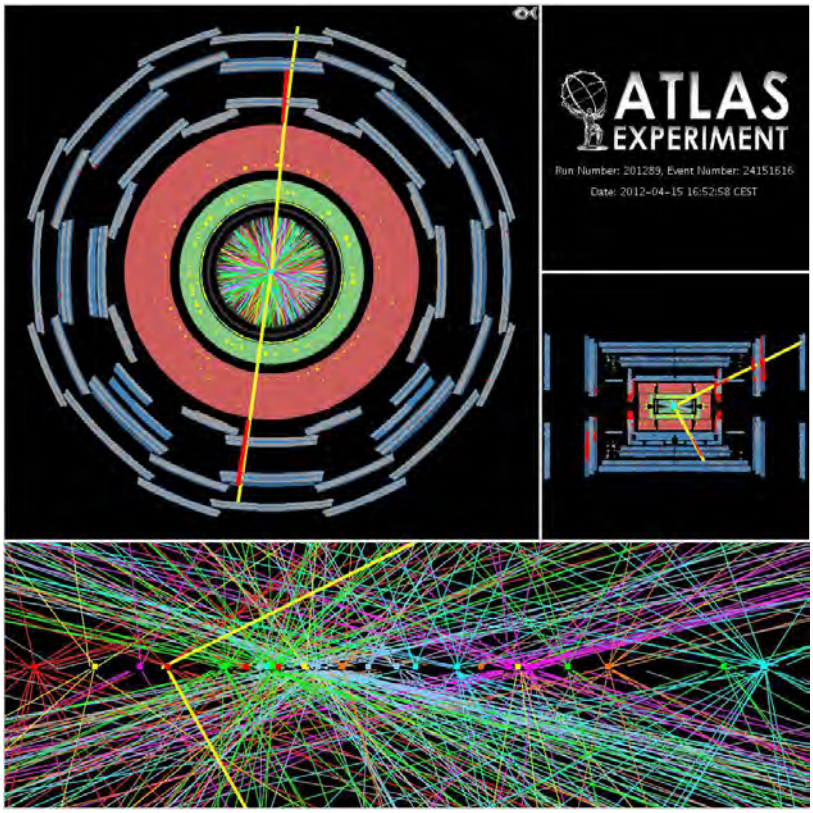

Figure 2.6: A candidate $Z \rightarrow \mu^+\mu^-$ event with 25 reconstructed interactions is shown in different projections of the ATLAS detector. The bottom panel shows a zoom-in of the view that the detector has of the event on the line where the collisions happened [29].

magnetic monopoles and for highly-ionising massive particles; A Large Ion Collider Experiment (ALICE) [33] is dedicated to studying the physics of strongly interacting matter at extreme energy densities, where a quark-gluon plasma forms; Large Hadron Collider beauty (LHCB) [34] focuses on b-physics, in particular, to measure the parameters of CP violation in the interactions of B hadrons; Compact Muon Solenoid (CMS) [35] and **A Toroidal LHC ApparatuS (ATLAS)** [36] are general-purpose detectors, designed to study a wide range of physics in pp and heavy ions collisions. The last two collaborations work independently and cross-check each other's results.

2.2 The ATLAS detector

ATLAS is a general-purpose detector that has as its main goals the investigation of the SM, as well as searches for beyond SM physics, if accessible at the LHC. The detector's aim is to record the interesting collisions happening right in its centre. Collisions take place at a nominal bunch crossing rate of 40 MHz and triggers (Section 2.3.1) select in real time which collision to store because it is impossible to store all data from all bunch crossing. The layout of the detector (see Figure 2.7) is symmetric in the forward-backward direction, with a cylindrical geometry with a radius of 12 m, a length of 44 m and a weight of approximately 7000 tons.

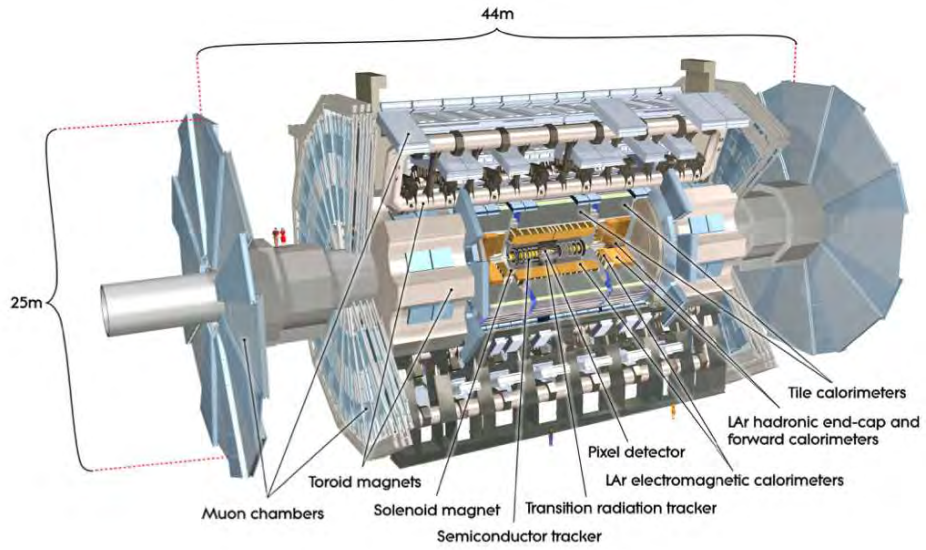

Figure 2.7: Schematic view of the ATLAS detector showing the main sub-detectors and the magnet systems [36] described in the text.

The components of the detector, arranged in an onion-like design, from the interaction point (IP) outwards, are:

- inner detector (ID), to reconstruct charged particles tracks and the interaction vertices,
- electromagnetic calorimeter (ECAL), used for electron and photon energy reconstruction,

- hadronic calorimeter (HCAL), for hadron detection
- muon spectrometer (MS), equipped for muon identification

The whole system is immersed in a magnetic field to measure the charged particle momenta in the ID and MS.

2.2.1 Coordinate system

The ATLAS detector uses a right-handed coordinate system with its origin set at the nominal IP in the centre of the detector and the z-axis set along the beam pipe. The x-axis points from the IP towards the centre of the LHC ring, and the y-axis points upwards. All the kinematic transverse quantities associated with an event are defined in the $x - y$ plane. Cylindrical coordinates (r, ϕ) are used in the transverse plane, $\phi \in (-\pi, \pi]$ being the azimuthal angle around the z-axis. In order to have a Lorentz-invariant set of angular coordinates,the pseudorapidity η is defined as a function of the polar angle θ with respect to the z-axis as:

$$\eta = -\ln\left[\tan\left(\frac{\theta}{2}\right)\right].$$

The angular distance ΔR between physics objects is defined as:

$$\Delta R \equiv \sqrt{(\Delta\eta)^2 + (\Delta\phi)^2},$$

where

$$\Delta\phi \equiv \min(|\phi_1 - \phi_2|, 2\pi - |\phi_1 - \phi_2|).$$

2.2.2 Inner detector

The ID [37], depicted in Figure 2.8, is the main charged particle tracking device of ATLAS. For this purpose, it is placed as close as possible to the IP. It is designed to measure the momenta and trajectories of charged particles with high resolution and to resolve both primary and secondary vertices. Due to its position, the ID needs to maintain a low material density, not to alter particle trajectories. Additionally, it requires high resistance to radiation for the sensors, electronics, mechanical structures, and services.

The inner detector is immersed in a 2 T solenoidal magnetic field and provides pseudorapidity coverage up to $|\eta| = 2.5$ thanks to a barrel and two end caps sub-detectors. The ATLAS solenoid magnet system [39] consists of a coil of superconducting material providing an axial magnetic field of 2 T for the ID with a stored energy of 38 MJ. It is 5.3 m long, 4.5 cm thick and with a 2.4 m inner diameter. In order to optimize the material budget the coil is placed inside the calorimeter cryostat.

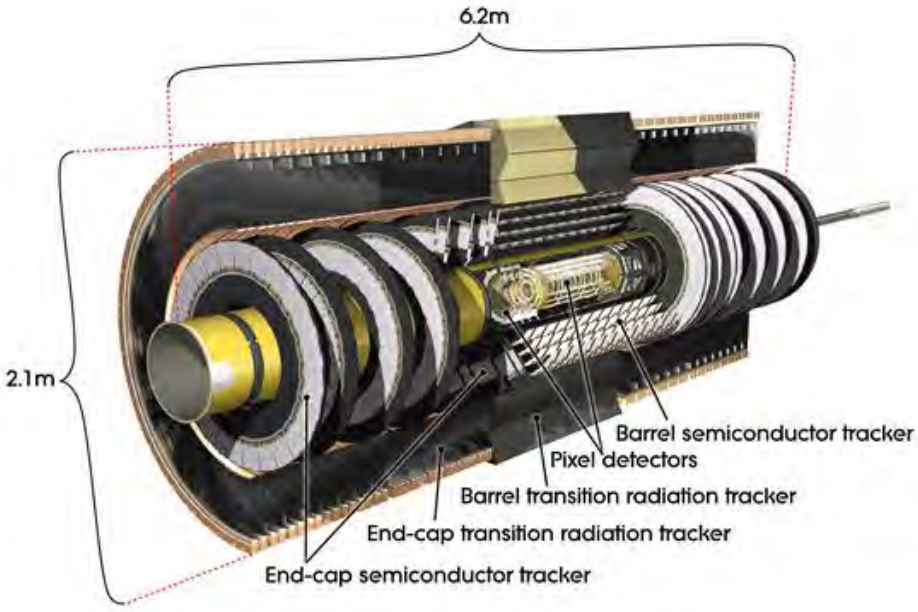

Figure 2.8: Sketch of ATLAS ID showing the arrangements of its sub-detectors [38].

A solenoid consists of a long wire wrapped around a cylinder in a helical shape, a sketch of which is depicted in Figure 2.9. When a current with intensity I flows through the wire, a magnetic field B is generated inside the coil. The field depends on the length of the solenoid l and the number of turns N:

$$B = \mu_0 \frac{NI}{l}.$$

If the length of the solenoid is longer than the wire diameter (which is the case for the ATLAS solenoid) B is parallel to the axis of the solenoid. The direction of $\vec{B}$ can be found with the *Right-hand rule* (and it is depicted with blue lines in Figure 2.9).

The ID is composed of 3 sub-detectors, and while they are different in design they share the same principle of detection: the charged particle passing through each sub-detector ionizes the detector material, and the reconstructions of the measured charge provide evidence of passing particles. The two detectors close to the beam are silicon-based, while the outer detector is gas-based.

The ID transverse momentum (p_{T}) resolution [40] in the central region can be roughly parametrized as:

$$\frac{\sigma_{p_{\mathrm{T}}}}{p_{\mathrm{T}}} \sim 0.5\% \cdot p_{\mathrm{T}} \oplus 1\%.$$

Pixel detector

The Pixel detector [41] consists of 1744 silicon pixel modules, with individual pixels size of $50 \times 400\,\mu\mathrm{m}^4$ and $250\,\mu\mathrm{m}$ thick. The pixels are arranged in four layers in the form of concentric cylinders in the barrel region and three disks perpendicular to the beamline in the end-cap regions.

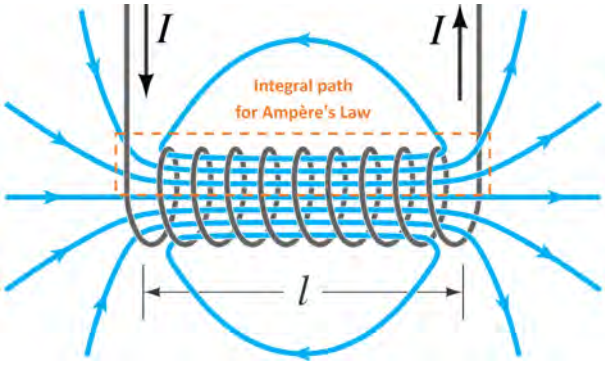

Figure 2.9: Sketch of a solenoid, which is composed of a long wire wrapped around in a helical shape in which a current with intensity I flows. The direction of the magnetic field is indicated by the blue arrows.

The layers in the barrel are placed at radial distances from the beam pipe of 31 mm, 50.5 mm, 88.95 mm and 122.5 mm covering a pseudorapidity range of $|\eta| < 2.5$. The disks in the end-cap regions are arranged at radial distances of 49.5 mm, 58 mm, 65 mm. The sensors are segmented in $R - \phi$ and z and they can resolve a hit with an accuracy of 10 µm in the transverse direction and 115 µm in the longitudinal direction.

The insertable B-layer

The innermost pixel layer in the barrel is called insertable B-layer (IBL) [42]. It was installed between Run 1 and Run 2 between the previously inner-most pixel layer and the beam pipe. The additional space for the installation of the IBL was obtained by reducing the inner diameter of the beryllium beam pipe from 59 mm to 47 mm. IBL is made of 12 million pixels of size $50 \times 250\,\mu m^4$, mounted on 14 staves that are placed at overlapping angles to provide coverage around the beam pipe. The hit resolution of the hit provided by the IBL is 8.5 µm in the transverse plane and 47 µm in the longitudinal direction. The motivation for this extra pixel layer, very close to the beamline, is the need to maintain high tracking and vertex finding efficiency with the increased luminosity of Run 2. Figure 2.10 shows the improvement of the resolution on d_0 (the transverse impact parameter) and on z_0 (the longitudinal impact parameter) as a function of p_T for values of $0 < |\eta| < 0.2$ due to the addition of the IBL.

The semi-conductor tracker

The semi-conductor tracker (SCT) is a strip detector consisting of 4088 modules mounted on four layers in the barrel and nine disks in each end-cap [44, 45]. Located at medium radii of the ID volume (299 mm $< r <$ 514 mm), the SCT offers a hit resolution of 17 µm in the $R - \phi$ plane and a 115 µm in the longitudinal direction.

The transition radiation tracker

The transition radiation tracker (TRT) [46, 47] is a straw tube detector, it works both as a drift chamber and as a transition radiation detector, where the amount of transition radiation depends on the mass of the particle.

The total energy loss of a charged particle in the transition of material is mostly directed forward

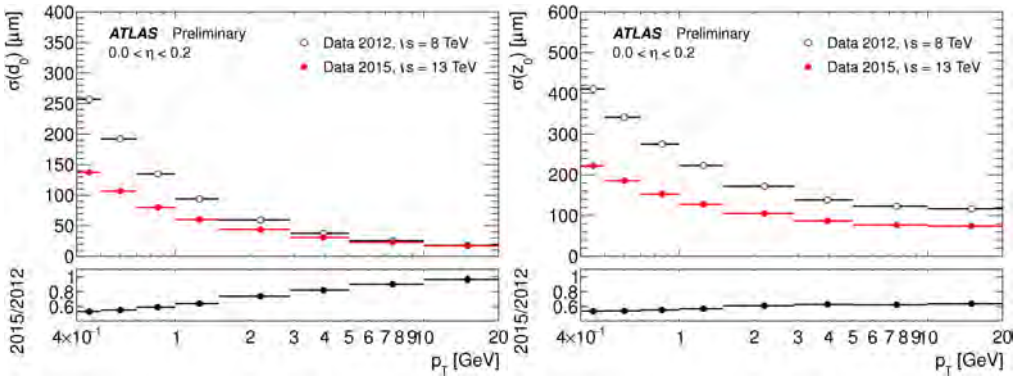

(a) $\sigma(d_0)$. **(b)** $\sigma(z_0)$.

Figure 2.10: Comparison of transverse and longitudinal impact parameters with and without the IBL as function of p_{T} for values of $0 < |\eta| < 0.2$, with data taken in 2012 at $\sqrt{s} = 8\,\mathrm{TeV}$ (no IBL) and data taken in 2015 at $\sqrt{s} = 13\,\mathrm{TeV}$ (with IBL). The lower plots show the ratio between the data collected in 2015 and 2012 [43].

and depends on $\gamma = E/mc^2$ where m is the mass of the particle:

$$I = \frac{z^2 e^2 \gamma w_p}{3c}.$$

The hit resolution of the TRT is $130\,\mu\mathrm{m}$ in the transverse direction.

2.2.3 Calorimeters

A particle traveling in a medium interacts with it. In the case of a calorimeter, the medium is highly dense in order to favor the interactions that lead to the deposit of energy that is collected. The cascade generated by the interaction of the particle with the medium is called a *shower* and it lasts until all particles of the shower are absorbed. Detecting the light emitted by a scintillating material, or detecting the charge produced when ionizing a gas or a liquid, are two different ways to estimate the deposited energy. An electromagnetic shower is produced when photons or electrons interact at high energy with matter via pair production and bremsstrahlung respectively. The parameters for caracterizing an electromagnetic shower are its depth and width.
The depth is defined as the length L of material that contains 95% of the longitudinal energy profile. The length L depends on the incident particle energy E_0, the atomic number Z of the material in which the particle is showering Z, and a parameter C_j that depends on whether the incident particle is a photon (+0.5) or an electron (-0.5):

$$L = [\ln\left(\frac{E_0}{E_c}\right) + C_j] + 0.08 \cdot Z + 9.6[X_0].$$

In the previous equation, E_c represents the critical energy, below which energy is mainly dissipated through ionization and excitation, and the radiation length X_0 which represents the amount of material that causes an electron beam to have a reduction of its energy by a factor e ($E = E_0 e^{-\frac{x}{X_0}}$). The values of E_c and X_0 are parametrized as follows:

$$E_c = \frac{610\text{MeV}}{Z + 1.24}, \quad X_0 = \frac{716.4[\text{g cm}^{-2}] \cdot A}{Z(Z+1)\ln\left(287/\sqrt{Z}\right)},$$

2

with A being the atomic weight of the material. For the material used in the electromagnetic calorimeter (ECAL) and forward calorimeter (FCAL) the parameters for liquid argon (LAr) and lead (Pb) are the following:

$$E_c^{\text{LAr}} = 32.84\,\text{MeV}, X_0^{\text{LAr}} = 14\,\text{cm},$$
$$E_c^{\text{Pb}} = 7.43\,\text{MeV}, X_0^{\text{Pb}} = 0.56\,\text{cm}.$$

The width of an electromagnetic shower is defined as the radius of a cylinder containing 95% of the shower's energy deposition:

$$R = \frac{21\,\text{MeV}}{E_c} X_0,$$

this quantity is named after German physicist Paul Molière, as *Molière radius*.
Hadronic showers are produced by hadron, as the name suggests, mostly via the strong nuclear force. Such showers consist of an electromagnetic component from the decay of photons and light particles generated in the absorption process, and of a hadronic component in which hadrons are produced. At every material interaction, about one-third of the deposited energy goes into an electromagnetic shower. Furthermore, a fraction of energy is *lost* for detection due to hadrons breaking up nuclear bonds, or the formation of long-lived or stable neutral particles escape (neutrons, K_L^0). The depth of a hadronic shower (longitudinal length in which 95% of the shower is contained, L) is given from the definition of the nuclear interaction length λ:

$$\lambda \simeq 35 \cdot A^{1/3}\text{g cm}^{-2},$$

as

$$L = 2\lambda E^{0.13} + 0.2\ln(E[\text{GeV}]) + 0.7[\lambda].$$

The width of a hadronic shower is approximately 2 times the Molière radius.

The ATLAS calorimeter system [48], shown in Figure 2.11, surrounds the ID and the solenoid magnet and its purpose is to measure the energy and direction of incident electrons, photons, hadrons, and jets. It consists of electromagnetic and hadronic sampling calorimeters with a total coverage of up to $|\eta| = 4.9$. The ECAL, the calorimeter closer to the beam pipe, covers the pseudorapidity region $|\eta| < 3.2$, is based on liquid argon as scintillator, with lead plates as absorbers.
The hadronic calorimeter (HAD), the outermost layer of the calorimeter, covers the pseudorapidity region $|\eta| < 3.9$, and uses scintillating tiles interleaved with steel plates as absorbers. The FCAL, covering the pseudorapidity range $3.1 < |\eta| < 4.9$, uses liquid argon with a copper absorber for the electromagnetic part, and two tungsten absorbers for hadronic measurements.

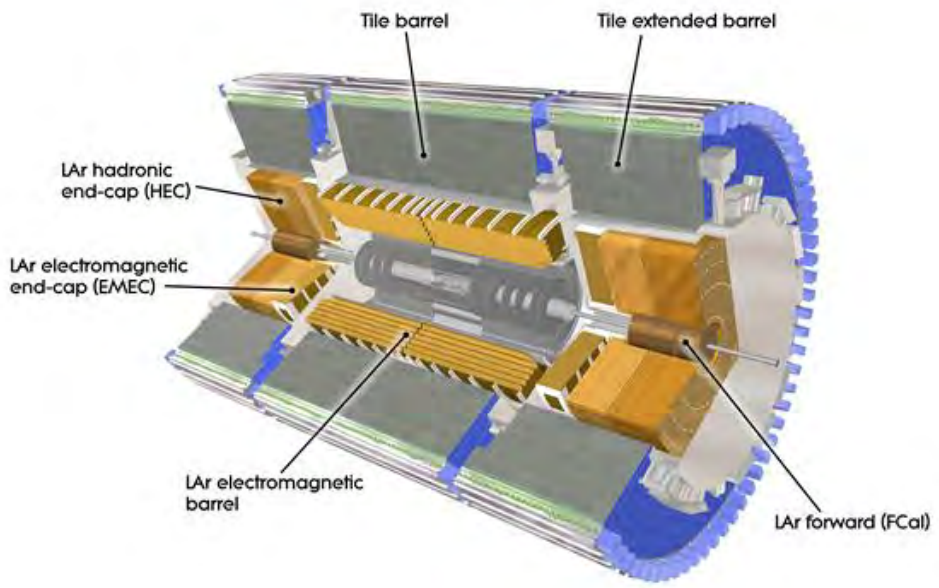

Figure 2.11: Sketch of the calorimeters of ATLAS, showing the end-cap and barrel components of the sub-calorimeters [38].

The relative uncertainty on energy measurement is of the form:

$$\sigma_E/E = \frac{a}{\sqrt{E}} \oplus \frac{b}{E} \oplus c,$$

where a, b, and c are parameters dependent on the specific detector:

a dominates at low energy and it is also referred to *stochastic term* since it depends on the statistical nature of the particle showers. It also depends on the fraction of active medium in the calorimeter.

b is the noise term, which depends on pile-up and includes electronic noise. It is usually negligible in the range of energies studied by ATLAS.

c dominates at high energy and it is mostly due to non-uniformities of the instrumentation.

The design energy resolution of the ECAL is parametrized as $\sigma_E/E = \frac{10\%}{\sqrt{E/\text{GeV}}} \oplus 0.7\%$. For the FCAL the resolution is $\sigma_E/E = \frac{50\%}{\sqrt{E/\text{GeV}}} \oplus 3\%$, and for the HAD the resolution is $\sigma_E/E = \frac{100\%}{\sqrt{E/\text{GeV}}} \oplus 10\%$ [49].

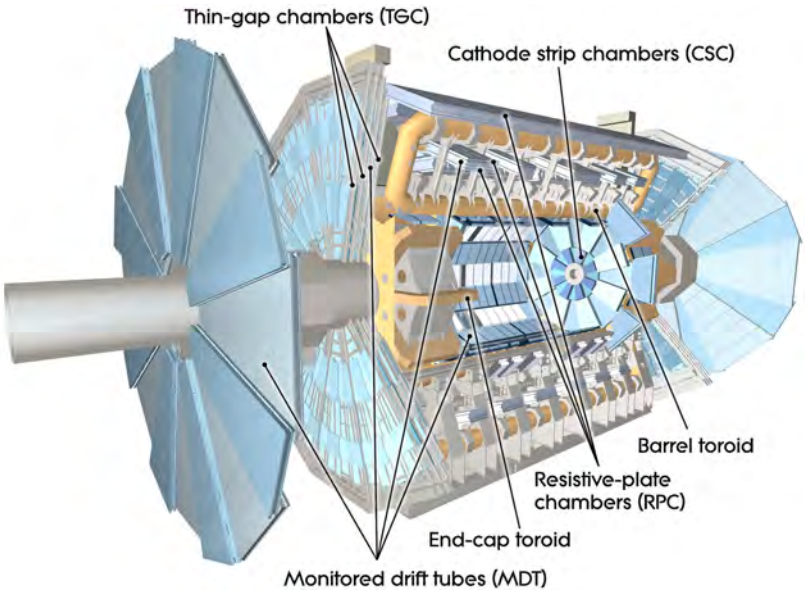

Figure 2.12: Sketch of the magnetic system of ATLAS showing the components of the MS [38].

2.2.4 Muon spectrometer

The MS [50] depicted in Figure 2.12 is located beyond the HAD, and as the name suggests, it is dedicated to muon identification. The MS consists of one central barrel and two end-caps to cover the pseudorapidity region $|\eta| < 2.7$, apart from a gap for $|\eta| < 0.1$ needed for services.

Specifically, there are

- resistive plate chamberss (RPCs) covering the range $|\eta| < 1.05$ and thin gap chambers (TGCs) in the range $1.05 < |\eta| < 2.4$ that provide rapid information to the trigger system. These chambers measure the position of the muons in η (bending plane) and ϕ (non-bending plane) with a resolution of 5-10mm. The RPCs are wireless chambers with anode and cathode plates based on an organic gas mixture. The TGCs are multi-wire proportional chambers filled with a mixture of n-pentane and CO_2, where the wire-to-cathode distances are smaller than the wire-to-wire distances;
- eight layers of monitored drift tubes (MDTs) with anode wires reaching up to $|\eta| < 2.7$ (except for the innermost end-cap layer ending at $|\eta| < 2.0$) to measure the curvature of tracks with a per-tube resolution of $80\,\mu$m and cathode strip chamber (CSC) multi-wire proportional chambers with the cathodes segmented into strips in the orthogonal directions, with a resolution of $60\,\mu$m, both using an argon-based gas mixture.

The MS is immersed in a toroidal magnetic field composed by

- a barrel Toroid system, consisting of 8 separate coils providing each a field of 0.5 T. These magnets are placed outside the calorimeters. Each barrel is 25.3 m long, with a 20.1 m outer diameter.
- an end-cap Toroid system, composed of 2 separate end-cap coils providing a field of 2 T. These magnets are placed outside the calorimeters as well. Each end-cap has 5 m axial length and 10.7 m outer diameter.

A toroid is an effectively endless solenoid in the form of a ring, see Figure 2.13. The generated magnetic field B is similar to the solenoidal one, and can be calculated according to Ampere's law and depends additionally on the radius of the torus:

$$B = \mu_0 \frac{NI}{2\pi R}.$$

If R is very large compared with the radius of the cross-section of the torus, the field is approximately uniform inside the torus, while the magnetic field is 0 outside (i.e. the net current passing through any circular path laying outside the toroid is zero).

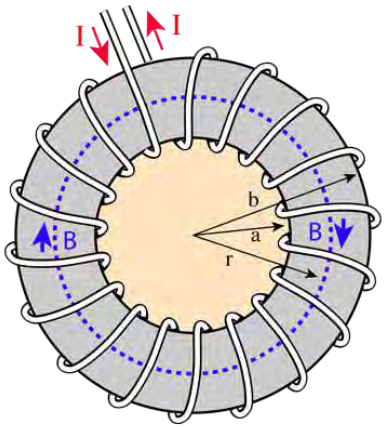

Figure 2.13: Sketch of a toroid where in red is indicated the direction of the flow of the current, and in blue the direction of the magnetic fields.

The total uncertainty on the measured p_T of muons is around 3% over a wide range of p_T, and up to 10% for muons with 1 TeV of transverse momentum [51].

2.3 From the experiment to physics objects

Each kind of detectable particle leaves a characteristic signature, since it interacts differently with the various sub-detectors. Interpreting that information together is the main purpose of the reconstruction procedure. Figure 2.14 is a computer-generated image showing how various particles leave different signatures in ATLAS.

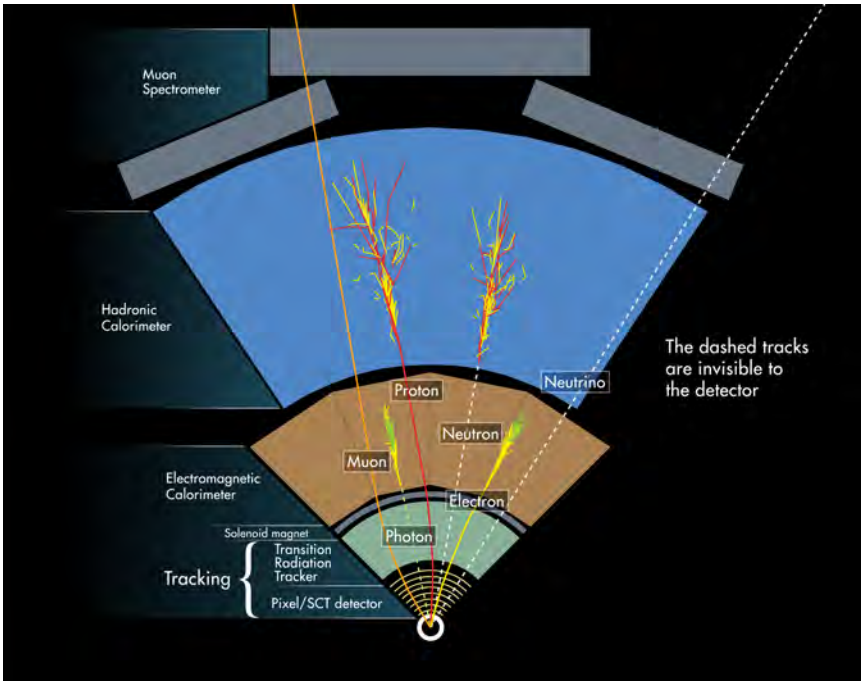

Figure 2.14: Computer generated images of particle paths in the ATLAS detector [38].

In ATLAS the translation of detector signals to physics objects is perfomed by a variety of different algorithms, which influence efficiency and performance of the reconstruction process. In order to account for that, the procedures used for reconstructions and calibration of objects are applied in the same way also to Monte Carlo (MC) simulated events.

It is necessary to mention that the collisions processed by the ATLAS detector are only a subset of all collisions that happen. This selection is performed by the ATLAS trigger system described in the next section.

2.3.1 Trigger system

The ATLAS detector is designed to observe up to 1.7 billion pp collisions per second, far larger than the number of events than can be possibly be recorded. The ATLAS trigger system reduces the flow of data to manageable levels by selecting approximately 1000 out of the 1.7 billion collisions.

The trigger system is thus responsible to make fast and educated decisions on accepting or discarding events. The ATLAS trigger system has two decision levels:

level-1 trigger (L1) , [52] implemented in custom electronic hardware. L1 uses information from the RPCs and TGCs in the muon system, as well as calorimeter information. The performed reduction of the data rate is from $\sim$40 MHz to 100 kHz. Moreover, this trigger identifies

regions of interest (RoIs) which are portions of the detectors where an object coming from a hard scatter is present.

the high level trigger (HLT) [53] is a software-based trigger that uses reconstruction algorithms close to the ones used for off-line reconstruction on the detector areas identified by the RoIs. The HLT reduces the events rate further to roughly 1 kHz.

Multiple trigger classes are present in the sequence of the HLT, and they aim at selecting:

single object triggers, consisting of at least one characteristic object

multiple object triggers, consisting of at least two characteristic objects of the same time

combined object triggers, consisting of at least two characteristic objects of different types

topological object triggers, based on information from more than one RoI.

Events selected by any trigger are written to disk and reconstructed on the *Worldwide LHC Computing Grid*, which is also used for generating of simulation data.

2.3.2 Tracking

The bases for the creation of tracks are *hits*, which represent the interactions of the particle with the sensitive material of the tracking detectors. The procedure of tracking can be divided into four stages [54]:

space-point formation: clusters of individual cells from the silicon detectors are formed by connecting adjacent hits. The splitting of clusters caused by multiple nearby particles is performed with a neural network.

space-point seeded track finding: three hits are requested to initiate a track. They are processed by applying initial cuts and a combinatorial Kalman filter technique [55] in order to form a combined particle track.

ambiguity solving: in case of ambiguities, track candidates are given a score, based on fit quality and usage of hits, e.g. a track sharing hits with other track candidates is penalized.

TRT extension: tracks that are identified as not ambiguous, and which are within the coverage of the TRT detector are then extended into the TRT volume. A successful extension increases the momentum resolution significantly.

2.3.3 Vertex finding

Vertices are reconstructed by combining tracks through three main steps: seeding, track assignment, and fitting [56] that can be roughly outlined as follows:

- The information on the impact parameter z_0 of all the reconstructed tracks is used to generate seeds, where z_0 of a track is defined as the longitudinal distance with respect to the primary vertex. A Likelihood maximization method is fed with the seed and used to find the most likely value of the vertex position.
- All the tracks compatible with the chosen seed are grouped together for fitting.
- The adaptive vertex fitting algorithm [57] is used to estimate the position of the vertex and its uncertainty.
- Tracks that are not used in the vertex, are available to repeat the procedure starting with the creation of a new seed.

2.3.4 Calorimeter clusters

The signals deriving from the calorimeters are combined into topological clusters [58]. The procedure used is guided by reconstructing three-dimensional "energy clusters" from particle showers in the active calorimeter volume. The aim is to attempt to extract a significant signal from the background of electronic noise. For this reason, the topological clusters are seeded by calorimeter cells with absolute energy $|E^{\text{cell}}| > 4\sigma_{\text{noise}}$, where σ_{noise} is the average noise in the respective cell. The seed cell forms a proto-cluster. If a neighboring proto-cluster has $|E^{\text{cell}}| > 2\sigma_{\text{noise}}$, it is added to the first one, and this procedure is repeated iteratively. Neighboring cells are defined as a) cells in the same layer and subsystem that are directly adjacent, b) those in the adjacent layer of the same calorimeter that have at least partial overlap on η and ϕ and c) adjoint cells in the transition regions between two subsystems. The resulting proto-cluster obtained in this way can be large and contain deposits from several particles, most likely in cases with collimated jets. They are subsequently split, using a topological algorithm, to obtain the final topological clusters representing particles.

The described approach here is called the *Super cluster approach* [59] and it differs from the *Sliding window approach* [60] used in 2015-2016, which is operating with a fixed window size for the cluster. Topological clusters allow modeling the behavior of the EM showers more closely.

2.3.5 Physics objects

As seen from Figure 2.14, each detectable particle leaves a set of signals in the various sub-detectors: the reconstructed vertex, the tracks, and energy deposits are combined to construct physics objects and to identify the particles from which the signal originated. The following sections present an

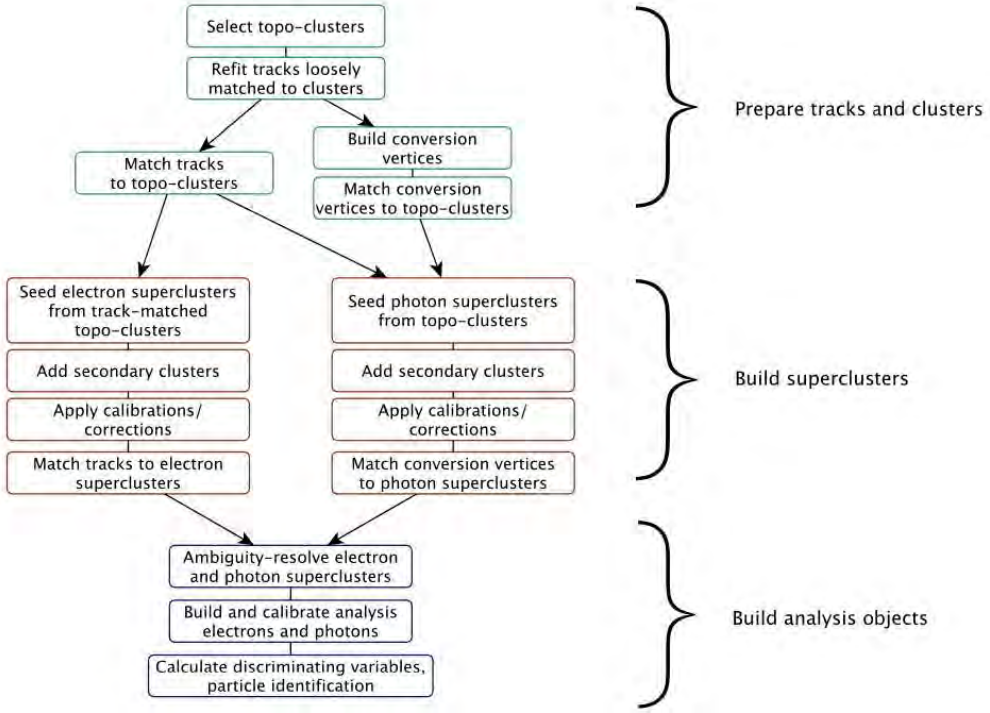

Figure 2.15: Algorithm flow diagram for the electron and photon reconstruction [59].

overview of how objects are reconstructed. Specific criteria of identification and/or isolation are described later in the text (Section 4.3) if they depend on the analysis in which they are used.

Electrons and Photons

A typical electron signature consists of an associated track in the ID, an energy cluster in the ECAL and a presampler [61]. A converted photon has a deposit in the calorimeter as well, is matched to a conversion vertex (or vertices), but has no "proper" associated track since it is a neutral particle (it does has a track when it is converted). A photon has a deposit in the calorimeter as well, with no associated tracks and matched to neither an electron track nor a conversion vertex. The described objects are reconstructed in the region with $|\eta| < 2.5$. The reconstructions process of electrons and photons is shown in Figure 2.15 and consists of the following steps [59]:

- preparing the tracks and the clusters (as illustrated in Section 2.3.2 and in Section 2.3.4)
- building clusters of energy after applying calibrations and corrections
- building analysis objects after resolving ambiguities among the objects. These ambiguities can come from the fact that electron and photon superclusters are built independently making it possible that a given seed cluster can produce both an electron and a photon. In these cases, a procedure illustrated in Figure 2.16 is followed.

Muons

The reconstruction of muons [62] is performed independently in the ID, the MS, and the calorimeters.

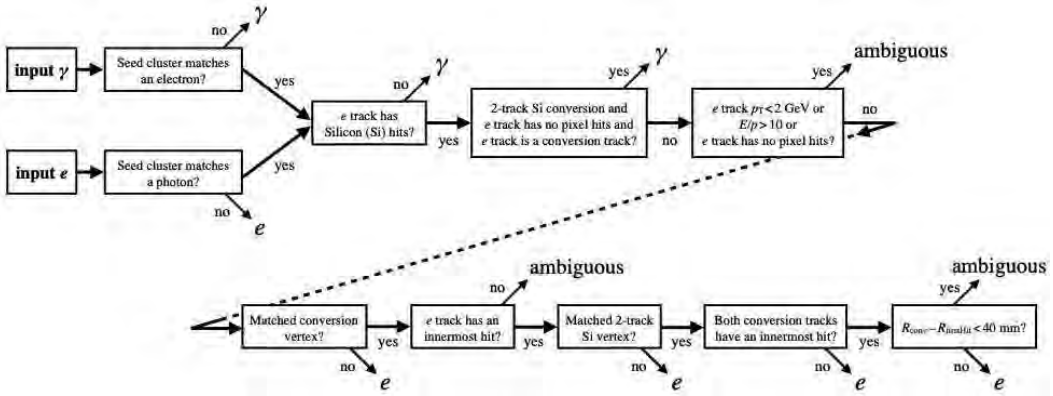

Figure 2.16: Flowchart showing how the ambiguity between an electron and a photon is resolved during object reconstructions. An *innermost hit* is a hit in the pixel layer nearest to the beam line along the track trajectory, E/p is the ratio of the energy of the supercluster and the measured momentum of the matched track, R_{conv} is the radial position of the conversion vertex and R_{firstHit} is the smallest radial position of a hit in the track or tracks that make a conversion vertex [59].

Depending on which sub-detector information is used in reconstruction, five types of muons can be defined:

- Combined (CB) muons, if the track reconstruction is performed independently in the ID and in the MS. The combined track is formed with a global refit that uses the hits coming from the two sub-detectors. If muons are reconstructed first in the MS and then extrapolated inwards to match an ID track the procedure is called *outside-in pattern recognition*, while the complementary approach (*inside-out*) happens when the ID tracks are extrapolated outwards.
- Segment-tagged (ST) muons, a track in the ID is classified as a muon if it is associated with at least one local MS track segment, once extrapolated to the MS.
- Calorimeter-tagged (CT) muons, if a track in the ID can be matched to an energy deposit in the calorimeter compatible with a minimum-ionizing particle. This algorithm recovers muon passing through the region with $|\eta| < 0.1$, which is only partially instrumented.
- Extrapolated (ME) muons, when the muon is reconstructed from the MS track only, extrapolated and loosely matched to the IP. The track in the MS needs to be well reconstructed with segments at least in two layers.
- Inside-out combined (IO) muons are reconstructed using a complementary inside-out algorithm, which extrapolates ID tracks to the MS and searches for at least three aligned MS hits to be used in a combined track fit. This algorithm recovers low-p_{T} muons which do not reach the middle MS station.

In case of a track shared among different two muon tracks, preference is given to CB muons, then IO, then ST, and lastly to CT ones.

Jets

Jet reconstruction starts by combining the four-momenta of all particle signals found within a cone

around each other. These inputs can be either obtained from energy deposits in the calorimeter or from a combination of the latter and tracks in the ID. Jets reconstructed using only calorimeter information are referred to as EMTopo jets and are used for the analysis of the 2015-2016 dataset in Chapter 6. Jets whose reconstruction uses also ID information are called particle flow (PFlow), this approach is used for the analysis of the full 2015-2018 dataset in Chapter 7. The calorimeter energy and track information is used as input to the anti-k_t algorithm [63] that defines the jets. For each pair of objects i, j, the distance measure

$$d_{ij} = \min(k_{ti}^{-2}, k_{tj}^{-2}) \frac{\Delta R_{ij}^2}{\Delta R^2}$$

is introduced, where k_t describes the transverse momentum, ΔR_{ij} the distance between both objects in η-ϕ space. The other parameter ΔR determines the characteristic size of the final jets and is chosen to be $\Delta R = 0.4$. In each iteration, the procedure groups the two objects i and j with the smallest distance d_{ij} together. The iteration stops when $d_{ij} > k_{ti}^{-2}$ for all other objects j and the remaining objects are then called jets.

The energy of each jet is then calibrated [64] in order to match the jet energy scale (JES) of truth jets defined at particle-level, with a procedure that consists of the following steps:

- The reconstructed energy is corrected for contributions from pile-up interactions, which depend on the jet area size and the number of pile-up interactions.
- The energy in the reconstructed jets and the energy of particle-level jets are compared for di-jets events and from that comparison, the absolute energy calibration is defined.
- More detailed corrections, dependent on information from all detector parts, are applied. These corrections can be for example dependent on hadron flavor and energy leakage.
- Lastly, differences between simulation and data are removed by comparing jets to well-measured reference objects.

The assumptions that are made in each step in order to perform the calibration are taken into account in specific uncertainties, e.g. pile-up uncertainties and jet energy resolution (JER), as detailed in Section 5.3.2. Figure 2.17 gives an overview of the calibration process described above.

Di-jets are also useful to generate a two-dimensional likelihood, which is at the basis of the multivariate discriminate jet vertex tagger (JVT) [65]. The JVT is used to reduce the impact of pile-up on jet reconstruction in the central region. The two observables considered are:

- Jet vertex fraction (JVF), defined as the ratio of the scalar p_{T} sum of all the tracks associated with the jet which originate from the same primary vertex over the scalar p_{T} sum of all the tracks corrected for its dependence on the number of vertices, nk, in the event :

$$\mathrm{JVF} = \frac{\sum_k p_{\mathrm{T}}^{\mathrm{trk}_k}(PV_0)}{\sum_l p_{\mathrm{T}}^{\mathrm{trk}_l}(PV_0) + \frac{\sum_{n\geq 1}\sum_l p_{\mathrm{T}}^{\mathrm{trk}_l}(PV_n)}{nk}},$$

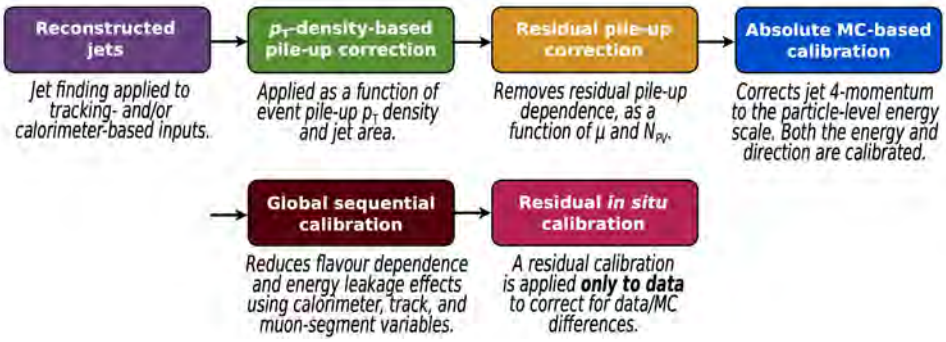

Figure 2.17: Stages of jet energy scale calibrations. Each one is applied to the four-momentum of the jet [64].

where (PV_0) is the primary vertex and (PV_n), corresponds to additional primary vertices due to pileup interactions in the same bunch crossing.

- R_{p_T}, defined as the ratio of scalar p_T sum of all the tracks in the jet originating from the same primary vertex over the fully calibrated measured p_T of the jet:

$$R_{p_T} = \frac{\sum_k p_T^{\mathrm{trk}_k}(PV_0)}{p_T^{\mathrm{jet}}}.$$

In the case of jets initiated by c or b-quarks, slightly different signatures are exhibited, which are used in flavor-tagging algorithms [66]. As c and b hadrons have a sufficiently long lifetime, they travel away, often on the scale of millimeters, before decaying. The presence of a secondary vertex, together with the presence of a soft muon in the jet, can be an indicator of a heavy quark flavor. Dedicated identifiers, usually multivariate analysis discriminants, are built in order to provide discrimination between jets of different quark flavor.

τ-leptons

Given its short lifetime, the τ-lepton typically decays before reaching the active regions of the ATLAS detector, and given its mass, it can decay either leptonically ($\sim 35\%$ of the time, $\tau \to \ell\nu_\ell\nu_\tau, \ell = e, \mu$) or hadronically ($\tau \to$ hadrons ν_τ). While in leptonic decays the light leptons are reconstructed, for hadronic decays a procedure similar to jets is needed. Hadronic reconstruction is seeded from anti-k_t 0.4 jets with $p_T > 10$GeV and $\eta < 2.5$, excluding the region $1.37 < \eta < 1.52$. In order to form a τ vertex, the candidate vertex with the largest fraction of momentum from tracks associated with $\Delta R < 0.2$ with respect to the jet is chosen. The tracks within $0.2 < \Delta R < 0.4$ are used to define isolation criteria (*Loose*, *Medium*, and *Tight*) with an efficiency independent of p_T, but dependent on the number of charged particles in the final state ("prongs"). In turn, these isolation criteria are employed in a multivariate identification algorithm, to discriminate the τ-jets from the quark- or gluon-initiated jets background [67].

Missing transverse energy

Given the nature of the pp collision at the LHC, it can be assumed that the transverse momenta of the interacting protons are balanced, leading to the vectorial sum of all traverse momenta in

the final state of the event always equal to zero. This is true unless undetectable particles such as neutrinos escape. This yields to an effective mechanism to measure invisible particles via $E_{\mathrm{T}}^{\mathrm{miss}}$, missing transverse energy (MET) [68], a vector fully determined by its magnitude and its azimuthal angle. The x and y components of the $E_{\mathrm{T}}^{\mathrm{miss}}$ are a sum of the reconstructed physics objects:

$$E_{x,y}^{\mathrm{miss}} = \sum_{i} E_{x,y}^{\mathrm{miss},i} \quad \text{with } i = e, \mu, \gamma, \tau, \text{jets, soft} \tag{2.1}$$

where each term is given by the negative vectorial sum of the momenta of the respective calibrated objects and the soft term is reconstructed from detector signal objects not associated with any object passing the selection criteria used in the particle identification algorithms. The soft term is from deposits in the calorimeter and tracks. From Equation (2.1) the magnitude of $E_{\mathrm{T}}^{\mathrm{miss}}$ and its azimuthal angle ϕ^{miss} are calculated as:

$$\begin{aligned} E_{\mathrm{T}}^{\mathrm{miss}} &= \sqrt{(E_x^{\mathrm{miss}})^2 + (E_y^{\mathrm{miss}})^2} \\ \phi^{\mathrm{miss}} &= \arctan\left(E_y^{\mathrm{miss}} / E_x^{\mathrm{miss}}\right) \end{aligned}.$$

There exist several different definitions for this quantity and they will be presented in Section 4.4.

2.4 Future of LHC

Significant changes will be made to the LHC and the ATLAS detector during the Long shutdown 2 (LS2) (the operational break from the end of 2018 to the beginning of 2021) in order to reach and cope with the ultimate design luminosity of Phase-I [69]. After a data-taking period of 4 years, at the end of 2025, another break in the LHC data taking, called Long shutdown 3 (LS3) will occur, during which the High Luminosity-Large Hadron Collider (HL-LHC) will be installed. In this period the ATLAS detector will be further upgraded.

2.4.1 LHC upgrade

In order to increase the potential for discoveries, the LHC is upgraded to HL-LHC [70]. The objective is to increase luminosity by a factor of 10 beyond the current design value. This increase will enable the observation of rare processes which occur below the current sensitivity level. The HL-LHC will be operational after 2029 and will make use of several new technologies:

- More powerful focusing magnets, generating a 12 T magnetic field, will substitute the current ones (producing 8 T) in order to produce more intense and more concentrated beams.
- New beam optics will be employed to maintain the luminosity at a constant level throughout the lifespan of the beam.

- More compact and powerful bending magnets will be installed in order to bend the trajectory of the protons over 11 m instead of 15m.
- LINAC4 will replace the current Linear accelerator 2 (LINAC2), pre-accelerating the protons beam to 160 MeV (instead of to 50 MeV).

2.4.2 ATLAS upgrade

The main improvements to the ATLAS detector during the LS2 involve:

- L1 trigger - LAr Super cells. These improve the trigger energy resolution and efficiency to select electrons, photons, leptons, jets, and $E_{\mathrm{T}}^{\mathrm{miss}}$, while enhancing the discrimination against backgrounds and fakes in an environment with high instantaneous luminosity. The improvement will be achieved by exploiting the higher resolution and the longitudinal shower information from the calorimeter used in the Level-1 trigger processors [71].
- New Small Wheels. The new detector will help reduce the large background rate suffered in the muon detector end-caps [72].

The main improvements to the ATLAS detector during the LS3, called also ATLAS Phase-II, will involve:

- New all-silicon inner tracking detector.
- New L1 trigger system architecture, where the MDT chambers will be part of the L1 trigger providing extra background reduction at low-p_{T}. (At the moment the current L1 trigger rate is $\sim$200 kHz with a latency of $\sim$20 µs is constrained by the MDT read out speed).
- New calorimeter and muon system electronics, required by the new trigger rates [73–75].

2.5 References

[4] P.A. Zyla et al. "Review of Particle Physics". In: *PTEP* 2020.8 (2020), p. 083C01. DOI: 10.1093/ptep/ptaa104 (cit. on pp. 4, 5, 17, 18, 21, 23, 36, 71, 72, 86, 89, 92).

[22] Lyndon R Evans and Philip Bryant. "LHC Machine". In: *JINST* 3 (2008). This report is an abridged version of the LHC Design Report (CERN-2004-003), S08001. 164 p. DOI: 10.1088/1748-0221/3/08/S08001 (cit. on p. 32).

[23] *LEP design report*. Copies shelved as reports in LEP, PS and SPS libraries. Geneva: CERN, 1984 (cit. on p. 32).

[24] John David Jackson. *Classical electrodynamics; 2nd ed.* New York, NY: Wiley, 1975 (cit. on p. 32).

[25] R Scrivens et al. "Overview of the status and developments on primary ion sources at CERN*". In: (Sept. 2011), 4 p (cit. on p. 33).

[26] Helmut Wiedemann. *Particle Accelerator Physics*. Graduate Texts in Physics. Berlin, Germany: Springer, 2015 (cit. on p. 34).

[27] V Parma and L Rossi. "Performance of the LHC magnet system". In: (Sept. 2009), 6 p (cit. on p. 34).

[28] *"Website of ATLAS Public Luminosity Results."* 2021. URL: https://twiki.cern.ch/twiki/bin/view/AtlasPublic/Luminosity%5C%5CPublicResultsRun2#Pileup_Interactions_and_Data_Tak (cit. on pp. 36, 37).

[29] *ATLAS Stand-Alone Event Displays*. URL: https://twiki.cern.ch/twiki/bin/view/AtlasPublic/EventDisplayStandAlone#2_vertices (cit. on p. 38).

[30] The TOTEM Collaboration et al. "The TOTEM Experiment at the CERN Large Hadron Collider". In: *Journal of Instrumentation* 3.08 (Aug. 2008), S08007–S08007. DOI: 10.1088/1748-0221/3/08/s08007 (cit. on p. 37).

[31] The LHCf Collaboration et al. "The LHCf detector at the CERN Large Hadron Collider". In: *Journal of Instrumentation* 3.08 (Aug. 2008), S08006–S08006. DOI: https://doi.org/10.1088/1748-0221/3/08/s08006 (cit. on p. 37).

[32] James Pinfold et al. *Technical Design Report of the MoEDAL Experiment*. Tech. rep. June 2009 (cit. on p. 37).

[33] The ALICE Collaboration et al. "The ALICE experiment at the CERN LHC". In: *Journal of Instrumentation* 3.08 (Aug. 2008), S08002–S08002. DOI: 10.1088/1748-0221/3/08/s08002 (cit. on p. 39).

[34] The LHCb Collaboration et al. "The LHCb Detector at the LHC". In: *Journal of Instrumentation* 3.08 (Aug. 2008), S08005–S08005. DOI: 10.1088/1748-0221/3/08/s08005 (cit. on p. 39).

[35] The CMS Collaboration et al. "The CMS experiment at the CERN LHC". In: *Journal of Instrumentation* 3.08 (Aug. 2008), S08004–S08004. DOI: 10.1088/1748-0221/3/08/s08004 (cit. on p. 39).

[36] The ATLAS Collaboration et al. "The ATLAS Experiment at the CERN Large Hadron Collider". In: *Journal of Instrumentation* 3.08 (Aug. 2008), S08003–S08003. DOI: 10.1088/1748-0221/3/08/s08003 (cit. on p. 39).

[37] ATLAS Collaboration. "The ATLAS Inner Detector commissioning and calibration". In: *Eur. Phys. J. C* 70 (2010), p. 787. DOI: 10.1140/epjc/s10052-010-1366-7. arXiv: 1004.5293 [hep-ex] (cit. on p. 40).

[38] *"ATLAS EXPERIMENT."* 2021. URL: http://atlas.ch/ (cit. on pp. 41, 45, 46, 48).

[39] *ATLAS central solenoid: Technical Design Report*. Technical design report. ATLAS. Electronic version not available. Geneva: CERN, 1997 (cit. on p. 40).

[40] Ewa Stanecka. *ATLAS Inner Tracker Performance at the Beginning of the LHC Run 2*. Tech. rep. Geneva: CERN, Apr. 2016. DOI: 10.5506/APhysPolB.47.1739 (cit. on p. 41).

[41] M. S. Alam et al. “ATLAS pixel detector: Technical design report”. In: (May 1998) (cit. on p. 41).

[42] M Capeans et al. *ATLAS Insertable B-Layer Technical Design Report*. Tech. rep. Sept. 2010 (cit. on p. 42).

[43] ATLAS Collaboration. *Impact Parameter Resolution*. URL: https://atlas.web.cern.ch/Atlas/GROUPS/PHYSICS/PLOTS/IDTR-2015-007/ (cit. on p. 43).

[44] A. Abdesselam et al. “The ATLAS semiconductor tracker end-cap module”. In: *Nuclear Instruments and Methods in Physics Research Section A: Accelerators, Spectrometers, Detectors and Associated Equipment* 575.3 (2007), pp. 353–389 (cit. on p. 42).

[45] A. Abdesselam et al. “The barrel modules of the ATLAS semiconductor tracker”. In: *Nuclear Instruments and Methods in Physics Research Section A: Accelerators, Spectrometers, Detectors and Associated Equipment* 568.2 (2006), pp. 642–671 (cit. on p. 42).

[46] The ATLAS TRT collaboration et al. “The ATLAS TRT Barrel Detector”. In: *Journal of Instrumentation* 3.02 (Feb. 2008), P02014–P02014 (cit. on p. 42).

[47] The ATLAS TRT collaboration et al. “The ATLAS TRT end-cap detectors”. In: *Journal of Instrumentation* 3.10 (Oct. 2008), P10003–P10003 (cit. on p. 42).

[48] ATLAS Collaboration. *ATLAS Calorimeter Performance: Technical Design Report*. ATLAS-TDR-1; CERN-LHCC-96-040. 1996 (cit. on p. 44).

[49] ATLAS Collaboration. “The ATLAS Experiment at the CERN Large Hadron Collider”. In: *JINST* 3 (2008), S08003. DOI: 10.1088/1748-0221/3/08/S08003 (cit. on p. 45).

[50] ATLAS Collaboration. *ATLAS Muon Spectrometer: Technical Design Report*. ATLAS-TDR-10; CERN-LHCC-97-022. CERN, 1997 (cit. on p. 46).

[51] ATLAS Collaboration. “Muon reconstruction performance of the ATLAS detector in proton–proton collision data at $\sqrt{s} = 13\,\text{TeV}$”. In: *Eur. Phys. J. C* 76 (2016), p. 292. DOI: 10.1140/epjc/s10052-016-4120-y. arXiv: 1603.05598 [hep-ex] (cit. on pp. 47, 75).

[52] ATLAS Collaboration. *ATLAS Level-1 Trigger: Technical Design Report*. ATLAS-TDR-12; CERN-LHCC-98-014. 1998 (cit. on p. 48).

[53] ATLAS Collaboration. *ATLAS High-Level Trigger, Data Acquisition and Controls: Technical Design Report*. ATLAS-TDR-16; CERN-LHCC-2003-022. 2003 (cit. on p. 49).

[54] Andreas Salzburger. “Optimisation of the ATLAS Track Reconstruction Software for Run-2”. In: *Journal of Physics: Conference Series* 664.7 (Dec. 2015), p. 072042 (cit. on p. 49).

[55] R. Kálmán. “A new approach to linear filtering and prediction problems” transaction of the asme journal of basic”. In: 1960 (cit. on p. 49).

[56] G Borissov et al. “ATLAS strategy for primary vertex reconstruction during Run-2 of the LHC”. In: *Journal of Physics: Conference Series* 664.7 (Dec. 2015), p. 072041 (cit. on p. 50).

[57] R. Fruhwirth, W. Waltenberger, and P. Vanlaer. “Adaptive vertex fitting”. In: *J. Phys. G* 34 (2007), N343. DOI: 10.1088/0954-3899/34/12/N01 (cit. on p. 50).

[58] ATLAS Collaboration. "Topological cell clustering in the ATLAS calorimeters and its performance in LHC Run 1". In: *Eur. Phys. J. C* 77 (2017), p. 490. DOI: 10.1140/epjc/s10052-017-5004-5. arXiv: 1603.02934 [hep-ex] (cit. on p. 50).

[59] ATLAS Collaboration. "Electron and photon performance measurements with the ATLAS detector using the 2015–2017 LHC proton–proton collision data". In: *JINST* 14 (2019), P12006. DOI: 10.1088/1748-0221/14/12/P12006. arXiv: 1908.00005 [hep-ex] (cit. on pp. 50–52, 95).

[60] ATLAS Collaboration. "Electron reconstruction and identification in the ATLAS experiment using the 2015 and 2016 LHC proton–proton collision data at $\sqrt{s} = 13$ TeV". In: *Eur. Phys. J. C* 79 (2019), p. 639. DOI: 10.1140/epjc/s10052-019-7140-6. arXiv: 1902.04655 [hep-ex] (cit. on p. 50).

[61] ATLAS Collaboration. "Electron efficiency measurements with the ATLAS detector using 2012 LHC proton–proton collision data". In: *Eur. Phys. J. C* 77 (2017), p. 195. DOI: 10.1140/epjc/s10052-017-4756-2. arXiv: 1612.01456 [hep-ex] (cit. on p. 51).

[62] ATLAS Collaboration. "Muon reconstruction and identification efficiency in ATLAS using the full Run 2 *pp* collision data set at $\sqrt{s} = 13$ TeV". In: *Eur. Phys. J. C* 81 (2021), p. 578. DOI: 10.1140/epjc/s10052-021-09233-2. arXiv: 2012.00578 [hep-ex] (cit. on pp. 51, 95).

[63] Matteo Cacciari, Gavin P. Salam, and Gregory Soyez. "The anti-k_t jet clustering algorithm". In: *JHEP* 04 (2008), p. 063. DOI: 10.1088/1126-6708/2008/04/063. arXiv: 0802.1189 [hep-ph] (cit. on p. 53).

[64] ATLAS Collaboration. *Jet energy scale and resolution measured in proton-proton collisions at $\sqrt{s} = 13$ TeV with the ATLAS detector*. 2020. arXiv: 2007.02645 [hep-ex] (cit. on pp. 53, 54).

[65] K G Tomiwa. "Performance of Jet Vertex Tagger in suppression of pileup jets and E_T^{miss} in ATLAS detector". In: *Journal of Physics: Conference Series* 802 (Jan. 2017), p. 012012 (cit. on p. 53).

[66] ATLAS Collaboration. *Optimisation and performance studies of the ATLAS b-tagging algorithms for the 2017-18 LHC run*. ATL-PHYS-PUB-2017-013. 2017 (cit. on pp. 54, 77, 138).

[67] ATLAS Collaboration. *Measurement of the tau lepton reconstruction and identification performance in the ATLAS experiment using pp collisions at $\sqrt{s} = 13$ TeV*. ATLAS-CONF-2017-029. 2017 (cit. on p. 54).

[68] ATLAS Collaboration. "Performance of missing transverse momentum reconstruction with the ATLAS detector using proton–proton collisions at $\sqrt{s} = 13$ TeV". In: *Eur. Phys. J. C* 78 (2018), p. 903. DOI: 10.1140/epjc/s10052-018-6288-9. arXiv: 1802.08168 [hep-ex] (cit. on pp. 55, 96).

[69] Vincenzo Izzo. *ATLAS Upgrades*. Tech. rep. Geneva: CERN, Sept. 2020 (cit. on p. 55).

[70] I Béjar Alonso et al. *High-Luminosity Large Hadron Collider (HL-LHC): Technical design report*. Ed. by I Béjar Alonso. CERN Yellow Reports: Monographs. Geneva: CERN, 2020. DOI: 10.23731/CYRM-2020-0010 (cit. on p. 55).

[71] ATLAS Collaboration. *ATLAS Liquid Argon Calorimeter Phase-I Upgrade: Technical Design Report*. ATLAS-TDR-022; CERN-LHCC-2013-017. 2013 (cit. on p. 56).

[72] ATLAS Collaboration. *ATLAS New Small Wheel: Technical Design Report*. ATLAS-TDR-020; CERN-LHCC-2013-006. 2013 (cit. on p. 56).

[73] ATLAS Collaboration. *ATLAS LAr Calorimeter Phase-II Upgrade: Technical Design Report*. ATLAS-TDR-027; CERN-LHCC-2017-018. 2017 (cit. on p. 56).

[74] ATLAS Collaboration. *ATLAS Tile Calorimeter Phase-II Upgrade: Technical Design Report*. ATLAS-TDR-028; CERN-LHCC-2017-019. 2017 (cit. on p. 56).

[75] ATLAS Collaboration. *ATLAS TDAQ Phase-II Upgrade: Technical Design Report*. ATLAS-TDR-029; CERN-LHCC-2017-020. 2017 (cit. on p. 56).

3

How: Statistics framework

The statistical tools used in the analyses contained in this thesis are described in this Chapter. Section 3.1 illustrates how to construct a test statistic. How the uncertainties of a fit model are estimated is described in Section 3.2. The picture is completed with the prescription on how to produce the post-fit distribution (Section 3.3) and an illustration of the morphing technique advantageous for simulating and testing different values of the parameter of models beyond SM (Section 3.4).

Contents

3.1 Hypothesis testing

Statistical methods are the tools that allow testing the data collected at ATLAS against theoretical predictions.

Given a set of observations $y = y_1, y_2, ..., y_N$ resulting from the outcome of an experiment, one can define the probability of these data given a certain hypothesis.
In order to construct a test statistic with good discriminating power, two hypotheses need to be provided: a null one, H_0 representing the possibility that the model predictions are true and any observed deviation is a result of pure chance, and H_1 representing the alternative hypothesis, which implies the presence of new physics effects producing the observed deviations.
Both hypotheses can depend on several parameters:

***nuisance* parameters (NPs)** are parameters related to the effects of simulation statistics and systematics uncertainties, they can be allowed to float within physical limits or fixed to some value. In the latter case, these parameters are no longer NPs. The NPs are usually indicated with θ_j, where $\vec{\theta}$ refers to the total set of NPs.

parameters of interest (POIs) are the free parameters the analysis is focused on. Typical choices for a POI are the signal strength $\vec{\theta}$, as in equation (1.22), the mass of a particle as in Figure 1.7 or the angle among two different CP hypothesis as in Figure 1.8.

Given an observed signal, one can define the statistical significance by using the *p*-value, defined as the probability, under the tested hypothesis, to observe a deviation at least as extreme as the observed deviation or more. Defining α as a predefined threshold of confidence, two different cases can be distinguished:

- *p*-value(H_0)$< \alpha$: in this case H_0 can be discarded. Commonly used thresholds are $p < 2.87 \cdot 10^{-7}$ that defines a *discovery* and $p < 1.35 \cdot 10^{-3}$ that defines an *evidence*. For a Gaussian probability distribution, a discovery corresponds to a deviation of 5σ with respect to the expectation value, while evidence corresponds to 3σ.
- *p*-value(H_1)$< \alpha$: in this case H_1 can be discarded and considered an *exclusion*. A commonly used value is $p < 0.05$ corresponding for a Gaussian probability distribution to a deviation of 2σ with respect to the expectation value.

There is actually a third option, for the case in which one does not aim to exclude a fixed hypothesis H_1, a floating hypothesis H_μ can be defined, where μ is a parameter which is varied to find the point where *p*-value(H_1)$< \alpha$.

One can construct a test statistic using the given definitions to estimate a quantity from the data. This test statistic helps in assessing the probability of the observed results being consistent with either the null or the alternative hypothesis.

3.1.1 The Likelihood function

The Likelihood function [76] for a binned counting experiment, meaning that the measurements are taken in multiple independent i regions of the explored phase space, in which the yields d_i are measured, has the form

$$L = \prod_{\text{bin } i} P(d_i|n_i(\mu, \vec{\theta})) \cdot \prod_{\theta_k} C_k(\theta_k) \tag{3.1}$$

where $n_i(\mu, \vec{\theta})$ represents the expected yield in the bin i as function of POIs and the set of NPs and $P(d|n)$ is the Poisson probability of observing d events when the theory predicts n events:

$$P(d|n) = \frac{n^d}{d!} e^{-n}.$$

The C_k terms represent PDFs from subsidiary measurements that act as constraints on the parameters θ_k. The estimation of the POIs is obtained by maximizing the Likelihood with respect to $\vec{\theta}$ and $\vec{\mu}$ or equivalently minimizing the negative log-likelihood (NLL). Given that most PDFs C_k are implemented in the form of a unit Gaussian, the possible shift of the value of the parameters θ with respect to their nominal value ($\hat{\theta}_k - \theta_{k,\text{nominal}}$) can be interpreted as a *pull*.

3.1.2 The log-Likelihood ratio

In order to test a chosen value of μ, the *profiled Likelihood ratio* $\lambda(\mu)$ can be constructed:

$$\lambda(\mu) = \frac{L(\mu, \hat{\hat{\vec{\theta}}}(\mu))}{L(\hat{\mu}, \hat{\hat{\vec{\theta}}})}. \tag{3.2}$$

$L(\mu, \hat{\hat{\vec{\theta}}})$ is the profiled likelihood, in which $\hat{\hat{\vec{\theta}}}$ is the set of NP values that maximizes the Likelihood for some given value of μ; while $\hat{\mu}$ and $\hat{\vec{\theta}}$ are the values which maximize the Likelihood over the full parameter spaces of μ and θ.

Thus, one can call the numerator the *conditional* maximum-Likelihood, whereas the denominator is the *unconditional* maximum-likelihood. From Equation (3.2) one can see that $0 \leq \lambda(\mu) \leq 1$, $\lambda(\mu)$ values close to 1 indicate that the observed data is very probable under the hypothesis μ. A test statistic can be constructed as follows,

$$t_\mu = -2 \ln \lambda(\mu) = 2\Delta\text{NLL}, \tag{3.3}$$

where $t_\mu = 0$ now expresses the maximal compatibility of the data with the tested hypothesis. The advantage of using the equation (3.3) is that Wilks' theorem can be applied. This theorem states that the distribution of t_μ is asymptotically distributed as a χ^2 with $N_{parameters}$ degrees of freedom [77, 78]. This allows to directly calculate the *p*-value from $\lambda_\mu^{observed}$.

Testing the presence of the signal

Denoting s the expected signal yields, and b the background one, the expected yield in the bin i is $n_i(\mu, \vec{\theta}) = b(\vec{\theta}) + \mu s(\vec{\theta})$. The null hypothesis H_0 does predict no signal and therefore only the presence of background, $L(H_0) = L(0, \vec{\theta}(0))$, while the unconditional or alternative hypothesis H_μ has an associated $L(H_\mu) = L(\hat{\mu}, \hat{\vec{\theta}}(\mu))$, and therefore it predicts the presence of signal in addition to background.

Generally, retrieving the *p*-value is straightforward, one needs to know the distribution of the test statistic expected, $f_t\mu(x)$, for the hypothesis that is being tested:

$$p = \int_{x^{\text{observed}}}^{\infty} f_t\mu(x)dx.$$

By applying Willks' theorem, with one degree of freedom, the *p*-value is calculated as:

$$p = \int_{x^{\text{observed}}}^{\infty} \frac{1}{\sqrt{2}\Gamma(1/2)} e^{-x/2} e^{-x/2} dx.$$

The *p*-value can be translated into the significance Z, defined as the number of standard deviations from the expected result as

$$\begin{aligned} Z &= \Phi^{-1}(1-p) \quad \text{for a one-sided distribution} \\ Z &= \Phi^{-1}(1-2p) \quad \text{for a two-sided distribution} \end{aligned}$$

where Φ is the quantile of the cumulative of a Gaussian distribution.

Asimov Dataset

A measurement's expected sensitivity is studied by creating an artificial dataset, an *Asimov dataset* where the $\vec{\theta}$ are taken at their nominal value. This peculiar dataset allows also the study of the constraints of the NPs that could be obtained with the expected data distributions and statistical uncertainties. Any difference in constraints of a given nuisance parameter between the result of the Asimov dataset fit and the data helps to diagnose unexpected constraints from data in the fit.

3.2 Modelling and estimation of uncertainties

As introduced in Section 3.1, the NPs describe the effect of the experimental and theoretical uncertainties, as well as the Monte Carlo (MC) statistical uncertainties. Prior knowledge on this parameter is often available and is used to constrain these parameters within certain bounds. The form of this prior knowledge is parametrized as C_k in Equation (3.1).

After performing the minimization of the likelihood, the NPs are measured from data.

3.2.1 Form of the *nuisance* parameter constraints

According to the type of uncertainty the NP is associated to, the constraint C_k follows a different distribution, where $\hat{\theta}$ is the maximum Likelihood estimation of θ:

Statistical uncertainties are related to statistical fluctuations of data in each bin of the input distribution and thus their distribution is Poissonian

$$Poisson(\hat{\theta}|\theta\lambda) = \frac{(\theta\lambda)^{\hat{\theta}}}{\hat{\theta}!}e^{-\theta\lambda},$$

with λ constant, often taken as the nominal value of θ.

Systematic uncertainties are all uncertainties that are not directly due to the statistics of the data, and they can be split into two groups. The uncertainty related to the statistical fluctuation of the simulated events, which follow a Poissonian distribution, depending on the predicted signal and background composition, and the uncertainties related to subsidiary measurements which are assumed to have a Gaussian constraint distribution:

$$G(\hat{\theta}|\theta,\sigma) = \frac{1}{\sqrt{2\pi\sigma^2}}e^{-\frac{(\hat{\theta}-\theta)^2}{2\sigma^2}}$$

By convention θ is scaled such that the distribution is $G(\hat{\theta}|0,1)$.

Nomenclature of the *nuisance* parameters used
The uncertainties used in the analyses presented in this thesis follow the scheme

theo_: identifies the theory uncertainties, they can be both normalization and shape uncertainties;

ATLAS_norm_: identifies the normalization uncertainty of a background process that is constrained by data in a phase space region enriched in that background sample;

ATLAS_: (except ATLAS_norm_) identifies the experimental uncertainties in the model of the detector;

gamma_stat_: identifies the MC statistical uncertainties. The Barlow Beeston [79] approximation is used, *i.e.* one gamma_stat_ is defined per bin i and it contains the MC uncertainties of all the samples in that bin.

3.2.2 Uncertainty estimation

After performing the minimization of the likelihood, the post-fit uncertainty for a given NP can be obtained from the diagonal elements of the covariance matrix $V_{ij} = cov(\hat{\theta}_i, \hat{\theta}_j)$ which is related to

the Hessian of the NLL in the following way:

$$H_{ij}(\hat{\theta}) = (V^{-1})_{ij} = -\frac{\partial^2 \log L(\hat{\vec{\theta}})}{\partial\theta_i \partial\theta_j}$$

near the minimum. Alternatively, the uncertainty of the NP can be estimated separately for each θ_i by using the profile log-Likelihood ratio

$$t_\mu(\theta_i') = -2\log \frac{L(\mu, \hat{\hat{\vec{\theta}}}(\theta_k = \theta_k'))}{L(\hat{\mu}, \hat{\vec{\theta}}(\theta_k = \hat{\theta}_k))}$$

where the condition $\theta_k = \theta_k'$ reflects the condition of the fit. According to the asymptotic approximation, $t_\mu(\theta_i')$ is distributed according to a χ^2 distribution whose confidence level (CL) can be given in terms of two-sided confidence intervals of a normal distribution with standard deviation σ. In particular the confidence interval corresponds to $n \cdot \sigma$ where $n = \sqrt{2\Delta\text{NLL}}$.

Ranking of uncertainties

In order to quantify the impact of a specific NP θ_i on the total uncertainty of a POI μ, two commonly used methods can be used: *impacts* and *breakdowns*. The impact approach computes the positive and negative impacts $I_i^{\pm}(\theta_i)$ comparing:

- an unconditional fit giving $\hat{\theta}_i$ (for which the POI $\mu = \hat{\mu}(\theta_i = \hat{\theta}_i)$)
- a conditional fit with a fixed $\theta_i = \hat{\theta}_i \pm \sigma_{\hat{\theta}_i}$ (for which the POI $\mu = \mu(\hat{\theta}_{i,nominal} \pm \sigma_{\hat{\theta}_i})$),

and then performs the difference as

$$I_i^{\pm}(\theta_i) = \mu(\hat{\theta}_{i,nominal} \pm \sigma_{\hat{\theta}_i}) - \hat{\mu}(\theta_i = \hat{\theta}_i).$$

The breakdown approach performs a conditional fit where θ_i is set constant at its best-fit value from the unconditional fit and then it computes the positive and negative breakdown $B^{\pm}(\theta_i)$ as:

$$B^{\pm}(\theta_i) = \sqrt{(\sigma^{\pm}_{\text{unconditional}})^2 - (\sigma^{\pm}_{\text{conditional}})^2}.$$

Extending the concept, the breakdown of *groups* of uncertainties is similarly defined. The effect of the limited data statistics is quantified as the residual uncertainties of the POI taken after fixing all nuisance parameters to their best-fit values.

3.3 Post-fit distributions

With the minimization of the NLL $n_{i,\text{post-fit}} = n_i(\hat{\vec{\theta}}_{\text{unconditional}})$ is calculated, and through that the *post-fit* yields. Retrieving the yields in another observable bin (m_j for example), or in another region that did not enter the fit is not exactly possible[1], but the following approximation can be

[1] In order to have a correct estimate, a mapping of the event is necessary.

used: $m_{j,\text{post-fit}} = m_{j,\text{pre-fit}} \cdot \frac{\sum_i n_{i,post-fit}}{\sum_i n_{i,pre-fit}}$.
The post-fit uncertainties, related to the yield of one or more processes l, are calculated by taking into account the linear correlation coefficient from the covariance matrix, as follows:

$$\sigma_l = \delta l(\theta_i)(V^{-1})_{ij}\delta l(\theta_j),$$

where $\delta l(\theta_i)$ is the symmetrized yield change of l depending on the NP θ_i defined as:

$$\delta l(\theta_i) = [l(\hat{\theta}_i + 1\sigma_{\text{post-fit}}(\theta_i)) - l(\hat{\theta}_i - 1\sigma_{\text{post-fit}}(\theta_i))]/2.$$

3.4 The morphing technique

The Lagrangian Morphing technique [80] allows for a continuous description of an arbitrary observable in a multidimensional space of couplings parameters. This technique is useful when testing different values of the parameter of a BSM model. Instead of generating a MC sample for each point in the parameter space, the morphing method can be used to interpolate between a few existing MC samples, generated for small or finite parameter choices.

This technique is crucial to be able to use statistical methods that require models with a continuous parametrization in their parameters such as the profile likelihood ratio method.
In general, a physical observable T depends on a configuration of a set of beyond-SM Higgs boson couplings $\vec{g}_{\text{target}} \equiv \{g_{SM}, g_{BSM,1}, .., g_{BSM,n}\}$ to known particles in the following way

$$T_{\text{out}}(\vec{g}_{\text{target}}) = \sum_i w_i(\vec{g}_{\text{target}}; \vec{g}_i) T_{\text{in}}(\vec{g}_i),$$

where T_{in} are the input distributions that can be both scalars or differential distributions of selected discrete coupling configurations $\vec{g}_i = \{\tilde{g}_{SM,i}, \tilde{g}_{BSM,1}, .., \tilde{g}_{BSM,n}\}$. The input distributions T_{in} are normalized to their expected cross sections such that T_{out} includes not only the correct shape, but also the correct cross section prediction.
The T_{in} are obtained from the MC simulation of the signal process for a given coupling configuration $\vec{g}_i$. In order to describe the signal at all possible coupling configurations, N samples are needed, where N depends on how many coupling parameters enter the production (n_p) and the decay (n_d) vertex:

$$\begin{aligned} N = \quad & \frac{n_p\,(n_p+1)}{2} \cdot \frac{n_d\,(n_d+1)}{2} + \binom{4+n_s-1}{4} && (3.4)\\ & + \left(n_p \cdot n_s + \frac{n_s\,(n_s+1)}{2}\right) \cdot \frac{n_d\,(n_d+1)}{2} && (3.5)\\ & + \left(n_d \cdot n_s + \frac{n_s\,(n_s+1)}{2}\right) \cdot \frac{n_p\,(n_p+1)}{2} && (3.6)\\ & + \frac{n_s\,(n_s+1)}{2} \cdot n_p \cdot n_d + (n_p+n_d)\binom{3+n_s-1}{3}, && (3.7) \end{aligned}$$

and where n_s is the number of couplings shared in production and in decay.

In this expression the individual contribution can be identified:

- Equation (3.4) contains the terms affecting only production, only decay, or only shared couplings (this is the case where one coupling parameter is affecting either only production/decay and one or more are affecting the other vertex (decay/production) or the case where there are only parameters that are shared among production and decay);
- Equation (3.5) contains the terms that are of second order in decay-only couplings (this is the case where there are couplings affecting the production, couplings shared between the production and decay, and only one coupling parameter affects the decay) ;
- Equation (3.6) contains the terms that are of second order in production-only couplings (this is the case where there are couplings affecting only the decay, couplings that are shared between the production and decay, and only one coupling parameter is affecting the production);
- Equation (3.7) contains the terms that are in first order in either production or decay or both (this is the case where there are multiple coupling parameters affecting only the production, multiple couplings affecting only the decay, and couplings affecting both vertices)

In the case of the Higgs gluon fusion process with subsequent decays to vector bosons, the production and decay will have a completely disjoint set of couplings, and the number of input samples will be given by equation Equation (3.4) by setting $n_s = 0$, $n_p = 2$ (CP-even and CP-odd couplings), $n_d = 1$ (only the SM CP-even HWW coupling):

$$N_{ggF} = \frac{n_p(n_p + 1)}{2} = 3.$$

3.5 References

[76] R. J. Barlow. *Statistics: A Guide to the Use of Statistical Methods in the Physical Sciences (Manchester Physics Series)*. Reprint. WileyBlackwell, 1989 (cit. on p. 63).

[77] S. S. Wilks. "The Large-Sample Distribution of the Likelihood Ratio for Testing Composite Hypotheses". In: *Annals Math. Statist.* 9.1 (1938), pp. 60–62. DOI: 10.1214/aoms/1177732360 (cit. on p. 63).

[78] Glen Cowan et al. "Asymptotic formulae for likelihood-based tests of new physics". In: *The European Physical Journal C* 71.2 (2011), p. 1554 (cit. on p. 63).

[79] Roger Barlow and Christine Beeston. "Fitting using finite Monte Carlo samples". In: *Computer Physics Communications* 77.2 (1993), pp. 219–228 (cit. on p. 65).

[80] M. Baak et al. "Interpolation between multi-dimensional histograms using a new non-linear moment morphing method". In: *Nuclear Instruments and Methods in Physics Research Section A: Accelerators, Spectrometers, Detectors and Associated Equipment* 771 (Jan. 2015), pp. 39–48. DOI: 10.1016/j.nima.2014.10.033 (cit. on p. 67).

4

The $H \to WW^*$ analysis concepts

This thesis presents two analyses, one, the ***Properties*** analysis, with the aim of studying the CP properties of the top-Yukawa coupling (Section 1.1.5), while the second, the ***Couplings*** analysis studies the ggF and VBF cross section of the Higgs boson in the $H \to WW^*$ decay channel.
This Chapter is to be intended as a general illustration of the common points of the two analyses: the topology of the $H \to WW^*$ decay (Section 4.1), the backgrounds that affect it (Section 4.2), and how the physics objects used are defined (Section 4.3). The Chapter concludes with the observables useful for signal-background discrimination (Section 4.4).

Contents

4.1 The $H\to WW^*\to \ell\nu\ell\nu$ decay channel

As presented in Section 1.2.2, the second highest branching fraction decay mode of the Higgs boson is a pair of opposite charge W bosons. The W bosons live too shortly to be detected, while their decay products can be measured. The measured branching fractions of all relevant decay modes are depicted in Figure 4.1. While electrons and muons are stable enough to be measured by the detector, taus generally decay further inside the ATLAS detector, and it is for this reason that in Figure 4.1 the observed τ decay branching ratios are also shown.

The total branching fraction of the W boson to leptons, $\mathcal{B}_{W\to e\mu/\mu\nu/\tau\nu}$, is $\sim$ 32.7%, with the branching fraction $\mathcal{B}_{\tau\to e\mu/\mu\nu}$ of τ decaying to lighter leptons ($l = e, \mu$) being $\sim 35.2\%$. The decays $W \to \tau\nu_\tau \to l\nu_l\nu_\tau$ are included in the notation that is used in the text: $H\to WW^*\to \ell\nu\ell\nu$.

Given the numbers in Figure 4.1, the approximate total chances of finding a Higgs boson decay via a pair of W bosons to two leptons, a single lepton or a fully hadronic final state can be calculated. Indeed in 37% of the $H\to WW^*$ cases, the final state contains a single lepton, in 6.4% of the cases two leptons, and in the remaining cases, the final state will be fully hadronic (55.9% of the time). This calculation is only an approximation, since the numbers of Figure 4.1 refer to an on-shell W boson, while in the $H\to WW^*$ decay one of the W boson is off-shell.

Despite the really small percentage of $H\to WW^*$ ending up with a final state containing two leptons, having two highly energetic and oppositely charged leptons allows to select events by using dedicated triggers on leptons. These two leptons are ordered with respect to their transverse momentum: $p_{\mathrm{T}}^{\mathrm{lead}}$ (or p_{T}^{l1}) denotes the lepton with the highest, or *leading*, transverse momentum, and $p_{\mathrm{T}}^{\mathrm{sublead}}$ (or p_{T}^{l2}) indicates the sub-leading one. The two leptons used in the analyses are selected to be of different-flavour (DF) to reduce the background which arises from the Drell-Yan (DY) processes, or from pair production. For this reason, the process is denoted from here on as $H\to W^\pm W^{\mp *}\to l^-\bar{\nu}_l l'^+\nu_{l'}$.

In the next sections, the spin and kinematic properties of the decay will be used to distinguish these $H\to W^\pm W^{\mp *}\to l^-\bar{\nu}_l l'^+\nu_{l'}$ decays from other processes producing opposite sign lepton pairs.

4.1.1 The spin-correlation argument

Figure 4.2 shows, in the Higgs rest frame, the three possible decays $H\to W^\pm W^{\mp *}\to l^-\bar{\nu}_l l'^+\nu_{l'}$, allowed by spin conservation, where the black arrows indicate the particles' direction of motion and the blue arrow indicate their spin projection. Since the Higgs boson has spin 0, there are three possible scenarios:

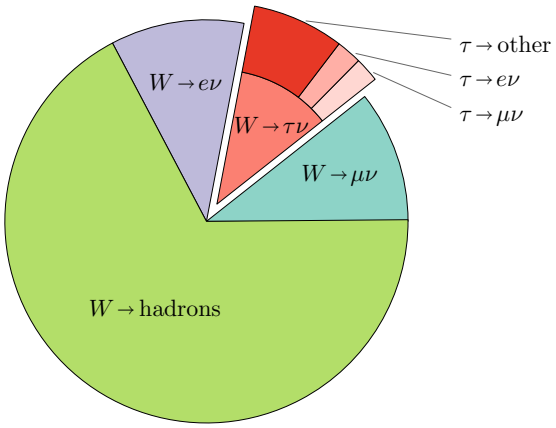

(a)

Decay mode	%
$W \to e\nu$	10.71±0.16
$W \to \tau\nu$	11.38±0.21
$W \to \mu\nu$	10.63±0.15
$W \to$ hadrons	67.41±0.27
$\tau \to e\nu$	17.82±0.04
$\tau \to \mu\nu$	17.39±0.04
$\tau \to$ other	64.79±0.06

(b)

Figure 4.1: Measured branching fraction of the decay of the W boson in percentage with the respective uncertainty. The measured decay branching ratio of the τ lepton is also shown, [4].

- (left) the W bosons exhibit a positive helicity[1] λ. The direction of the spin of the decay products of the W^+ needs to be the same: the neutrino, being right-handed has its spin opposite to the direction of motion, while the anti-lepton has its spin aligned with the direction of motion. For the W^- the same argument applies: the anti-neutrino needs to have positive helicity, and the lepton negative one.
- (right) the W bosons exhibit a negative helicity. The direction of the spin of the decay products of the W^+ needs to be the same: the neutrino has its spin opposite to its direction of motion, while the anti-lepton has positive helicity. Similarly for the W^-: the anti-neutrino shows positive helicity and the leptons negative one.
- (middle) the W bosons have helicity equal to 0. The direction of the spin of the decay products of the W^+ needs to be opposite, therefore the neutrino has negative helicity and the anti-lepton is forced to have negative helicity as well. The same reasoning applies to the W^-: the positive helicity of the anti-neutrino forces the lepton to have positive helicity. Despite the fact that the light leptons are not massless, their mass is infinitesimal with respect to the mass of the W bosons (even in the off-shell scenario), forcing them to have their helicity equal to their chirality. For this reason, this decay is suppressed.

In conclusion, the charged leptons, are preferably emitted in the same direction with the opening angle decay between them tending to be small, whereas the two neutrinos are emitted in the opposite direction resulting in a large missing transverse energy, E_{T}, due to the structure of the weak interaction.

[1] The helicity of a particle is defined as the projection of the spin onto the direction of its momentum. In the case of massless particles, or particles with an extremely small mass, helicity coincides with chirality. This leads to the fact that massless right-handed particles *need* to have positive helicity, and left-handed ones need to have negative helicity.

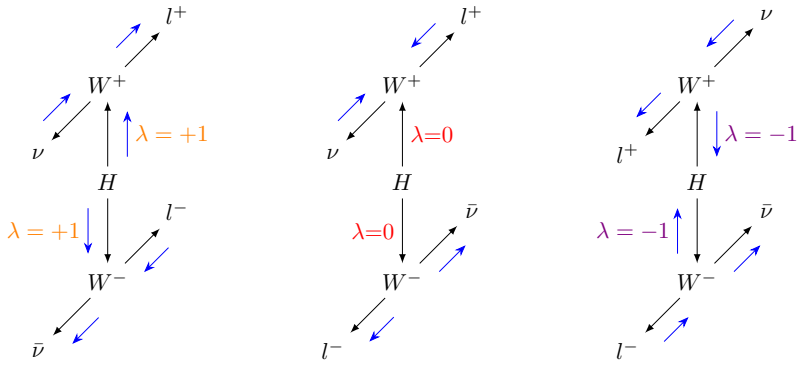

Figure 4.2: Spin-correlation in the $H \to W^{\pm}W^{\mp *} \to l^-\bar{\nu}_l l'^+\nu_{l'}$ decay channel. The black arrows indicate the direction of motion of the particles, and the blue arrows indicate the direction of the spin. The left (right) configuration exhibits a positive (negative) helicity (λ) with the two charged leptons emitted in the same hemisphere, opposite to the neutrinos. The middle configuration is suppressed.

4.2 Main backgrounds

Several processes mimic the final state of the $H \to WW^* \to \ell\nu\ell\nu$, the most important ones are top production ($t\bar{t}$ and Wt), WW, W + jets, $Z \to \tau\tau$, $Z \to ee/\mu\mu$, and WZ. Further significant contributions stem from $W\gamma^{(*)}$, and ZZ production.

Top quark background
Top quark production, mainly $t\bar{t}$ and Wt, produces the majority of the di-lepton+$E_{\mathrm{T}}^{\mathrm{miss}}$ events at the LHC. This happens because the decay width of the top quark is dominated by the two-body channel $t \to Wb$ [4]. When the W bosons decay leptonically, this final state is similar to the final state of the signal process, with the exception of the presence of b-jets. Because of that distinction, a veto on the presence of the b-quarks is usually applied to reduce this background.

WW background
The WW contribution includes the $gg \to WW$ and $q\bar{q}/g \to WW$ processes, which are further split in contributions containing only electroweak vertices (EW WW) and those containing a QCD vertex (QCD WW).

Z+jets background
The $Z/\gamma^* \to \tau\tau$ background arises from pair production of τ leptons, where one τ decays to an electron and a neutrino and the other decays to a muon and a neutrino, thus mimicking the final state signature of the $H \to WW^* \to \ell\nu\ell\nu$ analysis. However, the two charged leptons tend to be oppositely aligned, resulting in a lower total momentum, which makes it possible to reduce this background with kinematic selection criteria.

W+jets background
When a W boson is produced in association with one or more jets, it is usually referred to as W+jets background. It is considered a background for the signal when one of the jets is misidentified

as prompt lepton. A misidentified lepton can be a *non-prompt lepton* which arises from leptonic decays of heavy quarks, or a *fake lepton* when light jets are accounted as leptons. The method to estimate the amount of fake leptons is described in Section 5.4.1.

Other diboson backgrounds
$W\gamma^{(*)}$ production can mimic the signal final state when a photon converts to an electron-positron pair and the lepton with the highest p_{T} is reconstructed as a lepton candidate. Furthermore, WZ and ZZ final states containing two, three, or four leptons constitute a background when the additional leptons are lost or misidentified.

Other Higgs backgrounds
The Higgs production modes that are not targeted by the specific analysis, as well as VH, $H \to \tau\tau$, and $t\bar{t}H$, are considered backgrounds.

4.2.1 Modelling of the backgrounds

In order to model some of the backgrounds and to cross-check the accuracy of their simulation, control regions (CRs), are defined. These regions are enriched in a given type of background events and have a negligible contribution from the signal events. The regions enriched in signal are called signal regions (SRs).
When defining a region CR_X enriched of background X, a normalization factor (NF) is defined as the ratio between the number of observed data events over the number of simulated background events in the CR:

$$\mathrm{NF}_X = \frac{N^{data}_{\mathrm{CR}_X}}{N^{X,MC}_{\mathrm{CR}_X}}.$$

Using the NF_X scale factor the number of background events in the SR can be corrected as

$$N^{X}_{\mathrm{SR}} = \mathrm{NF}_X \cdot N^{X,MC}_{\mathrm{SR}}.$$

However, this approach is valid only if there are no large kinematic differences between the SR and the CR.

In case of multiple CRs, a *Matrix Inversion* method is used to calculate the different NFs, by taking into account that a single background can be present in multiple CRs. The matrix relation for two CRs is defined as follows:

$$\begin{pmatrix} N^{data}_{\mathrm{CR}_X} \\ N^{data}_{\mathrm{CR}_Y} \end{pmatrix} = \begin{pmatrix} N^{X,MC}_{\mathrm{CR}_X} & N^{Y,MC}_{\mathrm{CR}_X} \\ N^{X,MC}_{\mathrm{CR}_Y} & N^{Y,MC}_{\mathrm{CR}_Y} \end{pmatrix} \cdot \begin{pmatrix} \mathrm{NF}_X \\ \mathrm{NF}_Y \end{pmatrix},$$

from which the NFs can be extracted:

$$\begin{pmatrix} \mathrm{NF}_X \\ \mathrm{NF}_Y \end{pmatrix} = \begin{pmatrix} N_{\mathrm{CR}_X}^{X,MC} & N_{\mathrm{CR}_X}^{Y,MC} \\ N_{\mathrm{CR}_Y}^{X,MC} & N_{\mathrm{CR}_Y}^{Y,MC} \end{pmatrix}^{-1} \cdot \begin{pmatrix} N_{\mathrm{CR}_X}^{data} \\ N_{\mathrm{CR}_Y}^{data} \end{pmatrix}. \tag{4.1}$$

The total number of background events X and Y is calculated as

$$N_{\mathrm{SR}}^{X+Y} = \begin{pmatrix} N_{\mathrm{SR}}^{X,MC} & N_{\mathrm{SR}}^{Y,MC} \end{pmatrix} \cdot \begin{pmatrix} \mathrm{NF}_X \\ \mathrm{NF}_Y \end{pmatrix}.$$

The matrix inversion method is used to correct the background events in the SRs for optimization and illustration purposes only. When the signal extraction is performed the NFs are free parameters that are constrained simultaneously in the SRs and CRs.

4.3 Object definition

4

After being reconstructed, as presented in Section 2.3, the physics objects are classified according to further requirements listed below.

4.3.1 Electrons

Identification
A likelihood approach is used to distinguish the real electrons originating from hard scattering, from the falsely reconstructed ones, e.g. jets faking electrons. The features of the electron candidate are evaluated with multivariate analysis techniques, thanks to which the electron is categorized as *true* or *fake*. Three operating points, optimized in bins of $|\eta|$ and E_{T}, are constructed in order to have three nested levels of identification: *LooseLH*, *MediumLH* and *TightLH*, so that the tighter selections include the looser ones.

Isolation
The energy of the particles produced nearby the identified electron is used to distinguish prompt electrons from electrons originating from converted photons, from heavy flavour hadron decays, and from light hadrons wrongly identified as electrons. Five isolation working points are defined: *Loose*, *Tight*, *Gradient*, *GradientLoose* and *LooseTrackOnly* using two discriminating variables:

- $E_{\mathrm{T}}^{cone0.2}$, defined as the sum of transverse energies of topological clusters found within a cone of $\Delta R = 0.2$, with $\Delta R = \sqrt{\Delta\Phi^2 + \Delta\eta^2}$ around the electron candidate, excluding the clusters of the electron itself;
- $p_{\mathrm{T}}^{varcone0.2}$, defined as the sum of transverse momenta of all the tracks found within a cone of $\Delta R = 0.2$ around the electron candidate track, excluding the track of the electron itself.

The *Loose* and *Tight* requirements provide an isolation efficiency not depending on p_{T}, of 99% and 95% respectively. Instead, *Gradient* and *GradientLoose* provide isolation efficiency depending on p_{T}. Finally, *LooseTrackOnly* provides an isolation efficiency depending only on tracks, not depending on p_{T}.

Definition

In order to be considered, an identified and isolated electron needs to have an $E_{\mathrm{T}} > 15$ GeV. Electrons with $E_{\mathrm{T}} < 25$ GeV have to pass the *TightLH* identification criteria, while electrons with $E_T > 25$ GeV must pass the *MediumLH* identification definition [81].
The absolute value of the longitudinal impact parameter of each electron track, calculated with respect to the primary vertex, is required to fulfill $|z_0 \sin\theta| < 0.5$ mm, whereas the transverse impact parameter significance needs to satisfy $|d_0|/\sigma_{d_0} < 5$.

Properties analysis: Objects are rejected if they have been reconstructed as both an electron candidate and as a converted photon. Additionally, electron candidates are required to be sufficiently isolated from hadronic activity to reduce the background from hadrons faking electron signatures or heavy-flavour decays inside jets. For candidates with $E_{\mathrm{T}} < 25$ GeV, $E_{\mathrm{T}}^{\Delta R=0.2}$ has to be smaller than $0.11 \cdot E_{\mathrm{T}}$. In addition, the transverse momentum sum around the electron track in a radius $\Delta R = 0.4$ in the Inner Detector is required to be smaller than $0.06 \cdot E_{\mathrm{T}}$. For candidates with $E_{\mathrm{T}} > 25$ GeV, the E_{T} and η dependent *Gradient* isolation criterion is applied.

Couplings analysis: An additional identification working point is defined: *VeryLooseLH*. In this working point, the energy sum within $\Delta R = 0.2$ in the calorimeter system around the electron cluster has to be smaller than $0.06 \cdot p_{\mathrm{T}}$ and the transverse momentum sum around the electron track in $\Delta R = 0.2$ in the ID is required to be smaller than $0.06 \cdot E_{\mathrm{T}}$ independently of the p_{T} of the electron.

A summary of the various electron selection requirements is given in Table 4.1.

4.3.2 Muons

Identification

The identification procedure for muons aims at discriminating prompt muons from background muons coming from pion and kaon decays, by looking at discriminate variables such as CB tracks, charge and momentum ratio of the muons, p_{T} of the tracks. Based on the quality of the reconstructed objects, muon candidates are defined as either *Loose*, *Medium* or *Tight* [51], with increasing purity of prompt muons.

Isolation

Similarly to the electron case, in order to distinguish prompt muons from the ones originated by

jets, two discriminating variables are built to create the isolation working point: $E_{\mathrm{T}}^{cone0.2}$ defined as in the electron case, $p_{\mathrm{T}}^{varcone0.3}$ defined as the sum of transverse momenta of all the tracks found within a cone of $\Delta R = 0.3$ around the muon candidate track, excluding the track of the muon itself, with $p_{\mathrm{T}} > 1$ GeV.

Definition
In order to be considered, an identified and isolated electron needs to have an $p_{\mathrm{T}} > 15$ GeV and $|\eta| < 2.5$. The candidates are required to comply with *Tight* quality criteria. The requirements on the longitudinal and transverse impact parameters are $|z_0 \sin\theta| < 0.5$ mm and $|d_0|/\sigma_{d_0} < 3$, respectively. As for electron candidates, muons are required to be sufficiently isolated from hadronic activity.

Properties analysis: In order to be considered as isolated, the energy sum within a radius ΔR equal to 0.3 in the calorimeter system around the combined track has to be smaller than $0.09 \cdot p_{\mathrm{T}}$. In addition, the transverse momentum sum around the muon track in a radius $R = 0.2$ in the ID is required to be smaller than $0.06 \cdot p_{\mathrm{T}}$.

4

Couplings analysis: An extra identification working point is defined: *High-p_T*. The energy sum within a radius $\Delta R = 0.3$ in the calorimeter system around the combined track has to be smaller than $0.04 \cdot p_{\mathrm{T}}$. In addition, the transverse momentum sum around the muon track in a radius $R = 0.2$ in the ID is required to be smaller than $0.15 \cdot p_{\mathrm{T}}$.

A summary of the various muon selection requirements is given in Table 4.1.

4.3.3 Jets

After being reconstructed, as described in Section 2.3.5, only the jets with an absolute value of the pseudorapidity smaller than 4.5 and with $p_{\mathrm{T}} \geq 30$ GeV are accepted. To reduce the number of jets originating from pile-up vertices, jets with $p_{\mathrm{T}} < 60$ GeV and $|\eta| < 2.4$ are required to have a JVT response (Section 2.3.5) larger than 0.59[82]. Furthermore, to reduce pile-up contributions in the forward regions, the forward jet vertex tagger (FJVT) tagger is applied [83] on jets with $2.5 < |\eta| < 4.5$ with an operating point that has an overall efficiency of 90% for jets originating from the hard process.

Jets containing b-hadrons
Algorithms for recognizing jets originating from b-hadron decays are implemented to define b-jets. A working point is adopted that has an average 85% b-jet tagging efficiency, as estimated from simulated $t\bar{t}$ events. For the purpose of finding b-jets, also sub-threshold jets are considered as long as their p_{T} is larger than 20 GeV.

Properties analysis: The algorithm used is called MV2c10 [84, 85].

	Electrons		Muons
Identification	$15\text{ GeV} < p_{\mathrm{T}} < 25\text{ GeV}$ *TightLH*	$p_{\mathrm{T}} > 25\text{ GeV}$ *MediumLH*	$p_{\mathrm{T}} > 15\text{ GeV}$ *Tight*
η range	$\lvert\eta\rvert < 2.47$ excluding $1.37 < \lvert\eta\rvert < 1.52$		$\lvert\eta\rvert < 2.5$
Impact parameter	$z_0 \sin\theta < 0.5$ mm $d_0/\sigma(d_0) < 5$		$d_0/\sigma(d_0) < 3$
Isolation	***Properties***:		
	$E_{\mathrm{T}}^{\Delta R=0.2} < 0.11 \cdot E_{\mathrm{T}}$ $p_{\mathrm{T}}^{\Delta R=0.4} < 0.06 \cdot E_{\mathrm{T}}$	Gradient isolation	$E_{\mathrm{T}}^{\Delta R=0.3} < 0.09 \cdot p_{\mathrm{T}}$ $p_{\mathrm{T}}^{\Delta R=0.2} < 0.06 \cdot p_{\mathrm{T}}$
	Couplings:		
	$E_{\mathrm{T}}^{\Delta R=0.2} < 0.06 \cdot p_{\mathrm{T}}$ $p_{\mathrm{T}}^{\Delta R=0.2} < 0.06 \cdot E_{\mathrm{T}}$		$E_{\mathrm{T}}^{\Delta R=0.3} < 0.04 \cdot p_{\mathrm{T}}$ $E_{\mathrm{T}}^{\Delta R=0.2} < 0.15 \cdot p_{\mathrm{T}}$

Table 4.1: Object definition requirements for electron and muon candidates.

Couplings analysis: The algorithm used consists of a neural network discriminant, DL1r, based on lower-level taggers [66, 86].

4

4.3.4 Overlap removal

Since the different object reconstruction algorithms are largely independent, there is a potential overlap in their result. In case of an overlap between two objects, the following procedure is applied:

electron-electron: if there is an overlapping second layer cluster or a shared track, the lower p_{T} electron is removed.

electron-muon: if a combined muon shares an ID track with an electron, the electron is removed. These correspond to cases in which the muon's final state radiation (FSR) photon is misidentified as an electron. If instead, a CT muon shares an ID track with an electron, the muon is removed.

electron/muon-jet: since a physical electron has a track and leaves a deposit in the calorimeter, it can be reconstructed as a jet, as well as an electron produced during the jet evolution. The two case are distinguished by using a proximity criterion: if the jet is within $\Delta R < 0.2$ of an electron and it is not b-tagged it is rejected in favour o keepingf the electron, if an electron is within $0.2 < \Delta R < \min(0.4, 0.4 + 10\text{ GeV}/p_{\mathrm{T}})$ of any remaining jet, then the electron is removed, unless the jet is identified as a pile-up jet. While considering the overlap with a muon, the jet is only removed if it has less than three associated tracks with $p_{\mathrm{T}} > 500$ MeV or if $\frac{p_{\mathrm{T}}^{muon}}{p_{\mathrm{T}}^{jet}} > 0.5$ and $\frac{p_{\mathrm{T}}^{muon}}{\Sigma p_{\mathrm{T}}^{jet,}} > 0.7$.
In addition, electron candidates are removed if they share an ID track with a muon candidate. However, if a CT muon shares an ID track with an electron, the muon is removed instead.

4.4 Variables for signal-background discrimination

Two production modes of the $H\to WW^*$ are targeted in the analyses presented in this thesis: gluon-fusion and vector-boson fusion. In order to isolate the signal from the main backgrounds the following variables are defined and used:

- $p_{\mathrm{T}}^{\ell\ell}$: is transverse momentum of the di-lepton system. This variable is used to reject DY events: DY events tend to have the charged leptons emitted in opposite directions with similar p_{T}, which leads to small $p_{\mathrm{T}}^{\ell\ell}$.
- $\Delta\phi_{ll}$: the products of the leptonic $H\to WW^*\to \ell\nu\ell\nu$ decay tend to be collimated because of the spin correlation argument described in Section 4.1.1.
- $m_{\ell\ell}$: the invariant mass of the two leptons originating from the hard scattering interaction. The signal tends to concentrate at low $m_{\ell\ell}$ because of the small $\Delta\phi_{\ell\ell}$ given the relation

$$m_{\ell\ell} \sim \sqrt{2p_{\mathrm{T}}^{\mathrm{electron}}p^{\mathrm{muon}}(1-\Delta\phi_{\ell\ell})}.$$

- $m_{\tau\tau}$ is the estimated mass of di-τ lepton systems decaying leptonically. In the DY events of $Z\to\tau\tau\to e\mu+4\nu$ an approximation to reconstruct the event can be used (given the difficulty in the reconstruction of 4 neutrinos): the Z boson is much more massive than the τ leptons, so a large fraction of the Z-boson energy is passed onto the τ leptons as kinetic energy. When the τleptons decay further, their comparatively small mass is not sufficient to change the direction of flight of the daughter particles significantly. In this scenario the collinear approximation [88] to $m_{\tau\tau}$ is used: the charged leptons and neutrinos continue on the same trajectory as their respective mother particles, and the entire $E_{\mathrm{T}}^{\mathrm{miss}}$ originates from the four neutrinos. In this approximation, $m_{\tau\tau}$ is then constructed as [89]:

$$\begin{aligned} m_{\tau\tau} &= \frac{m_{\ell\ell}}{\sqrt{x_1x_2}} \\ x_1 &= \frac{A}{p_y^\mu E_x^{\mathrm{miss}} - p_x^\mu E_y^{\mathrm{miss}} + A} \\ x_2 &= \frac{A}{p_x^e E_y^{\mathrm{miss}} - p_y^e E_x^{\mathrm{miss}} + A} \\ A &= p_x^e p_y^\mu - p_y^e p_x^\mu, \end{aligned}$$

  where the indices x, y specify the components of the vectors.
- $E_{\mathrm{T}}^{\mathrm{miss}}$, defined as in Equation 2.1, helps reduce discriminating the signal from the background arising from QCD and DY background where most events do not contain high-p_{T} neutrinos in the final state. Multiple methods of calculating the $E_{\mathrm{T}}^{\mathrm{miss}}$ are possible: CST $E_{\mathrm{T}}^{\mathrm{miss}}$, based only on calorimeter measurements pile-up interactions, and TRACK $E_{\mathrm{T}}^{\mathrm{miss}}$ based only on the momenta of the tracks in the ID. These two methods alone are vulnerable to either pile-up interactions (CST $E_{\mathrm{T}}^{\mathrm{miss}}$), or fail in taking into account neutral particles (TRACK $E_{\mathrm{T}}^{\mathrm{miss}}$). A good compromise between the two just described methods is called TST $E_{\mathrm{T}}^{\mathrm{miss}}$, constructed from calorimeter-based measurements for the hard objects and from tracks to estimates

soft terms, [87]. The TST $E_{\mathrm{T}}^{\mathrm{miss}}$ is the $E_{\mathrm{T}}^{\mathrm{miss}}$ used in the presented $H \to WW^*$ analyses unless stated differently.

- m_{T}: the transverse mass defined as:

$$m_{\mathrm{T}} = \sqrt{\left(E_{\ell\ell} + E_{\mathrm{T}}^{\mathrm{miss}}\right)^2 - \left|\vec{p}_{\mathrm{T},\ell\ell} + \vec{E}_{\mathrm{T}}^{\mathrm{miss}}\right|^2}$$

  where $E_{\ell\ell} = \sqrt{|\vec{p}_{\mathrm{T},\ell\ell}|^2 + m_{\ell\ell}^2}$, and $\vec{p}_{\mathrm{T},\ell\ell}$ is the combined di-lepton momentum in the transverse plane. The distribution of m_{T} has an upper bond at the Higgs boson mass, making it a powerful discriminating variable against the WW and top backgrounds.
- m_{T}^{ℓ}, defined as the transverse masse of a single lepton ℓ:

$$m_{\mathrm{T}}^{\ell} = \sqrt{2 \cdot p_{\mathrm{T}}^{\ell} \cdot E_{\mathrm{T}}^{\mathrm{miss}} \cdot (1 - \cos\Delta\phi_{\ell, E_{\mathrm{T}}^{\mathrm{miss}}})}.$$

  m_{T}^{ℓ} has large values in the signal process, due to the high momentum of the leptons and the large opening angle, while for the DY background it tends to have small values because the leptons and the $E_{\mathrm{T}}^{\mathrm{miss}}$ tend to travel in a similar direction.
- $p_{\mathrm{T}}^{\mathrm{tot}}$: defined as $\boldsymbol{p}_{\mathrm{T}}{}^{l1} + \boldsymbol{p}_{\mathrm{T}}{}^{l2} + E_{\mathrm{T}}^{\mathrm{miss}} + \sum \boldsymbol{p}_{\mathrm{T}}{}^{\mathrm{jets}}$, where the sum over jets runs over all jets which pass the final selection criteria. The signal process tends to result in relatively small values of $p_{\mathrm{T}}^{\mathrm{tot}}$: two collimated neutrinos give a precise $E_{\mathrm{T}}^{\mathrm{miss}}$ estimation and the process is balanced in the transverse plane. For background events, for example in the $t\bar{t}$ process with an emitted soft radiation, the $2\ell\ell + 2j$ system recoils against the emitted radiation that might not be detected because the produced jet is not enough energetic to pass the selection criteria.
- m_{jj}: defined as the invariant mass of the two leading jets. It tends to be large for signal events.

The two highly energetic forward jets present in the event are originating from the incoming quarks that are part of the protons. Given that the other produced particles do not interact via the strong force, the level of hadronic activity between the two leading jets is expected to be small for signal events. What it is expected in the resulting rapidity gap is low p_{T} QCD jets. Three further observables are defined:

- central-jet p_{T}: defined as the jet with the largest p_{T} among all jets that lie within the rapidity gap of the two leading jets. The p_{T} of this jet is used to define the central-jet veto (CJV) as

$$\text{CJV} \begin{cases} = 1 & \text{: no central jet or central jet with } p_{\mathrm{T}} < 30 \text{ GeV is present in the event.} \\ = 0 & \text{: a central jet with } p_{\mathrm{T}} > 30 \text{ GeV is present in the event.} \end{cases}$$

- C_{ℓ} quantifies how central the leptons are with respect to the two tag jets in the η-plane: This observable is illustrated in Figure 4.3. A lepton is defined as "central" if its centrality has a value between 0 and 1, corresponding to the red region in the Figure.
- $E_{\mathrm{T}}^{\mathrm{miss}}$ significance [91] is a observable that quantifies how compatible the $E_{\mathrm{T}}^{\mathrm{miss}}$ measurement is with the hypothesis that the event does not contain real $E_{\mathrm{T}}^{\mathrm{miss}}$. This variable provides a good discrimination against $t\bar{t}$ for the following reason: the top mass is significantly larger than the sum of its decay products (the b-quark and the W boson), resulting in them being

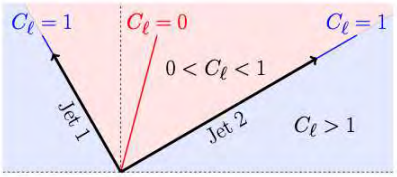

Figure 4.3: Schematic view of the centrality ([90]) which is calculated with respect to two reference objects. A lepton is central if the value of its centrality is smaller than 1, ending up in the red region of the picture.

boosted. This gives rise to higher $E_{\mathrm{T}}^{\mathrm{miss}}$ with respect to what is expected from the off-shell W from a Higgs decay.

4.5 References

[4] P.A. Zyla et al. "Review of Particle Physics". In: *PTEP* 2020.8 (2020), p. 083C01. DOI: 10.1093/ptep/ptaa104 (cit. on pp. 4, 5, 17, 18, 21, 23, 36, 71, 72, 86, 89, 92).

[51] ATLAS Collaboration. "Muon reconstruction performance of the ATLAS detector in proton–proton collision data at $\sqrt{s} = 13$ TeV". In: *Eur. Phys. J. C* 76 (2016), p. 292. DOI: 10.1140/epjc/s10052-016-4120-y. arXiv: 1603.05598 [hep-ex] (cit. on pp. 47, 75).

[66] ATLAS Collaboration. *Optimisation and performance studies of the ATLAS b-tagging algorithms for the 2017-18 LHC run.* ATL-PHYS-PUB-2017-013. 2017 (cit. on pp. 54, 77, 138).

[81] ATLAS Collaboration. *Electron efficiency measurements with the ATLAS detector using the 2015 LHC proton–proton collision data.* ATLAS-CONF-2016-024. 2016 (cit. on p. 75).

[82] ATLAS Collaboration. *Tagging and suppression of pileup jets with the ATLAS detector.* ATLAS-CONF-2014-018. 2014 (cit. on p. 76).

[83] ATLAS Collaboration. *Forward Jet Vertex Tagging: A new technique for the identification and rejection of forward pileup jets.* ATL-PHYS-PUB-2015-034. 2015 (cit. on p. 76).

[84] ATLAS Collaboration. "Performance of b-jet identification in the ATLAS experiment". In: *JINST* 11 (2016), P04008. DOI: 10.1088/1748-0221/11/04/P04008. arXiv: 1512.01094 [hep-ex] (cit. on pp. 76, 138).

[85] ATLAS Collaboration. *Optimisation of the ATLAS b-tagging performance for the 2016 LHC Run.* ATL-PHYS-PUB-2016-012. 2016 (cit. on pp. 76, 138).

[86] ATLAS Collaboration. "ATLAS b-jet identification performance and efficiency measurement with $t\bar{t}$ events in pp collisions at $\sqrt{s} = 13$ TeV". In: *Eur. Phys. J. C* 79 (2019), p. 970. DOI: 10.1140/epjc/s10052-019-7450-8. arXiv: 1907.05120 [hep-ex] (cit. on pp. 77, 96, 138).

[87] ATLAS Collaboration. *Expected performance of missing transverse momentum reconstruction for the ATLAS detector at $\sqrt{s} = 13$ TeV.* ATL-PHYS-PUB-2015-023. 2015 (cit. on p. 79).

[88] T. Plehn, David L. Rainwater, and D. Zeppenfeld. "A Method for identifying $H \to \tau^+\tau^- \to e^\pm\mu^\mp p_T$ at the CERN LHC". In: *Phys. Rev.* D61 (2000), p. 093005. DOI: 10.1103/PhysRevD.61.093005. arXiv: hep-ph/9911385 [hep-ph] (cit. on p. 78).

[89] ATLAS Collaboration. *Multi-Boson Simulation for* 13 *TeV ATLAS Analyses*. ATL-PHYS-PUB-2017-005. 2017 (cit. on pp. 78, 94).

[90] Koos van Nieuwkoop. "Evidence for the Production of the Standard Model Higgs Boson Produced via Vector Boson Fusion in the WW^* Channel at the ATLAS Detector". PhD thesis. Simon Fraser U., 2017 (cit. on p. 80).

[91] ATLAS Collaboration. *Object-based missing transverse momentum significance in the ATLAS Detector*. ATLAS-CONF-2018-038. 2018 (cit. on pp. 79, 152).

5

Data sets, simulation and systematic uncertainties

The interesting events for the $H \to WW^*$ analyses are hiding among the 1.7 billion pp collisions happening per second. The job of the trigger is to draw them out. Section 5.1 lists the trigger requirements for an event to enter the $H \to WW^*$ analyses. In order to describe, as closely as possible, the pp collision events to analyze, Monte Carlo (MC) generators are employed. MC generators provide the estimate of background processes and signal templates. The different stages of simulation are illustrated in Section 5.2, followed by the list of the generators used. The estimation of background and signal processes have associated uncertainties that are described in Section 5.3.

The chapter closes with the *Data Driven methods* described in Section 5.4, together with their associated uncertainties used to estimate the contribution of those backgrounds where it is hard to trust simulation from first principles. In these cases, we use simulation in a control region together with the measured data to draw the estimation of the background.

Contents

5.1 ATLAS data sets

As anticipated in Section 2.3.1, the trigger system of ATLAS is responsible for deciding whether to keep or discard a particular event. The trigger requirements aim at selecting characteristic signatures and they can depend on the instantaneous luminosity during the run. As a general idea, the more interactions take place, the more the trigger requirements need to be tightened, in order not to receive an amount of data that is too big to process. An alternative solution can be using a looser threshold but saving only a fraction of the events passing the trigger requirements. In this case, what is used is a *prescaled* trigger. Multiple triggers are active at the same time, and each event can fire multiple triggers. This information is stored in the event data, and it is accessible for reprocessing. The same triggers are also applied to the MC samples used in the analyses.

For the two analyses described in this thesis, four lists of triggers, or *menus*, have been used. While they are common in their goal to select light leptons, they do not always share energy and momentum thresholds, identification, and isolation working points. The triggers used in these analyses are described in Table 5.1.

The ***Properties*** analysis used *menu A* for selecting data collected in 2015, *menu B* for the data collected in the year 2016 up to June. For the rest of the data collected in 2016 the *menu C* has been used. The reason for tightening the triggers thresholds is that at the end of June 2016, in a period called *D4*, a luminosity of $10^{34}\text{cm}^{-2}\,\text{s}^{-1}$ was reached, [92].
For the ***Couplings*** analysis, *menu A* was employed on the 2015 year data set, but a different approach, a single trigger menu, *menu D*, was employed for the data in the period 2016-2018. While for the ***Properties*** analysis, it made sense to use low thresholds in the first part of the year 2016 to process more data, for the ***Couplings*** analysis, instead, the gain in a lower threshold in triggers did not justify the effort of having too many triggers menus.

The following description is for *Menu B*. For other menus, refer to Table 5.1. Three different HLT triggers on leptons are used and their output is combined by a logic OR:

a single-electron trigger selects events with at least one electron candidate satisfying a $p_{\text{T}}^{e} > 24\text{GeV}$, tight identification and an isolation requirement. Given that the rate of high transverse momenta is lower, an additional trigger is created with p_{T} thresholds at 60 and 120 GeV, with looser identification criteria and no isolation requirements. For all three p_{T} thresholds, at stage L1 an electromagnetic calorimeter object is required, with a cut on the energy deposit of E_{T}, which varies as a function of $|\eta|$ to account for energy loss.

a single-muon trigger for the muons passing the $p_{\text{T}} > 20\text{GeV}$ thresholds at stage L1, two HLT triggers are defined: $p_{\text{T}}^{\mu} > 24\text{GeV}$ requiring that the muon is isolated and $p_{\text{T}}^{\mu} > 50$ without isolation criteria.

a di-lepton trigger which combines an electron and a muon requirement and allows to collect events with lower-p_{T} leptons. The L1 thresholds are at 15 GeV and 10 GeV, respectively.

Next, the events passing the trigger requirements need to pass the data quality check [93], in order to be used in physics analyses. Given the complexity of the subsystems of ATLAS, the events are scrutinized to ensure they are clean from any hardware or software-related issues. Thanks to the

Lepton		L1 threshold	HLT threshold	HLT e LH	HLT μ Isolation	Used by
Year 2015. Menu A.						
e		$E_{\mathrm{T}} \gtrsim 20\,\mathrm{GeV}$	$p_{\mathrm{T}}^{e} > 24\,\mathrm{GeV}$	medium		***Properties*** and ***Couplings***
			$p_{\mathrm{T}}^{e} > 60\,\mathrm{GeV}$	medium		
			$p_{\mathrm{T}}^{e} > 120\,\mathrm{GeV}$	loose		
μ		$p_{\mathrm{T}} > 15\,\mathrm{GeV}$	$p_{\mathrm{T}}^{\mu} > 20\,\mathrm{GeV}$		✓	
			$p_{\mathrm{T}}^{\mu} > 50\,\mathrm{GeV}$			
$e\mu$	(e)	$E_{\mathrm{T}} \gtrsim 15\,\mathrm{GeV}$	$p_{\mathrm{T}}^{e} > 17\,\mathrm{GeV}$	loose		
	(μ)	$p_{\mathrm{T}} > 10\,\mathrm{GeV}$	$p_{\mathrm{T}}^{\mu} > 14\,\mathrm{GeV}$			
Year 2016 before D4. Menu B.						
e		$E_{\mathrm{T}} \gtrsim 20\,\mathrm{GeV}$	$p_{\mathrm{T}}^{e} > 24\,\mathrm{GeV}$	tight	✓	***Properties***
			$p_{\mathrm{T}}^{e} > 60\,\mathrm{GeV}$	medium		
			$p_{\mathrm{T}}^{e} > 120\,\mathrm{GeV}$	loose		
μ		$p_{\mathrm{T}} > 15\,\mathrm{GeV}$	$p_{\mathrm{T}}^{\mu} > 24\,\mathrm{GeV}$		✓	
			$p_{\mathrm{T}}^{\mu} > 50\,\mathrm{GeV}$			
$e\mu$	(e)	$E_{\mathrm{T}} \gtrsim 15\,\mathrm{GeV}$	$p_{\mathrm{T}}^{e} > 17\,\mathrm{GeV}$	loose		
	(μ)	$p_{\mathrm{T}} > 10\,\mathrm{GeV}$	$p_{\mathrm{T}}^{\mu} > 14\,\mathrm{GeV}$			
From Year 2016 after D4 to Year 2016. Menu C.						
e		$E_{\mathrm{T}} \gtrsim 20\,\mathrm{GeV}$	$p_{\mathrm{T}}^{e} > 26\,\mathrm{GeV}$	tight	✓	***Properties***
			$p_{\mathrm{T}}^{e} > 60\,\mathrm{GeV}$	medium		
			$p_{\mathrm{T}}^{e} > 120\,\mathrm{GeV}$	loose		
μ		$p_{\mathrm{T}} > 15\,\mathrm{GeV}$	$p_{\mathrm{T}}^{\mu} > 24\,\mathrm{GeV}$		✓	
			$p_{\mathrm{T}}^{\mu} > 50\,\mathrm{GeV}$			
$e\mu$	(e)	$E_{\mathrm{T}} \gtrsim 15\,\mathrm{GeV}$	$p_{\mathrm{T}}^{e} > 17\,\mathrm{GeV}$	loose		
	(μ)	$p_{\mathrm{T}} > 10\,\mathrm{GeV}$	$p_{\mathrm{T}}^{\mu} > 14\,\mathrm{GeV}$			
From Year 2016 - 2018. Menu D.						
e		$E_{\mathrm{T}} \gtrsim 22\,\mathrm{GeV}$	$p_{\mathrm{T}}^{e} > 26\,\mathrm{GeV}$	tight	✓	***Couplings***
			$p_{\mathrm{T}}^{e} > 60\,\mathrm{GeV}$	medium		
			$p_{\mathrm{T}}^{e} > 140\,\mathrm{GeV}$	loose		
μ		$p_{\mathrm{T}} > 20\,\mathrm{GeV}$	$p_{\mathrm{T}}^{\mu} > 26\,\mathrm{GeV}$		✓	
			$p_{\mathrm{T}}^{\mu} > 50\,\mathrm{GeV}$			
$e\mu$	(e)	$E_{\mathrm{T}} \gtrsim 15\,\mathrm{GeV}$	$p_{\mathrm{T}}^{e} > 17\,\mathrm{GeV}$	loose		
	(μ)	$p_{\mathrm{T}} > 10\,\mathrm{GeV}$	$p_{\mathrm{T}}^{\mu} > 14\,\mathrm{GeV}$			

Table 5.1: Event triggers for the $H \to WW^*$ analyses. The energy and momentum thresholds of the L1 and HLT triggers are listed as well as the electron identification and isolation criteria. For single-lepton triggers, each line defines an independent trigger. For the di-lepton trigger, the criteria for both the electron and muon need to be satisfied.

continuous improvements, for the full Run 2, 95% of the collected data passes all quality checks. It is worth mentioning that the reconstruction of objects for trigger purposes is performed with fast algorithms in order to be executable *on-line*. Once an event has passed the trigger selection, its objects are reconstructed *off-line* with the more computing-intensive procedures, described in Section 4.3. A procedure, called trigger matching, ensures that the on-line triggered object(s) match the off-line reconstructed one(s).

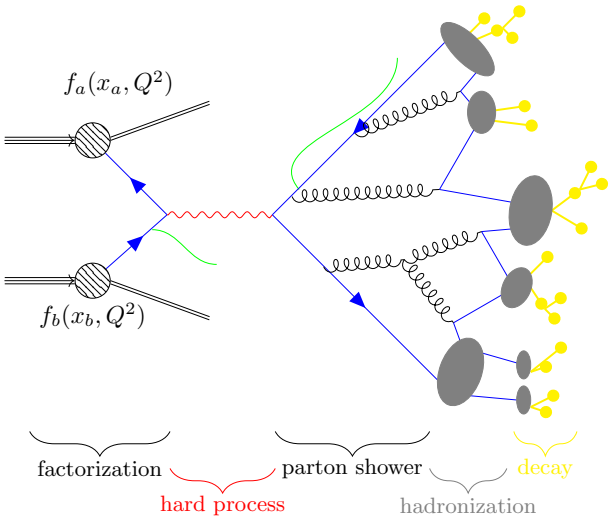

Figure 5.1: Schematic overview of the effects complicating the calculation of a process with two baryons in the initial state (left) and hadrons in the final state (right). In green are indicated the possible initial and final state radiations, in red the hard scattering part, in grey blobs the hadronization process, and in yellow the decay products.

5.2 Monte Carlo simulation

In order to compare the measured data with theory predictions, signal and backgrounds samples predictions are produced with MC generators, or with data-driven methods when the simulations are not reliable enough.
The SM, described in Section 1.1, predicts the existence of physics processes that can be calculated up to a certain precision, for example, QCD processes. Their simulations are usually done in two phases: the highly energetic interactions, characterized by small coupling constants, are computed with perturbation theory, while the low energy ones need to be described empirically. For the non-perturbative physics inside the proton, this is performed with PDFs. A schematic view of a hadron collision event showing the evolution of the produced particles is shown in Figure 5.1. The individual stages and the basic ingredients of the used MC generators follow, [4, 94].

5.2.1 Hard process

A proton-proton (pp) collision can be categorized as a:

Soft Collision: the protons do not collide head-on with low transferred momentum. This results in final state particles with small transverse momentum. These events are called *minimum bias*.

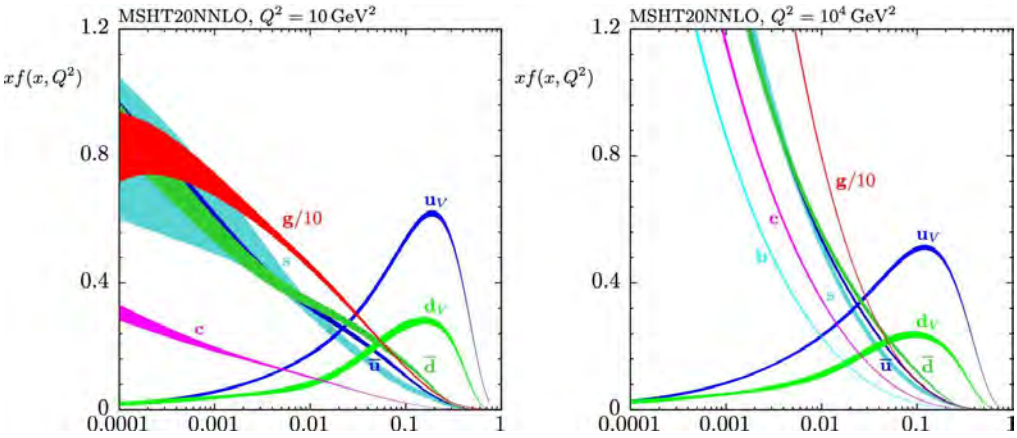

Figure 5.2: PDFs computed for $Q^2 = 10\,\text{GeV}^2$ and $Q^2 = 10^4\,\text{GeV}^2$, where Q^2 is the energy scale where the interaction happens [95].

Hard Collision: only one of the partons for each proton takes part in the interaction while the others act as *spectators*. The spectators act as in the soft collision. These partons are generally still present in the final state, and this contribution is usually referred to as underlaying event (UE). A hard collision is characterized by high momentum exchange and the production of high-momentum particles.

In the latter case, the most interesting one from the experimental point of view, the center-of-mass energy $\sqrt{\hat{s}}$ depends on the fraction of the momentum carried by the initial partons taking part in the interaction. This energy is lower than the pp centre-of-mass energy $\sqrt{s}$ and depends on the fraction of the proton momenta (x_a,x_b) carried by the scattering partons (a, b) in the following way:

$$\sqrt{\hat{s}} = \sqrt{s x_a x_b}.$$

The cross section for the hard pp collision producing X, with a center-of-mass energy $\sqrt{\hat{s}}$, can be written by using *factorization*[1], in the following way:

$$\sigma_{pp\to X} = \int \mathrm{d}x_a \mathrm{d}x_b f_a(x_a, Q^2) f_b(x_b, Q^2) \hat{\sigma}_{ab\to X}(x_a, x_b), \tag{5.1}$$

where $f_a(x_a, Q^2)$, $f_b(x_b, Q^2)$ are the PDFs, defined as the probability density for finding the partons with longitudinal momentum fractions x_a, x_b at an energy scale of Q^2, and $\hat{\sigma}_{ab\to X}(x_a, x_b)$ is the cross-section of the elementary interaction among two partons a and b. The functional form of the PDFs needs to be obtained from experiments since it is not known *at priori*. Figure 5.2 shows the PDFs for the quarks in a proton evaluated for an energy scale at $Q^2 = 10\,\text{GeV}^2$ and $Q^2 = 10^4\,\text{GeV}^2$. The cross section ($\hat{\sigma}_{ab\to X}$) term of equation (5.1) can be written explicitly as function of the matrix

[1] Factorization is the ability to independently describe the effect of short-distance physics and the long-distance physics in a given process.

element $\mathcal{M}_{ab\to X}$ in the following way

$$\hat{\sigma}_{ab\to X} = \int \mathrm{d}\Phi_X |\mathcal{M}_{ab\to X}|^2,$$

in order to stress that the matrix element is integrated all over the allowed phase space $\mathrm{d}\Phi_X$ of the final particles X. This latter term, $\mathcal{M}_{ab\to X}$ is calculated with the perturbation theory and its precision depends on the number of Feynman diagrams included in the calculation. The hard interaction is depicted in red in Figure 5.1.

5.2.2 Parton shower

Once the two initial partons have interacted, thanks to the running of the QCD coupling constant, a multitude of low-energetic partons is produced. In order to give an estimation of how probable it is to generate a certain amount of additional parton radiation, parton shower (PS) methods are employed.
Given the cross-section $\sigma_{ab\to X}$, the cross-section for the same process, but with a radiated parton, $\sigma' = \sigma_{ab\to X+x}$ can be computed if the emission angle is small (collinear approximation) and the emission is low-energetic (i.e. the soft approximation). This approximation is valid up to a cut-off scale since the calculation of the cross-section σ' diverges in the limiting case of an emission angle of 0 and extremely low energetic emitted partons. However, these very collinear emissions are not physically distinguishable, given that any physical measurement cannot tell apart a collinear pair of partons from a single parton with the same total momentum and other quantum numbers. Defining as *hardness* the ordering variable in which the energy and angular dependence of the cross-section are incorporated, the comparison between σ and σ' returns the emission probability at a certain hardness scale. In particular, the higher the hardness is, the lower the probability of emitting a parton. The modeling of the evolution of the PS is done as follows: the hardness scale of the primary process is considered, using the emission probability for the hardness at which the parton split that occurs can be determined. This process is iterated until the hardness reaches the *hadronization* scale at which hadrons form and the perturbation theory is no longer valid.
PS methods are also used to calculate the probability of both initial state radiation (ISR) and final state radiation (FSR), depicted in green in Figure 5.1. The only difference is in the treatment of the time evolution of the emissions. For ISR emissions, this is calculated backward in time.

Matching
In order to obtain a good description of any partonic states, the two methods described above need to be combined. While the matrix element calculations work when simulating well-separated hard partons (in a small number), a shortcoming is represented by the calculation of collinear and soft partons. For the latter, the PS algorithms are able to help. The combination of the two methods is possible, but it needs to be performed in a way such that double counting or undercounting are avoided. Multiple methods of matching have been developed that provide a matching scheme for LO and NLO.

5.2.3 Hadronization, decays and soft interactions

The mentioned cut-off in the PS is used to construct the hadronization scale, which is defined as the energy at which partons start forming hadron states. The process of forming hadrons cannot be treated with perturbative methods. MC generators use QCD-inspired phenomenological models to describe this stage, [4]. Among the models used, two are commonly used and they are at the base of the MC generators used in this thesis:

The String model
A color-connected $q\bar{q}$ pair emerging from the PS are considered affected by a linear potential, a string. As the quarks drift apart, the string can break with a probability proportional to the distance. The energy released by the breaking creates another color-connected $q\bar{q}$ pair. The process is repeated until the di-quark mass is too low to create further quarks. In this picture, the gluons are inserted by introducing a kink in the string potential. In this way, new systems, like $qg\bar{q}$, $qggg\bar{q}$, and so on, are included. The set of quarks that is left at the end of the string-breaking process is then combined into hadrons, with a momentum that is determined by energy conservation laws.

The Cluster model
The gluons are forced to split into $q\bar{q}$ pairs at the end of the PS. After the breaking up, a new $q\bar{q}$ pair, with lower mass, is produced. During this step, due to mass differences, the production of strange quarks is suppressed in favor of light quarks. If the newly formed $q_i\bar{q}_j$ pair has a mass higher than a cut-off, it is forced to decay as $q_i\bar{q}_j \rightarrow q_i\bar{q}_k + q_k\bar{q}_j$, where the index of q labels the flavor of the parton. Next, close-by pairs of $q\bar{q}$ are combined into meson-like clusters. Depending on the energy of each cluster, low-energetic states, hadrons with heavy flavor or strange quarks can be produced. The hadronization processes is depicted as grey blobs in Figure 5.1.

The primary hadrons, originated by either string or cluster decays, are unstable states that are going to decay further until their products are stable particles. A particle is defined as stable if, according to [4], its mean life τ times the speed of light c (i.e. $c\tau$) is greater than $10\ mm$. Typically, MC generators responsible for simulating the hadronization step, implement this through dedicated matrix elements. The stable hadrons are usually produced in a cone around the primary hadron, which is reconstructed in the detector as a jet. The decay products are depicted as yellow blobs on the right-hand side of Figure 5.1.
The effects not directly related to the hard interaction, are referred to UE, and characterized as mentioned in Section 5.2.1, with low transferred momentum. Also, pile-up collisions are simulated. These are soft collisions between protons that happen in the same readout window of the hard event.
At this point, the physical information of the hard interacting partons has been encoded into the final states particles, this information is usually referred to as the *particle level*. What is missing is the simulation of how the detector records the specific event, the *reconstruction level* information. The GEANT4 [96] is the framework used in the ATLAS experiment, to simulate how the particles

interact with the detector matter. On top of this, the effect of the pile-up interaction is added, as well as the detector noise.

5.2.4 Monte Carlo generators

The main generators employed in this thesis are the following:

- Sherpa [97] is a multi-purpose MC generator, it computes the matrix element, ISR and FSR, UEs, as well as PS, In this thesis, it is mainly employed in modeling background events, except for top final states. Its PS modelling is performed with the cluster model.
- Powheg-Box [98] is a NLO MC generator which simulates the hard scattering, for the samples used in this thesis it is usually interfaced with the Pythia generator for the PS and to model signal events, and top background events.
- Pythia [99] is a multi-purpose MC generator. However, in this thesis it is used for the modeling of PS, when matched to Powheg-Box and MadGraph5_aMC@NLO, and it is used for pile-up modeling. It uses the String Model for PS modeling.
- MadGraph5_aMC@NLO [100] is a MC generator that calculates the matrix element at NLO as suggested by the name, and it is interfaced with Pythia or Herwig for the samples in this thesis.
- Herwig [101] is a multi-purpose MC generator, but in this thesis is mainly employed for PS and hadronization. It uses the cluster model for the modelling of the PS.

5

As described in Section 4.2, the main background for the two analyses presented in this thesis are top ($t\bar{t}$ and Wt), WW, $Z \to \tau\tau$, $Z \to ee/\mu\mu$, WZ, $W\gamma^{(*)}$ and ZZ, which can be simulated with MC generators, and W + jets, for which a data-driven approach (Section 5.4) is used.

Properties analysis: Table 5.2 shows an overview of the samples used in the analysis and the generators used to produce their matrix element, the UEs and the PS (UE/PS), the PDF used, as well as the accuracy at which the calculation of the cross-section normalization has been performed. The simulated events were overlaid with additional inelastic pp interactions that were generated with Pythia 8.153 in order to match the pile-up conditions[2] observed in the ATLAS data recorded during the 2015 and 2016 runs of the LHC.

Couplings analysis: The MC generators used to model signal and background processes are listed in Table 5.3. For most processes, separate programs are used to generate the hard scattering process and to model the PS, hadronization and the UE. All simulated samples include the effect of pile-up from multiple interactions in the same and neighboring bunch crossing.

[2] An average of 13 (21) interactions per bunch crossing were observed during the 2015 (2016) run.

Process	Matrix element (alternative model)	UE/PS	PDF set	Perturbative accuracy of total cross section
ggF H	MG5_aMC@NLO 2.4.2 [102, 103] (MG5_aMC@NLO 2.4.2 + Herwig 7.0.1)	Pythia 8.212[104, 105]	NNPDF3.0 NLO [106]	NNNLO QCD[107]
VBF H	Powheg-Box v2 [98] (MG5_aMC@NLO 2.3.3 + Pythia 8.212) (Powheg-Box v2 + Herwig 7.0.1)	Pythia 8.212	PDF4LHC15 NLO	NNLO QCD+NLO EW[108]
VH	Powheg-Box v2 [109, 110]	Pythia 8.186	PDF4LHC15 NLO	NNLO QCD+NLO EW
$t\bar{t}$	Powheg-Box v2 (Sherpa 2.2.1) (Powheg-Box v2 + Herwig 7.0.1)	Pythia 8.210	NNPDF3.0 NLO[111]	NNLO+NNLO QCD [112].
Wt	Powheg-Box v2 (MG5_aMC@NLO 2.2.2 + Herwig++) (Powheg-Box v2 + Herwig++)	Pythia 6.428	CT10 [101]	NLO QCD [113]
WZ/γ^*, ZZ/γ^*	Sherpa 2.2.2[114, 115] (MG5_aMC@NLO 2.3.3 + Pythia 8.212)		NNPDF3.0 NNLO	NLO QCD [116]
$W\gamma$, $Z\gamma$	Sherpa 2.2.2 (MG5_aMC@NLO 2.3.3 + Pythia 8.212)		NNPDF3.0 NNLO	NLO QCD
$qq, qg \to WW$	Sherpa 2.2.2 (MG5_aMC@NLO 2.3.3 + Pythia 8.212)		NNPDF3.0 NNLO	NLO QCD
$gg \to WW$	Sherpa 2.1.1		CT10	NLO QCD
Z/γ^*	Sherpa 2.2.1 (MG5_aMC@NLO 2.2.2 + Pythia 8.186)		NNPDF3.0 NNLO	NNLO QCD

Table 5.2: Overview of the simulation tools used to generate signal and background processes, and to model the UE and PS, in the ***Properties*** analysis. The PDF sets are also summarised. Alternative event generators and configurations used to estimate systematic uncertainties are shown in parentheses.

5

Process	Matrix element (alternative)	PDF set	UE/PS model (alternative model)	Prediction order for total cross section
ggF H	Powheg-Box v2 [98, 117–120] NNLOPS [117, 133, 134] (MG5_aMC@NLO) [135, 136]	PDF4LHC15 NNLO [121]	Pythia 8 [122] (Herwig 7) [137]	NNNLO QCD + NLO EW [123–132]
VBF H	Powheg-Box v2 [98, 119, 120, 133] (MG5_aMC@NLO)	PDF4LHC15 NLO	Pythia 8 (Herwig 7)	NNLO QCD + NLO EW [138–140]
VH excl. $gg \to ZH$	Powheg-Box v2	PDF4LHC15 NLO	Pythia 8	NNLO QCD + NLO EW [141–145]
$t\bar{t}H$	Powheg-Box v2	NNPDF3.0NLO	Pythia 8	NLO [107]
$gg \to ZH$	Powheg-Box v2	PDF4LHC15 NLO	Pythia 8	NNLL [146, 147]
$qq \to WW$	Sherpa 2.2.2 [148] (Q_{cut})	NNPDF3.0NNLO [106]	Sherpa 2.2.2 [149–154] (Sherpa 2.2.2 [150, 157]; μ_{q})	NLO [116, 155, 156]
$qq \to WWqq$	MadGraph [135]	NNPDF3.0NLO	Pythia 8 (Herwig 7)	LO
$gg \to WW/ZZ$	Sherpa 2.2.2	NNPDF3.0NNLO	Sherpa 2.2.2	LO [158]
$WZ/V\gamma^*/ZZ$	Sherpa 2.2.2	NNPDF3.0NNLO	Sherpa 2.2.2	NLO [159]
$V\gamma$	Sherpa 2.2.8 [148]	NNPDF3.0NNLO	Sherpa 2.2.8	NLO [159]
VVV	Sherpa 2.2.2	NNPDF3.0NNLO	Sherpa 2.2.2	LO
$t\bar{t}$	Powheg-Box v2 (MG5_aMC@NLO)	NNPDF3.0NLO	Pythia 8 (Herwig 7)	NNLO+NNLL [160–166]
Wt	Powheg-Box v2 (MG5_aMC@NLO)	NNPDF3.0NLO	Pythia 8 (Herwig 7)	NNLO [167, 168]
Z/γ^*	Sherpa 2.2.1 (MG5_aMC@NLO)	NNPDF3.0NNLO	Sherpa 2.2.1	NNLO [169]

Table 5.3: Overview of simulation tools used to generate signal and background processes, and to model the UE/PS, in the ***Couplings*** analysis. The PDF sets are also summarised. Alternative event generators and configurations used to estimate systematic uncertainties are shown in parentheses.

5.3 Systematic uncertainties

The systematics uncertainties can be divided into two main groups, the experimental uncertainties, related to the ATLAS detector and its simulation, and the theory uncertainties, describing systematic effects related to the MC simulation. The handling of systematic uncertainties is very similar to all the analyses presented in this thesis. This section thus contains a general summary of the treatment, that will be elaborated in the individual chapters in case of discrepancies.

5.3.1 Theory uncertainties

Theory systematics are in general estimated by comparing different MC generators. The alternative generator, for each considered sample, is listed in parenthesis in Table 5.2 for the ***Properties*** analysis, and in Table 5.3 for the ***Couplings*** one. The versions of the generators used are omitted from the text, but they are listed in the reference tables. For each process, the theoretical uncertainties considered are related to the choice of the QCD scale, the PDF set and the PS model. The uncertainties are computed for the observable providing discrimination in the fit.

Signal uncertainties

- Perturbative QCD: the impact of missing higher order corrections in fixed-order perturbative predictions is estimated via the Stewart-Tackmann (ST) [170] method that evaluates uncertainties in exclusive jet binning based on scale variations in inclusive bins. The idea of the method is to determine the uncertainties in the inclusive N-jet cross section $\sigma_{\geq N}$, and then compute the uncertainty of the exclusive N-jet cross section σ_N as

  $$\sigma_{\geq N} = \sigma_N - \sigma_{\geq N+1}.$$

  The uncertainty $\Delta\sigma_N$ on σ_N is calculated as $\Delta\sigma_N^2 = \Delta\sigma_{\geq N}^2 + \Delta\sigma_{\geq N+1}^2$.
  The results are propagated across bins in terms of yield components, which are correlated across bins, and migration components which are anti-correlated across bins. The largest of the variations is taken as a symmetrized uncertainty. For ***Couplings***, when a measurement of the cross-section is performed in bins of other observables, like p_{T}^H, a modified ST method is used: the Higgs Weight Tool (HWT). The HWT is an ATLAS tool that encodes the yield and migration components that result from applying the ST method to kinematic bins as NPs and exist for the binning prescribed by the STXS.
- PDFs: the PDFs uncertainties are estimated comparing the event yields of the nominal MC sample with an alternative prediction using a different set of PDFs. For the QCD uncertainties, the largest variation among the different models is taken. For ***Couplings*** only, variations in the strong coupling constant value $\alpha_s = 0.1180 \pm 0.0015$, [4, 94], are considered.
- PS: the PS model uncertainties are evaluated by comparing the selection efficiencies resulting from the nominal generator configuration to the alternative predictions. This translates, for ***Properties***, into the comparison of (MadGraph5_aMC@NLO +Pythia)

vs (MadGraph5_aMC@NLO +Herwig) for ggF and (Powheg-Box +Pythia) vs (Powheg-Box +Herwig) for VBF, while for ***Couplings*** (Powheg-Box +Pythia) vs (Powheg-Box +Herwig).

- Hard scattering (for ***Couplings*** only): the uncertainty on the matrix element is performed by comparing Powheg-Box and MadGraph5_aMC@NLO. Powheg-Box computes the hard scatter using fixed order perturbation theory accurate to NNLO and it is interfaced to Pythia 8 PS showering at NNLO order. MadGraph5_aMC@NLO combines NLO $H + 0, 1, 2$ jet processes and it is interfaced to Pythia via the FxFx merging scheme [171]. There is an inevitable bit of double-counting between this uncertainty evaluation and the evaluation of perturbative QCD scales; nevertheless, both are kept as a conservative estimates.

Background uncertainties

The uncertainty due to neglected higher orders in QCD is estimated by simultaneously increasing (decreasing) the renormalization and factorization scales μ_R and μ_F by a factor of 2 (0.5). The largest variation is symmetrized and used as uncertainty. The effect of PDF uncertainties is evaluated by comparing the event yields of the nominal MC sample with an alternative prediction using a different set of PDFs. Similarly, the effect of α_s is evaluated using replicas with different settings of α_s. The computation of the PS uncertainty is performed by comparing the nominal MC generator to an alternative one. The details of this procedure for each process are described below

- $t\bar{t}$:
  - ***Properties***: Powheg-Box + Pythia are compared to Sherpa to extract differences in the matching between the matrix element and PS. PS modeling uncertainties are derived by replacing Pythia with Herwig and comparing the corresponding yields and shapes with those from the nominal set-up.
  - ***Couplings***: the nominal Powheg-Box + Pythia is compared with MadGraph5_aMC@NLO + Pythia for the computation of the matrix element and matching, while the comparison with Powheg-Box +Herwig is used for the PS uncertainty.

  The uncertainty due to additional radiation is evaluated by increasing/decreasing the internal weights for ISR and FSR.

- Wt:
  - ***Properties***: Powheg-Box +Pythia are compared to MadGraph5_aMC@NLO +Herwig, for the uncertainties in the matching between the matrix element and PS, while the uncertainty on the PS is obtained by comparing the nominal sample with Powheg-Box +Herwig.
  - ***Couplings***: the treatment for Wt is identical to that of the $t\bar{t}$.

  An additional uncertainty is applied to single-top processes to account for the effect of the interference with the $t\bar{t}$ samples. It is computed by comparing samples with different diagram removal (DR) scheme and with diagram subtraction (DS) scheme [172].

- Z+jets:

  - ***Properties***: matrix element and PS uncertainty are computed by comparing the predictions of the Sherpa generator with those of MadGraph5_aMC@NLO + Pythia.
  - ***Couplings***: the matrix element uncertainty is calculated by comparing the predictions of the Sherpa with MadGraph5_aMC@NLO +Pythia.

- $qq \to WW$:
  - ***Properties***: The uncertainties in the modeling of the production of diboson with jets are evaluated by comparing the predictions of the Sherpa and MadGraph5_aMC@NLO + Pythia generators, where the latter provides NLO precision in QCD for the simulation of production modes, with up to one parton in addition to the diboson system [89]. The FxFx matching scheme is used, [171]. Variations of the matching scale are also considered, where the nominal value, 20 GeV, is changed to 30 GeV and 15 GeV.
  - ***Couplings***: The Sherpa PS allows to vary how the momentum recoil is evaluated during the parton shower evolution. Therefore, the nominal Sherpa PS is compared with Sherpa with momentum recoil changed to compute the PS uncertainties. Merging and matching variations are implemented for this sample.

- EW $qq \to WWqq$
  For ***Couplings*** only: For the PS uncertainty, MadGraph5_aMC@NLO +Herwig is compared to MadGraph5_aMC@NLO +Pythia. On top of this, the EW WW process has a 15% symmetrized normalization uncertainty due to NLO EW corrections, as calculated using the leading-log approximation [173].

- Other diboson (WZ/γ^*, ZZ/γ^*, $V\gamma$):
  - ***Properties***: Matrix element uncertainties are computed by comparing the predictions of the Sherpa and MadGraph5_aMC@NLO + Pythia. Variations of the matching scale are also considered.
  - ***Couplings***:
    For $V\gamma$ a −50%/+100% normalization uncertainty is applied to account for potential mis-modeling of the $\gamma \to e$ misidentification rate primarily affecting events with $m_{\mathrm{T}} \lesssim 80$GeV. For WZ/γ^*, ZZ/γ^* a $\pm$12% normalisation uncertainty is applied.

- $gg \to WW$:
  For ***Couplings*** only: the $gg \to WW$ process is simulated at LO precision for up to one additional parton emission, and normalized to NLO calculations. Therefore, a conservative −50%/+100% normalization uncertainty is assigned on this process for the $N_{\mathrm{jets}\geq 2}$ categories, while for the $N_{\mathrm{jets}<2}$ categories the NLO scale uncertainties are considered with the latest theoretical prediction.

- Triboson with jets:
  For ***Couplings*** only: for triboson processes, a 12% normalization uncertainty is applied.

- VH and $t\bar{t}H$:
  The associated production of Higgs boson with a vector boson or a pair of $t\bar{t}$ is considered as background.
  A flat $\pm 50\%$ normalization uncertainty is applied.

For background samples that are normalized to CR yields, uncertainties are estimated on the extrapolation factors between the CRs and SRs. Only uncertainties that change the ratio between the yields in the SRs and CRs affect the extrapolation. The uncertainties on the extrapolation factors are treated as uncorrelated between different jet multiplicities.

5.3.2 Experimental uncertainties

Three types of experimental uncertainties are considered:

- *four-vector* or P4 systematics, related to the kinematic properties of an object, for example, the uncertainty linked to the momentum measurement of a muon;
- *scale factor* or SF systematics, accounting for the difference in efficiency among data and MC that the various algorithms involved in the reconstruction of the physics objects have;
- *fake factor* systematics, related to the estimation of the fakes, which will be described in Section 5.4.3.

The procedure to estimate the effect of P4 and SF systematics in the analysis is presented with a simplified example. The Combined Performance groups provide uncertainties on the elementary physics objects, for example stating that the p_{T} of a muon is known with 1% uncertainty. The $H\rightarrow WW^*$ analysis is then repeated by varying the p_{T} of the muons up and down with 1%. From the comparison of these two scenarios, the uncertainty affecting the $H\rightarrow WW^*$ analysis is obtained.
In particular, the original samples are reprocessed with modified weights to account for uncertainty in selection efficiencies, or with modified kinematic properties. In the first case, the modification affects the yields that are predicted by the sum of weight, while in the second it is the momenta of the reconstructed objects that are chosen. The final $\pm 1\sigma$ variation of the nuisance parameters associated with the uncertainties is taken as the difference between the nominal and the interpolation among the varied distributions [174].

Leptons
Decays of $Z \rightarrow \ell^+\ell^-$, $W^\pm \rightarrow \ell^\pm\nu$ and $J/\psi \rightarrow \ell^+\ell^-$ are studied in order to estimate the uncertainties on leptons related to momentum and energy scale, as well as what concerns the identification of the leptons: identification, isolation, reconstruction, and trigger. Scale factors are obtained in order to match the simulation with the observed data. For electrons, it is worth mentioning, that in order to describe the uncertainty of the lengthy reconstruction procedure accurately 17 distinct variations are used, [59]. Lastly, for muons, an additional correction for the efficiency of the muon track-to-vertex association is considered, [62].

Jets

The jet energy scale (JES) and jet energy resolution (JER) are the two components of the jet uncertainties. They are derived as a function of p_{T} and η of the jet as well as the pile-up conditions and average expected flavor composition. A combination of simulated and data samples is used to measure and model the response of the detector at jets, [175]. On top of this, an uncertainty on the JVT performance is assigned. For the identification of jets via algorithms, scale factors are derived to correct their performances in comparison with data. The uncertainties of these scale factors are described by independent eigenvectors for each jet flavor [86, 176].

$\boldsymbol{E}_{\mathrm{T}}^{\mathrm{miss}}$

Given its construction (Equation (2.1)), the uncertainties on $E_{\mathrm{T}}^{\mathrm{miss}}$ are strictly connected with the uncertainties on its components, and no separate uncertainty is defined. Variations for the $E_{\mathrm{T}}^{\mathrm{miss}}$ scale and resolution are taken into account [68].

Pile-up

In order to model pile-up conditions correctly, a data scale factor is applied to the MC samples before re-weighting them to match the data. The uncertainty on the pile-up reweighting is evaluated by varying upward and downward this parameter. Uncertainties originating from the pileup jet rejection tool are also included.

Luminosity

On top of all the previously mentioned uncertainties, a NP is defined to quantify the relative Luminosity uncertainty, $\pm 2\%$ for the ***Properties*** analysis, and $\pm 1.7\%$ for the ***Couplings*** one. This uncertainty is applied to all MC processes that do not have a normalization factor constrained in a CR [177]. These uncertainties are based on the separate luminosity measurements for the dataset used by the ***Properties*** analysis (36 ± 0.8 fb^{-1}), and for the full Run 2 dataset ($\mathcal{L} = 136 \pm 2.4$ fb^{-1}).

The experimental uncertainties above described are encoded in the NPs whose names are given in the following tables: Table 5.4 for electron and muons and Table 5.5 for jets and $E_{\mathrm{T}}^{\mathrm{miss}}$. In the tables, the information related to the type of uncertainty, the naming code (without the ATLAS_ as described in Section 3.2.1), and the purpose of the NP is illustrated. Besides, the letter in the last column of each table indicates if the NP is used in the ***Properties*** analysis (P), in the ***Couplings*** one (C), or in both (B).

	Electrons			
resolution	EG_RESOLUTION_ALL	track smearing in the inner detector	P4	B
scale	ATLAS_EG_SCALE_ALLCORR, ATLAS_EG_SCALE_E4SCINTILLATOR, ATLAS_EG_SCALE_LARCALIB_EXTRA2015PRE, ATLAS_EG_SCALE_LARTEMPERATURE_EXTRA2015PRE, ATLAS_EG_SCALE_LARTEMPERATURE_EXTRA2016PRE	variations in momentum scale originating from different sources	P4	P
	EG_SCALE_ALL,EG_SCALE_AF2		P4	C
identification	EL_EFF_ID_CorrUncertainty_NP, EL_EFF_ID_UncorrUncertainty_NP	correlated and uncorrelated variations in identification efficiency	SF	B
isolation	EL_EFF_Iso_TOTAL_1NPCOR_PLUS_UNCOR	variations in isolation efficiency	SF	B
reconstruction	EL_EFF_Reco_TOTAL_1NPCOR_PLUS_UNCOR	variation in reconstruction efficiency	SF	B
trigger	EL_EFF_Trigger_TOTAL_1NPCOR_PLUS_UNCOR	variation in trigger efficiency	SF	B
	Muons			
resolution	MUONS_ID, MUONS_MS	track momentum smearing in the inner detector and muon spectrometer	P4	B
	ATLAS_MUONS_SAGITTA_RHO, ATLAS_MUONS_SAGITTA_RESBIAS		P4	C
scale	MUONS_SCALE	variation in muon momentum scale	P4	B
identification	MUONS_EFF_STAT, MUONS_EFF_SYS	statistical and systematic variations in identification efficiency	SF	P
reconstruction	MUONS_EFF_RECO_STAT, MUONS_EFF_RECO_SYS	variation in reconstruction efficiency	SF	C
	ATLAS_MUON_EFF_TTVA_STAT, ATLAS_MUON_EFF_TTVA_SYS	statistical and systematic variations of the additional correction for the efficiency of the muon track-to-vertex association cuts	SF	B
isolation	MUON_ISO_STAT, MUON_ISO_SYS	statistical and systematic variations in isolation efficiency	SF	B
trigger	MUONS_EFF_TrigUncertainty_STAT, MUONS_EFF_TrigUncertainty_SYS	statistical and systematic variations in trigger efficiency	SF	B

Table 5.4: Experimental systematic uncertainties connected with electrons and muons. The type of uncertainty, its typical name, and what it aims to model is included in the table, as well as the information on which analysis the uncertainty is applied on: in the ***Properties*** analysis (P), in the ***Couplings*** one (C), or in both (B).

	Jets			
resolution	JER	Single nuisance parameter covering jet energy resolution uncertainties	P4	P
	JER_DataVsMC	Jet energy resolution uncertainty comparing data and MC	P4	C
	JER_Effective_NP	Linear decomposition of jet energy resolution uncertainties	P4	C
scale	JES_AFII	Uncertainty arising from the use of the ATLFast-II fast simulation framework	P4	P
	JES_BJES	Heavy-flavour jet energy scale uncertainty	P4	B
	JES_EffectiveNP_	Linear decomposition of jet energy scale uncertainties	P4	B
	JES_EtaInter_Model, JES_EtaInter_NonClosure, JES_EtaInter_Stat	Uncertainties covering η-dependence of the jet energy scale	P4	B
	JES_Flavor_Comp, JES_Flavor_Resp	Uncertainties covering flavour-dependence of the jet energy scale	P4	B
	JES_HighPt	High-p_{T} jet energy scale uncertainty	P4	B
	JES_PU_OffsetMu, JES_PU_OffsetNPV, JES_PU_PtTerm, JES_PU_Rho	Uncertainties covering the effects of pile-up on the jet energy scale	P4	B
	JES_PunchThrough	Uncertainty covering effects of the calorimeter not covering the entirety of the shower due to insufficient thickness	P4	B
	JVT	Uncertainty on jet vertex tagging	SF	B
flavour tagging	FT_EFF_Eigen_B_	Eigen-vector decomposition of b-tagging uncertainties	SF	B
	FT_EFF_Eigen_C_	Eigen-vector decomposition of c-tagging uncertainties	SF	B
	FT_EFF_Eigen_Light_	Eigen-vector decomposition of light flavour tagging uncertainties	SF	B
	FT_EFF_extra	uncertainty covering extrapolation from Run 1 to Run 2	SF	B
	FT_EFF_extrapolation_from_charm	charm-quark specific extrapolation uncertainty	SF	B
	$E_{\mathrm{T}}^{\mathrm{miss}}$			
	MET_SoftTrk_ResoPara, MET_SoftTrk_ResoPerp	Soft term resolution	P4	B
	MET_SoftTrk_Scale	Soft term scale	P4	B
	ATLAS_MET_JetTrk_Scale			C

Table 5.5: Experimental systematic uncertainties connected with jets and $E_{\mathrm{T}}^{\mathrm{miss}}$. The type of uncertainty, its typical name, and what it aims to model is included in the table, as well as the information on which analysis the uncertainty is applied on: in the ***Properties*** analysis (P), in the ***Couplings*** one (C), or in both (B).

5.4 Data driven estimates

A data driven method is commonly used when it is not possible to rely on MC simulation, to describe a physics process for example when trying to estimate the rate of misidentified leptons. Indeed, despite the fact that the chance of having a jet misidentified as lepton is extremely small (with a ratio of 1:1000 for electrons and 1:10000 for muons [178]), the high cross section for multi-jet production leads to a large number of jets being misidentified. In analyses where the number of leptons is a key signature of the physical process, a precise estimation of fakes is thus needed.

5.4.1 The fake factor method

The aim of the so-called *fake factor method* is to estimate the number of events containing fake leptons. In order to do so, in addition to the *signal selection* that is used in the nominal analysis, a *control selection* is defined as enriched in events with fake leptons. In order to identify these selections and their leptons, the following notation is introduced:
a lepton is called *ID* (i) if it passes the quality cuts and *Anti-ID* (a) if it satisfies the control-selection criteria. The corresponding requirements are listed in Table 5.6, and they are valid for both analyses.

From the mathematical derivation of the method [179], the number of events with two leptons passing the signal selection (ID,ID), in which at least one lepton is fake, $N^{\text{i,i}}_{\geq 1\text{ fake}}$, is equal to:

$$N^{\text{i,i}}_{\geq 1\text{ fake}} = F_2(N^{\text{i,a}} - N^{\text{i,a}}_{2\text{ prompt}}) + F_1(N^{\text{a,i}} - N^{\text{a,i}}_{2\text{ prompt}}) - F_1F_2(N^{\text{a,a}} - N^{\text{a,a}}_{2\text{ prompt}}), \qquad (5.2)$$

where the superscript and the subscript specify the following:

$$N^{\text{identification of the leptons}}_{\text{how many leptons are prompt leptons(i.e. non-fake)}},$$

and F_1, F_2 are the *fake factors* for the first and second lepton (using the same order as the superscript), and depend on the properties of the lepton they applied to. The order of the superscript indicates the leading, and sub-leading lepton. If no subscript is given, no selection based on truth information is applied.
On the right-hand side of equation (5.2), the event yields without an index are measured in data. The number of events with 2 prompt leptons is sometimes referred to as "EW subtraction" and is simulated with MC samples. The first two terms of the right-hand side of equation (5.2) correspond to the contribution of single-fake events while the third one, with two fake factors applied, constitutes a correction for double-fake events.
The equation (5.2) is computed in two different selections and applied independently for the two leptons. $N^{\text{i,i}}_{\geq 1\text{ fake}}(\text{electron})$ and $N^{\text{i,i}}_{\geq 1\text{ fake}}(\text{muon})$ are functions of p_{T} and η of the lepton they are associated with. The factors F_x are defined as the ratio between the fake events passing the ID

Electron		Muon	
identified	anti-identified	identified	anti-identified
$p_{\mathrm{T}} > 15$ GeV		$p_{\mathrm{T}} > 15$ GeV	
$\lvert\eta\rvert < 2.47$,excluding $1.37 < \lvert\eta\rvert < 1.52$		$\lvert\eta\rvert < 2.5$	
$\lvert z_0 \sin\theta\rvert < 0.5$ mm		$\lvert z_0 \sin\theta\rvert < 0.5$ mm	
$\lvert d_0\rvert/\sigma(d_0) < 5$		$\lvert d_0\rvert/\sigma(d_0) < 3$	$\lvert d_0\rvert/\sigma(d_0) < 15$
Pass LHTight if $p_{\mathrm{T}} < 25$ GeV Pass LHMedium if $p_{\mathrm{T}} > 25$ GeV	Pass LHLoose	Pass Quality Tight	Pass Quality Medium
Pass Tight isolation		Pass Tight isolation	
Author $= 1$			
	Veto against identified electron		Veto against identified muon

Table 5.6: Requirements for fully identified and anti-identified leptons, in the ***Properties*** and ***Couplings*** analysis. Author $= 1$ is a variable that ensures that what is reconstructed is an electron and not a photon.

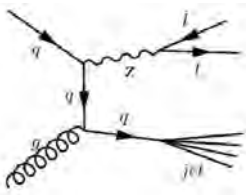

Figure 5.3: Feynman diagram of a Z+jet event. If the mass of the Z-boson is reconstructed via the di-lepton mass, and another lepton is found in the event, the latter is a fake one.

selection and the ones passing the Anti-ID selection:

$$F_x = \frac{N^i_{1\text{ fake}}}{N^a_{1\text{ fake}}}. \tag{5.3}$$

The calculation of F_1 and F_2 is performed in a region pure in leptonic Z-boson decays with a three-lepton selection, and it is illustrated in Section 5.4.2.

5.4.2 Z+jets fake factor

The selection of the fakes in the Z+jets events, of which the Feynman diagram is shown in Figure 5.3, is particularly convenient given the topology of the event: if the mass of the Z-boson is reconstructed via the di-lepton mass, and another lepton is found in the event, the latter is a fake one. In order to perform the measurement, an analysis region sufficiently pure in Z+jets needs to be defined. Its requirements follow. Three leptons with $p_{\mathrm{T}} > 15$ GeV must be found, two of which must be of the same flavor and of opposite charge to qualify as Z decay particles. They are selected with the same criteria in Table 5.6, with the exception that they only need to be *Loose* isolated and pass a *LooseLH* identification point for the electron, or *Medium* for the muon. Moreover, if they

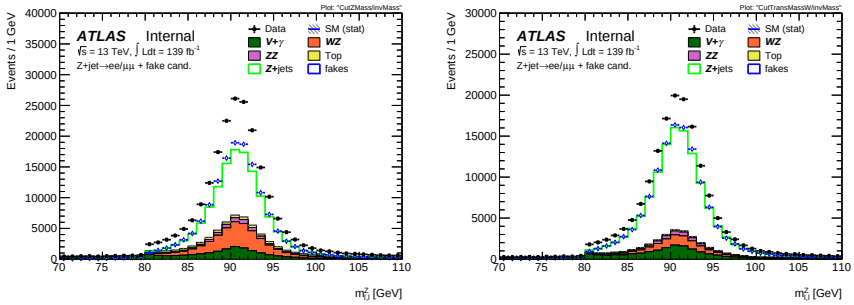

Figure 5.4: Distributions of the invariant mass of the reconstructed Z-boson candidate at the stage of Z-boson identification (left) and after applying a cut on the transverse mass $m_T^W < 50$ GeV (right). Normalization factors are not applied. The stacked histograms are background MC processes not including Z+fake. The measured data is shown in black data points. The blue data points are the data-driven Z+fake estimate. They are calculated by taking the difference between data and the stacked MC processes. They can be compared to the green Z+jets MC, which is not stacked on top of the other MC processes. The agreement between the data-driven fakes estimate and Z+jets MC can be seen by comparing the blue data points to the green Z+jets MC, although it should be noted that good closure between the two is not necessarily expected due to inaccuracies in the Z+jets MC to predict the rate at which fake leptons are produced.

5

are muons, they need to be in an invariant-mass window of [70, 110] GeV, while electrons need to be in a tighter window of [70, 110] GeV in order to reduce the $Z\gamma$ background. If at least one of the two leptons is matched to an object firing the single-lepton trigger, the leptons are accepted as Z-boson candidates. If multiple lepton combinations satisfy this requirement, the pair with the invariant mass closest to the Z boson is chosen. The remaining lepton is the fake candidate. When applied to a Z+jets MC sample, this algorithm correctly assigns leptons to the Z boson in about 99% of all cases. In order to reject events with leptonic WZ decays, a cut on $m_T^W < 50$ GeV is applied, where $m_T^W = \sqrt{2E_{\mathrm{T}}^{\mathrm{miss}} E_{\mathrm{T}}^{\text{fake cand.}}(1 - \cos\phi_{E_{\mathrm{T}}^{\mathrm{miss}},\text{fake cand}})}$. The pseudorapidity of the fake candidate is restricted to $|\eta| < 2.5$ for muons and $|\eta| < 2.47$ for electrons, which corresponds to the lepton acceptance region in the main analysis. Then, for each fake lepton type, electron and muon, two regions are constructed depending on whether the fake lepton passes the ID or Anti-ID cuts. The region above a transverse mass m_T^W of 50 GeV, where the fake candidate is required to pass the ID criteria, is used as a control region for the WZ process.The reconstructed Z-boson peak can be seen in Figure 5.4 before (a) and after (b) the cut on m_T^W, for the ***Couplings*** analysis.

The fake factors defined in equation (5.3) are measured as a ratio of events in the 3-lepton selection:

$$F = \frac{N^{\mathrm{i,i,i}} - N^{\mathrm{i,i,i}}_{\text{non-}Z\text{+jets}}}{N^{\mathrm{i,i,a}} - N^{\mathrm{i,i,a}}_{\text{non-}Z\text{+jets}}}.$$

When being applied to equation (5.2), the terms with one Anti-ID lepton cancel out and the yield

with only ID leptons remains in the numerator.

5.4.3 Uncertainties associated with the determination of the fake factor

Sample composition

Using a different phase space to estimate the F that is used in the analysis is justified by the assumption that the fake lepton efficiency only depends on the properties of the lepton, not on the remainder of the event. Therefore, the fake factor can be estimated in a three-lepton selection, where two leptons originate from a Z-boson decay and the additional lepton is the fake candidate, which is still valid when applied in a two-lepton selection. What can affect a precise computation of the F is the characteristic of the fake lepton[3], which may cause important differences, thus the fake factor must be corrected for potential sample dependencies. A way of proceeding consists in calculating a *correction factor*, defined as the ratio between the fake factor measured in Z+jets and W+jets MC, where the same selections are applied to the MC samples as are used in data. The correction factor, $CF = \frac{F^W_{\text{MC}}}{F^Z_{\text{MC}}}$, is then multiplied by the fake factor derived in the three-lepton Z+jets selection in data to give a fake factor that can be applied to W+jets data $F^W_{\text{data}} = CF \times F^Z_{\text{data}}$.

It should be generally noted that: the data-driven estimation is used because generally, the MC simulations are not accurate enough in modeling fake leptons. This translates into a correction factor that has the same MC limitation. In the end, the CF is valid as long as MC mis-estimates the data-driven fake factor by the same factor x across samples, $\frac{F^W_{\text{MC}}}{F^W_{\text{data}}} = \frac{F^Z_{\text{MC}}}{F^Z_{\text{data}}} = x$. Since fake factors are found by taking the ratio of ID to Anti-ID leptons, this translates to the requirement that MC mis-estimates the ratio of ID to Anti-ID leptons by the same factor in W+jets and Z+jets selections.

EW subtraction

The Z+jets analysis region, constructed to calculate the F factor, is not composed of 100% Z+jets events. Some other backgrounds, with their uncertainty, need to be *subtracted* from the data yield, to calculate the F factor. The uncertainty related to this process is usually referred to as the EW subtraction uncertainty. The estimate of the EW subtraction uncertainty is performed by recalculating the F with the backgrounds varied up and down according to their theoretical uncertainties. For small background, a conservative 10% up and down variation is considered.

The error associated with the F factor takes also into account the statistical uncertainties of the sample used.

Finally, lepton properties that commonly affect the fake factor, are p_{T} and η. Therefore these are variables in which the F factors are measured. The specific values of the F and their errors in the two analyses follow.

[3] What is intended here with the characteristic of the lepton is basically the flavor of the quark that has originated the jets misidentified as lepton.

Properties analysis

The uncertainties on the Z+jets fake factor are summarized in Table 5.7. The systematic uncertainties are of the order of 40% for electrons and range from 30% to 150% for muons depending on their p_{T}. For electrons, the uncertainty is not completely dominated by one source, but at the low p_T the sample composition uncertainty is the largest, at high p_T the statistical and EW subtraction uncertainties are more important. For muons, the EW subtraction uncertainty is very large at high-p_T.

Kinematic region ($\lvert\eta\rvert$ and p_T range)	Value	Statistical	EW Subtraction	Sample Composition	Total
Electron:					
$0.0 < \lvert\eta\rvert < 1.5$					
$15 - 20$ GeV	0.030	27	13	32	44
$20 - 25$ GeV	0.080	25	16	32	44
$25 - 35$ GeV	0.170	23	16	13	31
$35 - 1000$ GeV	0.284	26	33	13	44
$1.5 < \lvert\eta\rvert < 2.5$					
$15 - 20$ GeV	0.046	26	13	32	43
$20 - 25$ GeV	0.058	54	16	32	65
$25 - 35$ GeV	0.224	27	16	13	34
$35 - 1000$ GeV	0.259	32	33	13	47
Muon:					
$0.0 < \lvert\eta\rvert < 2.5$					
$15 - 20$ GeV	0.108	11	9	23	27
$20 - 25$ GeV	0.125	24	17	23	37
$25 - 1000$ GeV	0.112	76	143	23	163

Table 5.7: Summary of the fake factors from the Z+jets estimates with uncertainties in the ***Properties*** analysis. All uncertainties are quoted in percent on the nominal value. *Value* denotes the nominal fake factor value. *Statistical* denotes the statistical uncertainties on the fake factors including the extrapolation uncertainty for the highest muon p_{T} bin. *EW Subtraction* denotes the uncertainty due to the EW backgrounds that enter the Z+jets fake factor estimate. *Sample Composition* denotes the uncertainty that accounts for differences in fake factors between Z+jets and W+jets processes and includes both statistical and systematic uncertainty on the correction factors. The column *Total* sums all individual contributions in quadrature to give an overview of the total uncertainty of the fake factor. In the fit, however, the EW subtraction and sample composition uncertainties are treated as correlated between different bins, while the statistical uncertainty is uncorrelated.

Couplings analysis

The uncertainties on the Z+jets fake factor are summarized in Table 5.8. The electron fake factor was observed to be very similar between high and low η bins. Therefore, it is not measured as a function of η. The binning in p_{T} is mainly determined by the limited statistics and high background contamination in the ID selections. Since fake leptons are very rare at high p_{T}, the fake factor is only binned at small transverse momenta. In order to reduce the EW subtraction uncertainty, the highest bin in p_{T} for muons, is extrapolated from the neighboring p_{T} bin.

Kinematic region ($\lvert\eta\rvert$ and p_T range)	Value	Statistical	EW Subtraction	Sample Composition	Total
Electron:					
$0.0 < \lvert\eta\rvert < 2.5$					
$15.0 - 20.0$ GeV	0.076	6.2	3.9	7.5	10
$20.0 - 25.0$ GeV	0.086	11	8.1	31	34
$25.0 - 35.0$ GeV	0.14	13	14	7.4	20
$35.0 - \infty$ GeV	0.21	12	25	21	35
Muon:					
$0.0 < \lvert\eta\rvert < 1.05$					
$15.0 - 20.0$ GeV	0.042	8.4	7.1	8.1	14
$20.0 - 25.0$ GeV	0.017	35	34	11	50
$25.0 - 50.0$ GeV	0.026	39	58	11	71
$50.0 - \infty$ GeV	0.043	47	58	11	75
$1.05 < \lvert\eta\rvert < 2.5$					
$15.0 - 20.0$ GeV	0.060	6.7	5.3	8.1	12
$20.0 - 25.0$ GeV	0.042	17	14	11	25
$25.0 - 50.0$ GeV	0.065	19	28	11	36
$50.0 - \infty$ GeV	0.11	32	28	11	44

Table 5.8: Summary of the fake factors from the Z+jets estimate with uncertainties in the ***Couplings*** analysis. All uncertainties are quoted in percent on the nominal value. *Value* denotes the nominal fake factor value. *Statistical* denotes the statistical uncertainties on the fake factors including the extrapolation uncertainty for the highest muon p_{T} bin. *EW Subtraction* denotes the uncertainty due to the EW backgrounds that enter the Z+jets fake factor estimate. *Sample Composition* denotes the uncertainty that accounts for differences in fake factors between Z+jets and W+jets processes, and includes both statistical and systematic uncertainty on the correction factors. The column *Total* sums all individual contributions in quadrature to give an overview of the total uncertainty of the fake factor. In the fit, however, the EW subtraction and sample composition uncertainties are treated as correlated between different bins, while the statistical uncertainty is uncorrelated.

5.5 References

[4] P.A. Zyla et al. "Review of Particle Physics". In: *PTEP* 2020.8 (2020), p. 083C01. DOI: 10.1093/ptep/ptaa104 (cit. on pp. 4, 5, 17, 18, 21, 23, 36, 71, 72, 86, 89, 92).

[59] ATLAS Collaboration. "Electron and photon performance measurements with the ATLAS detector using the 2015–2017 LHC proton–proton collision data". In: *JINST* 14 (2019), P12006. DOI: 10.1088/1748-0221/14/12/P12006. arXiv: 1908.00005 [hep-ex] (cit. on pp. 50–52, 95).

[62] ATLAS Collaboration. "Muon reconstruction and identification efficiency in ATLAS using the full Run 2 pp collision data set at $\sqrt{s} = 13$ TeV". In: *Eur. Phys. J. C* 81 (2021), p. 578. DOI: 10.1140/epjc/s10052-021-09233-2. arXiv: 2012.00578 [hep-ex] (cit. on pp. 51, 95).

[68] ATLAS Collaboration. "Performance of missing transverse momentum reconstruction with the ATLAS detector using proton–proton collisions at $\sqrt{s} = 13\,\text{TeV}$". In: *Eur. Phys. J. C* 78 (2018), p. 903. DOI: 10.1140/epjc/s10052-018-6288-9. arXiv: 1802.08168 [hep-ex] (cit. on pp. 55, 96).

[86] ATLAS Collaboration. "ATLAS b-jet identification performance and efficiency measurement with $t\bar{t}$ events in pp collisions at $\sqrt{s} = 13\,\text{TeV}$". In: *Eur. Phys. J. C* 79 (2019), p. 970. DOI: 10.1140/epjc/s10052-019-7450-8. arXiv: 1907.05120 [hep-ex] (cit. on pp. 77, 96, 138).

[89] ATLAS Collaboration. *Multi-Boson Simulation for 13 TeV ATLAS Analyses*. ATL-PHYS-PUB-2017-005. 2017 (cit. on pp. 78, 94).

[92] *COMA Period Description Report*. https://atlas-tagservices.cern.ch/tagservices/RunBrowser/runBrowserReport/rBR_Period_Report.php?fnt=data16_13TeV&pn=D (cit. on p. 84).

[93] G. Aad et al. "ATLAS data quality operations and performance for 2015–2018 data-taking". In: *Journal of Instrumentation* 15.04 (Apr. 2020), P04003–P04003. DOI: 10.1088/1748-0221/15/04/p04003 (cit. on p. 84).

[94] Andy Buckley et al. "General-purpose event generators for LHC physics". In: *Physics Reports* 504.5 (July 2011), pp. 145–233. DOI: 10.1016/j.physrep.2011.03.005 (cit. on pp. 86, 92).

[95] S. Bailey et al. "Parton distributions from LHC, HERA, Tevatron and fixed target data: MSHT20 PDFs". In: *The European Physical Journal C* 81.4 (Apr. 2021). DOI: 10.1140/epjc/s10052-021-09057-0 (cit. on p. 87).

[96] S. Agostinelli et al. "Geant4—a simulation toolkit". In: *Nuclear Instruments and Methods in Physics Research Section A: Accelerators, Spectrometers, Detectors and Associated Equipment* 506.3 (2003), pp. 250–303 (cit. on p. 89).

[97] T Gleisberg et al. "Event generation with SHERPA 1.1". In: *Journal of High Energy Physics* 2009.02 (Feb. 2009), pp. 007–007. DOI: 10.1088/1126-6708/2009/02/007 (cit. on p. 90).

[98] Simone Alioli et al. "A general framework for implementing NLO calculations in shower Monte Carlo programs: the POWHEG BOX". In: *JHEP* 06 (2010), p. 043. DOI: 10.1007/JHEP06(2010)043. arXiv: 1002.2581 [hep-ph] (cit. on pp. 90, 91).

[99] Torbjörn Sjöstrand, Stephen Mrenna, and Peter Skands. "A brief introduction to PYTHIA 8.1". In: *Computer Physics Communications* 178.11 (2008), pp. 852–867 (cit. on p. 90).

[100] J. Alwall et al. "The automated computation of tree-level and next-to-leading order differential cross sections, and their matching to parton shower simulations". In: *Journal of High Energy Physics* 2014.7 (July 2014). DOI: 10.1007/jhep07(2014)079 (cit. on p. 90).

[101] Hung-Liang Lai et al. "New parton distributions for collider physics". In: *Phys. Rev. D* 82 (7 Oct. 2010), p. 074024. DOI: 10.1103/PhysRevD.82.074024 (cit. on pp. 90, 91).

[102] J. Alwall et al. "The automated computation of tree-level and next-to-leading order differential cross sections, and their matching to parton shower simulations". In: *JHEP* 07 (2014), p. 079. DOI: 10.1007/JHEP07(2014)079. arXiv: 1405.0301 [hep-ph] (cit. on p. 91).

[103] Stefano Frixione and Bryan R. Webber. "Matching NLO QCD computations and parton shower simulations". In: *JHEP* 06 (2002), p. 029. arXiv: hep-ph/0204244 (cit. on p. 91).

[104] T. Sjöstrand et al. "A Brief Introduction to PYTHIA 8.1". In: *Comput. Phys. Commun.* 178 (2008), pp. 852–867. DOI: 10.1016/j.cpc.2008.01.036. arXiv: 0710.3820 [hep-ph] (cit. on p. 91).

[105] ATLAS Collaboration. *ATLAS Pythia 8 tunes to 7 TeV data.* ATL-PHYS-PUB-2014-021. 2014 (cit. on p. 91).

[106] Richard D. Ball et al. "Parton distributions for the LHC run II". In: *JHEP* 04 (2015), p. 040. DOI: 10.1007/JHEP04(2015)040. arXiv: 1410.8849 [hep-ph] (cit. on p. 91).

[107] D. de Florian et al. "Handbook of LHC Higgs Cross Sections: 4. Deciphering the Nature of the Higgs Sector". In: 2/2017 (Oct. 2016). DOI: 10.23731/CYRM-2017-002. arXiv: 1610.07922 [hep-ph] (cit. on pp. 91, 161, 164, 170).

[108] M. Cacciari et al. "Fully Differential Vector-Boson-Fusion Higgs Production at Next-to-Next-to-Leading Order". In: *Phys. Rev. Lett.* 115.8 (2015). [Erratum: Phys. Rev. Lett. 120 (2018) 139901], p. 082002. DOI: 10.1103/PhysRevLett.115.082002. arXiv: 1506.02660 [hep-ph] (cit. on p. 91).

[109] G. Luisoni et al. "$HW^{\pm}$/HZ + 0 and 1 jet at NLO with the POWHEG BOX interfaced to GoSam and their merging within MiNLO". In: *JHEP* 10 (2013), p. 083. DOI: 10.1007/JHEP10(2013)083. arXiv: 1306.2542 [hep-ph] (cit. on p. 91).

[110] ATLAS Collaboration. "Measurement of the Z/γ^* boson transverse momentum distribution in pp collisions at $\sqrt{s}$ = 7 TeV with the ATLAS detector". In: *JHEP* 09 (2014), p. 145. DOI: 10.1007/JHEP09(2014)145. arXiv: 1406.3660 [hep-ex] (cit. on p. 91).

[111] J. M. Lindert et al. "An NLO+PS generator for $t\bar{t}$ and Wt production and decay including non-resonant and interference effects". In: *Eur. Phys. J. C* 76.12 (2016), p. 691. DOI: 10.1140/epjc/s10052-016-4538-2. arXiv: 1607.04538 [hep-ph] (cit. on p. 91).

[112] M. Czakon et al. "Top++: A program for the calculation of the top-pair cross-section at hadron colliders". In: *Comput. Phys. Commun.* 185 (2011), p. 2930. DOI: 10.1016/j.cpc.2014.06.021. arXiv: 1112.5675 [hep-ph] (cit. on p. 91).

[113] H. L. Lai et al. "New parton distributions for collider physics". In: *Phys. Rev. D* 82 (2010), p. 074024. DOI: 10.1103/PhysRevD.82.074024. arXiv: 1007.2241 [hep-ph] (cit. on p. 91).

[114] T. Gleisberg et al. "Event generation with SHERPA 1.1". In: *JHEP* 0902 (2009), p. 007. DOI: 10.1088/1126-6708/2009/02/007. arXiv: 0811.4622 [hep-ph] (cit. on p. 91).

[115] E. Bothmann et al. “Event generation with SHERPA 2.2”. In: *SciPost Physics* 7.3 (Sept. 2019). DOI: 10.21468/scipostphys.7.3.034 (cit. on p. 91).

[116] Fabio Cascioli, Philipp Maierhöfer, and Stefano Pozzorini. “Scattering Amplitudes with Open Loops”. In: *Phys. Rev. Lett.* 108 (2012), p. 111601. DOI: 10.1103/PhysRevLett.108.111601. arXiv: 1111.5206 [hep-ph] (cit. on p. 91).

[117] Keith Hamilton et al. “NNLOPS simulation of Higgs boson production”. In: *JHEP* 10 (2013), p. 222. DOI: 10.1007/JHEP10(2013)222. arXiv: 1309.0017 [hep-ph] (cit. on p. 91).

[118] Keith Hamilton, Paolo Nason, and Giulia Zanderighi. “Finite quark-mass effects in the NNLOPS POWHEG+MiNLO Higgs generator”. In: *JHEP* 05 (2015), p. 140. DOI: 10.1007/JHEP05(2015)140. arXiv: 1501.04637 [hep-ph] (cit. on p. 91).

[119] Paolo Nason. “A new method for combining NLO QCD with shower Monte Carlo algorithms”. In: *JHEP* 11 (2004), p. 040. DOI: 10.1088/1126-6708/2004/11/040. arXiv: hep-ph/0409146 (cit. on p. 91).

[120] Stefano Frixione, Paolo Nason, and Carlo Oleari. “Matching NLO QCD computations with parton shower simulations: the POWHEG method”. In: *JHEP* 11 (2007), p. 070. DOI: 10.1088/1126-6708/2007/11/070. arXiv: 0709.2092 [hep-ph] (cit. on p. 91).

[121] Jon Butterworth et al. “PDF4LHC recommendations for LHC Run II”. In: *J. Phys. G* 43 (2016), p. 023001. DOI: 10.1088/0954-3899/43/2/023001. arXiv: 1510.03865 [hep-ph] (cit. on p. 91).

[122] Torbjörn Sjöstrand et al. “An introduction to PYTHIA 8.2”. In: *Comput. Phys. Commun.* 191 (2015), p. 159. DOI: 10.1016/j.cpc.2015.01.024. arXiv: 1410.3012 [hep-ph] (cit. on p. 91).

[123] Charalampos Anastasiou et al. “High precision determination of the gluon fusion Higgs boson cross-section at the LHC”. In: *JHEP* 05 (2016), p. 058. DOI: 10.1007/JHEP05(2016)058. arXiv: 1602.00695 [hep-ph] (cit. on p. 91).

[124] Charalampos Anastasiou et al. “Higgs Boson Gluon-Fusion Production in QCD at Three Loops”. In: *Phys. Rev. Lett.* 114 (2015), p. 212001. DOI: 10.1103/PhysRevLett.114.212001. arXiv: 1503.06056 [hep-ph] (cit. on p. 91).

[125] Falko Dulat, Achilleas Lazopoulos, and Bernhard Mistlberger. “iHixs 2 – Inclusive Higgs cross sections”. In: *Comput. Phys. Commun.* 233 (2018), pp. 243–260. DOI: 10.1016/j.cpc.2018.06.025. arXiv: 1802.00827 [hep-ph] (cit. on p. 91).

[126] Robert V. Harlander and Kemal J. Ozeren. “Finite top mass effects for hadronic Higgs production at next-to-next-to-leading order”. In: *JHEP* 11 (2009), p. 088. DOI: 10.1088/1126-6708/2009/11/088. arXiv: 0909.3420 [hep-ph] (cit. on p. 91).

[127] Robert V. Harlander and Kemal J. Ozeren. “Top mass effects in Higgs production at next-to-next-to-leading order QCD: Virtual corrections”. In: *Phys. Lett. B* 679 (2009), pp. 467–472. DOI: 10.1016/j.physletb.2009.08.012. arXiv: 0907.2997 [hep-ph] (cit. on p. 91).

[128] Robert V. Harlander et al. "Higgs production in gluon fusion at next-to-next-to-leading order QCD for finite top mass". In: *Eur. Phys. J. C* 66 (2010), pp. 359–372. DOI: 10.1140/epjc/s10052-010-1258-x. arXiv: 0912.2104 [hep-ph] (cit. on p. 91).

[129] Alexey Pak, Mikhail Rogal, and Matthias Steinhauser. "Finite top quark mass effects in NNLO Higgs boson production at LHC". In: *JHEP* 02 (2010), p. 025. DOI: 10.1007/JHEP02(2010)025. arXiv: 0911.4662 [hep-ph] (cit. on p. 91).

[130] Stefano Actis et al. "NLO electroweak corrections to Higgs boson production at hadron colliders". In: *Phys. Lett. B* 670 (2008), pp. 12–17. DOI: 10.1016/j.physletb.2008.10.018. arXiv: 0809.1301 [hep-ph] (cit. on p. 91).

[131] Stefano Actis et al. "NNLO computational techniques: The cases $H \to \gamma\gamma$ and $H \to gg$". In: *Nucl. Phys. B* 811 (2009), pp. 182–273. DOI: 10.1016/j.nuclphysb.2008.11.024. arXiv: 0809.3667 [hep-ph] (cit. on p. 91).

[132] Marco Bonetti, Kirill Melnikov, and Lorenzo Tancredi. "Higher order corrections to mixed QCD-EW contributions to Higgs boson production in gluon fusion". In: *Phys. Rev. D* 97.5 (2018), p. 056017. DOI: 10.1103/PhysRevD.97.056017. arXiv: 1801.10403 [hep-ph] (cit. on p. 91). Erratum: in: *Phys. Rev. D* 97 (2018), p. 099906. DOI: 10.1103/PhysRevD.97.099906.

[133] Paolo Nason and Carlo Oleari. "NLO Higgs boson production via vector-boson fusion matched with shower in POWHEG". In: *JHEP* 02 (2010), p. 037. DOI: 10.1007/JHEP02(2010)037. arXiv: 0911.5299 [hep-ph] (cit. on p. 91).

[134] John M. Campbell et al. "NLO Higgs boson production plus one and two jets using the POWHEG BOX, MadGraph4 and MCFM". In: *JHEP* 07 (2012), p. 092. DOI: 10.1007/JHEP07(2012)092. arXiv: 1202.5475 [hep-ph] (cit. on p. 91).

[135] J. Alwall et al. "The automated computation of tree-level and next-to-leading order differential cross sections, and their matching to parton shower simulations". In: *JHEP* 07 (2014), p. 079. DOI: 10.1007/JHEP07(2014)079. arXiv: 1405.0301 [hep-ph] (cit. on p. 91).

[136] Rikkert Frederix and Stefano Frixione. "Merging meets matching in MC@NLO". In: *JHEP* 12 (2012), p. 061. DOI: 10.1007/JHEP12(2012)061. arXiv: 1209.6215 [hep-ph] (cit. on p. 91).

[137] Johannes Bellm et al. "Herwig 7.0/Herwig++ 3.0 release note". In: *Eur. Phys. J. C* 76.4 (2016), p. 196. DOI: 10.1140/epjc/s10052-016-4018-8. arXiv: 1512.01178 [hep-ph] (cit. on p. 91).

[138] M. Ciccolini, Ansgar Denner, and S. Dittmaier. "Strong and Electroweak Corrections to the Production of a Higgs Boson + 2 Jets via Weak Interactions at the Large Hadron Collider". In: *Phys. Rev. Lett.* 99 (2007), p. 161803. DOI: 10.1103/PhysRevLett.99.161803. arXiv: 0707.0381 [hep-ph] (cit. on p. 91).

[139] Mariano Ciccolini, Ansgar Denner, and Stefan Dittmaier. "Electroweak and QCD corrections to Higgs production via vector-boson fusion at the CERN LHC". In: *Phys. Rev. D* 77 (2008), p. 013002. DOI: 10.1103/PhysRevD.77.013002. arXiv: 0710.4749 [hep-ph] (cit. on p. 91).

[140] Paolo Bolzoni et al. "Higgs Boson Production via Vector-Boson Fusion at Next-to-Next-to-Leading Order in QCD". In: *Phys. Rev. Lett.* 105 (2010), p. 011801. DOI: 10.1103/PhysRevLett.105.011801. arXiv: 1003.4451 [hep-ph] (cit. on p. 91).

[141] M. L. Ciccolini, S. Dittmaier, and M. Krämer. "Electroweak radiative corrections to associated WH and ZH production at hadron colliders". In: *Phys. Rev. D* 68 (2003), p. 073003. DOI: 10.1103/PhysRevD.68.073003. arXiv: hep-ph/0306234 [hep-ph] (cit. on p. 91).

[142] Oliver Brein, Abdelhak Djouadi, and Robert Harlander. "NNLO QCD corrections to the Higgs-strahlung processes at hadron colliders". In: *Phys. Lett. B* 579 (2004), pp. 149–156. DOI: 10.1016/j.physletb.2003.10.112. arXiv: hep-ph/0307206 (cit. on p. 91).

[143] Oliver Brein et al. "Top-quark mediated effects in hadronic Higgs-Strahlung". In: *Eur. Phys. J. C* 72 (2012), p. 1868. DOI: 10.1140/epjc/s10052-012-1868-6. arXiv: 1111.0761 [hep-ph] (cit. on p. 91).

[144] Ansgar Denner et al. "HAWK 2.0: A Monte Carlo program for Higgs production in vector-boson fusion and Higgs strahlung at hadron colliders". In: *Comput. Phys. Commun.* 195 (2015), pp. 161–171. DOI: 10.1016/j.cpc.2015.04.021. arXiv: 1412.5390 [hep-ph] (cit. on p. 91).

[145] Oliver Brein, Robert V. Harlander, and Tom J. E. Zirke. "vh@nnlo – Higgs Strahlung at hadron colliders". In: *Comput. Phys. Commun.* 184 (2013), pp. 998–1003. DOI: 10.1016/j.cpc.2012.11.002. arXiv: 1210.5347 [hep-ph] (cit. on p. 91).

[146] Lukas Altenkamp et al. "Gluon-induced Higgs-strahlung at next-to-leading order QCD". In: *JHEP* 02 (2013), p. 078. DOI: 10.1007/JHEP02(2013)078. arXiv: 1211.5015 [hep-ph] (cit. on p. 91).

[147] Robert V. Harlander et al. "Soft gluon resummation for gluon-induced Higgs Strahlung". In: *JHEP* 11 (2014), p. 082. DOI: 10.1007/JHEP11(2014)082. arXiv: 1410.0217 [hep-ph] (cit. on p. 91).

[148] Enrico Bothmann et al. "Event generation with Sherpa 2.2". In: *SciPost Phys.* 7.3 (2019), p. 034. DOI: 10.21468/SciPostPhys.7.3.034. arXiv: 1905.09127 [hep-ph] (cit. on p. 91).

[149] Tanju Gleisberg and Stefan Höche. "Comix, a new matrix element generator". In: *JHEP* 12 (2008), p. 039. DOI: 10.1088/1126-6708/2008/12/039. arXiv: 0808.3674 [hep-ph] (cit. on p. 91).

[150] Steffen Schumann and Frank Krauss. "A parton shower algorithm based on Catani–Seymour dipole factorisation". In: *JHEP* 03 (2008), p. 038. DOI: 10.1088/1126-6708/2008/03/038. arXiv: 0709.1027 [hep-ph] (cit. on p. 91).

[151] Stefan Höche et al. "A critical appraisal of NLO+PS matching methods". In: *JHEP* 09 (2012), p. 049. DOI: 10.1007/JHEP09(2012)049. arXiv: 1111.1220 [hep-ph] (cit. on p. 91).

[152] Stefan Höche et al. "QCD matrix elements + parton showers. The NLO case". In: *JHEP* 04 (2013), p. 027. DOI: 10.1007/JHEP04(2013)027. arXiv: 1207.5030 [hep-ph] (cit. on p. 91).

[153] S. Catani et al. "QCD Matrix Elements + Parton Showers". In: *JHEP* 11 (2001), p. 063. DOI: 10.1088/1126-6708/2001/11/063. arXiv: hep-ph/0109231 (cit. on p. 91).

[154] Stefan Höche et al. "QCD matrix elements and truncated showers". In: *JHEP* 05 (2009), p. 053. DOI: 10.1088/1126-6708/2009/05/053. arXiv: 0903.1219 [hep-ph] (cit. on p. 91).

[155] Federico Buccioni et al. "OpenLoops 2". In: *Eur. Phys. J. C* 79.10 (2019), p. 866. DOI: 10.1140/epjc/s10052-019-7306-2. arXiv: 1907.13071 [hep-ph] (cit. on p. 91).

[156] Ansgar Denner, Stefan Dittmaier, and Lars Hofer. "Collier: A fortran-based complex one-loop library in extended regularizations". In: *Comput. Phys. Commun.* 212 (2017), pp. 220–238. DOI: 10.1016/j.cpc.2016.10.013. arXiv: 1604.06792 [hep-ph] (cit. on p. 91).

[157] Stefan Hoeche, Steffen Schumann, and Frank Siegert. "Hard photon production and matrix-element parton-shower merging". In: *Phys. Rev. D* 81 (2010), p. 034026. DOI: 10.1103/PhysRevD.81.034026. arXiv: 0912.3501 [hep-ph] (cit. on p. 91).

[158] Fabrizio Caola et al. "QCD corrections to W^+W^- production through gluon fusion". In: *Phys. Lett. B* 754 (2016), pp. 275–280. DOI: 10.1016/j.physletb.2016.01.046. arXiv: 1511.08617 [hep-ph] (cit. on p. 91).

[159] F. Cascioli et al. "Precise Higgs-background predictions: merging NLO QCD and squared quark-loop corrections to four-lepton + 0,1 jet production". In: *JHEP* 01 (2014), p. 046. DOI: 10.1007/JHEP01(2014)046. arXiv: 1309.0500 [hep-ph] (cit. on p. 91).

[160] M. Beneke et al. "Hadronic top-quark pair production with NNLL threshold resummation". In: *Nucl. Phys. B* 855 (2012), pp. 695–741. DOI: 10.1016/j.nuclphysb.2011.10.021. arXiv: 1109.1536 [hep-ph] (cit. on p. 91).

[161] Matteo Cacciari et al. "Top-pair production at hadron colliders with next-to-next-to-leading logarithmic soft-gluon resummation". In: *Phys. Lett. B* 710 (2012), pp. 612–622. DOI: 10.1016/j.physletb.2012.03.013. arXiv: 1111.5869 [hep-ph] (cit. on p. 91).

[162] Peter Bärnreuther, Michal Czakon, and Alexander Mitov. "Percent-Level-Precision Physics at the Tevatron: Next-to-Next-to-Leading Order QCD Corrections to $q\bar{q} \to t\bar{t} + X$". In: *Phys. Rev. Lett.* 109 (2012), p. 132001. DOI: 10.1103/PhysRevLett.109.132001. arXiv: 1204.5201 [hep-ph] (cit. on p. 91).

[163] Michal Czakon and Alexander Mitov. "NNLO corrections to top-pair production at hadron colliders: the all-fermionic scattering channels". In: *JHEP* 12 (2012), p. 054. DOI: 10.1007/JHEP12(2012)054. arXiv: 1207.0236 [hep-ph] (cit. on p. 91).

[164] Michal Czakon and Alexander Mitov. "NNLO corrections to top pair production at hadron colliders: the quark-gluon reaction". In: *JHEP* 01 (2013), p. 080. DOI: 10.1007/JHEP01(2013)080. arXiv: 1210.6832 [hep-ph] (cit. on p. 91).

[165] Michal Czakon, Paul Fiedler, and Alexander Mitov. "Total Top-Quark Pair-Production Cross Section at Hadron Colliders Through $O(\alpha_S^4)$". In: *Phys. Rev. Lett.* 110 (2013), p. 252004. DOI: 10.1103/PhysRevLett.110.252004. arXiv: 1303.6254 [hep-ph] (cit. on p. 91).

[166] Michal Czakon and Alexander Mitov. "Top++: A program for the calculation of the top-pair cross-section at hadron colliders". In: *Comput. Phys. Commun.* 185 (2014), p. 2930. DOI: 10.1016/j.cpc.2014.06.021. arXiv: 1112.5675 [hep-ph] (cit. on p. 91).

[167] Nikolaos Kidonakis. "Two-loop soft anomalous dimensions for single top quark associated production with a W^- or H^-". In: *Phys. Rev. D* 82 (2010), p. 054018. DOI: 10.1103/PhysRevD.82.054018. arXiv: 1005.4451 [hep-ph] (cit. on p. 91).

[168] Nikolaos Kidonakis. "Top Quark Production". In: *Proceedings, Helmholtz International Summer School on Physics of Heavy Quarks and Hadrons (HQ 2013)* (JINR, Dubna, Russia, July 15–28, 2013), pp. 139–168. DOI: 10.3204/DESY-PROC-2013-03/Kidonakis. arXiv: 1311.0283 [hep-ph] (cit. on p. 91).

[169] Charalampos Anastasiou et al. "High precision QCD at hadron colliders: Electroweak gauge boson rapidity distributions at next-to-next-to leading order". In: *Phys. Rev. D* 69 (2004), p. 094008. DOI: 10.1103/PhysRevD.69.094008. arXiv: hep-ph/0312266 (cit. on p. 91).

[170] Iain W. Stewart and Frank J. Tackmann. "Theory Uncertainties for Higgs and Other Searches Using Jet Bins". In: *Phys. Rev. D* 85 (2012), p. 034011. DOI: 10.1103/PhysRevD.85.034011. arXiv: 1107.2117 [hep-ph] (cit. on p. 92).

[171] R. Frederix et al. "Merging meets matching in MC@NLO". In: *JHEP* 12 (2012), p. 061. DOI: 10.1007/JHEP12(2012)061. arXiv: 1209.6215 [hep-ph] (cit. on pp. 93, 94).

[172] Stefano Frixione et al. "Single-top hadroproduction in association with aWboson". In: *Journal of High Energy Physics* 2008.07 (July 2008), pp. 029–029. DOI: 10.1088/1126-6708/2008/07/029 (cit. on p. 93).

[173] Ansgar Denner et al. "QCD and electroweak corrections to WZ scattering at the LHC". In: *Journal of High Energy Physics* 2019.6 (June 2019). DOI: 10.1007/jhep06(2019)067 (cit. on p. 94).

[174] Kyle Cranmer et al. *HistFactory: A tool for creating statistical models for use with RooFit and RooStats*. Tech. rep. New York: New York U., Jan. 2012 (cit. on p. 95).

[175] ATLAS Collaboration. "Jet energy scale and resolution measured in proton–proton collisions at $\sqrt{s} = 13$ TeV with the ATLAS detector". In: *Eur. Phys. J. C* 81 (2020), p. 689. DOI: 10.1140/epjc/s10052-021-09402-3. arXiv: 2007.02645 [hep-ex] (cit. on p. 96).

[176] ATLAS Collaboration. *Performance and Calibration of the JetFitterCharm Algorithm for c-Jet Identification*. ATL-PHYS-PUB-2015-001. 2015 (cit. on p. 96).

[177] ATLAS Collaboration. *Luminosity determination in pp collisions at $\sqrt{s} = 13$ TeV using the ATLAS detector at the LHC*. ATLAS-CONF-2019-021. 2019 (cit. on p. 96).

[178] G. Aad et al. "Expected Performance of the ATLAS Experiment - Detector, Trigger and Physics". In: (Dec. 2008) (cit. on p. 99).

[179] *Tools for estimating fake/non-prompt lepton backgrounds in ATLAS*. https://cds.cern.ch/record/2686919 (cit. on p. 99).

6

What: CP properties of the Higgs boson

"Is the Higgs boson a CP-even scalar ($J^{CP} = 0^{++}$) particle, as prescribed by the SM?" is the question that this Chapter is going to address. The motivation for this analysis is presented in Section 6.1, while the strategy and how the selection of the data is performed is described in Section 6.2. Following that are the statistical concepts, where the pruning procedure is described in Section 6.3. The results of the CP measurement of the Higgs boson are provided in Section 6.4, which is followed by the determination of the $\boldsymbol{\mu}_{\text{ggF+2jets}}$ signal strength measurement in Section 6.5.

Contents

6.1 Motivation

Searching for CP violation is one of the most important topics in searches for new physics. Measuring a CP-odd contribution to Higgs decay, in fact, would represent a sign of physics beyond the SM. As shown in Section 1.4.4, a previous analysis of the CP properties of the Higgs boson has been performed by using Run 1 data from $H \to WW^*$ and $H \to ZZ^*$ decays. That study analyzed the Higgs decay vertex, and a pure CP-odd scenario was excluded. However, a CP-mixed scenario is possible with a CP-odd contribution up to ~30%, [21].

What has not been investigated yet, and is the scope of this Chapter, is the amount of CP in the production vertex of the $H \to WW^*$ processes.

Given its high production rate, the gluon-fusion production mode has been chosen for this study. In this analysis, an additional two jets are required in order to define a CP sensitive observable in the final state.
According to the Higgs Characterization (HC) framework, described in Section 1.4.3, the effective Lagrangian that corresponds to the Higgs-gluon interaction is given by equation (1.24), i.e.:

$$\mathscr{L}_{X_0}^{\text{Higgs-gluon interaction}} = -\frac{g_{Hgg}}{4}(\cos(\alpha)\kappa_{gg}G_{\mu\nu}G^{\mu\nu} + \sin(\alpha)\kappa_{gg}G^a_{\mu\nu}\tilde{G}^{a,\mu\nu})H. \tag{6.1}$$

In equation (6.1), g_{Hgg} is the effective coupling for the SM CP-even ggH interaction, k_{gg} is the coupling-strength scale factor for the effective Higgs-gluon interaction and α is the CP-mixing angle. The gluon fields strength tensors G are defined as

$$G^a_{\mu\nu} = \partial_\mu G^a_\nu - \partial_\nu G^a_\mu - g_S f^{abc} G^b G^c.$$

6

The Lagrangian presented in Equation (6.1) not only describes the effective ggX_0 vertex that corresponds to diagrams like the one shown in Figure 6.1 (a), but also effective $gggX_0$ and $ggggX_0$ vertices (Figures 6.1(b), 6.1(c) respectively)

Three example benchmark scenarios with different CP properties are considered, illustrated in Table 6.1. The predictions of the SM are represented by the pure CP-even case, additionally, a pure CP-odd and a CP-mixed scenario (50% CP-even and 50% CP-odd) are generated. Further CP-mixing scenarios can be obtained by combining these three benchmark models within the morphing procedure illustrated in Section 3.4.

Scenario	Parameters
CP-even (SM)	$\kappa_{gg} = 1, cos(\alpha) = 1$
CP-odd	$\kappa_{gg} = 1, cos(\alpha) = 0$
CP-mix	$\kappa_{gg} = 1, cos(\alpha) = \frac{1}{\sqrt{2}}$

Table 6.1: Definition of the three exemplary benchmark scenarios used in the ggF +2jets analysis. The parameter settings correspond to a CP-even, a CP-odd and one CP-mixed scenario. The other parameters κ_i of the HC model that are not explicitly mentioned here are chosen to be equal to 0.

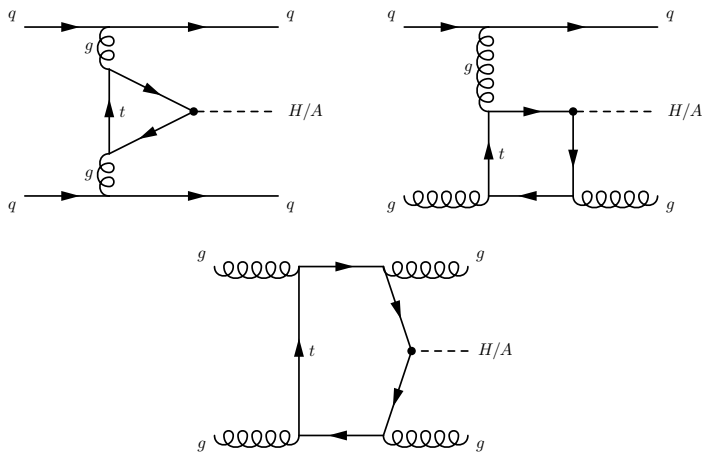

Figure 6.1: Exemplary Feynman diagrams contributing to the production of a Higgs boson in association with two jets via the fusion of two gluons at LO in QCD. The presented diagrams show examples for the subprocesses $qq \to Hjj$ (a), $qg \to Hjj$ (b) and $gg \to Hjj$ (c).

These three CP scenarios result in different shapes of the distribution of the azimuthal angle between the two associated jets, $\Delta\phi_{jj}$. The event fraction for CP-even, CP-odd and CP-mixed benchmark models in Hjj events that have been produced via gluon-fusion is shown in Figures 6.2 (a) and (b), for the inclusive case and the case with $|\Delta\phi_{jj}|$>3.0 respectively. Figure 6.2 (b) also shows that the differences between the $\Delta\phi_{jj}$ distributions of the three models is enhanced if the two leading jets have a large pseudo-rapidity gap.

In the context of the ***Properties*** analysis, four different quantities are studied: $\boldsymbol{\mu}_{\text{ggF+2jets}}$, $\tan\alpha$ $\kappa_{Hgg}\cos\alpha$ and $\kappa_{Agg}\sin\alpha$ of which the meaning is below explained.

- The signal strength parameter $\boldsymbol{\mu}_{\text{ggF+2jets}}$ for the ggF +2jets signal process. This parameter is defined as the ratio of the measured signal yield to that predicted by the SM. This analysis expands [180] where the signal strength for 0 and 1 jets was found to be $\mu_{\text{ggF+0/1jet}} = 1.10^{+0.10}_{-0.09}(\text{stat.})^{+0.19}_{-0.17}(\text{syst.})$.
- In order to constrain BSM effects in the effective Higgs–gluon coupling scenarios assuming different values of $\tan\alpha$ are scanned. Two different configurations are used in the fitting procedure:
  - The normalization of the signal process is unconstrained, in this case, the analysis only exploits the shape information of the fit input distribution to distinguish between the different CP scenarios.
  - The signal normalization is constrained to the model predictions. In this scenario, both the shape and rate information are considered for each CP hypothesis. Using rate information in addition to the shape in the fit increases the sensitivity to distinguish between the benchmark points of Table 6.1. However, the rate can also be affected

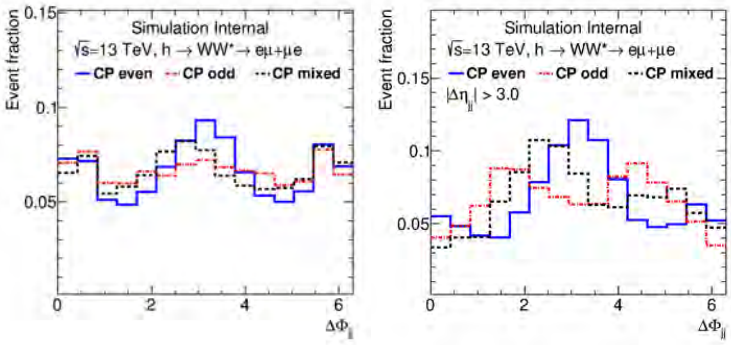

(a) Inclusive event sample

(b) Events with $|\Delta\eta_{jj}| > 3.0$ between the two leading jets

Figure 6.2: Distributions of the $\Delta\phi_{jj}$ observable are shown for ggF induced production modes of Hjj events for a CP-even, a CP-odd and a CP-mixed benchmark model. These distributions are depicted in an inclusive event sample (a) and for the case that only events are considered for which the two leading jets have a pseudorapidity gap $|\Delta\eta_{jj} > 3.0|$ (b).

by other BSM effects, while the shape information is more specifically sensitive to CP-dependent variations.

- A simultaneous fit of the coupling-strength scale factors $\kappa_{Hgg}\cos\alpha$ and $\kappa_{Agg}\sin\alpha$ is performed. This study exploits both shape and rate information.

6.2 Strategy and event selection

In order to perform the ***Properties*** analysis, final states corresponding to the production of the Higgs boson plus at least two jets via ggF and a subsequent $H\to WW^*\to \ell\nu\ell\nu$ decay are selected using the trigger configuration defined in Section 5.1.

Preselection

On top of the trigger selection, a preselection of the candidate events is applied. In order to be selected the candidates need to have:

- exactly two charged light leptons with opposite electrical charge and different flavor. This requirement suppresses Z+jets background;
- $p_{\mathrm{T}}^{\mathrm{lead}}$ >22 GeV, $p_{\mathrm{T}}^{\mathrm{sublead}}$ >15 GeV. These cuts are dictated by experimental triggers and efficiency and help reject the W+jets and QCD backgrounds;
- $m_{\ell\ell}$ >10 GeV, which suppresses backgrounds from low-mass resonances such as J/Ψ and DY processes;
- at least two jets with p_{T} > 30 GeV. This requirement suppresses contamination from QCD processes and pileup;

- the angular separation between the two leading jets ΔR_{jj} needs to be larger than 1.0. This cut reduces the contribution of $gg \to Hg$ events that do not carry any CP sensitive information.

After the preselection, further requirements are applied in order to create SR and CRs. The SR is created by applying specific selection cuts to decrease the contributions of the most dominant backgrounds, while a set of different cuts is instead used to create regions where the main backgrounds can be constrained, the CRs. In this analysis, a boosted decision tree is used to optimize the separation between the signal process and the most relevant backgrounds, and it is going to be described before the definition of the SR and CRs.

6.2.1 Signal discrimination with boosted decision tree

A boosted decision tree (BDT) is a multivariate analysis technique consisting of different decision trees [181]. These decisions aim at classifying events either as signal-like or background-like. Each decision tree takes a set of input features, i.e. physics quantities, and splits input data recursively based on those features, as shown in a sketch in Figure 6.3. From the root node, a succession of decision is completed until a score, typically a number within -1 to 1, is assigned to the event. This score, also known as $\text{BDT}_{\text{response}}$ and often specified with w_{BDT}, indicates if the particular event is more signal-like (high values scores) or background-like (low values scores).

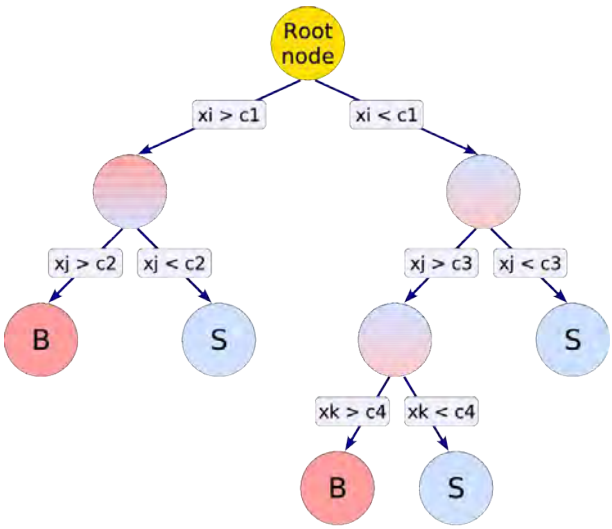

Figure 6.3: Example of a decision tree. Starting from the root node, in yellow, binary splits follow based on the values of the discriminating variables x_i. Each split uses the variable that at this node gives the best separation between signal and background when being cut on. The leaf nodes at the bottom end of the tree are labeled "S" for signal and "B" for background depending on the majority of events that end up in the respective nodes [182].

Before having the BDT applied to data, the classifier is trained and tested on MC samples. In order to be sure that the BDT response has no dependence on the statistical fluctuation of the training sample the following cross-evaluation approach is chosen:

- the input dataset is split into two independent parts: even and odd, accordingly to event numbers.
- BDT_{even} is trained on sample even and tested on sample odd
- BDT_{odd} is trained on sample odd and tested on sample even
- the final discriminant, the $\text{BDT}_{\text{response}}$, is used in the following way

$$\text{BDT}_{\text{response}} = \begin{cases} \text{BDT}_{\text{even}} & \text{applied on odd events} \\ \text{BDT}_{\text{odd}} & \text{applied on even events.} \end{cases}$$

Training of the BDT

The settings used to train the BDT are summarized in Table 6.2. These settings have been optimized to increase signal and background separation while avoiding overtraining.

Parameter	Value
Boosting type	Gradient
Separation type	Gini-Index
N^{Trees}	600
MinNodeSize	5%
nCuts	30
Depth	5

Table 6.2: Parameters of the boosted decision trees as they have been used in the training.

6

In order to enter the training, each MC event has to pass the SR event selection, which will be described in Section 6.2.2.

The signal sample used to train the signal selection BDT consists of a mixture of the three different CP hypotheses of the $gg \to Hjj$ process, while the background sample is composed of events stemming from VBF-induced Higgs-boson production and the main backgrounds as described in Section 4.2. On top of this, for top and Z+jets events, not only the nominal MC samples have been considered, but also the alternative MC samples used to obtain the theoretical uncertainty variations. This procedural choice has been made to decrease the dependence of the training result on a specific MC model. Multiple observables have been tested as input for the BDT, and the six most discriminating, which did not show strong correlations with each other, have been selected:

- invariant di-lepton mass $m_{\ell\ell}$,
- transverse mass m_{T},
- p_{T} of the di-lepton system $p_{\text{T}}^{\ell\ell}$,
- the $\Delta\phi$ of the two charged leptons $\Delta\phi_{\ell\ell}$,
- the minimum of the ΔR of the leading leptons with one of the jets $\min \Delta R(\ell^{\text{lead}}, j_i)$,

- the minimum of the ΔR of the subleading leptons with one of the jets min $\Delta R(\ell^{\text{sublead}}, j_i)$.

Their linear correlations are shown in Figure 6.4 for signal (a) and for the sum of backgrounds (b). Most of the input quantities show only a very weak correlation towards the other input quantities, with the expected exception of $[\Delta R\left(\ell^{\text{lead}}, j_i\right), \Delta R\left(\ell^{\text{sublead}}, j_i\right)]$ and $[p_{\text{T}}^{\ell\ell}, m_{\ell\ell}\,]$. The presence of these correlations does not represent a problem: given that they are different between signal and background, the BDT can use this information to further discriminate.

These observables are measured to have similar importance in the two training sets, as shown in Table 6.3.

Variable name	Variable importance
$m_{\ell\ell}$	0.257
m_{T}	0.199
$\Delta\phi_{\ell\ell}$	0.165
min $\Delta R(\ell_1^{\text{lead}}, j_i)$	0.135
$p_{\text{T}}^{\ell\ell}$	0.124
min $\Delta R(\ell_2^{\text{sublead}}, j_i)$	0.121

(a) Sample even

Variable name	Variable importance
$m_{\ell\ell}$	0.236
m_{T}	0.192
$\Delta\phi_{\ell\ell}$	0.190
min $\Delta R(\ell^{\text{lead}}, j_i)$	0.130
$p_{\text{T}}^{\ell\ell}$	0.127
min $\Delta R(\ell^{\text{sublead}}, j_i)$	0.126

(b) Sample odd

Table 6.3: Importance of the various BDT input quantities presented for the boosted decision trees that are trained in order to separate signal events from the various background processes. The exact values of the variable importance are normalised to all variables together having an importance equal to one. The values are presented separately for the case when the training is performed with the set even (a) and with set odd (b).

6.2.2 Signal and control regions definition

Signal region

The aim of the signal region is to suppress the main backgrounds as much as possible while leaving a significant amount of signal events. The observables $m_{\ell\ell}$ and m_{T} are required to be smaller than 90 GeV and 150 GeV, respectively, to reduce contributions from top-quark pairs, Wt and W+jets events. The observable $m_{\tau\tau}$, instead, needs to be below 66 GeV, with $p_{\ell\ell,\text{T}}$ >20 GeV to suppress Z+jets background. A veto of jets tagged as b-jet is applied to reduce contributions from single-top and $t\bar{t}$ pair production.

Top control region

The Top CR uses the same cuts as the SR, except for the requirement of having a jet b-tagged. The transverse momentum of this jet is required to be above 30 GeV. A normalization factor NF = 1.029±0.008 is calculated via equation (4.1) for the combined $t\bar{t}$ and Wt in the Top control region, which has a purity of 94%. This correction factor is then applied to both the $t\bar{t}$ and Wt backgrounds in order to adjust their normalization to the data in the pre-fit plots.

Preselection			
Two isolated, different-flavour leptons ($\ell = e, \mu$) with opposite charge			
$p_{\mathrm{T}}^{\mathrm{lead}} > 22$ GeV , $p_{\mathrm{T}}^{\mathrm{sublead}} > 15$ GeV			
$m_{\ell\ell} > 10$ GeV			
$N_{\mathrm{jets}}^{p_{\mathrm{T}}>30\ \mathrm{GeV}} = 2$			
ΔR_{jj}>1.0			
SR	Top CR	Z+jets CR	WW CR
$m_{\ell\ell}$ < 90 GeV			$m_{\ell\ell}$ > 90 GeV
m_{T} < 150 GeV			-
$m_{\tau\tau}$ < 66 GeV		$\lvert m_z - m_{\tau\tau}\rvert < 25$	$m_{\tau\tau}$ < 66 GeV
$p_{\ell\ell,\mathrm{T}}$ > 20 GeV		-	$p_{\ell\ell,\mathrm{T}}$ > 20 GeV
$N_{b\text{-jets}}^{p_{\mathrm{T}}>20\ \mathrm{GeV}} = 0$	$N_{b\text{-jets}}^{p_{\mathrm{T}}>30\ \mathrm{GeV}} = 1$	$N_{b\text{-jets}}^{p_{\mathrm{T}}>20\ \mathrm{GeV}} = 0$	

Table 6.4: Summary of the preselection cuts, signal region, Top CR, Z+jets CR and WW CR for the ***PROPERTIES*** analysis.

Z+jets control region

This CR aims at constraining the contribution of Z/γ^* decays. In order to construct this CR, the same cuts of the SR are used, with two exceptions: the $m_{\tau\tau}$ cut is replaced with $|m_z - m_{\tau\tau}| < 25$ GeV and the $p_{\ell\ell,\mathrm{T}}$ is removed in order to increase the statistics. A normalization factor NF = 0.829 $\pm$ 0.024 is calculated via equation (4.1) in the Z+jets CR which has a purity of 69.7%.

WW control region

The WW CR is obtained by inverting the requirement on $m_{\ell\ell}$: only events with $m_{\ell\ell}$ > 90 GeV enter this CR. In addition, the cut on m_{T} is omitted. A normalization factor NF = 0.829 $\pm$ 0.069 is calculated via equation (4.1), similar to previous listed CRs. The purity of this region is only 21.7%, due to the high contamination of $t\bar{t}$ and Wt backgrounds. This contamination is due to the fact that the leptons originating from the top quark decays are very similar in their kinematic properties to those coming from the WW backgrounds.

A summary of all requirements for the preselection, SR and CRs is shown in Table 6.4.

The three obtained NFs are applied to the pre-fit plots in order to validate the modeling of the backgrounds. The input observables to the BDT ($m_{\ell\ell}$, m_{T}, $p_{\mathrm{T}}^{\ell\ell}$, $\Delta\phi_{\ell\ell}$, $\Delta R(\ell^{\mathrm{lead}}, j_i)$, $\Delta R(\ell^{\mathrm{sublead}}, j_i)$) are shown in Figure 6.5 for the Top CR, in Figure 6.6 for the Z+jets CR, and in Figure 6.7 for the W+jets CR. The BDT response is shown in Figure 6.8 for all CRs. Moreover, the yields for each process are displayed in Table 6.5, where the Wt and $t\bar{t}$, Z+jets and WW NFs are again applied.

Same-sign validation region

A dedicated region to validate WZ, ZZ, $V\gamma$, as well as W+jets processes is obtained by exclusively selecting, events that have a pair of same-sign leptons, after the preselection. Figure 6.9 shows the

Process	Top CR Yields	%	Z+jets CR Yields	%	WW CR Yields	%
ggF	33.27 ± 1.24	0.2	19.43 ± 0.83	0.7	0.12 ± 0.04	0.0
VBF	8.72 ± 0.13	0.0	6.86 ± 0.10	0.2	0.01 ± 0.00	0.0
Other Higgs	6.09 ± 0.22	0.0	20.09 ± 0.35	0.8	2.45 ± 0.12	0.1
$t\bar{t}/Wt$	17761.83 ± 57.91	**93.8**	433.56 ± 8.64	15.2	3459.07 ± 25.82	72.3
Z+jets	246.85 ± 9.86	1.3	1970.83 ± 38.59	**69.2**	18.94 ± 2.79	0.4
WW	126.75 ± 2.33	0.7	150.32 ± 2.50	5.3	1036.07 ± 7.32	**21.7**
W+jets	692.51 ± 27.75	3.7	96.45 ± 15.16	3.3	151.20 ± 12.98	3.2
$WZ, ZZ, V\gamma$	54.70 ± 5.14	0.3	149.53 ± 11.01	5.2	113.65 ± 4.32	2.4
Sum	18930.72 ± 65.22		2847.08 ± 43.84		4781.52 ± 30.25	
Observed	18886		2800		4778	

Table 6.5: Event yields and relative sample composition in the CRs and the observed yields in data. The event yields of both the Wt and $t\bar{t}$, Z+jets and WW backgrounds are corrected by their normalisation factors. In addition, the statistical uncertainties on the respective signal and background processes are shown as well.

modeling in these regions of the input observables of the BDT, where the Wt and $t\bar{t}$, Z+jets and WW NFs are applied.

Low BDT response value region

As a blinding strategy is followed, the modeling of the input BDT quantities should not be studied in the SR. However, as mentioned in Section 6.2.1, at low values of the BDT response, only few signal events are supposed to be present. Given that, the modeling of the region with BDT response < 0 can be safely checked. Figure 6.10 shows the modeling of these regions, where the contributions of the Wt and $t\bar{t}$, Z+jets and WW backgrounds are corrected by the pre-fit normalisation scale factors. Additionally, Figure 6.11 shows the shape comparison between the ggF +VBF signal vs the sum of the backgrounds of the BDT response, when both distributions are normalized to a unit area.

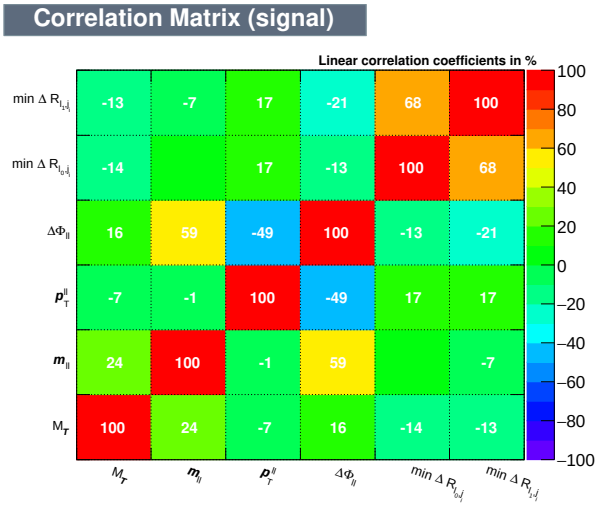

(a) Linear correlation coefficients for the signal

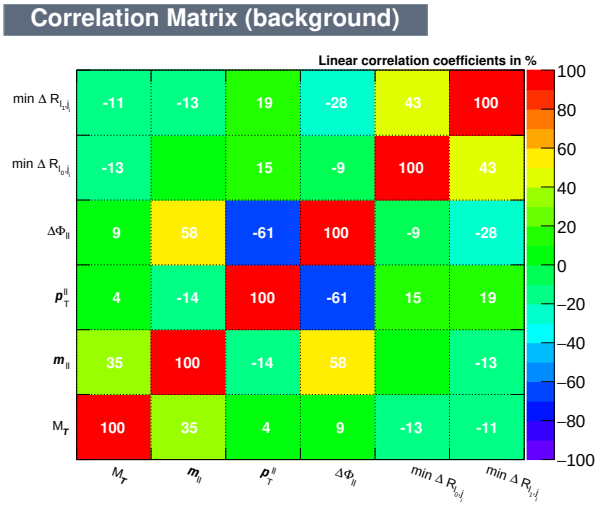

(b) Linear correlation coefficients for the sum of backgrounds

Figure 6.4: Matrices of the linear correlation coefficients for the final set of BDT input quantities for the signal (a) and the sum of background processes (b). A colour varying from light green to red indicates a positive correlation, while from dark green to violet a negative one. For simplicity the correlation coefficients are also displayed.

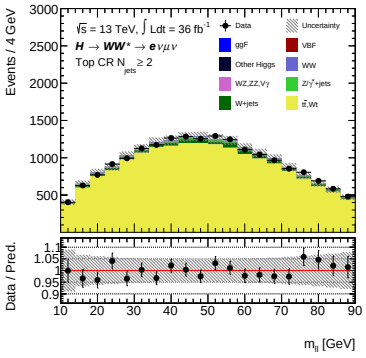

(a) Invariant di-lepton mass $m_{\ell\ell}$

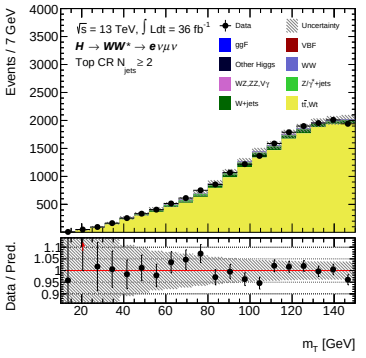

(b) Transverse mass m_{T}

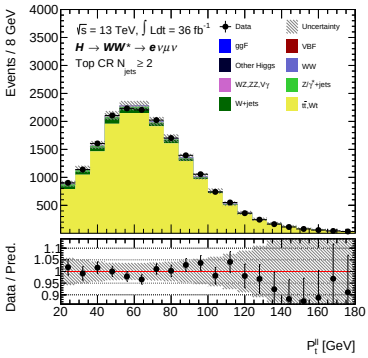

(c) p_{T} of di-lepton system

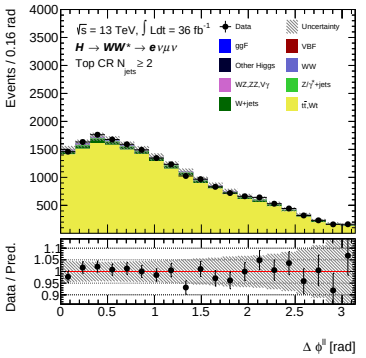

(d) $\Delta\phi_{\ell\ell}$

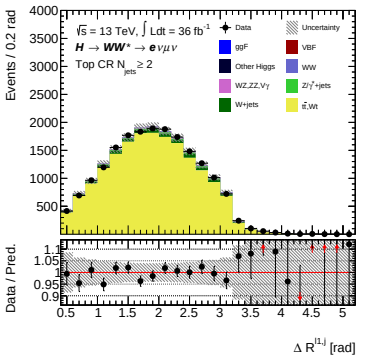

(e) $\Delta R(\ell^{\text{lead}}, j_i)$

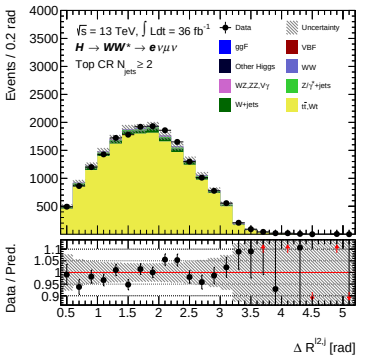

(f) $\Delta R(\ell^{\text{sublead}}, j_i)$

Figure 6.5: Pre-fit distributions of the six BDT input quantities $m_{\ell\ell}$ (a), m_{T} (b), $p_{\mathrm{T}}^{\ell\ell}$ (c), $\Delta\phi_{\ell\ell}$ (d), $\Delta R(\ell^{\text{lead}}, j_i)$ (e) and $\Delta R(\ell^{\text{sublead}}, j_i)$ (f) presented in the Top control region. Data-to-simulation ratios are shown at the bottom of each plot. The contributions of the Wt and $t\bar{t}$, Z+jets and WW backgrounds are corrected by the pre-fit normalisation scale factors. The uncertainty band represents the quadratic sum of the statistical and the dominant experimental uncertainties.

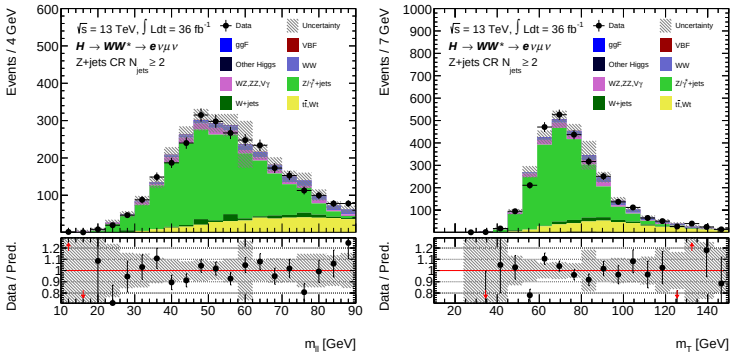

(a) Invariant di-lepton mass $m_{\ell\ell}$ **(b)** Transverse mass m_{T}

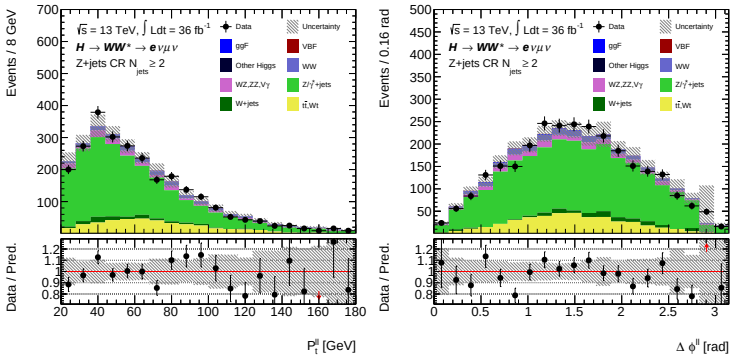

(c) p_{T} of di-lepton system **(d)** $\Delta\phi_{\ell\ell}$

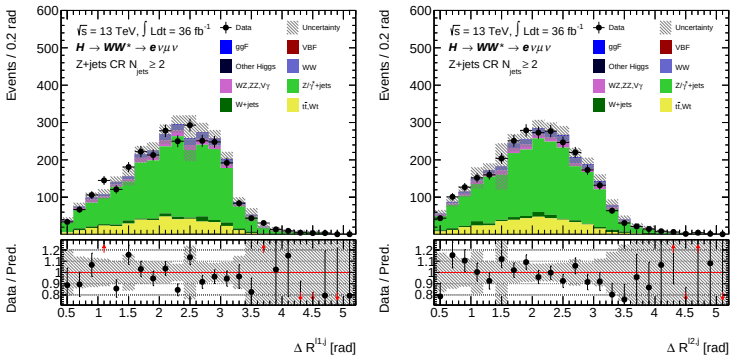

(e) $\Delta R(\ell^{\text{lead}}, j_i)$ **(f)** $\Delta R(\ell^{\text{sublead}}, j_i)$

Figure 6.6: Pre-fit distributions of the six BDT input quantities $m_{\ell\ell}$ (a), m_{T} (b), $p_{\mathrm{T}}^{\ell\ell}$ (c), $\Delta\phi_{\ell\ell}$ (d), $\Delta R(\ell^{\text{lead}}, j_i)$ (e) and $\Delta R(\ell^{\text{sublead}}, j_i)$ (f) presented in the Z+jets CR. Data-to-simulation ratios are shown at the bottom of each plot. The contributions of the Wt and $t\bar{t}$, Z+jets and WW backgrounds are corrected by the pre-fit normalisation scale factors. The uncertainty band represents the quadratic sum of the statistical and the dominant experimental uncertainties.

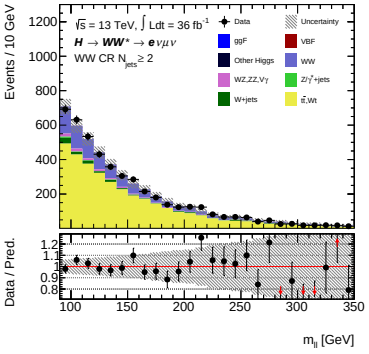

(a) Invariant di-lepton mass $m_{\ell\ell}$

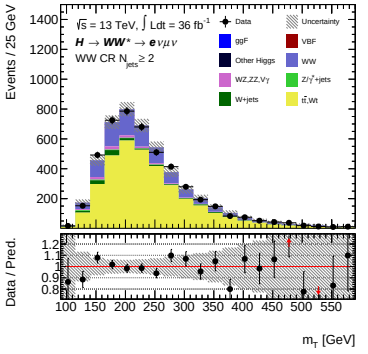

(b) Transverse mass m_{T}

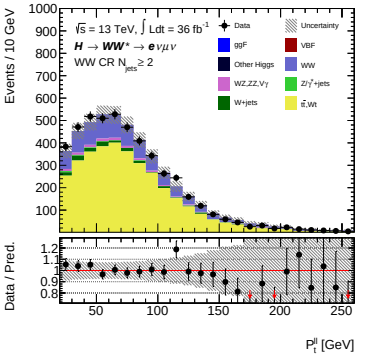

(c) p_{T} of di-lepton system

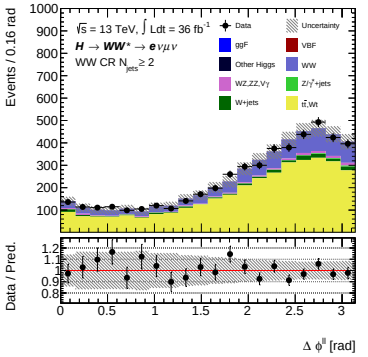

(d) $\Delta\phi_{\ell\ell}$

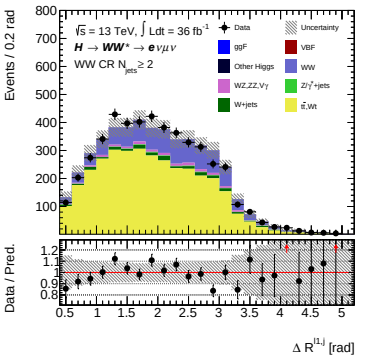

(e) $\Delta R(\ell^{\text{lead}}, j_i)$

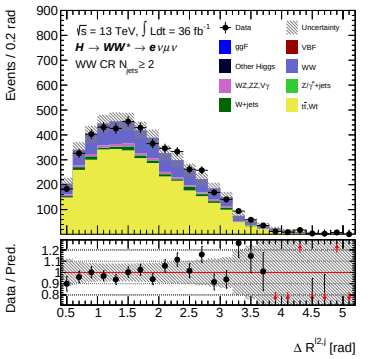

(f) $\Delta R(\ell^{\text{sublead}}, j_i)$

Figure 6.7: Pre-fit distributions of the six BDT input quantities $m_{\ell\ell}$ (a), m_{T} (b), $p_{\mathrm{T}}^{\ell\ell}$ (c), $\Delta\phi_{\ell\ell}$ (d), $\Delta R(\ell^{\text{lead}}, j_i)$ (e) and $\Delta R(\ell^{\text{sublead}}, j_i)$ (f) presented in the WW control region. Data-to-simulation ratios are shown at the bottom of each plot. The contributions of the Top, WW and Z+jets backgrounds are corrected by the pre-fit normalisation scale factors. The uncertainty band represents the quadratic sum of the statistical and the dominant experimental uncertainties.

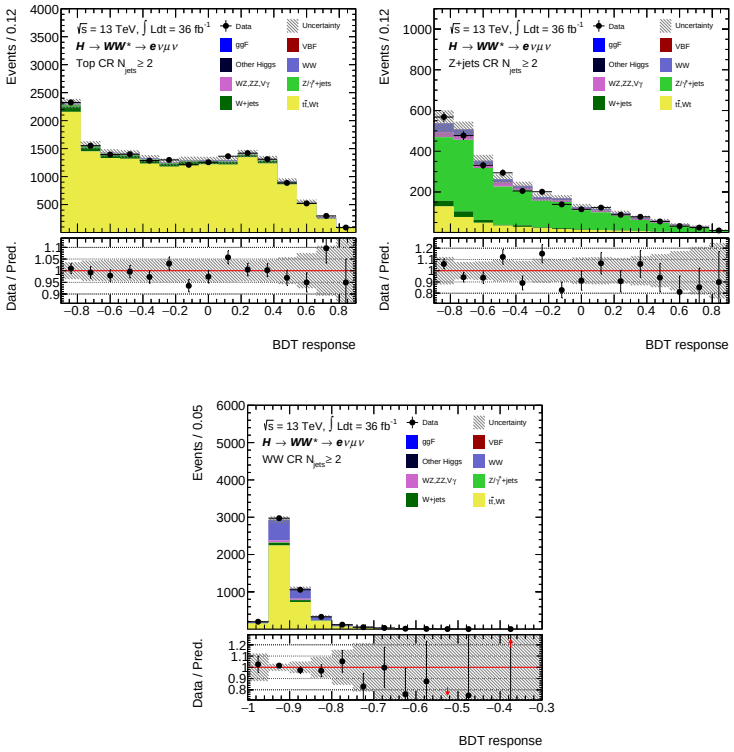

Figure 6.8: Pre-fit distributions of the BDT response in the Top CR (a), Z+jets CR (b), and WW CR (c). Data-to-simulation ratios are shown at the bottom of each plot. The contributions of the Wt and $t\bar{t}$, Z+jets and WW backgrounds are corrected by the pre-fit normalisation scale factors. The uncertainty band represents the quadratic sum of the statistical and the dominant experimental uncertainties.

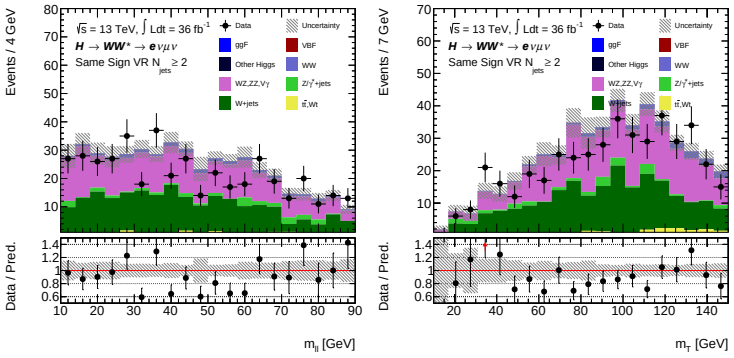

(a) Invariant di-lepton mass $m_{\ell\ell}$ **(b)** Transverse mass m_{T}

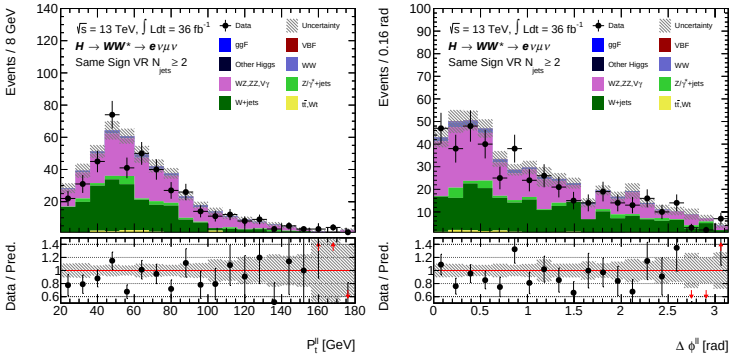

(c) p_{T} of di-lepton system **(d)** $\Delta\phi_{\ell\ell}$

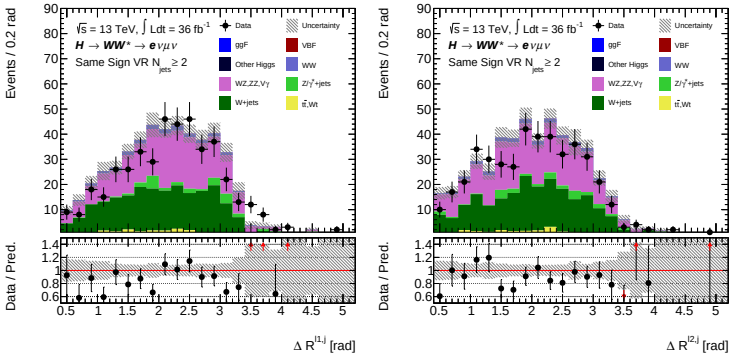

(e) **(f)**

Figure 6.9: Pre-fit distributions of the six BDT input quantities $m_{\ell\ell}$ (a), m_{T} (b), $p_{\mathrm{T}}^{\ell\ell}$ (c), $\Delta\phi_{\ell\ell}$ (d), $\Delta R(\ell^{\mathrm{lead}}, j_i)$ (e) and $\Delta R(\ell^{\mathrm{sublead}}, j_i)$ (f) presented in the same-sign region. Data-to-simulation ratios are shown at the bottom of each plot. The contributions of the Wt and $t\bar{t}$, Z+jets and WW backgrounds are corrected by the pre-fit normalisation scale factors. The uncertainty band represents the quadratic sum of the statistical and the dominant experimental uncertainties.

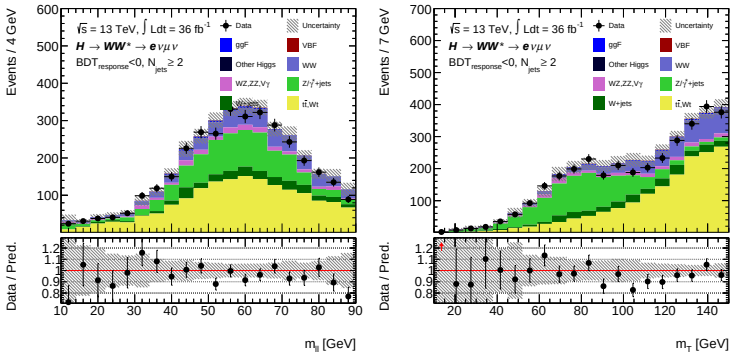

(a) Invariant di-lepton mass $m_{\ell\ell}$ **(b)** Transverse mass m_{T}

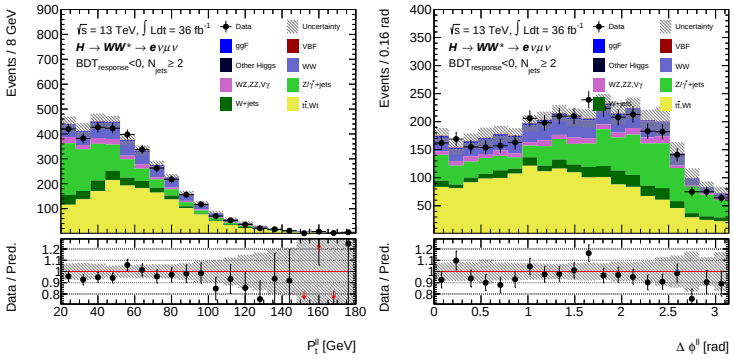

(c) p_{T} of di-lepton system **(d)** $\Delta\phi_{\ell\ell}$

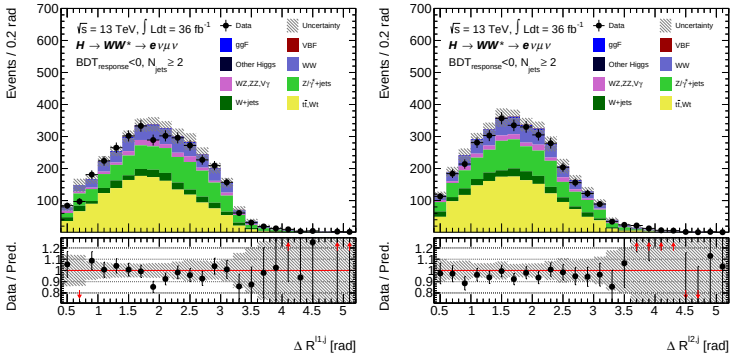

(e) $\Delta R(\ell^{\mathrm{lead}}, j_i)$ **(f)** $\Delta R(\ell^{\mathrm{sublead}}, j_i)$

Figure 6.10: Pre-fit distributions of the six BDT input quantities $m_{\ell\ell}$ (a), m_{T} (b), $p_{\mathrm{T}}^{\ell\ell}$ (c), $\Delta\phi_{\ell\ell}$ (d), $\Delta R(\ell^{\mathrm{lead}}, j_i)$ (e) and $\Delta R(\ell^{\mathrm{sublead}}, j_i)$ (f) presented in the low-BDT values region. Data-to-simulation ratios are shown at the bottom of each plot. The contributions of the Wt and $t\bar{t}$, Z+jets and WW backgrounds are corrected by the pre-fit normalisation scale factors. The uncertainty band represents the quadratic sum of the statistical and the dominant experimental uncertainties.

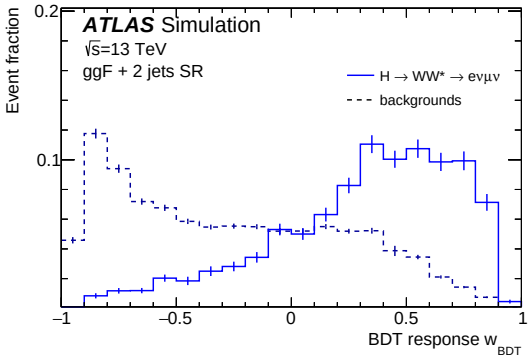

Figure 6.11: Shape comparison of the BDT response w_{BDT} distribution between $H(\rightarrow WW^* \rightarrow e\nu\mu\nu)$ + 2 jets events and the sum of backgrounds. The distribution for H + 2jets represents the sum of events produced via the ggF +2jets and VBF production modes. Both distributions are normalised to unit area. The errors are statistical only.

6.2.3 Fitted observables

As mentioned earlier in the text, two kinds of measurements are performed: the signal strength $\mu_{\text{ggF}+2jets}$, or the CP properties of the Higgs boson.

The BDT response is used as the fitting observable for the first case. The choice of the binning has been made with the intent of maximizing the significance[1], and it was tested using an Asimov dataset (Section 3.1.2). The chosen configuration has 24 bins and presents a finer binning for high values of the BDT response where the fraction of signal is higher. The bins definitions of the observables are shown in Table 6.6, while the distribution of the observable in simulated data is shown in Figure 6.12.

For the study of the CP properties of the top-Yukawa coupling the fitting observable consist of a three-dimensional distribution in w_{BDT}, $\Delta\eta_{jj}$ as well as the $\Delta\phi_{jj}$. This choice is motivated by the fact that the CP-even, CP-odd and CP-mixed benchmark models in Hjj produced by gluon-fusion show shape differences in the $\Delta\phi_{jj}$ on the two leading jets and that the shape difference is enhanced at large $\Delta\eta_{jj}$ values, as was already shown in Figure 6.2. Without loss of information, the three-dimensional distribution is unrolled to a one-dimensional distribution. This lead to the $\Delta\phi_{jj}$ distribution divided into several different BDT bins, and in turn split into several bins of $|\Delta\eta_{jj}|$. The binning has been chosen by testing it on the Asimov dataset and it was decided to define 5 bins in BDT response, 4 in $|\Delta\eta_{jj}|$ and 14 in $\Delta\phi_{jj}$, for a total of 280 bins. The procedure is illustrated in Table 6.7 and shown in Figure 6.13.

[1]The significance Z_0 is approximated as $\sqrt{2((s+b)\ln(1+s/b)-s)}$, where s indicates the signal events and b the background ones.

Bin	BDT response range	Bin	BDT response range
1	$w_{\text{BDT}} < -0.86$	13	$0.22 < w_{\text{BDT}} < 0.28$
2	$-0.86 < w_{\text{BDT}} < -0.72$	14	$0.28 < w_{\text{BDT}} < 0.34$
3	$-0.72 < w_{\text{BDT}} < -0.58$	15	$0.34 < w_{\text{BDT}} < 0.4$
4	$-0.58 < w_{\text{BDT}} < -0.44$	16	$0.4 < w_{\text{BDT}} < 0.46$
5	$-0.44 < w_{\text{BDT}} < -0.3$	17	$0.46 < w_{\text{BDT}} < 0.52$
6	$-0.3 < w_{\text{BDT}} < -0.22$	18	$0.52 < w_{\text{BDT}} < 0.58$
7	$-0.22 < w_{\text{BDT}} < -0.14$	19	$0.58 < w_{\text{BDT}} < 0.64$
8	$-0.14 < w_{\text{BDT}} < -0.06$	20	$0.64 < w_{\text{BDT}} < 0.7$
9	$-0.06 < w_{\text{BDT}} < 0.02$	21	$0.7 < w_{\text{BDT}} < 0.76$
10	$0.02 < w_{\text{BDT}} < 0.1$	22	$0.76 < w_{\text{BDT}} < 0.82$
11	$0.1 < w_{\text{BDT}} < 0.16$	23	$0.82 < w_{\text{BDT}} < 0.88$
12	$0.16 < w_{\text{BDT}} < 0.22$	24	$w_{\text{BDT}} > 0.88$

Table 6.6: Maps of the binning of the fitting variable for the signal strength measurement. Taken from [183].

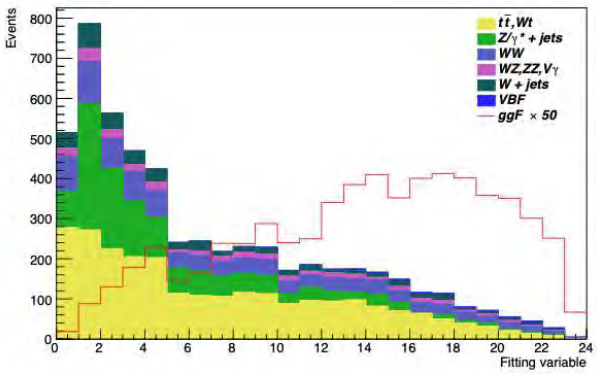

Figure 6.12: Binning of the fitting variable for the signal strength measurement of ggF +2jet. The x-axis shows the bin numbers.

As can be seen in Figure 6.13, the amount of MC in each bin is not always optimal. Indeed, several bins contain a negative amount of events in one of the samples[2], and others feature a sum of all background events smaller than one event. Both scenarios can cause instability in the fit, so a bin merging strategy is applied.

Starting from the rightmost bin of the unrolled distribution, bins are merged with the bin on their left until both the conditions that there is no less than one MC event and that there are no negative entries in a MC sample in the merged bin, are fulfilled. If the very first of a BDT distribution requires merging, the bin is merged with the first neighboring one on the right. An example of the merging strategy is shown in Figure 6.14. This procedure reduces the number of bins from 280 to 184 bins and the resulting distribution is shown in Figure 6.15.

[2]Negative entries are due to negative generator weights.

Bin	BDT response range
1	$w_{\text{BDT}} < -0.3$
2	$-0.3 < w_{\text{BDT}} < 0.1$
3	$0.1 < w_{\text{BDT}} < 0.4$
4	$0.4 < w_{\text{BDT}} < 0.7$
5	$w_{\text{BDT}} > 0.7$

(a)

Bin	$\lvert\Delta\eta_{jj}\rvert$ range
1	$\lvert\Delta\eta_{jj}\rvert < 1.0$
2	$1.0 < \lvert\Delta\eta_{jj}\rvert < 2.0$
3	$2.0 < \lvert\Delta\eta_{jj}\rvert < 3.0$
4	$\lvert\Delta\eta_{jj}\rvert > 3.0$

(b)

Bin	$\Delta\phi_{jj}$ response range
1	$\Delta\phi_{jj} < 2\pi/14$
2	$2\pi/14 < \Delta\phi_{jj} < 4\pi/14$
3	$4\pi/14 < \Delta\phi_{jj} < 6\pi/14$
4	$6\pi/14 < \Delta\phi_{jj} < 8\pi/14$
5	$8\pi/14 < \Delta\phi_{jj} < 10\pi/14$
6	$10\pi/14 < \Delta\phi_{jj} < 12\pi/14$
7	$12\pi/14 < \Delta\phi_{jj} < \pi$

(c)

Bin	$\Delta\phi_{jj}$ response range
8	$\pi < \Delta\phi_{jj} < 16\pi/14$
9	$16\pi/14 < \Delta\phi_{jj} < 18\pi/14$
10	$18\pi/14 < \Delta\phi_{jj} < 20\pi/14$
11	$20\pi/14 < \Delta\phi_{jj} < 22\pi/14$
12	$22\pi/14 < \Delta\phi_{jj} < 24\pi/14$
13	$24\pi/14 < \Delta\phi_{jj} < 26\pi/14$
14	$\Delta\phi_{jj} > 26\pi/14$

(d)

Table 6.7: Binning for the BDT response (a), $|\Delta\eta_{jj}|$ (b) and $\Delta\phi_{jj}$ (c-d) in the unrolled fitting variable for the CP measurement. Taken from [183].

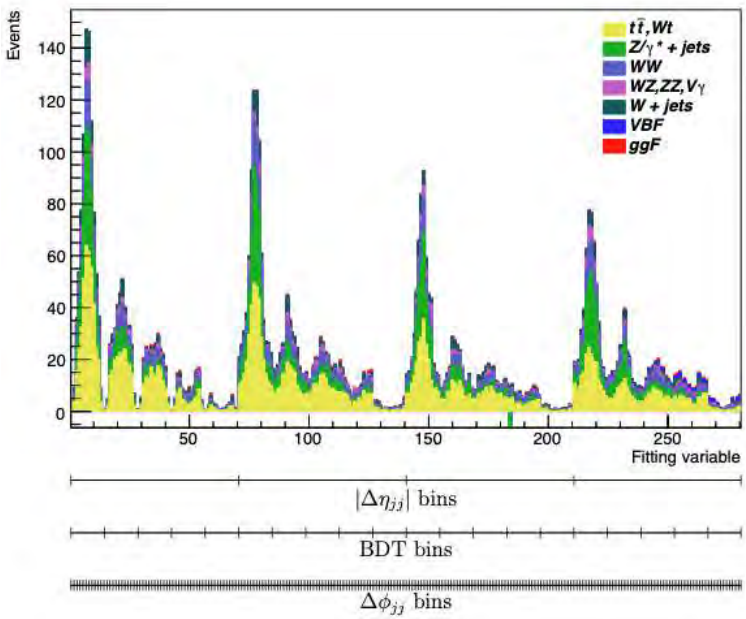

Figure 6.13: Binning of the fitting variable for the CP measurement. The x-axis shows the bin numbers. The different $|\Delta\eta_{jj}|$, BDT response and $\Delta\phi_{jj}$ bins are indicated. The CP-even ggF MC sample is shown. Taken from [183].

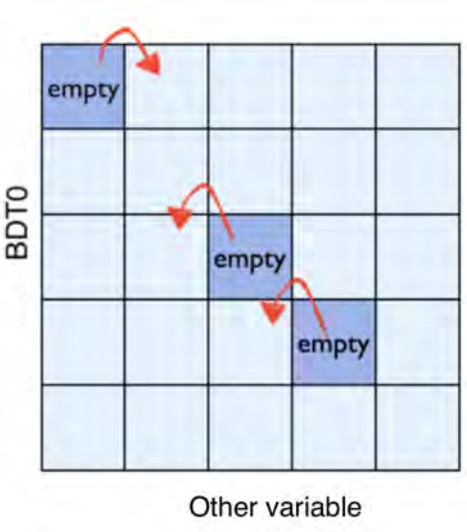

Figure 6.14: Unrolling example from 2D to 1D for bins with less than 1 event and negative entries for any MC sample. The red arrow shows the direction of the merging. In general, the empty bin is merged with the neighboring one on the left side in the same BDT row, with the exception of the case when there is no left bin, in that case, the empty bin is merged with the neighboring right bin, as happens in the first top row.

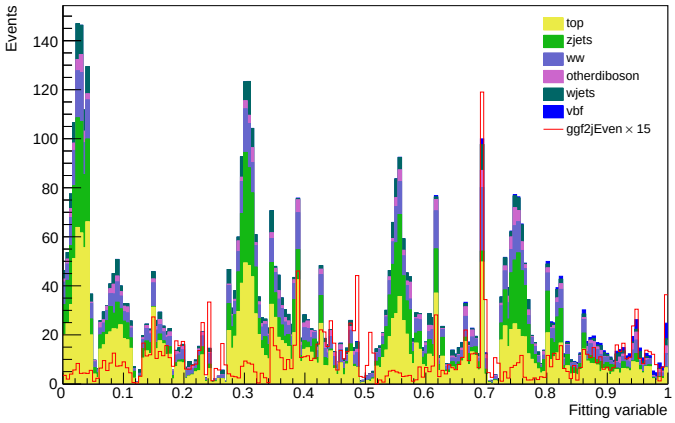

Figure 6.15: The distribution of the BDT response versus $\Delta\Phi_{jj}$ in 4 different $\Delta\eta_{jj}$ bins after merging all bins with negative entries or with a few events.

6.3 Statistical analysis

A maximum Likelihood fit, as described in Section 3.1.1 is used for the statistical interpretation of the data. The fit is jointly performed on all SR and CRs in order to simultaneously constrain the POI, the normalization of backgrounds and the NPs describing the systematic uncertainties. The list of defined uncertainties in the ***Properties*** analysis can be found in Section 5.3. Each uncertainty has a double effect on the MC sample is related to: it has a normalization component, affecting only its yield, and a shape component, which changes the shape of the MC sample in a specific distribution, but leaves untouched the yield. These two effects are parametrized by the same NP, but exceptions exist.

Contribution from ggF +0/1jet events
Due to the presence of pile-up jets or mis-measurements of jet energies, ggF +0/1jet events[3] can migrate into the ggF +2jets signal region. These ggF +0/1jet events are considered as background since they are not sensitive to the CP nature of the effective Higgs-gluon coupling. The statistics of the ggF +0/1jet templates are strongly limited, such that each $\Delta\Phi_{jj}$ distribution within the w_{BDT}-$\Delta\Phi_{jj}$-$\Delta\eta_{jj}$ observables, is dominated by statistical fluctuations. To mitigate unphysical behavior, the ggF +0/1jet background is assumed to have a flat $\Delta\Phi_{jj}$ distribution (i.e. the bin contents within every w_{BDT}-$\Delta\eta_{jj}$ region are set to the average value of the event yields of the corresponding 14 $\Delta\Phi_{jj}$ bins). To account for the lack of information on the $\Delta\Phi_{jj}$ shapes, a flat uncertainty of 100% is assumed on the ggF +0/1jet background contribution to the ggF +2jets signal region.

A comparison of the distributions of the (w_{BDT}-$\Delta\eta_{jj}$) observables for the ggF +2jets and ggF +0/1 jet production modes is shown in Figure 6.16[4].

Pruning procedure
An automatic parameter pruning procedure is applied to the likelihood function, in order to simplify the convergence of the minimization procedure and to reduce the fit execution time.

- Normalization systematics producing a normalization effect smaller than 1.0% are neglected.
- Shape systematics neglected if the variation in none of the bins is greater than 1.0%.

The pruning is applied independently for each systematic uncertainty in each analysis region for each process and may leave uncertainties with only one of the components (shape or normalization).

After the Likelihood maximization is performed, the best-fit values for all the parameters are extracted and used to build the post-fit model.

[3] The ggF +0/1jet contribution is defined as all gluon-fusion induced Higgs-boson events that do not have two or more jets at particle level with $p_{\text{T}} > 30$ GeV and $|\eta| < 4.5$

[4] The order of the bins in the following: the 5 BDT bins described in Table 6.13 (a) are repeated for the 4 bins of $\Delta\eta_{jj}$ (Table 6.13(b)). The ggF +2jets w_{BDT} individual distribution behaves as shown in Figure 6.11.

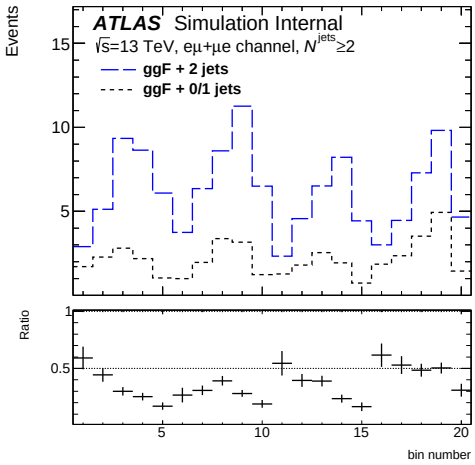

Figure 6.16: Comparison of the ggF +2jets and ggF +0/1 jet contributions to the signal region.

6.4 μ_{ggF} rate measurement

The signal strength parameter of the ggF +2jets process is found to be

$$\boldsymbol{\mu}_{\text{ggF+2jets}} = 0.5 \pm 0.4(\text{stat.})^{+0.7}_{-0.6}(\text{syst.})$$

and the post-fit distribution of the BDT weights is shown in Figure 6.17. In this measurement, the contribution of VBF is fixed to the SM predictions. The post-fit event yields in the signal region and the various control regions are presented in Table 6.8.

The $\boldsymbol{\mu}_{\text{ggF+2jets}}$ rate measurement precision is limited by the impact of systematic uncertainties, in particular, to the PS and the matrix element modeling for the $t\bar{t}$ process are limiting factors. On top of this also the uncertainty of the b-jet reconstruction algorithm plays an important role, as can be seen from the breakdown of uncertainties presented in Table 6.9.

In Table 6.9 only contributions larger than 0.01 are included in the breakdown. Given the correlations among the individual components, the sum of these in quadrature may differ slightly from the total uncertainty.

The measurement of $\boldsymbol{\mu}_{\text{ggF+2jets}}$ can also be performed when the VBF contribution is not fixed to the SM. In this case a simultaneous fit of $\boldsymbol{\mu}_{\text{ggF+2jets}}$ and $\boldsymbol{\mu}_{\text{VBF}}$ results in $\boldsymbol{\mu}_{\text{ggF+2jets}} = 0.7 \pm 0.4\,(\text{stat.})^{+0.8}_{-0.7}\,(\text{syst.})$ and $\boldsymbol{\mu}_{\text{VBF}} = 0.3 \pm 0.4\,(\text{stat.}) \pm 0.4\,(\text{syst.})$ respectively. The two signal strengths have a linear correlation coefficient of -0.34. The 2-dimensional fit result is also shown in Figure 6.18, where the red star indicates the SM prediction, and the black star indicates the observed best-fit values. Additionally, the 68% and 95% CL contours are shown as a solid and dotted line respectively.

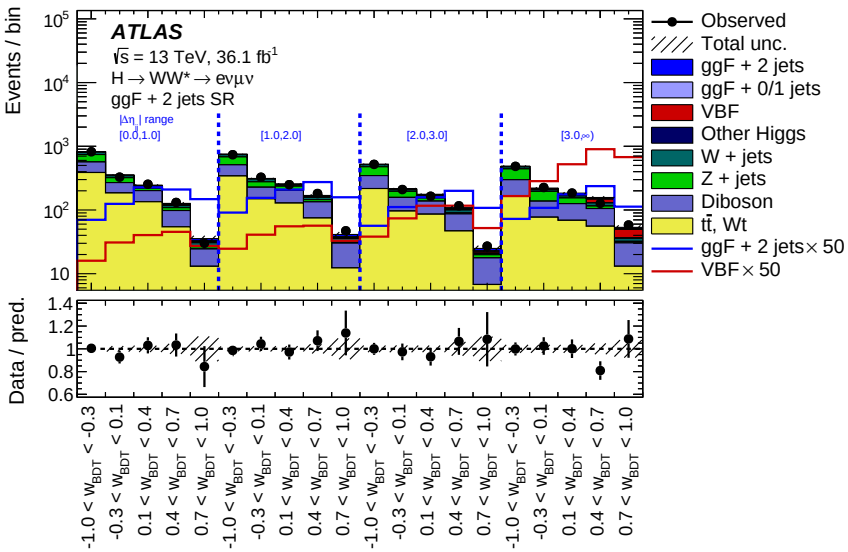

Figure 6.17: Post-fit distribution of the BDT response observable presented in the four $|\Delta\eta_{jj}|$ categories of the ggF + 2 jets signal region, with signal and background yields fixed from the fit for $\mu^{\text{ggF+2jets}}$. Data-to-simulation ratios are shown at the bottom of the plot. The shaded areas depict the total uncertainty. The distributions of the ggF + 2 jets and VBF processes are overlaid with their respective contributions multiplied by 50.

Process	Top CR	WW CR	$Z \to \tau\tau$ CR	SR
ggF + 2jets	20 ± 20	< 0.1	10 ± 10	60 ± 80
ggF + 0/1 jets	4 ± 1	< 0.1	3 ± 1	40 ± 20
VBF	8 ± 1	< 0.1	7 ± 1	70 ± 10
Other Higgs	6 ± 3	2 ± 1	20 ± 10	30 ± 10
$t\bar{t}, Wt$	17800 ± 200	3100 ± 500	390 ± 60	2300 ± 300
WW	180 ± 80	1400 ± 500	200 ± 70	1200 ± 400
Z+jets	220 ± 30	16 ± 3	1960 ± 70	1000 ± 100
W+jets	600 ± 200	140 ± 30	90 ± 20	390 ± 80
Non-WW dibosons	40 ± 30	100 ± 30	120 ± 50	240 ± 80
Observed	18886	4778	2800	5209

Table 6.8: Post-fit event yields in the signal and control regions obtained from the study of the signal strength parameter $\mu_{\text{ggF+2jets}}$. The quoted uncertainties include those from theoretical and experimental systematic sources and those due to sample statistics. The fit constrains the total expected yield to the observed yield.

Source	error contribution on $\mu_{\text{ggF+2jets}}$
Data statistical uncertainty	0.41
SR statistical uncertainty	0.38
CR statistical uncertainty	0.07
Total systematic uncertainty	0.68
MC statistical uncertainty	0.13
Theoretical uncertainty	0.44
Top-quark bkg.	0.33
ggF signal	0.13
WZ, ZZ, $W\gamma$, $Z\gamma$ bkg.	0.16
WW bkg.	0.1
Z/γ^* bkg.	0.05
VBF bkg.	0.06
Experimental uncertainty	0.36
b-tagging	0.33
Modelling of pile-up	0.17
Jets	0.04
Misidentified leptons	0.11
Luminosity	0.03
Total	0.82

Table 6.9: The contributions of the individual systematics grouped into categories together with the data statistical uncertainties in the observed fit of the $\mu_{\text{ggF+2jets}}$ signal strength. The theoretical and experimental uncertainties are subdivided further in categories.

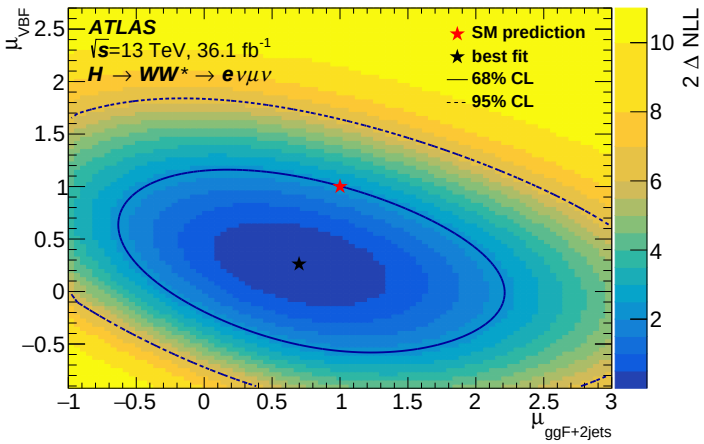

Figure 6.18: 68% and 95% CL two-dimensional Likelihood contours of the coupling strength parameters $\mu^{\text{ggF+2jets}}$ and μ^{VBF} for a fit to the ATLAS data within the ggF + 2 jets SR. The best-fit point is represented as a black star, while the SM prediction is represented by a red star. The signal strength parameters of the ggF + 2 jets and VBF processes are determined to be $\mu^{\text{ggF+2jets}} = 0.7 \pm 0.4\,(\text{stat.})^{+0.8}_{-0.7}\,(\text{syst.})$ and $\mu^{\text{VBF}} = 0.3 \pm 0.4\,(\text{stat.}) \pm 0.4\,(\text{syst.})$ respectively, with a linear correlation coefficient of -0.34.

6.5 Measurement of the CP properties of the Higgs boson

In order to retrieve the CP information, the values of the NLL (Section 3.1.1) are evaluated at fixed values of $\tan(\alpha)$, with a step size of 0.2 between the scenarios. The minima of all fits are consistent with zero, i.e. the SM hypothesis. If only the shape information is used, the data are not sensitive enough to provide 68% CL intervals on $\tan(\alpha)$, as can be seen from Figure 6.19 (a). The fit configuration that uses both shape and rate information provides a best-fit value of $\tan(\alpha) = 0.0 \pm 0.4\,(\text{stat.}) \pm 0.3\,(\text{syst.})$ for both the fits to data and to Asimov data as shown Figure 6.19 (b). The observed sensitivity is slightly worse than the expected sensitivity due to lower-than-expected signal yields, consistent with a signal strength value below unity. Hence, the fit to the observed data does not provide a 95% CL interval. The relative impact of the main uncertainties on the measurement of $\tan(\alpha)$ is presented in Table 6.10.

The uncertainty on the $\tan(\alpha)$ measurement is dominated by the limited data statistics, contrary to the $\boldsymbol{\mu}_{\text{ggF+2jets}}$ measurement, where the fitted distribution contains far fewer bins. Another big source of uncertainty is represented by thePS and matrix element modeling of the $t\bar{t}$ background, as well as the one on the $b-$jets reconstruction algorithm, similarly as for the $\boldsymbol{\mu}_{\text{ggF+2jets}}$ measurement. uncertainty on the measurement.

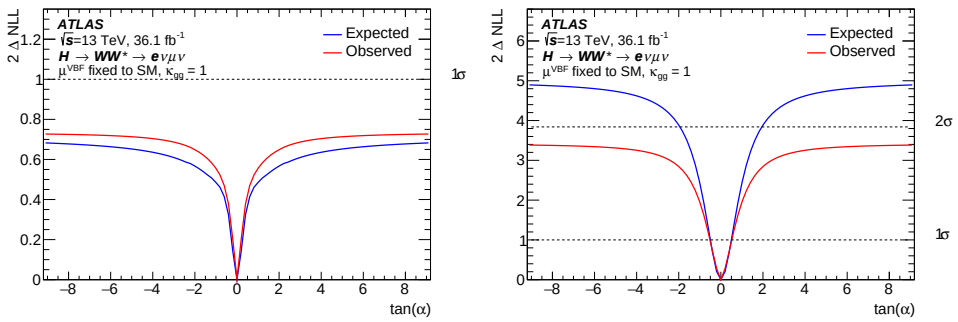

Figure 6.19: Expected and observed Likelihood curves for scans (a) over $\tan(\alpha)$ where only the shape is taken into account in the fit, and (b) over $\tan(\alpha)$ when both shape and normalisation are used.

The post-fit fitted estimate of the distribution of (w_{BDT}-$\Delta\Phi_{jj}$-$\Delta\eta_{jj}$) is shown in Figures 6.21 and 6.22 in bins of $|\Delta\eta_{jj}|$. The plots show the ratio between observed data and prediction, from which a good agreement can be inferred.

The two-dimensional 68% and 95% CL Likelihood contours of the scan over the CP-even and CP-odd coupling strength parameters $\kappa_{gg}\cos(\alpha)$ and $\kappa_{gg}\sin(\alpha)$, exploiting both shape and rate information, are presented in Figure 6.23. The best-fit values observed in the data are consistent with the SM predictions at the 68% CL, while $|\kappa_{gg}\cos(\alpha)|$ values above 1.6 and $|\kappa_{gg}\sin(\alpha)|$ values above 1.1 are excluded at 95% CL.[5]

[5]Precise measurements of the inclusive ggF cross section give tighter constraints on the individual parameters [184],

Source	error contribution on $\tan(\alpha)$
Data statistical uncertainty	0.4
SR statistical uncertainty	0.33
CR statistical uncertainty	0.10
Total systematic uncertainty	0.28
MC statistical uncertainty	0.14
Theoretical uncertainty	0.23
Top-quark bkg.	0.15
ggF signal	0.14
WZ, ZZ, $W\gamma$, $Z\gamma$ bkg.	0.06
WW bkg.	0.06
Z/γ^* bkg.	0.016
VBF bkg.	0.015
Experimental uncertainty	0.21
b-tagging	0.16
Modelling of pile-up	0.10
Jets	0.07
Misidentified leptons	0.04
Luminosity	0.034
Total	0.5

Table 6.10: Breakdown of the main contributions to the total uncertainty in $\tan(\alpha)$ based on the fit that exploits both shape and rate information. Individual sources of systematic uncertainty are grouped into either the theoretical or the experimental uncertainty. The sum in quadrature of the individual components differs from the total uncertainty due to correlations between the components.

The measurements presented in this Chapter can obviously be further improved in the future.

As for many other analyses in ATLAS, the modeling of complex processes like $t\bar{t}$, can represent a main source of uncertainty. For this reason, a continuous effort is made by the PMG (Physics Modelling Group), to develop, validate and correct MC modeling. This effect could reduce the differences among the nominal and alternative MC sample generators, leading to smaller generator-related uncertainties, as described in Section 5.3.1. In the case of the ***Properties*** analysis, the uncertainty is calculated as the difference between Powheg-Box + Pythia and Sherpa to extract differences in the matching between the matrix element and PS.

In order to reduce the uncertainty linked to the $b-$jets reconstruction algorithm and to improve its performance, the MV2c10 [84, 85] approach, mentioned in Section 4.3.3, is going to be replaced with a neural network discriminant algorithm, DL1r [66, 86] (which is already used in the ***Couplings*** analysis). According to [86], for a b-tagging efficiency of 85%, the MV2c10 used in the ***Properties*** analysis has a rejection factor for light-jets of 25, while DL1r results is a factor of 29. This difference translates into an improvement of rejecting light-jets of 16% when upgrading the b-jet tagging algorithm.

due to its dependence on $\kappa_{gg}^2 \cos^2(\alpha)$ and $\kappa_{gg}^2 \sin^2(\alpha)$.

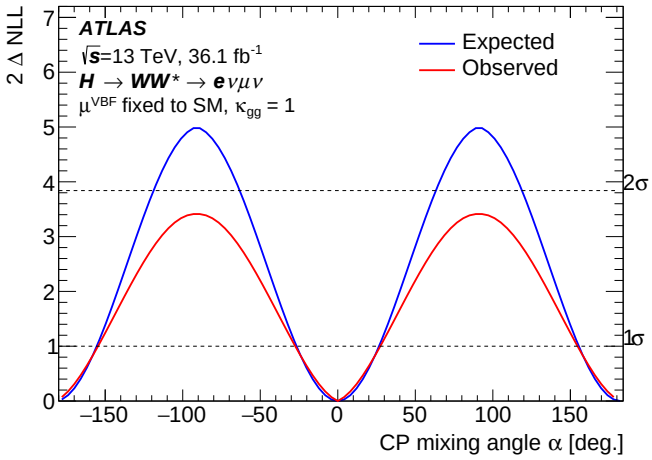

Figure 6.20: Expected and observed Likelihood curves for a scan over the CP-mixing angle α when both shape and normalization are used in the fit.

Finally, the collection of new data can strongly reduce the impact of limited data statistics. The current data statistics uncertainty can be reduced by a factor of 2 going from 36 fb^{-1}, the partial Run 2 dataset used in this analysis, to 139 fb^{-1}, which corresponds to the full Run 2 dataset.

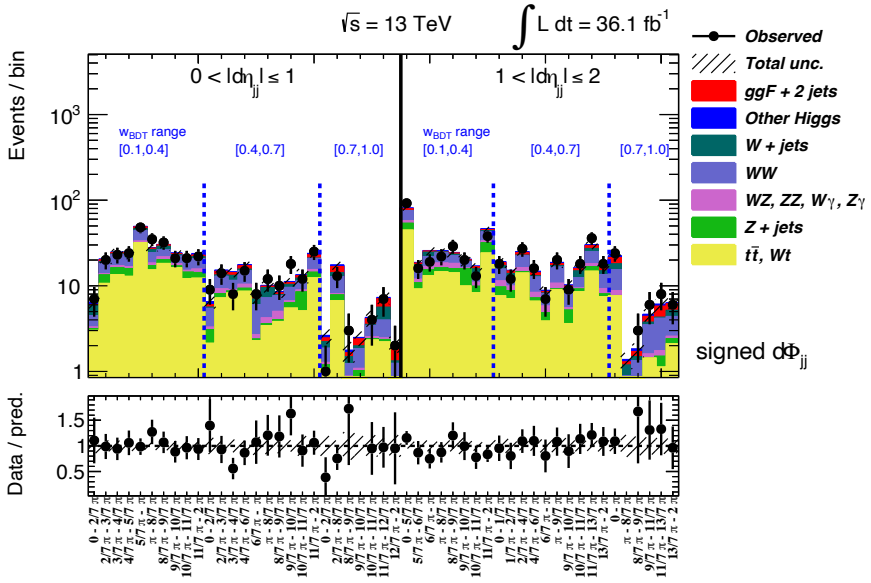

Figure 6.21: Post-fit distribution of the w_{BDT}-$\Delta\Phi_{jj}$-$\Delta\eta_{jj}$ variable in the range of 0<|$\Delta\eta_{jj}$|<1 and 1<|$\Delta\eta_{jj}$|<2. The total uncertainty is shown.

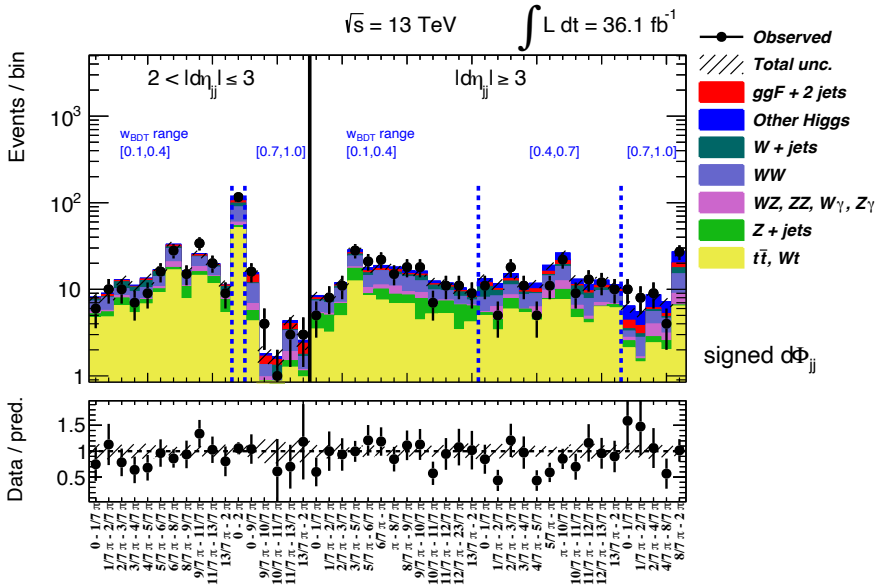

Figure 6.22: Post-fit distribution of the w_{BDT}-$\Delta\Phi_{jj}$-$\Delta\eta_{jj}$ variable in the range of 2<|$\Delta\eta_{jj}$|<3 and |$\Delta\eta_{jj}$|>3. The total uncertainty is shown.

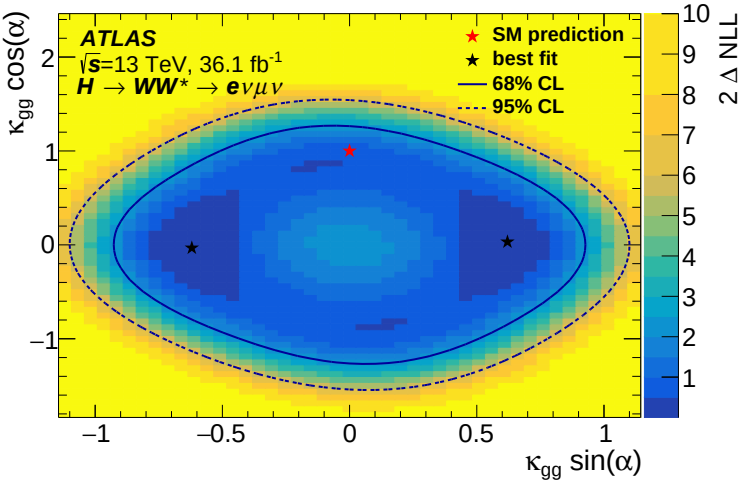

Figure 6.23: 68% and 95% CL two-dimensional Likelihood contours of the CP-even and CP-odd coupling parameters $\kappa_{gg}\cos(\alpha)$ and $\kappa_{gg}\sin(\alpha)$. The minima are represented by black stars, while the SM point is shown as a red star.

6.6 References

[21] ATLAS Collaboration. "Study of the spin and parity of the Higgs boson in diboson decays with the ATLAS detector". In: *Eur. Phys. J. C* 75 (2015), p. 476. DOI: 10.1140/epjc/s10052-015-3685-1. arXiv: 1506.05669 [hep-ex] (cit. on pp. 28, 114). Erratum: in: *Eur. Phys. J. C* 76 (2016), p. 152. DOI: 10.1140/epjc/s10052-016-3934-y.

[66] ATLAS Collaboration. *Optimisation and performance studies of the ATLAS b-tagging algorithms for the 2017-18 LHC run.* ATL-PHYS-PUB-2017-013. 2017 (cit. on pp. 54, 77, 138).

[84] ATLAS Collaboration. "Performance of b-jet identification in the ATLAS experiment". In: *JINST* 11 (2016), P04008. DOI: 10.1088/1748-0221/11/04/P04008. arXiv: 1512.01094 [hep-ex] (cit. on pp. 76, 138).

[85] ATLAS Collaboration. *Optimisation of the ATLAS b-tagging performance for the 2016 LHC Run.* ATL-PHYS-PUB-2016-012. 2016 (cit. on pp. 76, 138).

[86] ATLAS Collaboration. "ATLAS b-jet identification performance and efficiency measurement with $t\bar{t}$ events in pp collisions at $\sqrt{s} = 13$ TeV". In: *Eur. Phys. J. C* 79 (2019), p. 970. DOI: 10.1140/epjc/s10052-019-7450-8. arXiv: 1907.05120 [hep-ex] (cit. on pp. 77, 96, 138).

[180] Anne Kathrin Becker et al. *Measurement of gluon fusion and vector boson fusion Higgs boson production cross-sections in the $H \to WW^* \to e\nu\mu\nu$ decay channel in pp collisions at $\sqrt{s} = 13$ TeV with the ATLAS detector.* Tech. rep. Geneva: CERN, Mar. 2018 (cit. on p. 115).

[181] A. Hoecker, et al. "TMVA - Toolkit for Multivariate Data Analysis". In: *PoS* ACAT (2007), p. 040. arXiv: {\texttt{arXiv:physics/0703039}} [PHYSICS] (cit. on p. 117).

[182] Andreas Hocker et al. *TMVA - Toolkit for Multivariate Data Analysis with ROOT: Users guide. TMVA - Toolkit for Multivariate Data Analysis.* Tech. rep. TMVA-v4 Users Guide: 135 pages, 19 figures, numerous code examples and references. Geneva: CERN, Mar. 2007 (cit. on p. 117).

[183] Remco Johannes Adriana Maria Castelijn. "The CP Nature of the Top-Yukawa Coupling among other measurements in the gluon gluon fusion production channel". PhD thesis. Universiteit Nijmegen, 2019 (cit. on pp. 130, 131).

[184] ATLAS Collaboration. "Combined measurements of Higgs boson production and decay using up to 80 fb^{-1} of proton-proton collision data at $\sqrt{s} = 13$ TeV collected with the ATLAS experiment". In: *Phys. Rev. D* 101 (1 Jan. 2020), p. 012002. DOI: 10.1103/PhysRevD.101.012002 (cit. on p. 137).

7

What: Couplings measurement of the sm Higgs boson

In this Chapter the measurement of the ggF and VBF Higgs signal strength, and inclusive sections with the $H \to WW^* \to \ell\nu\ell\nu$ decay mode is presented. The study is performed using the full Run 2 integrated luminosity of 139 fb^{-1}, taken by the ATLAS detector in the years 2015 through 2018 at the center-of-mass energy $\sqrt{s} = 13$ TeV. In Section 7.1 the strategy of the analysis and the event selection procedure is described. Following that an illustration of the statistical methods used is presented, where the pruning is also treated, in Section 7.2. Then Section 7.3 presents the results of the analysis. The Chapter closes with the display of four events candidates as they are seen by the ATLAS detector, in Section 7.4.

Contents

7.1 Strategy and event selection

To perform the ***Couplings*** analysis, final states corresponding to the production of the Higgs boson via ggF and VBF with subsequent $H \to WW^* \to \ell\nu\ell\nu$ decay are selected thanks to the trigger defined in Section 5.1.

Preselection
On top of this, preselection cuts (apart from object definitions) on the candidate events are applied. In order to be selected for the analysis, the candidates need to have:

- exactly two charged light leptons with opposite electrical charge and different flavor ($e\mu+\mu e$). This requirement suppresses Z+jets background,
- no additional lepton, defined with looser identification criteria[1], and with p_{T} >15 GeV to ensure orthogonality to the VH analyses with $3l$ and $4l$ final states,
- $p_{\mathrm{T}}^{\mathrm{lead}}$ >22 GeV, $p_{\mathrm{T}}^{\mathrm{sublead}}$ >15 GeV. These cuts are dictated by experimental triggers and efficiency in rejection of the W+jets and QCD backgrounds,
- $m_{\ell\ell}$ >10 GeV, which suppresses backgrounds from low-mass resonances such as J/Ψ and DY processes,
- $p_{\mathrm{T}}^{\mathrm{miss}} > 20$ GeV, to significantly reduce both the $Z \to \tau\tau$ background and the multi-jet backgrounds with misidentified leptons, when targeting the ggF production mode,
- Events containing b-jets with $p_{\mathrm{T}} > 20$ GeV are vetoed to reject background from top-quark production.

After these cuts, a split into subsamples with different jet multiplicities (N_{jet}) is performed and different $E_{\mathrm{T}}^{\mathrm{miss}}$ selections are applied. Figure 7.1 shows the jet multiplicity distribution at the preselection level. The different background compositions as a function of jet multiplicity motivate the division of the data sample into N_{jet} categories, which are further subdivided into separate SRs. Four main analysis categories are defined: the $N_{\mathrm{jet}} = 0$ category targeting the ggF production mode described in Section 7.1.1, the $N_{\mathrm{jet}} = 1$ category targeting the ggF production mode described in Section 7.1.2, the $N_{\mathrm{jet}} \geq 2$ category targeting the VBF production mode described in Section 7.1.3, and the $N_{\mathrm{jet}} \geq 2$ category targeting the ggF production mode described in Section 7.1.4. It is worth mentioning that not only the background composition provides a good reason to split in jet multiplicity, but also the change of signal kinematics. When the Higgs is produced via ggF, with no associated jets, its transverse momentum is small, in contrast with Higgs boson events in the $N_{\mathrm{jet}} = 1$ bin, where a fair amount of traverse momentum is present to balance the p_{T} of the jet.

The additional selection criteria used to define the analysis SRs are described separately for each category of events below, while Table 7.1 provides a summary of the full set of SR selections.

[1] These looser working points are defined similarly as in Chapter 5.1. The differences are the isolation working points FixedCutLoose for both lepton flavors and the quality and likelihood working points Medium for muons and electrons.

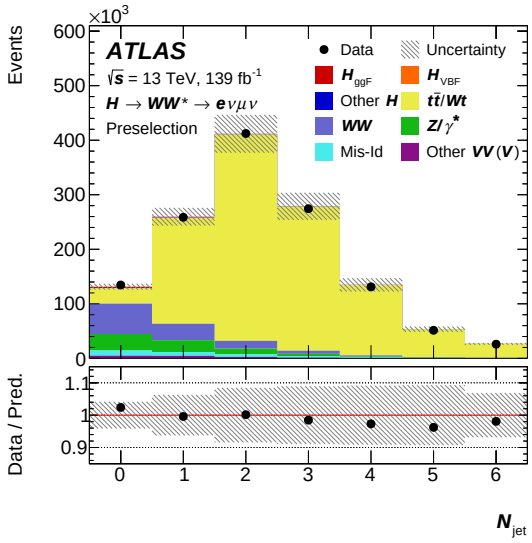

Figure 7.1: Jet multiplicity distribution, after applying the preselection criteria (pre-fit normalizations). The hatched band shows the normalization component of the total pre-fit uncertainty, assuming SM Higgs boson production. The various background components are discussed in more detail in Section 4.2.

Category	$N_{\text{jet},(p_T>30\text{ GeV})} = 0$ ggF	$N_{\text{jet},(p_T>30\text{ GeV})} = 1$ ggF	$N_{\text{jet},(p_T>30\text{ GeV})} \geq 2$ ggF	$N_{\text{jet},(p_T>30\text{ GeV})} \geq 2$ VBF
Preselection	Two isolated, different-flavor leptons ($\ell = e, \mu$) with opposite charge			
	$p_T^{\text{lead}} > 22$ GeV , $p_T^{\text{sublead}} > 15$ GeV			
	$m_{\ell\ell} > 10$ GeV			
	$p_T^{\text{miss}} > 20$ GeV			
Background rejection	$N_{b\text{-jet},(p_T>20\text{GeV})} = 0$			
	$\Delta\phi_{\ell\ell,E_T^{\text{miss}}} > \pi/2$	$m_{\tau\tau} < m_Z - 25$ GeV		
	$p_T^{\ell\ell} > 30$ GeV	$\max(m_T^{\ell}) > 50$ GeV		
$H\to WW^*\to e\nu\mu\nu$ topology	$m_{\ell\ell} < 55$ GeV			
	$\Delta\phi_{\ell\ell} < 1.8$			
			fail central jet veto or fail outside lepton veto	central jet veto outside lepton veto $m_{jj} > 120$ GeV
			$\lvert m_{jj} - 85\rvert > 15$ GeV or $\Delta y_{jj} > 1.2$	
Discriminating fit variable	m_T			DNN

Table 7.1: Event selection criteria used to define the SRs in the $H\to WW^*\to e\nu\mu\nu$ analysis. All the variables are defined in the text.

7.1.1 The $N_{\text{jet}} = 0$ category

In this category, the absence of a jet implies that the $E_{\text{T}}^{\text{miss}}$ vector and the $\Delta\phi_{\ell\ell}$ direction point away from each other: this reasoning justifies the $\Delta\phi_{\ell\ell,E_{\text{T}}^{\text{miss}}} > \pi/2$ cut. Given that the charged leptons are emitted preferably in the same direction due to spin-correlations (Section 4.1.1) their combined transverse momentum is expected to be large. The requirement of $p_{\text{T}}^{\ell\ell} > 30$ GeV reduces DY events in which the two leptons are emitted back-to-back (in which case $p_{\text{T}}^{\ell\ell}$ is small). To further reduce the DY and WW background, cuts on $m_{\ell\ell}(< 55$ GeV) and on $\Delta\phi_{\ell\ell}(< 1.8)$ are applied.

The $m_{\ell\ell}$ and $\Delta\phi_{\ell\ell}$ selections in the $N_{\text{jet}} = 0$ category with indicated by dashed lines in Figures 7.2(a) and 7.2(b), with an arrow at the top pointing to the region that is selected. The bottom panels show the normalized distributions for the signal and backgrounds, from which it can be inferred which background processes are primarily removed by the indicated selections. The $N_{\text{jet}} = 0$ SR is further split into four regions that are later used in the fit to extract the signal, with boundaries in $m_{\ell\ell}$ as well as in the p_{T} of the sub-leading lepton at $p_{\text{T}}^{\text{sublead}} = 20$ GeV.

WW control region

The background from continuum $qqWW \to l\nu l\nu$ production is normalized using a control region that differs from the signal region in the selection of the di-lepton invariant mass. The region used for the WW control region is $55 < m_{\ell\ell} < 110$ GeV. An additional cut $\Delta\phi_{\ell\ell} < 2.6$ reduces the $Z \to \tau\tau$ contamination. The WW control region is used to normalize the $qqWW$ background to the data. The associated scale factor is evaluated by subtracting the MC predicted non-$qqWW$ backgrounds and the predicted signal (1% of the expected yield in the control region) from the data events and taking the ratio of the remaining data yield to the predicted $qqWW$ yield. This ratio is used to correct the $qqWW$ contribution predicted by the MC generator in the signal region. The resulting normalization factor is 1.094 ± 0.012 (stat.). The control region is dominated by WW production and has a purity of $\sim 67\%$. Modeling of key kinematic distributions, including the variables which define the signal region, are presented in Figure A.1 in Appendix **??** for the WW $N_{jet} = 0$ control region, with the normalization factors applied.

Top control region

Top events are strongly suppressed by the jet and b-jet vetoes in the $N_{\text{jet}} = 0$ category but are still significant because of the large cross-section. The Top CR definition makes use of the b-tagging requirement on the sub-threshold jets. Specifically, $N_{b\text{-jet},(p_{\text{T}}>20\text{GeV})} > 0$ is required (at least one jet $20 < p_{\text{T}} < 30$ needs to identify as a b-jet). The remaining selection is as for the signal region, except that the cut on $m_{\ell\ell}$ is dropped and the cut on $\Delta\phi_{\ell\ell}$ is loosened. The resulting normalization factor is 1.023 ± 0.011 (stat.). The purity of the Top CR is 89%. Distributions for some of the characteristics variables in this CR are shown in Figure A.2 in A for $N_{\text{jet}} = 0$, with the normalization factors applied.

$Z \to \tau\tau$ control region

For the $Z \to \tau\tau$ CR the following cuts are applied: $\Delta\phi_{\ell\ell} > 2.8$, $m_{\ell\ell} < 80$ GeV, and b-jets veto. These additional requirements separate $Z \to \tau\tau$ control region from the signal region, in a way

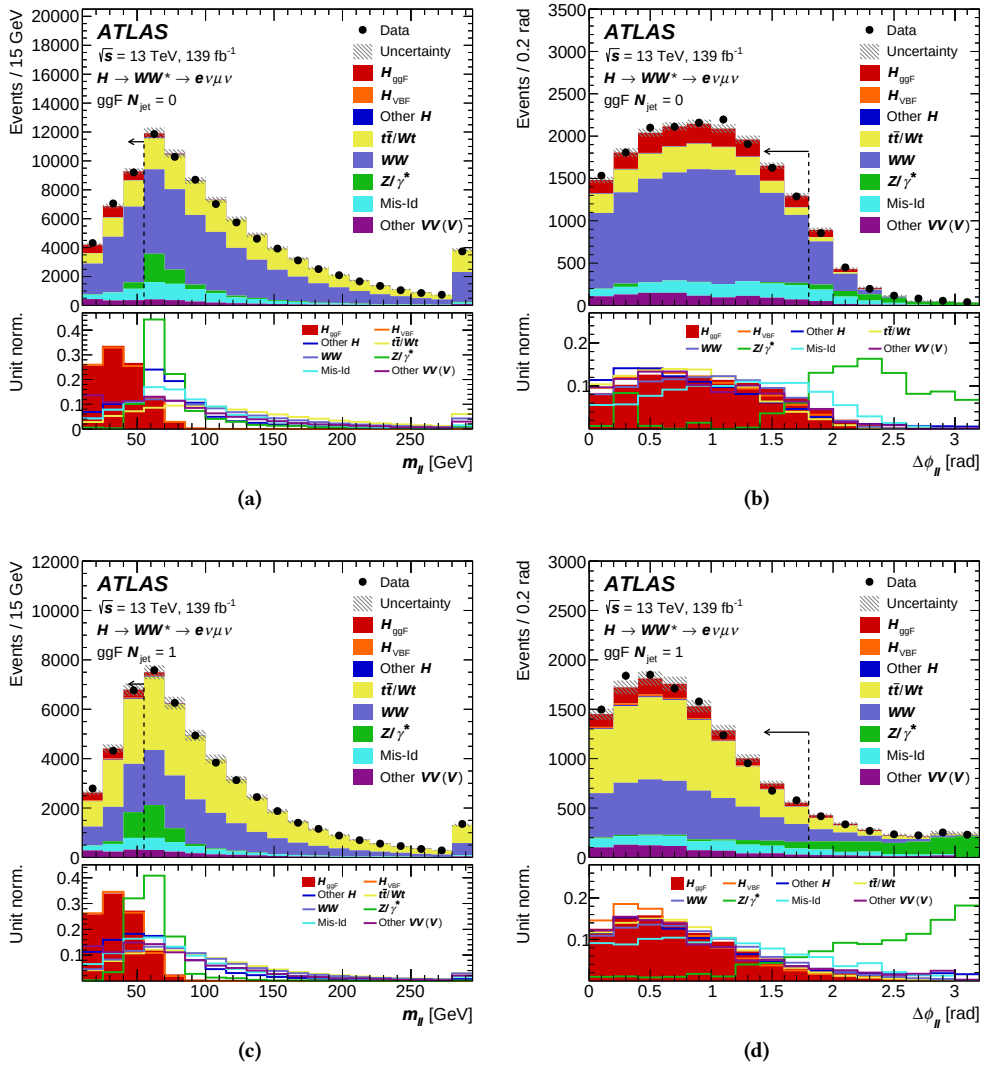

Figure 7.2: Distributions of $m_{\ell\ell}$ (a) and $\Delta\phi_{\ell\ell}$ (b) in the $N_{\text{jet}} = 0$ category as well as $m_{\ell\ell}$ (c) and $\Delta\phi_{\ell\ell}$ (d) in the $N_{\text{jet}} = 1$ category, after the preselection and background rejection steps, and also after the selection on $m_{\ell\ell}$ for the $\Delta\phi_{\ell\ell}$ plots. The dashed lines indicate where the selection on the observable is made. The distributions are normalised to their nominal yields, before the final fit to all SRs and CRs (pre-fit normalisations). The hatched band shows the normalisation component of the total pre-fit uncertainty, assuming SM Higgs boson production. The bottom panels show the normalised distributions for the signal and backgrounds, from which it can be inferred which background processes are primarily removed by the indicated selections.

that results in a control region that is completely dominated by $Z \to \tau\tau$ background. The purity of this control region, defined as a fraction of the $Z \to \tau\tau$ component of the total expectation, is

94%. The $Z \to ee/\mu\mu$ component is only 1.5% of the total DY yield. The resulting normalization factor is 0.9497 ± 0.0027 (stat.). Distributions for some of the characteristics variables in the $Z \to \tau\tau$ CR are shown in Appendix A Figure A.3 for $N_{\text{jet}} = 0$, with the normalization factors applied.

Same-sign validation region

In all of the $H \to WW^* \to \ell\nu\ell\nu$ validation regions, the charges of lepton pairs are required to have the opposite sign (OS), because the SM Higgs boson is neutral and decays to a pair of oppositely charged W bosons. Requiring same sign (SS) leptons ($--$ or $++$) rejects the signal and the WW, Top, and $Z/\gamma^* \to ee/\mu\mu/\tau\tau$ backgrounds, leaving the only "Non-WW" diboson backgrounds ($W\gamma$, $W\gamma^*$, WZ, and ZZ), along with W+jets. Therefore, kinematic regions with same-sign requirements could be used to validate the estimation of these backgrounds. The contribution of the $ZZ^{(*)}$ background is not completely symmetric between OS and SS because of the contribution from events in which both the leptons come from the decay of one of the $Z^{(*)}$ bosons to τ leptons. However, the $ZZ^{(*)}$ process is almost negligibly small in the $e\mu/\mu e$ SS CR and SRs, it is only 0.2% of the expected background in the $N_{\text{jet}} = 0$ SRs and less than 0.2% of the expected background in the CR. The other dominant process which contributes to the SS region is W+jets, with one fake lepton. Its contribution is not symmetric between SS and OS but it can be predicted separately for each of the SS and OS regions using the procedure described in Section 5.4.1. The same-sign region is built from the events passing all the signal region cuts, including the $\Delta\phi_{\ell\ell}$ requirement, but with the opposite sign requirement replaced by a same-sign one.

In Figure 7.3 the scheme of the selection criteria for the $N_{\text{jet}} = 0$ regions is depicted. Arrows are labeled with the cuts that are applied when moving from one region to another. Bold text indicates that a cut provides orthogonality between regions. A cut is crossed out if it is removed when going from one region to another.

7.1.2 The $N_{\text{jet}} = 1$ category

7

For the $N_{\text{jet}} = 1$ category, a new variable $m_{\text{T}}^{\ell_i}$ is defined for a single lepton ℓ_i:

$$m_{\text{T}}^{\ell_i} = \sqrt{2\, p_{\text{T}}^{\ell_i} \cdot E_{\text{T}}^{\text{miss}} \cdot (1 - \cos\Delta\phi\,(\ell_i, E_{\text{T}}^{\text{miss}}))},$$

where ℓ_i can be either the leading or the sub-leading lepton. $m_{\text{T}}^{\ell_i}$ tends to have small values for the DY background and large values for the signal process. It also has small values for multi-jet production, where misidentified leptons are frequently measured with an energy lower than the jets from which they originate. Therefore, these backgrounds are substantially reduced with a requirement of $\max\left(m_{\text{T}}^{\ell}\right) > 50$ GeV. A requirement of $m_{\tau\tau} < m_Z - 25$ GeV, where $m_{\tau\tau}$ is defined in Section 4.4, significantly reduces the DY contribution and is applied in all categories with $N_{\text{jet}} \geq 1$. The same $\Delta\phi_{\ell\ell}$ and $m_{\ell\ell}$ selections as described in Section 7.1.1 are also applied in the $N_{\text{jet}} = 1$ category and are illustrated in Figures 7.2(c) and 7.2(d), respectively. The bottom panels show the normalised distributions for the signal and backgrounds, from which it can be inferred

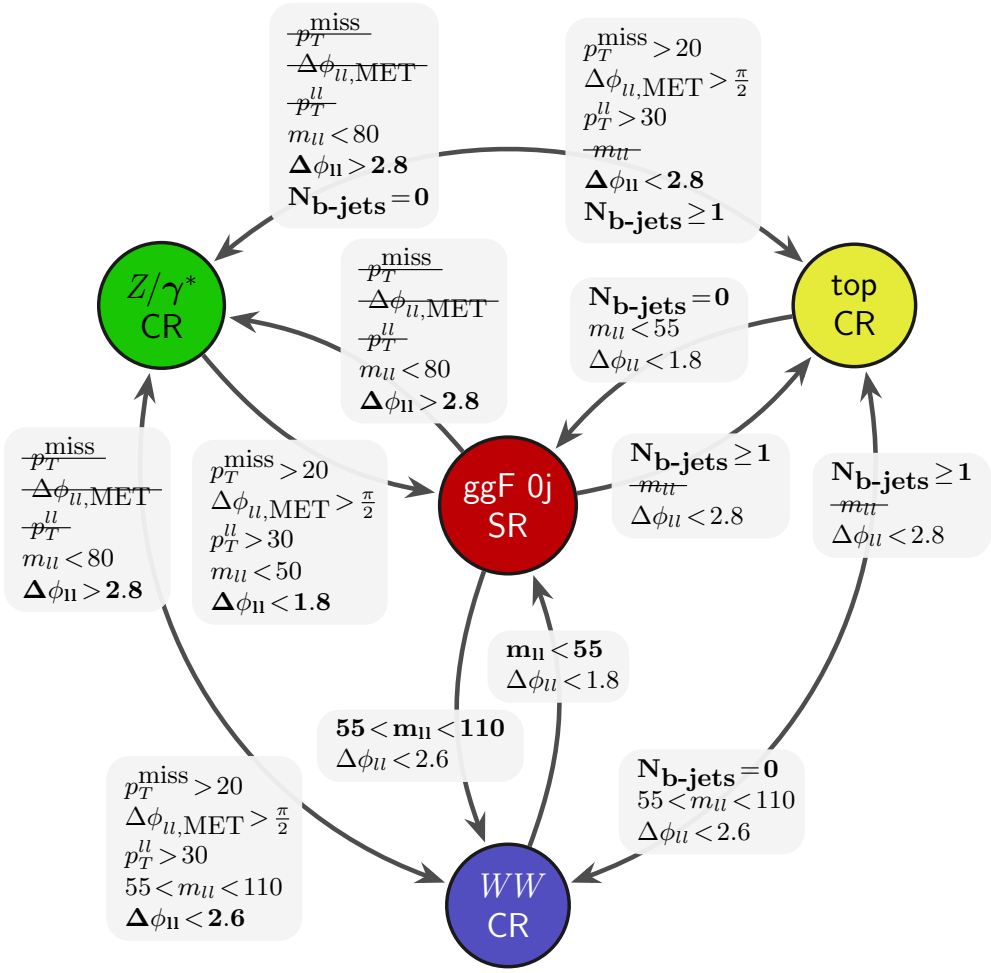

Figure 7.3: Visual representation of the cuts separating the SRs and the CRs for the $N_{\text{jet}} = 0$ analysis category. Arrows are labeled with the cuts that are applied when moving from one region to another. Bold text indicates that a cut provides orthogonality between regions. A cut is crossed out if it is removed when going from one region to another. Units of GeV have been omitted. Adapted from [185].

which background processes are primarily removed by the indicated selections. The $N_{\text{jet}} = 1$ SR is further split into four regions with the same boundaries as defined for the $N_{\text{jet}} = 0$ category.

WW control region

The $qqWW$ background is normalized using a dedicated control region as for the $N_{\text{jet}} = 0$ analysis. The control region is constructed after the cuts aiming to reject top and $Z \to \tau\tau$ backgrounds. These include: a veto of the events with b-jets with $p_{\text{T}} > 20$ GeV, a cut on m_{T}^{W} larger than 50 GeV, $m_{\tau\tau}$ required to be less than $m_Z - 25$ GeV and di-lepton invariant mass $m_{\ell\ell}$ required to be greater than 80 GeV. The purity of the WW $N_{\text{jet}} = 1$ control region is only 34% and the derived normalization factor for $qqWW$ is 0.883 ± 0.015 (stat.). Modeling of key kinematic distributions,

including the variables which define the signal region, are presented in Appendix A in Figure A.4 for the WW $N_{\text{jet}} = 1$ control region, with the normalization factor applied.

Top control region
In the $N_{\text{jet}} = 1$ category, the normalization of the top-quark background is determined from a control region distinguished from the signal region by requiring that the one jet with $p_{\text{T}} > 30$ GeV is b-tagged. A b-veto on the 20 GeV $< p_{\text{T}} < 30$ GeV jets is also applied resulting in a similar $t\bar{t}/Wt$ ratio than for the signal region. The purity of the CR is about 98%. The normalization factor is 1.021 ± 0.004 (stat.). Distributions for some of the characteristic variables in the Top-quark CR are shown in Appendix A in Figure A.5 for $N_{\text{jet}} = 1$.

$Z \to \tau\tau$ control region
The $Z \to \tau\tau$ control region is defined using events passing the nominal analysis selection for $N_{\text{jet}} = 1$ and including the b-jet veto and the max(m_{T}^{W}) requirement, except that the $E_{\text{T}}^{\text{miss, track}}$ requirement is dropped. The control region is then defined as the events with $m_{\ell\ell} < 80$ GeV and failing the $Z \to \tau\tau$ veto, $m_{\tau\tau} > m_Z - 25$ GeV. The purity of this control region is 76%. The resulting normalisation factor for the $Z \to \tau\tau$ MC prediction is 0.882 ± 0.011 (stat.). The $Z \to ee/\mu\mu$ component is only 3.0% of the total DY yield. Distributions for some of the characteristics variables in the $Z \to \tau\tau$ CR are shown in Appendix A in Figure A.6 for $N_{\text{jet}} = 1$.

Same-sign validation region
A $N_{\text{jet}} = 1$ (SS) validation region is defined with the same principles as the $N_{\text{jet}} = 0$ SS region. It is built from the events passing all the signal region cuts (including the $\Delta\phi_{\ell\ell}$ requirement) with the opposite sign requirement replaced by the same sign one. In Figure 7.4 the scheme of the cuts for the $N_{\text{jet}} = 1$ regions is depicted. Arrows are labeled with the cuts that are applied when moving from one region to another. Bold text indicates that a cut provides orthogonality between regions. A cut is crossed out if it is removed when going from one region to another.

7.1.3 The VBF-enriched $N_{\text{jet}} \geq 2$ category

7

The kinematics of the Higgs boson produced by VBF is characterized by the presence of (at least) two jets predominantly emitted in the forward region. Low levels of hadronic activity between these jets are registered due to the mediating weak bosons that do not exchange color charge. In order to construct a SR enriched in this VBF topology, events are rejected if they contain either additional jets with $p_{\text{T}} > 30$ GeV that lie in the gap between the two tagged jets in pseudo-rapidity (CJV), or if either lepton outside the gap between the two tagged jets in pseudo-rapidity (outside-lepton veto (OLV)). Furthermore, the invariant mass of the two leading jets, m_{jj}, is required to be above 120 GeV to ensure orthogonality with analyses targeting the $V(\to qq)H$ production mode. The events in this category are analyzed using a deep neural network (DNN) that is implemented through Keras [186] and TensorFlow [187], considering VBF Higgs boson production as signal and the rest of the processes as background (including the other Higgs boson production processes).

Signal discrimination with DNN
Similarly for what has been done for the ***Properties*** analysis, the ***Couplings*** one uses a machine

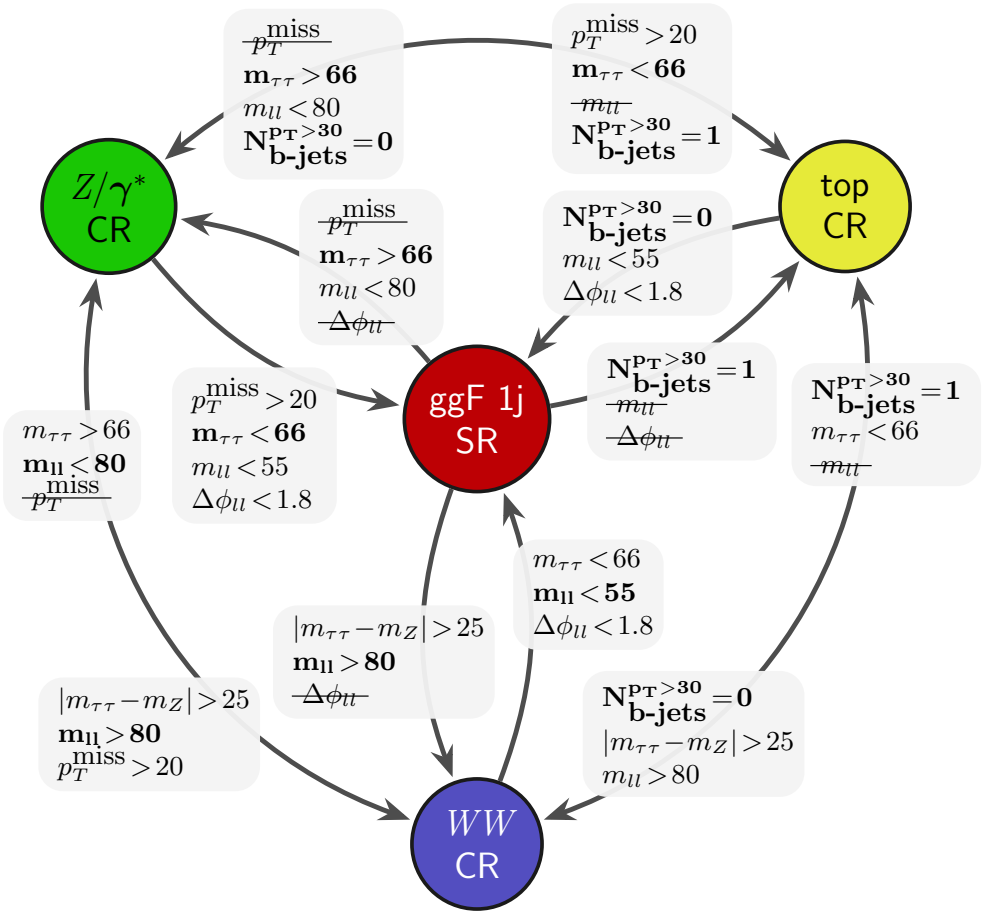

Figure 7.4: Visual representation of the cuts separating the SRs and the CRs for the $N_{\text{jet}} = 1$ analysis category. Arrows are labeled with the cuts that are applied when moving from one region to another. Bold text indicates that a cut provides orthogonality between regions. A cut is crossed out if it is removed when going from one region to another. Units of GeV have been omitted. Cuts based on the mass of the Z boson have been shortened, i.e. $m_Z - 25\,\text{GeV} \approx 66\,\text{GeV} \equiv 66$. Adapted from [185].

learning technique to take advantage of multiple discriminating variables for the VBF production mode. The BDT approach was deprecated in favor of the DNN [188]. Studies confirmed that the DNN approach in case of large enough datasets can exploit high statistics training samples better than the BDT can.

The DNN used is an artificial feed-forward network [189]. What characterizes this type of machine learning algorithm is the presence of one or more layers, on which nodes are arranged. In this specific case, the layers have $\{15, 256, 128, 64, 32, 16, 8, 1\}$ nodes, and adjacent layers are connected by edges. There is a weight associated with each edge and a bias assigned for each

node. Similar to the BDT, the goal of the training is to adjust weights and biases such that signal events are assigned an output value of 1 and background a value of 0.

Also in this case, a cross-evaluation approach is chosen where the training data is split in two and each half trains a different model. After multiple studies, 15 observables have been chosen as input to the DNN, after checking their modeling with MC simulation in comparison to data. The observables chosen can be classified as

- *kinematic variables linked to the VBF topology*: m_{jj}, the difference between the two jet rapidities (Δy_{jj}), the lepton η-centrality ($\eta_\ell^{\text{centrality}}$, where $C_\ell = |2\eta_\ell - \sum \eta_j|/\Delta\eta_{jj}$) as defined in Section **??**, the p_{T} of the three leading jets ($p_{\text{T}}^{\text{jet}_1}$, $p_{\text{T}}^{\text{jet}_2}$, $p_{\text{T}}^{\text{jet}_3}$, where $p_{\text{T}}^{\text{jet}_3}$ is set to 0 GeV if there is no third jet in the event), and the invariant masses of all four possible lepton–jet pairs between the leptons and the two leading jets ($m_{\ell 1 j 1}$, $m_{\ell 1 j 2}$, $m_{\ell 2 j 1}$, $m_{\ell 2 j 2}$).
- *kinematic variables regarding the $H \to WW^* \to e\nu\mu\nu$ topology*: $m_{\ell\ell}$, $\Delta\phi_{\ell\ell}$, and m_{T}
- *variables to reject $t\bar{t}$ events*: $p_{\text{T}}^{\text{tot}}$, $\text{E}_{\text{T}}^{\text{miss}}$ significance, which provides separation between events with undetected high-p_{T} particles and events where the $E_{\text{T}}^{\text{miss}}$ is the result of resolution effects [91].

The observables providing the best discrimination between signal and background are m_{jj} and Δy_{jj}, and their distributions in the $N_{\text{jet}} \geq 2$ VBF SR are shown in Figure 7.5.

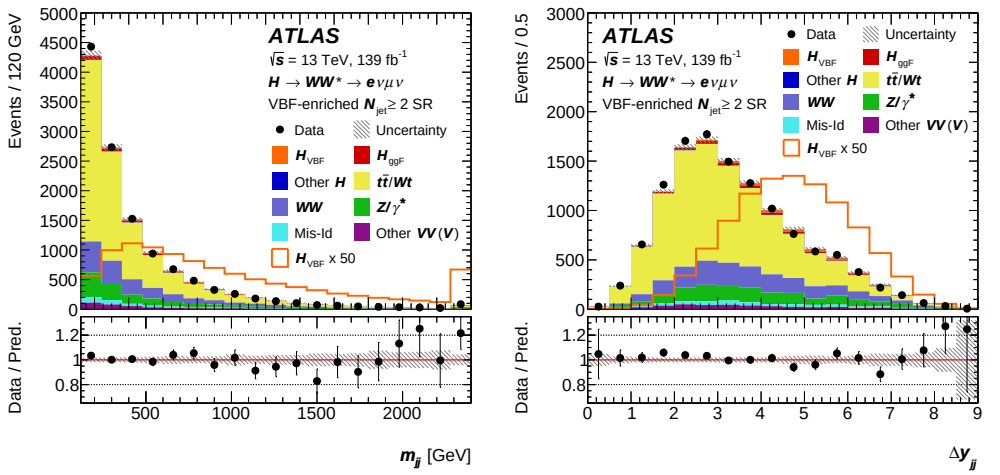

(a) (b)

Figure 7.5: Distributions of m_{jj} (a) and Δy_{jj} (b) in the $N_{\text{jet}} \geq 2$ VBF SR. The solid line shows the expected VBF signal scaled by a factor of 50. The signal and background yields are normalized to the output from the final fit to all SRs and CRs. The hatched band shows the normalization component of the total post-fit uncertainty, assuming SM Higgs boson production. The last bin of the distributions is inclusive (it includes the overflow).

The DNN output reflects the compatibility of an event with having VBF-like kinematics and thus is used as a classifier, with the signal purity improving as the output value increases. The DNN

bin boundaries in the VBF sensitive range are chosen with an algorithm that aims to split the bins as finely as possible, while also requiring at least 10 expected signal and background events each per bin as well as a maximum relative statistical uncertainty on the background of 20%. This yields smaller bin widths on average for larger values of the DNN output, resulting in a total of 7 bins. In the bin with the highest DNN output, the expected VBF signal-to-background ratio is approximately 2.

Correlation among observables

In addition to verifying that each training observable is well-modeled, the modeling of correlations among the DNN training observables have been investigated. For any two training observables X_i and X_j used in the DNN, distributions of $\langle X_i \rangle$ vs X_j as well as $\langle X_j \rangle$ vs X_i are plotted for the data and the MC model. Figure 7.6 presents the correlations of each pair of the training variables for the low DNN validation region (DNN < 0.25) at the VBF preselection stage. The dedicated normalization factors derived at this cut stage (see above) are applied. The profile plots compare the data (black) and MC model (red). The data/MC agreement is quantified using a simple χ^2 calculation. All uncertainties are statistical only. The canvas frame colour for each plot encodes the χ^2 probability $p(\chi^2)$ from the comparison: green represents $p > 0.05$, yellow represents $0.005 < p < 0.05$, and red represents $p < 0.005$. The fact that the latter case happen 13 times out of 210 times (when only a single case is expected) is not worrying. By looking more in detail at the red plots, it is clear that the agreement is qualitatively good, and that the low $p-$ value is mainly due to the fact that no systematics are included in the calculation.

Top control region

The Top CR is defined as exactly the same as the SR, with the b-jet veto replaced by requiring exactly one b-tagged jet ($N_{b-jet} = 1$). The reason for $N_{b-jet} = 1$ instead of an inclusive b-tagged region is to bring the flavour composition of tag jets closer to the b-vetoed SR. The obtained NF is 1.00 ± 0.01 (stat.), while the purity of the top control region is of about 97%. The modeling of some of the DNN training observables in the Top CR are shown in Figure A.10 in Appendix A. The DNN distribution in the Top CR is presented in Figure 7.7 with a uniform binning (top) and with the binning as used in the fit (bottom).

$Z \to \tau\tau$ control region

The $Z \to \tau\tau$ control region is defined as the VBF SR, but with an inverted $Z \to \tau\tau$ veto ($|m_{\tau\tau} - m_Z| < 25$) that selects a mass around the Z-peak, and ensures the orthogonality to the SR. Additionally, a cut on $m_{ll} < 70$ GeV is applied to purify the region. The obtained $Z \to \tau\tau$ NF is 1.00 ± 0.03 (stat.), while the purity of the $Z \to \tau\tau$ control region is 77%. The modeling of some of the DNN training observables in the $Z \to \tau\tau$ CR is shown in Figure A.11 in Appendix A. The DNN distribution in the $Z \to \tau\tau$ CR is shown in Figure 7.8 with a flat bin (top) and with the binning as used in the fit (bottom).

In Figure 7.9 the scheme of the cuts for the VBF-enriched $N_{\text{jet}} \geq 2$ regions is depicted. Arrows are labeled with the cuts that are applied when moving from one region to another. Bold text indicates that a cut provides orthogonality between regions. A cut is crossed out if it is removed when going from one region to another.

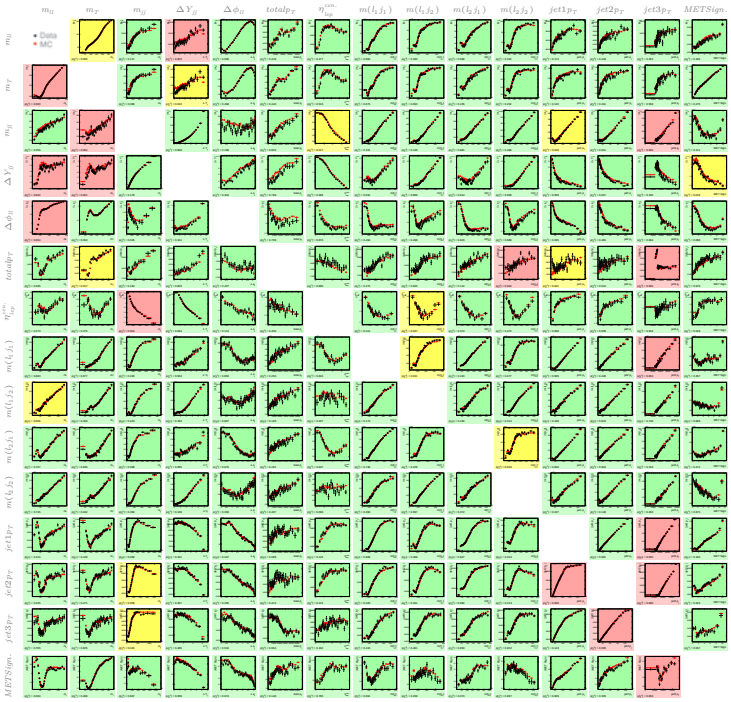

Figure 7.6: Correlation plots of DNN training variables for the low DNN validation region (DNN < 0.25). Distributions of $\langle X_i \rangle$ vs X_j as well as $\langle X_j \rangle$ vs X_i are shown for each pair of training variables in the DNN at the VBF pre-selection stage. The black points show the data profiles, the red points show the profiles of the MC model. The canvas frame colour for each plot encodes the χ^2 probability $p(\chi^2)$ from the comparison: green represents $p > 0.05$, yellow represents $0.005 < p < 0.05$, and red represents $p < 0.005$. The uncertainties are statistical only. If you are reading the paper version and you want to zoom in scan the QR Code in Figure 7.6 with your mobile device.

7.1.4 The ggF-enriched $N_{\text{jet}} \geq 2$ category

The $N_{\text{jet}} \geq 2$ events that are not selected in the VBF-enriched category are considered for the measurement of ggF production. The ggF-enriched category is forced to be mutually exclusive to the VBF-enriched category by requiring events to fail either the CJV or the OLV. Furthermore, $V(\to qq)H$ production is suppressed by rejecting events in a region defined by $|m_{jj} - 85| \leq 15$ GeV and $\Delta y_{jj} \leq 1.2$. The same $\Delta\phi_{\ell\ell}$ and $m_{\ell\ell}$ selections as described in Section 7.1.1 are

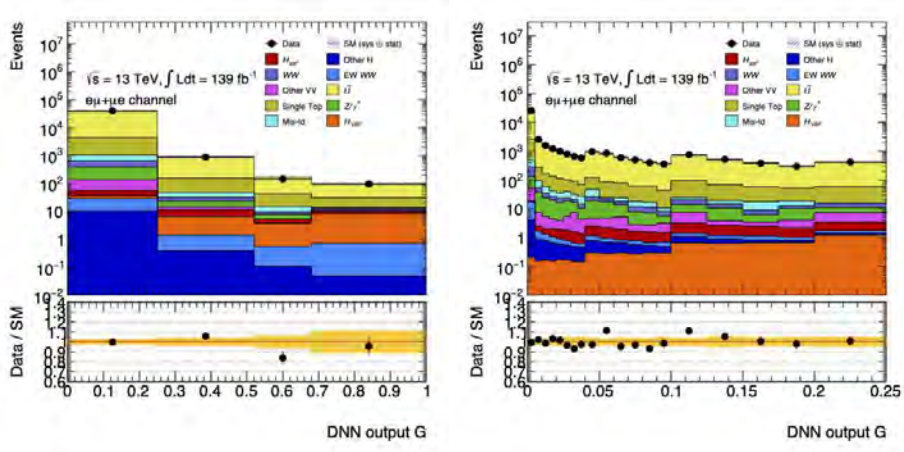

Figure 7.7: The DNN distribution in the Top CR with a binning that ensures the signal is not unblinded (left) and the unblinded region with a finer binning (right). The yellow band represents the MC statistical uncertainties and the main sources of experimental uncertainties.

also applied in the ggF-enriched $N_{\text{jet}} \geq 2$ category and are shown in Figures 7.10(a) and 7.10(b), respectively, together with the $m_{\tau\tau}$ selection in Figure 7.10(c), where an arrow at the top points to the region retained. The bottom panels show the normalized distributions for the signal and backgrounds, from which it can be inferred which background processes are primarily removed by the indicated selections. The ggF-enriched $N_{\text{jet}} \geq 2$ SR is further split into two regions that are later used in the fit with a boundary at $m_{\ell\ell} = 30$ GeV.

WW control region

The WW CR is defined by requiring: $E_{\text{T}}^{\text{miss, track}} > 20$GeV, $Z \to \tau\tau$ veto $m_{\tau\tau} < (m_Z - 25)$GeV, $m_{\ell\ell} > 80$GeV, and $m_{\text{T2}} > 165$GeV, where m_{T2} is used in decay chains with two resonances, that both partly decay into invisible particles. It takes as input the four vectors of the visible particles "vis" and the neutrinos from resonance 1 and 2 to calculate a transverse mass:

$$m_{\text{T2}} = \min_{\vec{p}_{\text{T},\nu_1} + \vec{p}_{\text{T},\nu_2} = \vec{E}_{\text{T}}^{\text{miss}}} \left(\max(m_{\text{T}}^2(p_{\text{vis}_1}^{\mu}, p_{\nu_1}^{\mu}),\ m_{\text{T}}^2(p_{\text{vis}_2}^{\mu}, p_{\nu_2}^{\mu})) \right).$$

The variable itself represents a lower bound on the mass of the parent particle, and can therefore be used to separate WW from top quark pair events. Further details can be found in [190]. Failure to pass either the OLV or the CJV is required to veto VBF events, and $\Delta y_{jj} > 1.2$ or $|m_{jj} - 85\text{GeV}| > 15$GeV to veto VH events. Orthogonality with the SR is achieved by inverting the cut on $m_{\ell\ell}$. The NF for $qqWW$ ($ggWW$ is not included in the NF) is 0.729 ± 0.083 (stat.), while the purity of the region is 39%. Figure A.8 in Appendix A shows a comparison of data and simulation for a number of kinematic variables in the WW region. The modeling is reasonably good for this region.

Top control region

The top quark events are the most abundant background process even after applying a veto on

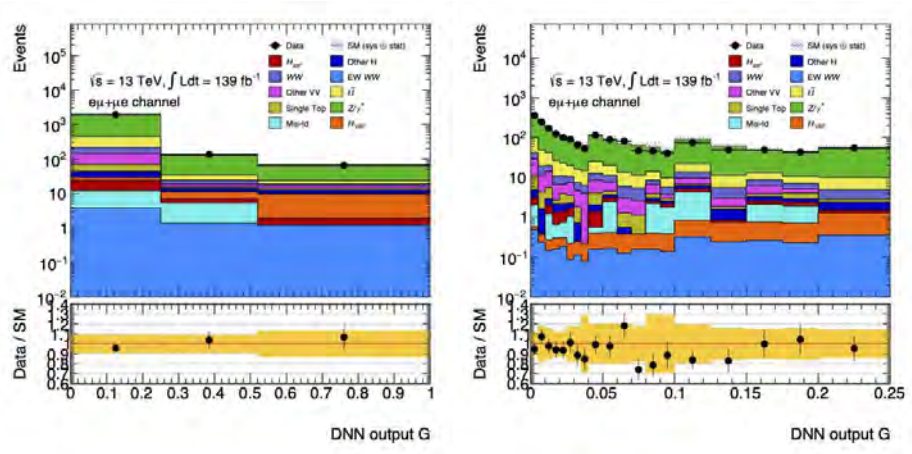

Figure 7.8: The DNN distribution in the $Z \to \tau\tau$ CR with a coarse binning and the signal stacked in the last bin (left) and the unblinded region with a finer binning (right). The yellow band represents the MC statistical uncertainties and the main sources of experimental uncertainties (JES/JER/MET/flavour-tagging).

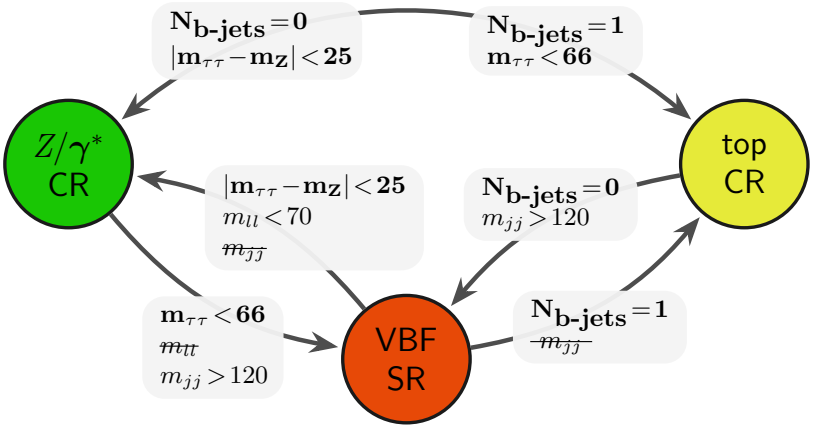

Figure 7.9: Visual representation of the cuts separating the SRs and the CRs for the VBF-enriched $N_{\text{jet}} \geq 2$ analysis category. Arrows are labeled with the cuts that are applied when moving from one region to another. Bold text indicates that a cut provides orthogonality between regions. A cut is crossed out if it is removed when going from one region to another. Units of GeV have been omitted. Cuts based on the mass of the Z boson have been shortened, i.e. $m_Z - 25\,\text{GeV} \approx 66\,\text{GeV} \equiv 66$. Adapted from [185].

events with b-jets. This allows a CR to be defined for top quark processes without making a requirement on b-tagged jets. The Top CR is defined as follows: $E_{\text{T}}^{\text{miss, track}}$ is required to be greater than 20 GeV, b-jet veto, a $Z \to \tau\tau$ veto that is implemented as cut on $m_{\tau\tau} < (m_Z - 25)$GeV, $m_{\ell\ell} > 80$GeV, and $m_{\text{T2}} < 165$GeV. On top of this, the events are required to fail either the OLV or the CJV to veto VBF events, and $\Delta y_{jj} > 1.2$ or $|m_{jj} - 85\text{GeV}| > 15$GeV to veto VH events.

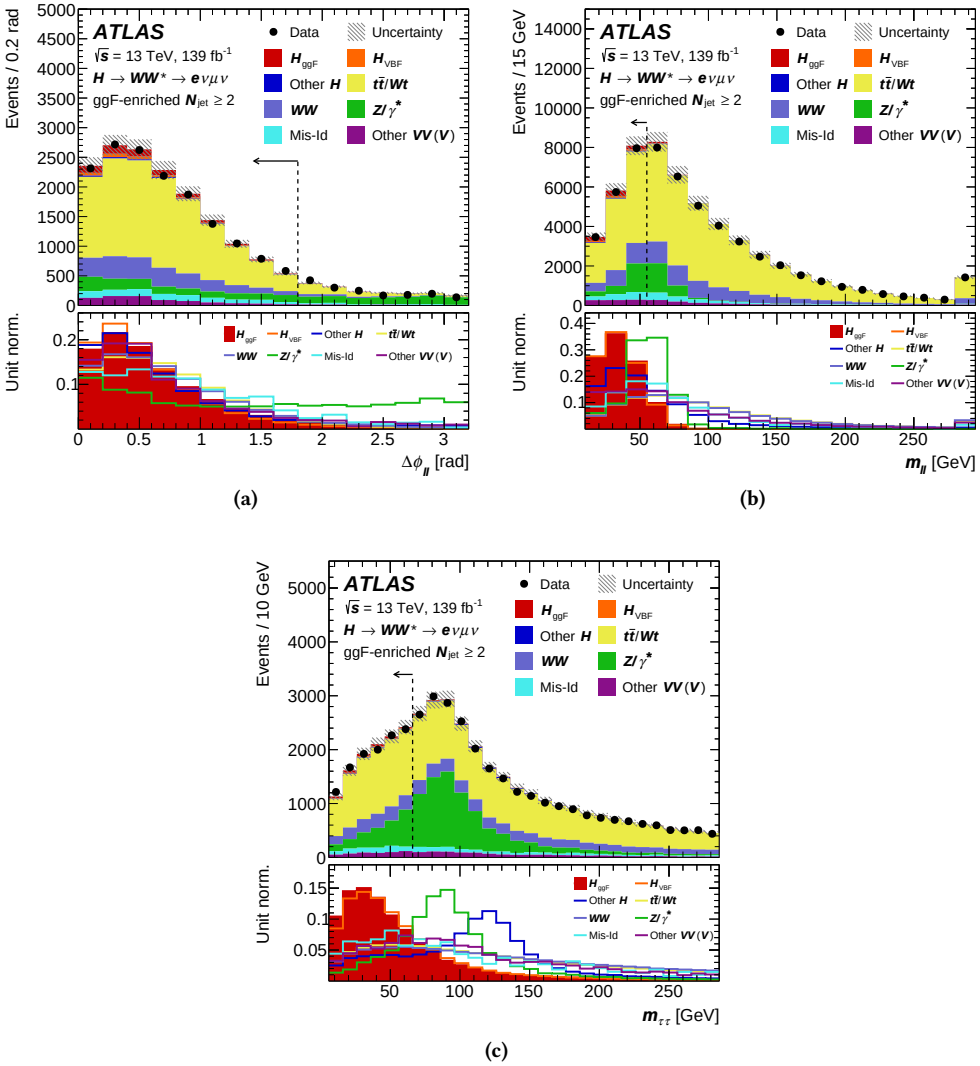

Figure 7.10: Distributions of $\Delta\phi_{\ell\ell}$ (a), $m_{\ell\ell}$ (b), and $m_{\tau\tau}$ (c) in the ggF-enriched $N_{\text{jet}} \geq 2$ category, after requiring all selections up to the corresponding observable. The dashed lines indicate where the selection on the observable is made. The distributions are normalized to their nominal yields, before the final fit to all SRs and CRs (pre-fit normalizations). The hatched band shows the normalization component of the total pre-fit uncertainty, assuming SM Higgs boson production. The bottom panels show the normalized distributions for the signal and backgrounds, from which it can be inferred which background processes are primarily removed by the indicated selections.

Since the b-tag requirement is the same as for the SR, the orthogonality with the latter is achieved by inverting the cut on $m_{\ell\ell}$. Since top quark events populate the high $m_{\ell\ell}$ region, the $m_{\ell\ell}$ cut is increased to $m_{\ell\ell} > 80$GeV, as was done in the Run 1 measurement [191]. The cut on m_{T2} is

included to maintain orthogonality with the WW CR, which otherwise would be kinematically identical to the Top CR. A NF for this region is found to be 1.05 ± 0.03 (stat.), while the purity for this region is around 71%. Figure A.7 in Appendix A shows a comparison of data and simulation for a number of kinematic variables in the b-veto Top CR. The modeling is fairly good for this region.

$Z \to \tau\tau$ control region
In the Run 1 measurement, this region was defined after the b-veto, with the requirement that $m_{\ell\ell} < 70$GeV and $\Delta\phi_{\ell\ell} > 2.8$, as well as requiring that events fail either the CJV or OLV cuts. The CR was around 73% pure in $Z/\gamma^* \to \tau\tau$ events and had a NF of 1.02 ± 0.09 (stat.). For the full Run 2 analysis, some modifications are made to this definition of the $Z/\gamma^* \to \tau\tau$ CR, in order to improve purity, modeling, and the NF uncertainty. The $m_{\ell\ell}$ requirement is made identical to the SR since this cut results in a NF closer to unity. The $\Delta\phi_{\ell\ell}$ cut is removed due to mismodeling of the $\Delta\phi_{\ell\ell}$ spectrum at high $\Delta\phi_{\ell\ell}$. The CR is defined then by requiring no $b-$jets, an inverse $Z \to \tau\tau$ veto $(m_Z - 25) < m_{\tau\tau}$, $m_{\ell\ell} < 55$GeV, together with the VBF veto and VH veto in the same way of the other two CRs. Orthogonality with the SR is achieved by making the inverse cut on $m_{\tau\tau}$. The VBF and VH vetos are applied to maintain orthogonality with the VBF and VH analyses. The NF is found to be 0.898 ± 0.020, while the purity for this region is around 76%. Figure A.9 in Appendix A shows a comparison of data and simulation for a number of kinematic variables in the $Z/\gamma^* \to \tau\tau$ CR.

In Figure 7.11 the scheme of the cuts for the ggF-enriched $N_{\text{jet}} \geq 2$ regions is depicted. Arrows are labeled with the cuts that are applied when moving from one region to another. Bold text indicates that a cut provides orthogonality between regions. A cut is crossed out if it is removed when going from one region to another.

7.2 Statistical analysis

Results are obtained from a profile likelihood fit to data in the SRs and CRs. The included uncertainties are described in Section 5.3. Experimental uncertainties affecting both signal and background are in general modeled as correlated between SRs and CRs in all analysis categories. Theoretical uncertainties on the backgrounds and the background NFs are assumed to be uncorrelated between different analysis categories.

The m_{T} distribution is used as the final discriminant in each of four regions, defined by $m_{\ell\ell}$ and sub-leading lepton p_{T} in both the $N_{\text{jet}} = 0$ and $N_{\text{jet}} = 1$ categories, as described in Sections 7.1.1 and 7.1.2. The same m_{T} distribution binning [0-90, 90-100, 100-110, 110-120, 120-130, 130-∞] is used in all regions. The SR in the ggF-enriched $N_{\text{jet}} \geq 2$ category is split in two bins of $m_{\ell\ell}$, but there is no split in sub-leading lepton p_{T}. In both regions, the m_{T} distribution is divided in six bins with the same boundaries as for the $N_{\text{jet}} = 0$ and $N_{\text{jet}} = 1$ categories. For the VBF-enriched $N_{\text{jet}} \geq 2$ category, the DNN output is used as the discriminating variable. The distribution is divided into seven bins: [0-0.25, 0.25-0.52, 0.52-0.68, 0.68-0.77, 0.77-0.83, 0.83-0.87, 0.87-1.00]. In the context of the ***Couplings*** analysis, two different scenarios are studied:

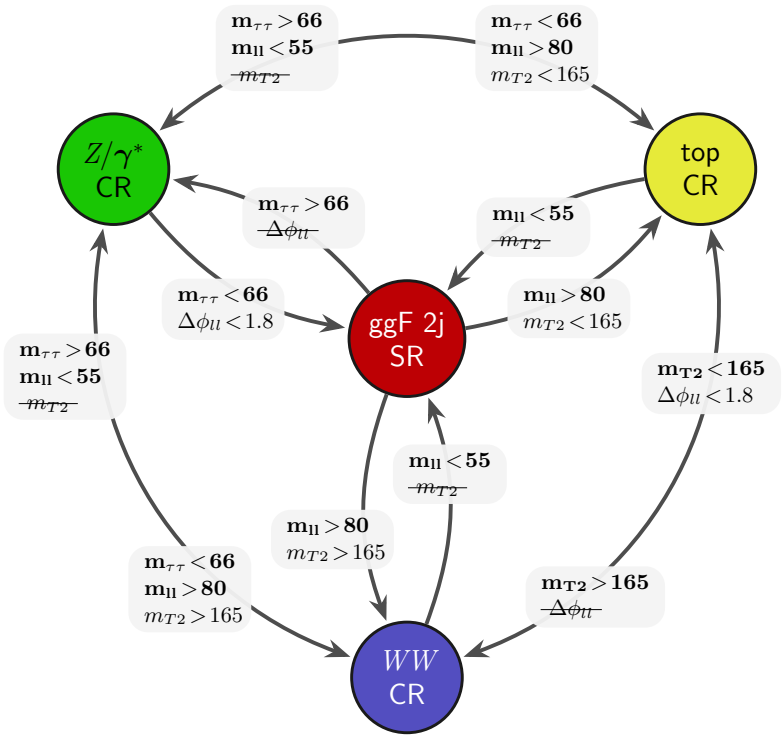

Figure 7.11: Visual representation of the cuts separating the SRs and the CRs for the ggF-enriched $N_{\text{jet}} \geq 2$ analysis category. Arrows are labeled with the cuts that are applied when moving from one region to another. Bold text indicates that a cut provides orthogonality between regions. A cut is crossed out if it is removed when going from one region to another. Units of GeV have been omitted. Cuts based on the mass of the Z boson have been shortened, i.e. $m_Z - 25\,\text{GeV} \approx 66\,\text{GeV} \equiv 66$. Adapted from [185].

- The signal strengths and cross sections for the ggF and VBF production modes are determined in a simultaneous fit to all nominal SRs and CRs in the $N_{\text{jet}} = 0$, $N_{\text{jet}} = 1$, and $N_{\text{jet}} \geq 2$ categories.
- A single POI for the combined ggF and VBF yield is extracted when using the same regions of the previous fit.

7

Pruning procedure

Similarly to the ***Properties*** analysis, a pruning procedure is applied, but not only on parameters with a negligible impact on the final uncertainty. The general rules for pruning are:

- Normalization uncertainties are neglected if their relative impact is $< 0.1\,\%$ or $> 80\,\%$. The latter is only applied in regions and for processes with small yields, where the large variations are caused by large MC statistical uncertainty.
- Normalization uncertainties are neglected if their relative impact is $< 0.2\sigma_{\text{stat}}$, where σ_{stat} is the statistical fluctuation of the MC simulation. This is only applied to uncertainties estimated with four-vector variations, where migrations between neighboring bins and regions can cause large statistical fluctuations.

- Shape uncertainties are neglected if they agree with the nominal distribution well within statistical uncertainties and their p-value is $p > 0.95$.
- Experimental shape uncertainties are neglected for $Z/\gamma^* \to \tau\tau$, other diboson, where the lack of statistics makes the precision of MC samples too low for a reliable estimate.

7.3 Results

Signal strength measurement

The signal strengths for the ggF and VBF production modes for a Higgs boson with mass $m_H = 125.09$ GeV in the $H \to WW^*$ decay channel are jointly measured to be

$$\begin{aligned}
\mu_{\text{ggF}} &= 1.15\ ^{+0.16}_{-0.15} \\
&= 1.15 \pm 0.06\ (\text{stat.})\ ^{+0.09}_{-0.08}\ (\text{exp syst.})\ ^{+0.09}_{-0.07}\ (\text{sig theo.})\ ^{+0.08}_{-0.07}\ (\text{bkg theo.}) \\
\mu_{\text{VBF}} &= 0.92\ ^{+0.24}_{-0.20} \\
&= 0.92\ ^{+0.14}_{-0.13}\ (\text{stat.})\ ^{+0.08}_{-0.07}\ (\text{exp syst.})\ ^{+0.15}_{-0.11}\ (\text{sig theo.})\ ^{+0.09}_{-0.08}\ (\text{bkg theo.})
\end{aligned}$$

with a correlation of -5%.

The post-fit SR yields for all of the four analysis categories defined in Section 7.1 are presented in Table 7.2. The uncertainty on the total expected yield reflects the knowledge of the observed yield in each analysis category and is not indicative of the precision of the analysis, which is better captured by the uncertainty on the signal component.

Process	$N_{\text{jet}} = 0$ ggF	$N_{\text{jet}} = 1$ ggF	$N_{\text{jet}} \geq 2$ ggF	$N_{\text{jet}} \geq 2$ VBF	
				Inclusive	DNN: $[0.87, 1.0]$
H_{ggF}	2100 ± 220	1100 ± 130	440 ± 90	209 ± 40	2.6 ± 0.9
H_{VBF}	23 ± 9	103 ± 30	46 ± 12	180 ± 40	28.8 ± 5.5
Other Higgs	40 ± 20	55 ± 28	55 ± 27	29 ± 15	0.04 ± 0.02
WW	9700 ± 350	3500 ± 410	1500 ± 470	2100 ± 340	4.6 ± 1.2
$t\bar{t}/Wt$	2200 ± 210	5300 ± 340	6100 ± 500	7600 ± 370	2.6 ± 0.8
Z/γ^*	140 ± 50	280 ± 40	930 ± 70	1300 ± 300	0.6 ± 0.1
Other VV	1400 ± 130	840 ± 100	470 ± 90	380 ± 80	0.6 ± 0.1
Mis-Id	1200 ± 130	720 ± 90	470 ± 50	330 ± 40	1.7 ± 0.2
Total	$16\,770 \pm 130$	$11\,940 \pm 110$	$10\,030 \pm 100$	$12\,200 \pm 180$	42.0 ± 5.1
Observed	16 726	11 917	9 982	12 189	38

Table 7.2: Post-fit MC and data yields in the ggF and VBF SRs. Yields in the bin with the highest VBF DNN output are also presented. The quoted uncertainties correspond to the statistical uncertainties, together with the experimental and theory modelling systematic uncertainties. The sum of all the contributions may differ from the total value due to rounding.

From the post-fit model, the m_{T} distributions for the separate $N_{\text{jet}} = 0$, $N_{\text{jet}} = 1$, and ggF-enriched $N_{\text{jet}} \geq 2$ SRs, as well as the combination of the ggF SRs can be extracted, and are shown in Figure 7.12.

The bottom panels of Figure 7.12 display the difference between the data and the total estimated background for m_{T} distribution of a SM Higgs boson with $m_H = 125.09$ GeV. The total observed signal in all categories of about 4000 events (see Table 7.2) is in agreement, in both shape and rate, with the expected SM signal. The observed (expected) signal yields using only the ggF-enriched $N_{\text{jet}} \geq 2$ category with the VBF contribution fixed to the standard model prediction reaches a significance of 2.2 (1.6) σ above the background only expectation.

The VBF DNN output distribution in the final SR is presented in Figure 7.13. The observed (expected) VBF signal reaches a significance of 5.8 (6.2)σ above the background only expectation. This result is the first of its kind: it provides an observation of the VBF production of Higgs bosons subsequently decaying to a pair of W bosons with the ATLAS detector.

Cross section measurement

The cross sections times branching fraction, $\sigma_{\text{ggF}} \cdot \mathcal{B}_{H\to WW^*}$ and $\sigma_{\text{VBF}} \cdot \mathcal{B}_{H\to WW^*}$, are jointly measured to be

$$\begin{aligned}
\sigma_{\text{ggF}} \cdot \mathcal{B}_{H\to WW^*} &= 12.0 \pm 1.4\,\text{pb} \\
&= 12.0 \pm 0.6\,(\text{stat.})^{+0.9}_{-0.8}\,(\text{exp syst.})^{+0.6}_{-0.5}\,(\text{sig theo.}) \pm 0.8\,(\text{bkg theo.})\,\text{pb} \\
\sigma_{\text{VBF}} \cdot \mathcal{B}_{H\to WW^*} &= 0.75^{+0.19}_{-0.16}\,\text{pb} \\
&= 0.75 \pm 0.11\,(\text{stat.})^{+0.07}_{-0.06}\,(\text{exp syst.})^{+0.12}_{-0.08}\,(\text{sig theo.})^{+0.07}_{-0.06}\,(\text{bkg theo.})\,\text{pb},
\end{aligned}$$

to be compared with the SM predicted values of 10.4 ± 0.6 pb and 0.81 ± 0.02 pb for ggF and VBF [107], respectively. The combined cross section times branching fraction, $\sigma_{\text{ggF+VBF}} \cdot \mathcal{B}_{H\to WW^*}$, is measured to be

$$\begin{aligned}
\sigma_{\text{ggF+VBF}} \cdot \mathcal{B}_{H\to WW^*} &= 12.3 \pm 1.3\,\text{pb} \\
&= 12.3 \pm 0.6(\text{stat.})^{+0.8}_{-0.7}(\text{exp syst.}) \pm 0.6(\text{sig theo.}) \pm 0.7(\text{bkg theo.})\,\text{pb},
\end{aligned}$$

in comparison to the SM predicted value of 11.3 ± 0.5 pb.

Figure 7.14 shows the best-fit values and uncertainties of the $H\to WW^*$ cross section times branching fraction for the ggF and VBF processes and their combination, normalised to the corresponding SM prediction. The relative impact of the main uncertainties on the measured cross-section values is shown in Table 7.3 for $\sigma_{\text{ggF+VBF}} \cdot \mathcal{B}_{H\to WW^*}$, $\sigma_{\text{ggF}} \cdot \mathcal{B}_{H\to WW^*}$, and $\sigma_{\text{VBF}} \cdot \mathcal{B}_{H\to WW^*}$.

It is nice to see that the amount of effort in collecting more data, has led to measurements not anymore dominated by systematic uncertainties. The largest contribution to the total uncertainty in the ggF and VBF analysis originates from the respective signal processes, in particular from the imprecise determination of the PS of these two processes. Similar to the ***Properties*** case, the modeling of the $t\bar{t}$ process plays a non-negligible role, with the main uncertainty originating from its matching uncertainty.

The next-largest group of uncertainty contains experimental effects, mainly coming from the $E_{\mathrm{T}}^{\text{miss}}$ resolution. It is worth mentioning how the change in the $b-$jet tagging algorithm reduces the impact of the flavor tagging drastically in both analyses.

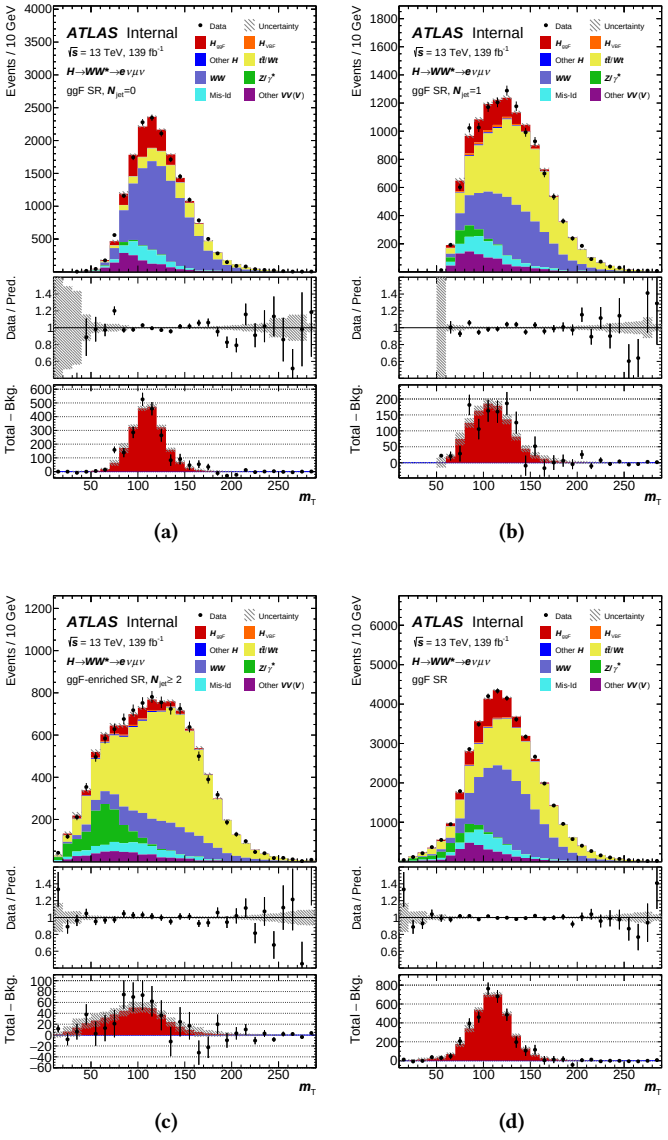

Figure 7.12: Post-fit m_{T} distributions with the signal and the background modeled contributions in the (a) $N_{\mathrm{jet}} = 0$, (b) $N_{\mathrm{jet}} = 1$, (c) ggF-enriched $N_{\mathrm{jet}} \geq 2$, and (d) combined signal regions. The last bin of the distributions is inclusive (it includes the overflow). The hatched band shows the total uncertainty, assuming SM Higgs boson production. The middle panel shows the ratio of the data to the sum of the fitted signal and background. The bottom panel displays the difference between the data and the estimated background compared to the distribution for a SM Higgs boson with $m_H = 125$ GeV, where the hatched band indicates the combined statistical and systematic uncertainty for the fitted signal and background.

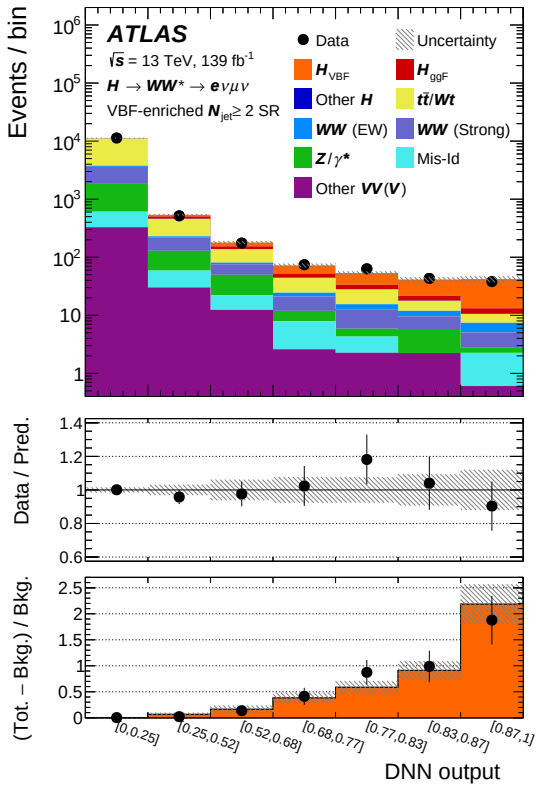

Figure 7.13: Post-fit distribution of the DNN output in the VBF SR. The hatched band shows the total uncertainty, assuming SM Higgs boson production. The middle panel shows the ratio of the data to the sum of the fitted signal and background. The bottom panel displays the signal-to-background ratio, where the hatched band indicates the combined statistical and systematic uncertainty for the fitted signal and background.

Another way of displaying the two-dimensional cross section fit is housed in Figure 7.15 where The 68% and 95% confidence level two-dimensional contours of $\sigma_{\text{ggF}} \cdot \mathcal{B}_{H\to WW^*}$ and $\sigma_{\text{VBF}} \cdot \mathcal{B}_{H\to WW^*}$ are shown. The measurement is consistent with the SM predictions.

As previously mentioned, the precision of the presented measurements is affected by uncertainties that can be individually reduced.
Starting from the main ones, efforts to produce more precise MC samples are ongoing, which will reduce modeling uncertainties. Thanks to the increasing computer power, the production of the MC samples, will also be more massive. This will contribute to a more precise measurement by reducing the total MC uncertainties and improving the background normalizations.
Last but not least, collecting twice the amount of data of the Full Run 2 will help in reducing the data statistics by ∼70%.

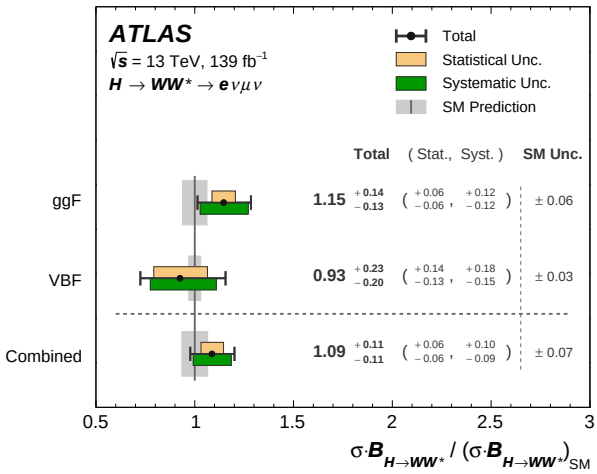

Figure 7.14: Best-fit values and uncertainties of the $H \to WW^*$ cross section times BF for the ggF and VBF processes and their combination, normalized to the corresponding SM prediction. The black error bars, green boxes, and yellow boxes show the total, systematic, and statistical uncertainties in the measurements, respectively. The grey band represents the theory uncertainty on signal production.

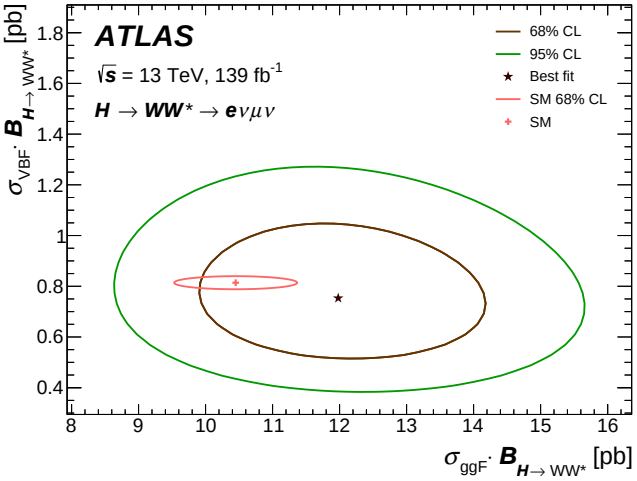

Figure 7.15: 68% and 95% confidence level two-dimensional likelihood contours of $\sigma_{\text{ggF}} \cdot \mathcal{B}_{H \to WW^*}$ versus $\sigma_{\text{VBF}} \cdot \mathcal{B}_{H \to WW^*}$, compared to the SM prediction shown by the red marker. The red 68% confidence level on the SM predictions for the ggF and VBF cross sections times branching fraction [107] is indicated by the red ellipse.

Source	$\frac{\Delta\sigma_{\text{ggF+VBF}}\cdot\mathcal{B}_{H\to WW^*}}{\sigma_{\text{ggF+VBF}}\cdot\mathcal{B}_{H\to WW^*}}$ [%]	$\frac{\Delta\sigma_{\text{ggF}}\cdot\mathcal{B}_{H\to WW^*}}{\sigma_{\text{ggF}}\cdot\mathcal{B}_{H\to WW^*}}$ [%]	$\frac{\Delta\sigma_{\text{VBF}}\cdot\mathcal{B}_{H\to WW^*}}{\sigma_{\text{VBF}}\cdot\mathcal{B}_{H\to WW^*}}$ [%]
Data statistical uncertainties	4.6	5.1	15
Total systematic uncertainties	9.5	11	18
MC statistical uncertainties	3.0	3.8	4.9
Experimental uncertainties	5.2	6.3	6.7
Flavour Tagging	2.3	2.7	1.0
Jet energy scale	0.9	1.1	3.7
Jet energy resolution	2.0	2.4	2.1
$E_{\text{T}}^{\text{miss}}$	0.7	2.2	4.9
Muons	1.8	2.1	0.8
Electrons	1.3	1.6	0.4
Fake factors	2.1	2.4	0.8
Pile-up	2.4	2.5	1.3
Luminosity	2.1	2.0	2.2
Theoretical uncertainties	6.8	7.8	16
ggF	3.8	4.3	4.6
VBF	3.2	0.7	12
WW	3.5	4.2	5.5
Top	2.9	3.8	6.4
$Z\tau\tau$	1.8	2.3	1.0
Other VV	2.3	2.9	1.5
Other Higgs	0.9	0.4	0.4
Background normalisations	3.6	4.5	4.9
WW	2.2	2.8	0.6
Top	1.9	2.3	3.4
$Z\tau\tau$	2.7	3.1	3.4
TOTAL	10	12	23

Table 7.3: Breakdown of the main contributions to the total uncertainty in $\sigma_{\text{ggF+VBF}}\cdot\mathcal{B}_{H\to WW^*}$, $\sigma_{\text{ggF}}\cdot\mathcal{B}_{H\to WW^*}$, and $\sigma_{\text{VBF}}\cdot\mathcal{B}_{H\to WW^*}$, relative to the measured value. The individual sources of systematic uncertainties are grouped together. The sum in quadrature of the individual components differs from the total uncertainty due to correlations between the components.

7.4 Example event displays for the *Couplings* analysis

This section shows four event candidates, one per analysis category. The displays are obtained with the ATLAS event visualization tool and they expose the transverse plane and the lateral plane of the detector, as well as the energy of the reconstructed objects. The color code is the following: yellow for electrons, blue for muons, red for the leading jet, green for the sub-leading jet, and white for $E_{\text{T}}^{\text{miss}}$.

Figure 7.16 displays the candidate event display for a Higgs boson produced via the ggF production mode entering the $N_{\text{jet}} = 0$ analysis category, while in Figure 7.17 a ggF event produced in association with one jet is shown. The latter event is the event in which the Higgs boson has the highest p_{T} in all the reconstructed events in the analysis.
Figure 7.18 shows a VBF event with a DNN score of 0.99 with a signal-to-background ratio of $\gtrsim 6$ and finally, Figure 7.19 displays a ggF + 2 jets event candidate.

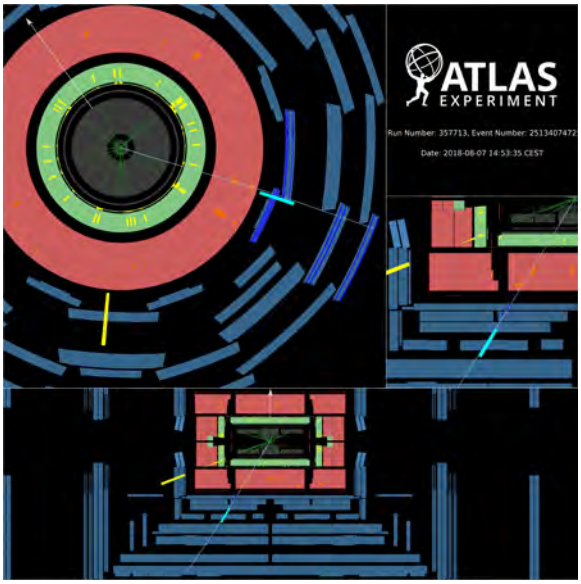

Figure 7.16: Candidate event display for a Higgs boson produced through the ggF production mode entering the $N_{\text{jet}} = 0$ analysis category. The Figure shows the transverse plane (top-left), the lateral plane of the detector (bottom), and a focus of the latter (top-right).

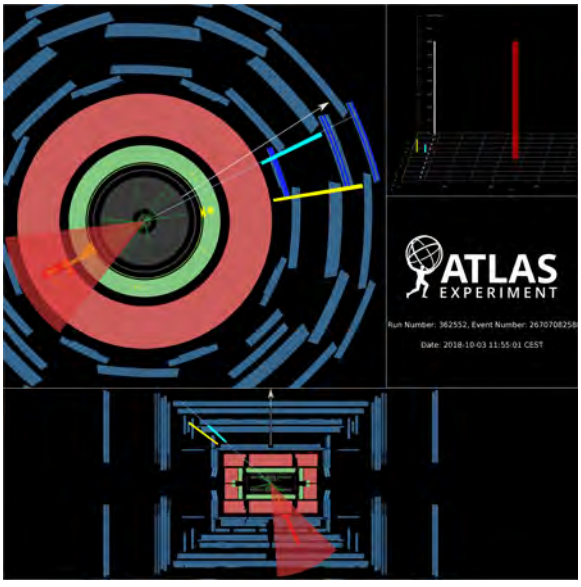

Figure 7.17: Candidate event display for a Higgs boson produced through the ggF production mode entering the $N_{\text{jet}} = 1$ analysis category. The value of p_{T}^{H} for the event is 625 GeV, the highest out of all reconstructed events in the analysis. The Figure shows the transverse plane (top-left), the lateral plane of the detector (bottom), and the energy of the objects (top-right).

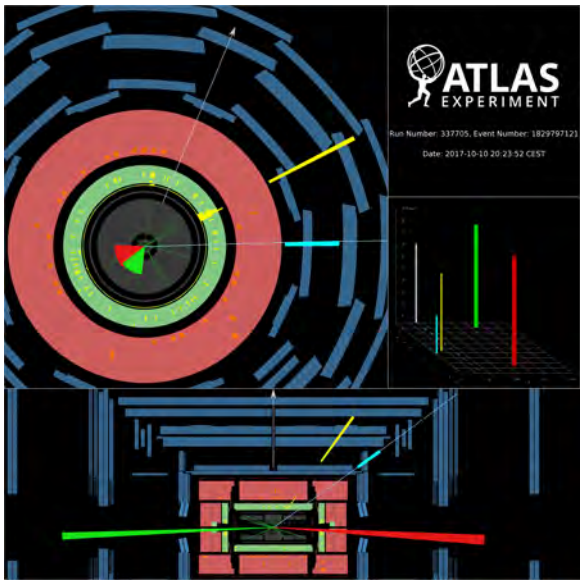

Figure 7.18: Candidate event display for a Higgs boson produced through the VBF production mode. The Figure shows the transverse plane (top-left), the lateral plane of the detector (bottom), and the energy of the objects (top-right). The DNN score of an event from the highest DNN bin, corresponding to a signal to background ratio of $\gtrsim 6$.

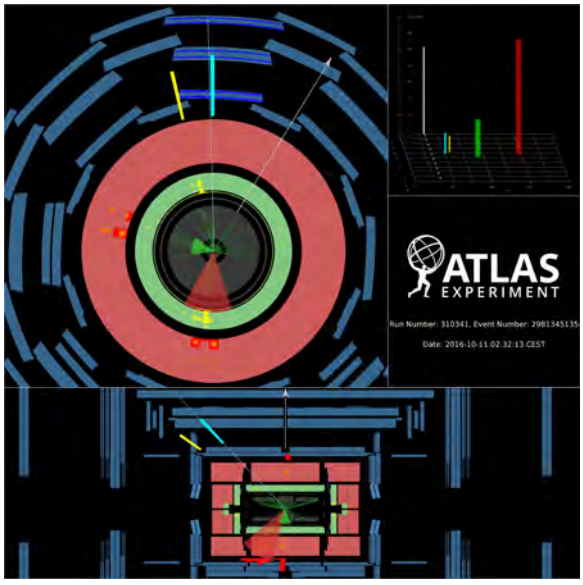

Figure 7.19: Candidate event display for a Higgs boson produced through the ggF production mode in association with two jets, entering the ggF-enriched $N_{\text{jet}} \geq 2$ analysis category. The Figure shows the transverse plane (top-left), the lateral plane of the detector (bottom), and the energy of the objects (top-right).

7.5 References

[91] ATLAS Collaboration. *Object-based missing transverse momentum significance in the ATLAS Detector*. ATLAS-CONF-2018-038. 2018 (cit. on pp. 79, 152).

[107] D. de Florian et al. "Handbook of LHC Higgs Cross Sections: 4. Deciphering the Nature of the Higgs Sector". In: 2/2017 (Oct. 2016). DOI: 10.23731/CYRM-2017-002. arXiv: 1610.07922 [hep-ph] (cit. on pp. 91, 161, 164, 170).

[185] Konstantin Lehmann. "Estimating deceiving signatures and their role in the observation of the VBF production mode in the Higgs-Boson decay into two W bosons". PhD thesis. Simon Fraser U., 2022 (cit. on pp. 149, 151, 156, 159).

[186] François Chollet et al. *Keras*. 2015. URL: https://keras.io (cit. on p. 150).

[187] Martín Abadi et al. *TensorFlow: Large-Scale Machine Learning on Heterogeneous Distributed Systems*. Preprint. version 2.4.1 (Software). 2015. arXiv: 1603.04467 [cs] (cit. on p. 150).

[188] Jen-Tzung Chien. "Chapter 7 - Deep Neural Network". In: *Source Separation and Machine Learning*. Ed. by Jen-Tzung Chien. Academic Press, 2019, pp. 259–320 (cit. on p. 151).

[189] Jürgen Schmidhuber. "Deep learning in neural networks: An overview". In: *Neural Networks* 61 (2015), pp. 85–117. DOI: 10.1016/j.neunet.2014.09.003 (cit. on p. 151).

[190] C. G. Lester and D. J. Summers. "Measuring masses of semiinvisibly decaying particles pair produced at hadron colliders". In: *Phys. Lett.* B463 (1999), pp. 99–103. DOI: 10.1016/S0370-2693(99)00945-4. arXiv: hep-ph/9906349 [hep-ph] (cit. on p. 155).

[191] ATLAS Collaboration. "Observation and measurement of Higgs boson decays to WW^* with the ATLAS detector". In: *Phys. Rev. D* 92 (2015), p. 012006. DOI: 10.1103/PhysRevD.92.012006. arXiv: 1412.2641 [hep-ex] (cit. on p. 157).

8

What: Simplified Template Cross Section Measurements

The STXS measurement formally belongs to the ***Couplings*** analysis. It can be treated indeed as an extension of it. This Chapter contains an introduction on the reasons behind the choice of the STXS methodology, Section 8.1, the analysis strategy follows in Section 8.2, and it finishes with an illustration of the results in Section 8.4, after a brief introduction of the statistical methods used in this part of the analysis (Section 8.3).

Contents

8.1 Motivation

Once the inclusive cross-sections for the ggF and VBF processes have been measured, a step forwards can be taken and a measurement of cross-sections of fiducial regions in phase space can be performed. The simplified template cross sections framework [107, 192, 193] has been developed mainly for two purposes: providing more finely-grained measurements for individual Higgs production modes, and reducing the theoretical uncertainties already folded into the measurements. These cross-sections are defined in mutually exclusive regions of phase space, called "bins" for simplicity, and are specific to the different production modes. In order to facilitate combinations of different decay channels, prescriptions on the bin characteristics have been given. In this thesis, stage-1.2 definition of STXS is used.

8.1.1 VBF Stage 1.2

The VBF template process for stage 1.2 is part of the electroweak *qqH* production, of this process the t-channel is represented by the usual VBF topology, while the s-channel is represented by the $pp \to V(\to q\bar{q})H$ topology with hadronic $V \to q\bar{q}$ decays. The two processes can only be distinguished by enriching either type of contribution via kinematic cuts.

Figure 8.1 depicts the maximal number of regions that are possible in STXS stage-1.2 which are described below:

- The *qqH* signal is first split into 0-jet, 1-jet and in $\geq$ 2-jet bins.
- The 0-jet and 1-jet bin contain only a small amount of VBF signal that is especially difficult to distinguish from the ggF background.
- The $\geq$ 2-jet bin is split into low-m_{jj} and high-m_{jj} bins with $m_{jj} < 350$ GeV and $m_{jj} > 350$ GeV , respectively.
  - In the kinematic region defined by $m_{jj} < 350$ GeV bin contributions from the actual VBF process of interest are still very hard to distinguish from the ggF background.
  - The $m_{jj} > 350$ GeV bin targets the nominal VBF production process.
- The m_{jj} >350 GeV bin is split into low-p_{T}^{H} and high-p_{T}^{H} bins with $p_{\mathrm{T}}^{H} < 200$ GeV and $p_{\mathrm{T}}^{H} > 200$ GeV, respectively. This bin has m_{jj} boundaries defined at m_{jj} = 700, 1000, and 1500 GeV. In addition, it has a bin boundary defined at p_{T}^{Hjj} = 25 GeV. The observable p_{T}^{Hjj} measures the transverse momentum of the combined system of the Higgs boson and the two leading jets. It is sensitive to the amount of additional radiation beyond the second jet. While the $p_{\mathrm{T}}^{H} < 200$ GeV bin contains most of the (accessible) VBF signal, the $p_{\mathrm{T}}^{H} > 200$ GeV bin only contains a small fraction. However, this last bin is sensitive to BSM contributions, because at a p_{T}^{H} value greater than the top mass, effects of the top quark can be resolved.

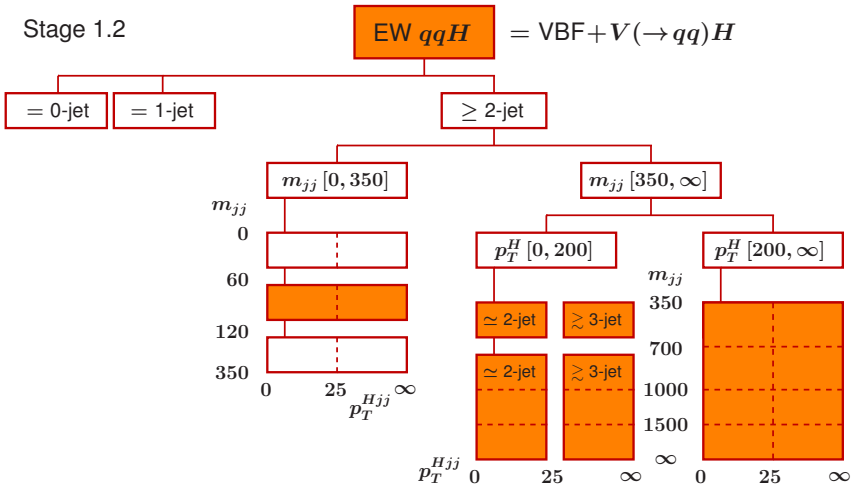

Figure 8.1: STXS scheme for Electroweak qqH production (VBF + Hadronic VH) Stage 1.2.

8.1.2 ggF Stage 1.2

The ggF template process for stage 1.2 is defined for the $gg \to H$ process plus higher-order QCD and electroweak corrections. Figure 8.2 depicts the maximal number of regions that is possible to define in STXS stage-1.2, which are described below:

- The ggH signal is first split into $p_{\mathrm{T}}^H < 200$ GeV and $p_{\mathrm{T}}^H > 200$ GeV bins.
- The $p_{\mathrm{T}}^H > 200$ GeV bin is sensitive to BSM effects.
  - This bin is further split into 4 p_{T}^H bins, namely $p_{\mathrm{T}}^H < 300$ GeV, 300 GeV $< p_{\mathrm{T}}^H < 450$ GeV, 450 GeV $< p_{\mathrm{T}}^H < 650$ GeV, $p_{\mathrm{T}}^H > 650$ GeV.
- The $p_{\mathrm{T}}^H < 200$ GeV bin contains most of the cross section.
- The latter bin is split into 0-jet, 1-jet, and $\geq$ 2-jets bins.
  - The 0-jet bin is split into $p_{\mathrm{T}}^H < 10$ GeV, which contains a sizeable fraction of the cross-section, and $p_{\mathrm{T}}^H > 10$ GeV.
  - The 1-jet bin is split into 3 p_{T}^H bins, namely $p_{\mathrm{T}}^H < 60$ GeV, 60 GeV $< p_{\mathrm{T}}^H < 120$ GeV, $p_{\mathrm{T}}^H > 120$ GeV.
  - The $\geq$2-jets bin has a split into low-m_{jj} and high-m_{jj} regions.
- The $\geq$ 2-jets bin into low-m_{jj} and high-m_{jj} bins with $m_{jj} < 350$ GeV and $m_{jj} > 350$ GeV. In addition, a boundary at p_{T}^{Hjj} is used in order to provide a separation into 2-jet and $\geq$ 3-jet like phase space.
  - The $m_{jj} < 350$ GeV bin contains most of the event of the $\geq$2 jets region . It is split into 3 p_{T}^H bins, namely $p_{\mathrm{T}}^H < 60$ GeV, 60 GeV $< p_{\mathrm{T}}^H < 120$ GeV, $p_{\mathrm{T}}^H > 120$ GeV, aligned with the 1-jet bin. The p_{T}^{Hjj} boundary here is kept as a sub-bin boundary.

– The $m_{jj} > 350$ GeV bin contains only a small fraction of the total cross-section, which however constitutes the main background to VBF production. Hence it uses the same splitting as the corresponding high-m_{jj} VBF bins (in section 8.1.1) with boundaries defined at m_{jj} = 700, 1000, and 1500 GeV. The p_{T}^{Hjj} boundary here is kept as a sub-bin boundary.

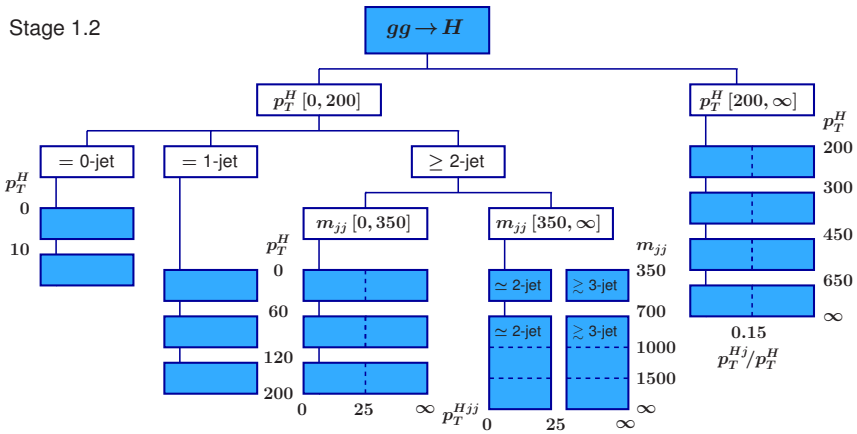

Figure 8.2: STXS scheme for ggH Stage 1.2.

8.1.3 Variation from the Stage 1.2 scheme

Due to limited experimental sensitivity, some of the bins previously described need to be merged, the resulting categorization is called "reduced stage-1.2", which is shown in the left-hand side of Figure 8.3, and includes the following modifications:

- The ggH 0-jet process is not split at $p_{\mathrm{T}}^H = 10$ GeV. This is not done because the low p_{T}^H bin is difficult to resolve due to the two neutrinos in the final state and due to the uncertainties carried by the $\vec{E}_{\mathrm{T}}^{\mathrm{miss}}$ reconstruction. Indeed, studies showed that the region with low p_{T}^H has only 32% purity, [194].
- The ggH $p_{\mathrm{T}}^H < 200$ GeV processes with two or more jets do not present a split in m_{jj}. These events in fact are very similar to the equivalent EW qqH events producing a strong correlation in the measurement. The observed anti-correlation is ∼80%, as shown in citeslides:correlations.
- The high-p_{T}^H ggH events are considered as a single category, without any further split in p_{T}^H or p_{T}^{Hjj}. This bin is measured separately in the 3 ggF phase space regions.
- For the EW qqH process, only events with $m_{jj} > 350$ GeV are considered in the reduced STXS 1.2. This is due to the difficult distinction between VBF and ggF, at low m_{jj}.
- The EW qqH $p_{\mathrm{T}}^H > 200$ GeV and $m_{jj} > 350$ GeV processes are grouped in a single bin.
- The bin EW qqH $p_{\mathrm{T}}^H < 200$ GeV with $m_{jj} > 350$ GeV does not present a p_{T}^{Hjj} split, but it is divided in m_{jj} sub-bins.

The reduced stage-1.2 scheme results in 11 particle-level-cross-sections-bin to measure.

8.2 Strategy and Event Selection

The definitions of the SRs and CRs for the STXS measurement are inherited from the inclusive cross-section measurement analysis, as well as the fitting observable m_{T} for the ggF categories and the DNN observable for the VBF one.

ggF $N_{\text{jet}} = 0$
Given that no split is present in the ggF $N_{\text{jet}} = 0$ reduced STXS scheme, the $N_{\text{jet}} = 0$ SRs and CRs remain the same as in the inclusive cross section measurement: 4 SRs split in $p_{\mathrm{T},\ell}{}^{\text{sublead}}$ and $m_{\ell\ell}$, and 3 CRs (Top, $Z \to \tau\tau$ and WW). In principle, a ggF $N_{\text{jet}} = 0$ $p_{\mathrm{T}}^{H} > 200\,\text{GeV}$ SR should be defined, however, has been estimated that the amount of ggH events with $p_{\mathrm{T}}^{H} > 200\,\text{GeV}$ is smaller than 0.1, hence it can be neglected.

ggF $N_{\text{jet}} = 1$
The p_{T}^{H} split in the $N_{\text{jet}} = 1$ phase space is reproduced in the SRs. However in order to not reduce the pre-bin statistics, the split in $p_{\mathrm{T},\ell}{}^{\text{sublead}}$ and $m_{\ell\ell}$ is removed. The ggF $N_{\text{jet}} = 1$ categories consist of 4 SRs and 12 CRs (Top, $Z \to \tau\tau$ and WW, times the 4 p_{T}^{H} categories).

ggF $N_{\text{jet}} \geq 2$
The particle-level split in the ggH categories is replicated in the ggF $N_{\text{jet}} \geq 2$ phase space by splitting the SRs and CRs according to p_{T}^{H}. The ggF $N_{\text{jet}} \geq 2$ categories are formed by 4 SRs (split in $m_{\ell\ell}$ and p_{T}^{H}) and 6 CRs (Top, $Z \to \tau\tau$ and WW times the 2 p_{T}^{H} categories).

VBF $N_{\text{jet}} \geq 2$
The same split as the particle-level categories is kept for the VBF SRs resulting in 5 SRs. For the background, due to limited statistics, only 3 CRs per background type (Top and $Z \to \tau\tau$) are formed: $350\,\text{GeV} < m_{jj} < 700\,\text{GeV}$ with $p_{\mathrm{T}}^{H} < 200\,\text{GeV}$, $m_{jj} > 700\,\text{GeV}$ with $p_{\mathrm{T}}^{H} < 200\,\text{GeV}$, and $p_{\mathrm{T}}^{H} > 200\,\text{GeV}$.

The SRs just defined are shown on the right-hand side of Figure 8.3 with the mapping between the *truth*-categories to measure and the reconstructed SRs.

The overview of the expected signal composition in the SRs is shown in Figure 8.4.

8.3 Statistical Analysis

The pruning procedure, which is utilized in the measurement of the inclusive cross-section, is also adopted and shared in the STXS analysis. In contrast, the binning scheme for m_{T} remains unchanged in the case of ggF analyses, previously defined as $\{0, 90, 100, 110, 120, 130, \infty\}$GeV. For the VBF analysis, various alternatives have been investigated. First, an optimized DNN for each SR was considered, but the improvement obtained did not justify the increasing complexity in the theory

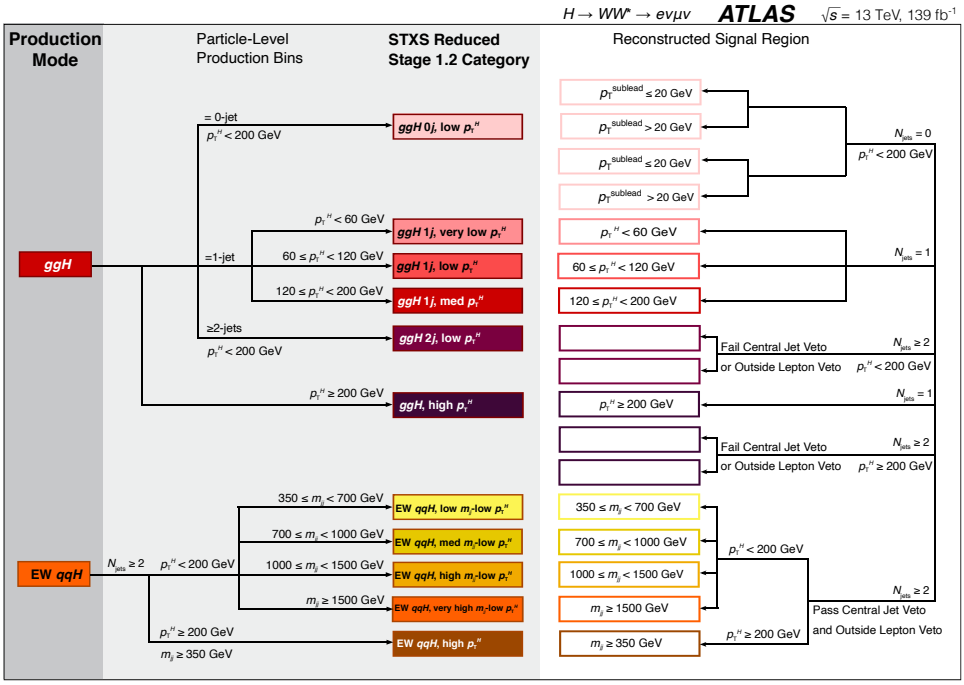

Figure 8.3: Two sets (Production Mode Stage and Reduced Stage 1.2) of exclusive phase-space regions (production bins) defined at particle-level for the measurement of the Higgs boson production cross sections (left and middle-left shaded panels), and the corresponding reconstructed signal regions (right panel). The colours of each reconstructed signal region box indicate the STXS category which provides the largest relative contribution, and it corresponds to the one in Figure 8.4.

systematics treatment. Second, a binning algorithm is implemented in order to optimize the binning choice in the 5 SR independently. As a result, the SR with $350\,\text{GeV} < m_{jj} < 700\,\text{GeV}$ has bin boundaries at $\{0, 0.27, 0.5, 0.84, 1\}$, while in the other 4 SRs the binning is $\{0, 0.5, 0.74, 0.87, 1\}$.

The uncertainties related to the signal are calculated separately for all the STXS categories. They cover both uncertainties on the overall ggF and VBF cross-sections, as well as the migration of events between the STXS regions. In the case of limited statistics in a particular region, merged regions are used to determine the uncertainties. Since only cross sections are measured for STXS (and not signal strengths), only acceptance uncertainties apply to the signal.

Lastly, the STXS categories not explicitly considered in this analysis, for example, the VBF $N_{\text{jet}} = 0$ or the forward components, have a cross-section assigned as predicted in the SM, and appropriate uncertainties.

As in the previously described analyses, the results are obtained from a profile likelihood fit to data in the SRs and CRs, in this case 17 SRs and 27 CRs. The included uncertainties are described in Section 5.3.

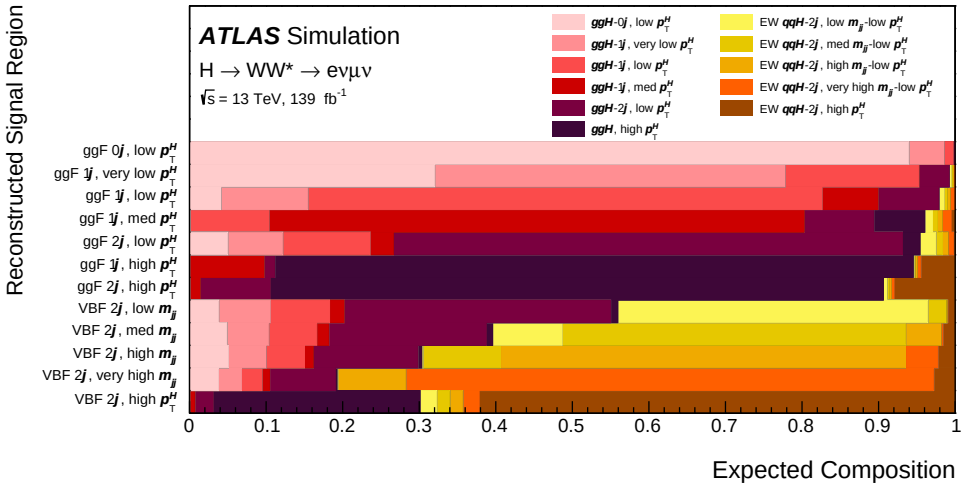

Figure 8.4: Relative SM signal composition in terms of the measured STXS categories for each reconstructed signal region. The $y-$axis shows the reconstructed signal regions while in the plot are displayed the truth categories. The colour code corresponds to the one in Figure 8.3.

8.4 Results

A summary of the cross sections measured in each of the 11 STXS categories and normalized to their corresponding SM prediction is provided in Figure 8.5.

For the ggH cross sections, the measurement is dominated by the systematics uncertainty, with the exception of the $N_{\text{jet}} = 1$ category with $120\,\text{GeV} < p_{\text{T}}^{H} < 200\,\text{GeV}$ and the high-p_{T}^{H} category.

The measured cross sections for the five STXS categories targeting the EW qqH production is on average lower than the μ_{VBF} measured in the inclusive analysis. Events with high m_{jj} or high p_{T}^{H} carry a larger statistical weight in the inclusive analysis compared to events at low m_{jj}, and in these STXS categories the measured value is close to one.

The breakdown of the main uncertainty groups for each POIS is shown in Figure 8.6, where Table 8.1 provides the central values and uncertainties on each of the measured STXS cross sections, together with the SM predictions.

In the ggH categories, the $N_{\text{jet}} = 0$ dominates the cross-section, so it is not a surprise that the $N_{\text{jet}} = 0$ STXS category has similar uncertainties to those shown in Table 7.3. The $N_{\text{jet}} = 1$ categories uncertainties are dominated by theoretical uncertainties on the background processes (mainly top and WW processes). The top background uncertainty also affects the ggH $N_{\text{jet}} \geq 2$ category strongly. For the EW qqH processes with lower m_{jj}, the theoretical uncertainties related to the ggF uncertainties become important, while in the higher m_{jj} regions the low statistics is dominant in the uncertainty composition. Last, the correlation matrix of the measured parameters is shown in Figure 8.7.

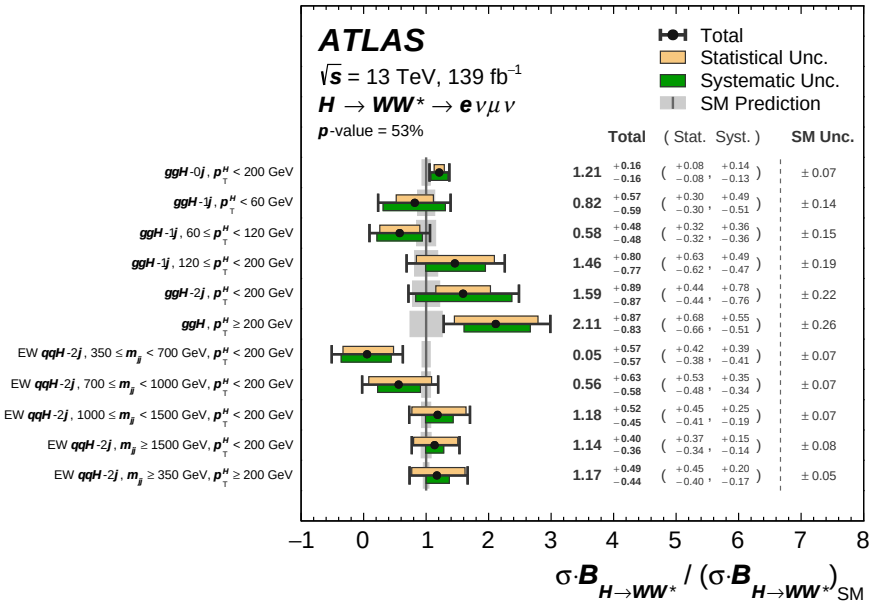

Figure 8.5: Best-fit values and uncertainties for the cross sections measured in each of the STXS categories normalized to the corresponding SM prediction. The black error bars, green boxes yellow tan boxes show the total, systematic, and statistical uncertainties in the measurements, respectively. The grey band represents the theory uncertainty on the signal production corresponding to the STXS category.

The obtained results (Figure 8.5) can be compared with the study performed by the CMS collaboration in the $H \to WW^*$ channel on a dataset of 138 fb^{-1}, [195]. Figure 8.8 shows the observed cross sections for the STXS measured categories. Even if some differences are present, a few points can be stressed:

- for the ggH, high p_{T}^{H} category, CMS offers a two-bin measurement with a precision compatible with the single bin of ATLAS, however, for the CMS study, the same-flavor category is included, that likely provides additional discrimination.
- ATLAS provides 4 bins measurement for the ggF $N_{\mathrm{jet}} = 1$ category, with a relative error going from 55% to 83%, while the two bins measured by CMS have a relative uncertainty of 24% and 117%.
- in the common EW qqH-2j, high p_{T}^{H} category, ATLAS outperforms the CMS measurement by a factor of almost 2.

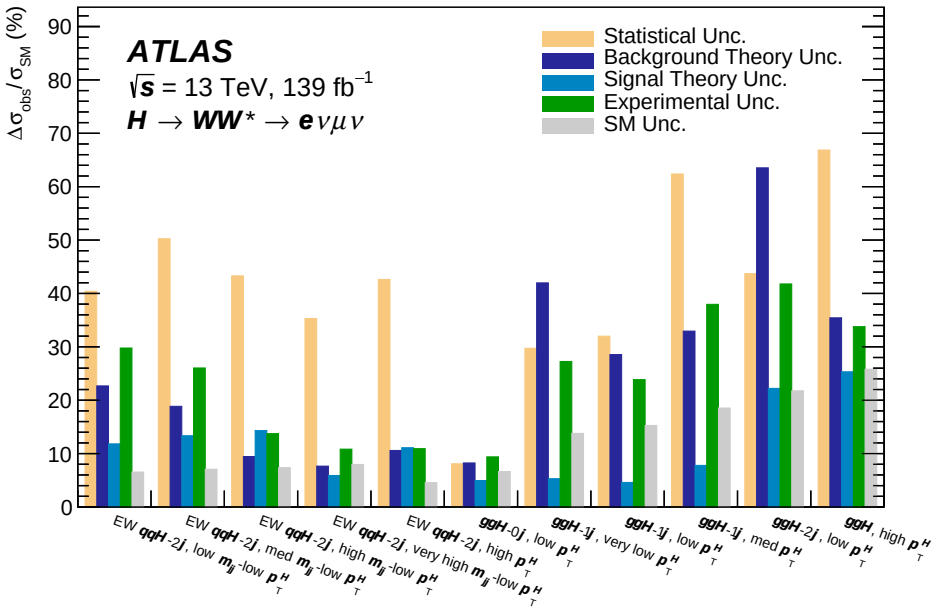

Figure 8.6: Contributions of statistical, background theory, signal theory, and experimental systematic uncertainties to the measured STXS cross sections, shown relative to the SM predicted cross-section. The relative uncertainty on the SM cross-section, which is not included in the measurement, is also shown for comparison.

Table 8.1: Best-fit values and uncertainties for the production cross-section times $H \to WW^*$ branching ratio ($\sigma_i \times \mathcal{B}_{H\to WW^*}$) in each STXS category.

STXS category ($\sigma_i \times \mathcal{B}_{H\to WW^*}$)	Value	Uncertainty [fb]					SM prediction
	[fb]	Total	Stat.	Exp. Syst.	Sig. Theo.	Bkg. Theo.	[fb]
ggH-0j, low p_{T}^H $p_{\mathrm{T}}^H < 200$ GeV	7100	$^{+950}_{-910}$	$^{+480}_{-470}$	$^{+570}_{-530}$	$^{+320}_{-260}$	$^{+490}_{-480}$	5870 ± 390
ggH-1j, very low p_{T}^H $p_{\mathrm{T}}^H < 60$ GeV	1140	$^{+800}_{-820}$	$^{+420}_{-410}$	$^{+380}_{-380}$	$^{+80}_{-70}$	$^{+570}_{-600}$	1400 ± 190
ggH-1j, low p_{T}^H $60 < p_{\mathrm{T}}^H < 120$ GeV	540	$^{+470}_{-470}$	$^{+310}_{-310}$	$^{+230}_{-230}$	$^{+42}_{-47}$	$^{+270}_{-280}$	970 ± 150
ggH-1j, med p_{T}^H $120 < p_{\mathrm{T}}^H < 200$ GeV	230	$^{+130}_{-120}$	$^{+100}_{-100}$	$^{+60}_{-60}$	$^{+10}_{-10}$	$^{+50}_{-50}$	160 ± 30
ggH-2j, low p_{T}^H $p_{\mathrm{T}}^H < 200$ GeV	1610	$^{+900}_{-890}$	$^{+440}_{-440}$	$^{+430}_{-420}$	$^{+300}_{-150}$	$^{+640}_{-650}$	1010 ± 220
ggH, high p_{T}^H $p_{\mathrm{T}}^H > 200$ GeV	260	$^{+100}_{-100}$	$^{+80}_{-80}$	$^{+40}_{-40}$	$^{+40}_{-20}$	$^{+40}_{-40}$	122 ± 31
EW qqH-2j, low m_{jj}-low p_{T}^H $350 < m_{jj} < 700$GeV, $p_{\mathrm{T}}^H < 200$ GeV	6	$^{+63}_{-62}$	$^{+46}_{-42}$	$^{+31}_{-34}$	$^{+11}_{-14}$	$^{+24}_{-26}$	109 ± 7
EW qqH-2j, med m_{jj}-low p_{T}^H $700 < m_{jj} < 1000$GeV, $p_{\mathrm{T}}^H < 200$ GeV	31	$^{+35}_{-33}$	$^{+30}_{-27}$	$^{+15}_{-14}$	$^{+8}_{-7}$	$^{+11}_{-10}$	56 ± 4
EW qqH-2j, high m_{jj}-low p_{T}^H $1000 < m_{jj} < 1500$GeV, $p_{\mathrm{T}}^H < 200$ GeV	60	$^{+26}_{-23}$	$^{+23}_{-21}$	$^{+7}_{-7}$	$^{+9}_{-5}$	$^{+5}_{-5}$	51 ± 4
EW qqH-2j, very high m_{jj}-low p_{T}^H $m_{jj} > 1500$ GeV, $p_{\mathrm{T}}^H < 200$ GeV	57	$^{+20}_{-18}$	$^{+18}_{-17}$	$^{+5}_{-5}$	$^{+3}_{-3}$	$^{+4}_{-4}$	50 ± 4
EW qqH-2j, high p_{T}^H $m_{jj} > 350$ GeV, $p_{\mathrm{T}}^H > 200$ GeV	37	$^{+16}_{-14}$	$^{+14}_{-13}$	$^{+4}_{-3}$	$^{+4}_{-3}$	$^{+3}_{-3}$	32 ± 1

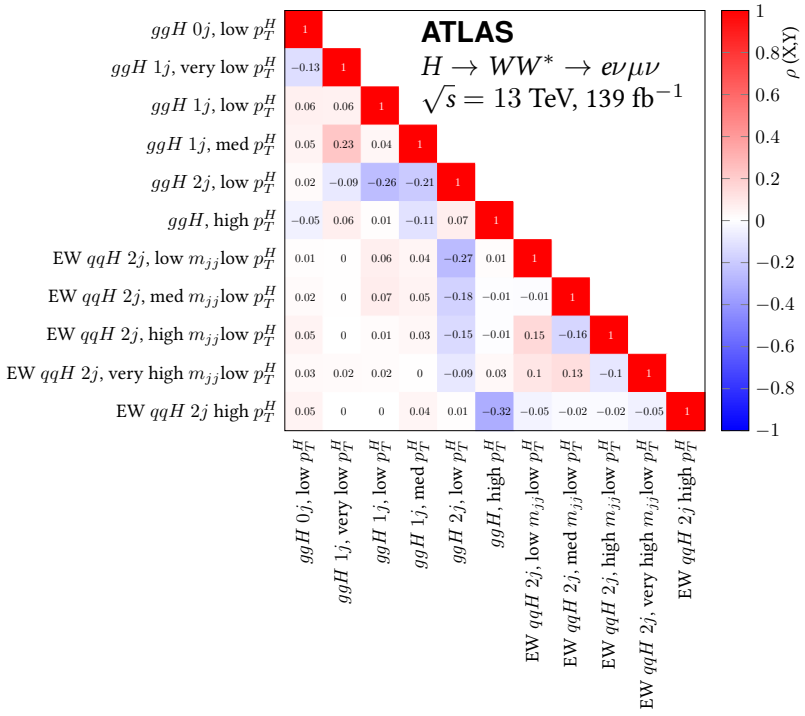

Figure 8.7: Correlations between the cross-section measurements in the 11 STXS categories for the $H \to WW^* \to e\nu\mu\nu$ analysis.

STXS bin	σ/σ_{SM}
ggH; 0j	$0.74 \pm 0.07(\text{stat}) \pm 0.04(\text{th})^{+0.08}_{-0.07}(\text{exp})$
ggH; 1j; $p_T^H < 60$	$1.7 \pm 0.3(\text{stat}) \pm 0.2(\text{th}) \pm 0.2(\text{exp})$
ggH; 1j; $p_T^H > 60$	$0.41 \pm 0.25(\text{stat})^{+0.10}_{-0.06}(\text{th}) \pm 0.17(\text{exp})$
ggH; $\geq$ 2j	$1.8 \pm 0.6(\text{stat}) \pm 0.4(\text{th}) \pm 0.4(\text{exp})$
ggH; $200 < p_T^H < 300$	$2.3 \pm 0.9(\text{stat}) \pm 0.1(\text{th}) \pm 0.6(\text{exp})$
ggH; $p_T^H > 300$	$-2.1^{+1.7}_{-1.5}(\text{stat})^{+0.2}_{-0.3}(\text{th})^{+1.6}_{-2.0}(\text{exp})$
VBF; $p_T^H < 200$; $350 < m_{jj} < 700$	$0.4^{+0.8}_{-0.7}(\text{stat}) \pm 0.2(\text{th}) \pm 0.5(\text{exp})$
VBF; $p_T^H < 200$; $m_{jj} > 700$	$0.7 \pm 0.3(\text{stat}) \pm 0.1(\text{th}) \pm 0.2(\text{exp})$
VBF; $p_T^H > 200$	$1.1^{+0.7}_{-0.6}(\text{stat}) \pm 0.1(\text{th}) \pm 0.3(\text{exp})$

Figure 8.8: Observed cross sections over SM cross section for the STXS categories measured by the CMS collaboration in the $H \to WW^*$ channel on a dataset of 138 fb^{-1}.

8.5 References

[107] D. de Florian et al. "Handbook of LHC Higgs Cross Sections: 4. Deciphering the Nature of the Higgs Sector". In: 2/2017 (Oct. 2016). DOI: 10.23731/CYRM-2017-002. arXiv: 1610.07922 [hep-ph] (cit. on pp. 91, 161, 164, 170).

[192] J. R. Andersen et al. "Les Houches 2015: Physics at TeV Colliders Standard Model Working Group Report". In: *9th Les Houches Workshop on Physics at TeV Colliders*. May 2016. arXiv: 1605.04692 [hep-ph] (cit. on p. 170).

[193] Nicolas Berger et al. "Simplified Template Cross Sections - Stage 1.1". In: (June 2019). arXiv: 1906.02754 [hep-ph] (cit. on p. 170).

[194] Federica Pasquali. *Slides on ggF purity studies*. URL: https://indico.cern.ch/event/924916/contributions/3887036/attachments/2048772/3434113/HWW_020620_STXS_statusupdate.pdf (cit. on p. 172).

[195] A.M. Sirunyan et al. "Measurements of properties of the Higgs boson decaying to a W boson pair in pp collisions at s=13TeV". In: *Physics Letters B* 791 (2019), pp. 96–129 (cit. on p. 176).

S

Summary

Similar to the way cats like to knock down objects, particle physicists appreciate colliding protons. While cats run experiments with gravity, our inquiries aim in proving or disproving the existing theories about how the subatomic world works.
The Standard Model of particle physics (SM) is *the* model that is currently used to describe the subatomic world. It is a complex mathematical theory which incorporates all the discoveries of new elementary particles starting from the discovery of the electron in 1897, to the Higgs boson (H), of which the discovery was claimed almost 10 years ago. The Higgs boson was not just the last missing piece of the elegant SM, but it was also a pretty important one. Its introduction, in fact, resolves divergences in the model that otherwise would lead to having processes, within the theory, with a probability to happen greater than one.
These past 10 years have seen multiple studies focusing the Higgs boson, but one of the questions still left to answer is whether the discovered particle is the one theorized by the SM, or just something that resembles it. This thesis' aim is to contribute to this effort. In particular, what is studied is the Higgs decay into two W bosons, the particles responsible for radioactive decays. This process is usually denoted as $H \to WW^*$, where the asterisk indicates that one of the W bosons is "off-shell" or "virtual", meaning that its mass is away from the normal W peak at $\sim$80 GeV. The $H \to WW^*$ process occurs relatively often: almost 22% of the time, a Higgs boson decays in this way, this allows to collect enough data for probing its decay characteristics with high precision. In this manuscript, two analyses performed at the LHC with the ATLAS experiment are presented.

The ***Couplings*** analysis quantifies the Higgs boson production in the gluon-fusion (ggF) and vector-boson fusion (VBF) channels, of which graphical representations are given by Feynman diagrams in Figure S.1.
There are multiple reasons to care about each of these processes: the ggF process, represented

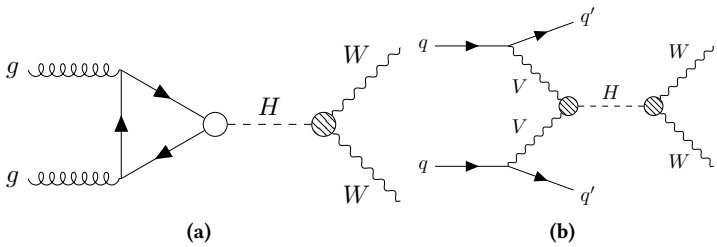

Figure S.1: Feynman diagrams for the ggF process (a) and VBF process (b).

S

with its Feynman diagram in Figure S.1(a), is the process that sees two gluons (g) fusing into a loop of massive quarks (triangle of solid lines) to generate a Higgs boson (white circle). The Higgs boson then couples with the two vector bosons W (striped circle). Because it is the largest Higgs production cross-section at the LHC, ggF provides us with sufficient data for sensitive measurement across many kinematic regions. The VBF process, of which the Feynman diagram is displayed in Figure S.1(b), instead sees two quarks (q) radiating two vector bosons V, which in turn couple with the Higgs boson (striped circle). The same physics interaction is again present in the Higgs decaying into the 2 W bosons. The VBF process is exciting because this production channel in $H \to WW^*$ has not been observed, until now. I am proud of having participated in this observation. Furthermore, this process is required to prevent unitarity violation in WW scattering at high energies. The VBF process includes two occurrences of Higgs-vector boson interaction (the two stripped circles) which makes it very sensitive to the Higgs coupling to vector bosons.
Observing these processes and measuring inclusive cross-section times branching ratio (a quantity indicating of how often this process happens) probes consistency with the SM. The same measurement can also be performed separately in mutually exclusive kinematic regions, according to the simplified template cross sections (STXS) prescription, to provide additional sensitivity to regions where effects of physics not in the SM might be enhanced.

The overall strategy of this analysis, of which a sketch is depicted in Figure S.2 is as follows: first,

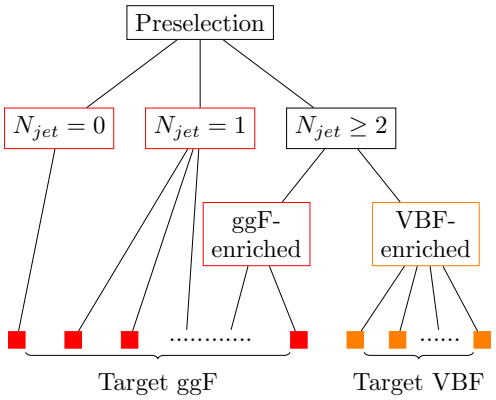

Figure S.2: Sketch of the overall strategy for the ***COUPLINGS*** analysis.

a preselection is performed where the signal processes are targeted. Two leptons with different flavors are selected in order to reduce backgrounds mimic the signal topology, then several features of the Higgs boson decay are exploited: given that one of the W bosons tends to be off-shell, asymmetric lepton cuts on the transverse momentum (p_{T}) of the leptons are used to maximize the signal acceptance. The spin-0 nature of the Higgs and the intrinsic property of the interaction (the chirality of the weak interaction) cause the two charged leptons to be preferably emitted with a small opening angle, which is exploited. Another core feature of the analysis is that it splits the data into channels according to jet multiplicity, which is done to take advantage of the varying background composition per jet bin. We end up with $N_{\mathrm{jet}} = 0$, $N_{\mathrm{jet}} = 1$ and $N_{\mathrm{jet}} \geq 2$ multiplicity bins targeting the ggF process. A series of selection cuts and machine learning techniques are

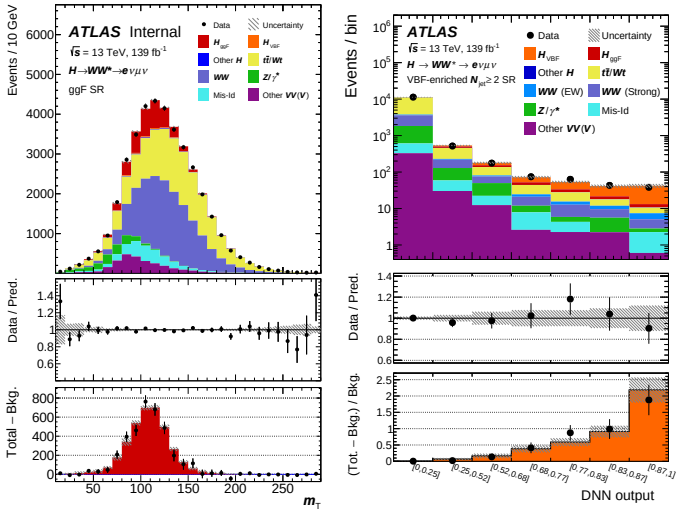

(a) (b)

Figure S.3: Post-fit m_{T} distributions with the signal and the background modeled contributions in the combined signal regions. More details in Figure 7.12(d) in the text (a). Post-fit distribution of the DNN output in the VBF SR. More details in Figure 7.13 in the text (b).

used to create signal regions in each of these channels that are sufficiently pure in the processes of interest to allow measurements of the cross-section times branching ratio for both ggF and VBF.

The ***Couplings*** analysis differentiates from the previous iteration through the inclusion of the ggF $N_{\text{jet}} \geq 2$ channel, a more advanced multivariate analysis technique (DNN instead of the BDT) and the study of the cross-section in STXS bins. For the final result, a simultaneous fit is performed across ggF and VBF channels where the final discriminant is either m_{T} (for ggF channels) shown in Figure S.3(a) or the DNN output score (for VBF channel) shown in Figure S.3(b).
The results in terms of signal strength and cross-sections both show good consistency with the SM. The products of the total ggF and VBF cross sections times the $H \to WW^*$ branching fraction are respectively measured to be 12.0 ± 1.4 pb and $0.75\ ^{+0.19}_{-0.16}$ pb, while the cross sections times the $H \to WW^*$ branching fraction measurements for the STXS categories are displayed in Figure S.4.
This analysis provides the first observation of VBF $H \to WW^*$ production with a significance of $Z_0 = 5.8\sigma$ (6.2 σ expected). A significance of 5.8σ means that the probability of that the observed signal being the result of a statistical fluctuation is less than 1 in 150 million.

These measurements have already entered the most recent Higgs combination where they contribute substantially to its precision.

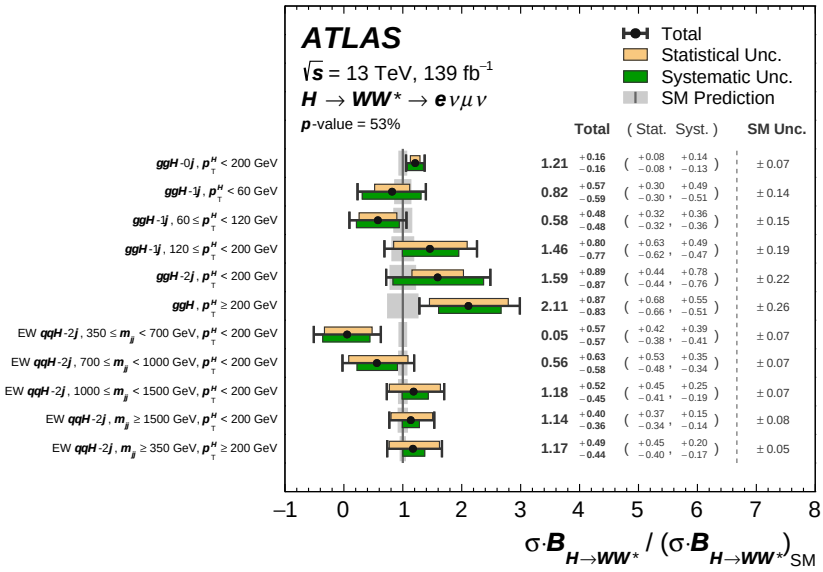

(a)

Figure S.4: Best-fit values for the measured STXS, more details in Figure 8.5 in the text.

The ***PROPERTIES*** analysis aims to constraint the CP properties of the Higgs boson, where C stands for "Charge conjugation", a discrete symmetry transformation that replaces particles with the corresponding anti-particles, and P stands for "Parity", a discrete symmetry transformation that corresponds to spatial inversion through the origin.
According to the SM, the Higgs boson is a CP-even scalar particle. However, the equation of motion representing the Higgs fields would allow also a CP-odd scenario, as well as a CP-mixed one, i.e. c_1CP-even + c_2CP-odd, where $c_1/c_2 = \cos\alpha$ is defined as mixing angle among the two scenarios. This study investigates the properties of the effective Higgs–gluon interaction by selecting Higgs bosons produced via ggF in association with two jets. The presence of these jets is crucial because their angular correlation expresses sensitivity to the CP properties of the interaction. The two outgoing jets indeed show a different distribution in $\Delta\eta_{jj}$ depending on the CP of the Higgs boson, as shown in Figure S.5.

Similarly to the ***COUPLINGS*** analysis, a preselection is applied, targeting the signal process (in this case only ggF $N_{\text{jet}} \geq 2$): two leptons with different flavors are selected, asymmetric p_{T} lepton cuts are used, as well as a small opening between the two charged leptons is required. Further cuts are used to define optimized signal and control regions so that the value of $\tan\alpha$ can be extracted. Lastly, this analysis makes use of a machine learning algorithm to better enhance the signal over background ratio and exploit the discrimination power of multiple observables.

The result is found to be $\tan(\alpha) = 0.0 \pm 0.4(\text{stat.}) \pm 0.3(\text{syst.})$, compatible with the SM prediction of $\tan(\alpha) = 0$.

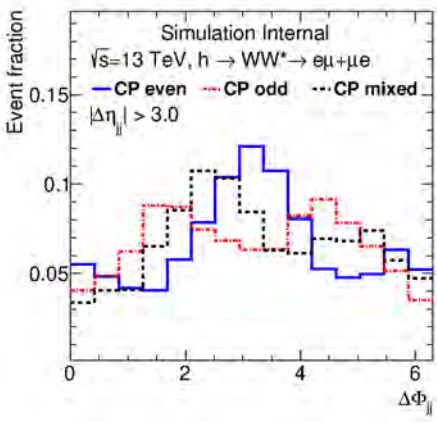

(a)

Figure S.5: Distributions of the $\Delta\phi_{jj}$ observable are shown for ggF induced production modes of Hjj events for a CP-even, a CP-odd and a CP-mixed benchmark model. Figure 6.2 in the text.

This measurement has been performed with a reduced dataset of 36 fb^{-1}, and is dominated by the limited statistics on data, leaving room for further more precise studies with Run-2 and Run-3 data in the next years. Stay tuned!

S

S

Samenvatting

Vergelijkbaar met de manier waarop katten objecten omver willen gooien, waarderen deeltjesfysici het botsen van protonen. Terwijl katten experimenten uitvoeren met zwaartekracht, streven onze onderzoeken ernaar om de bestaande theorieën over hoe de subatomaire wereld werkt, te bewijzen of te weerleggen.
Het Standaardmodel (Standard Model of particle physics) is het model dat momenteel wordt gebruikt om de subatomaire wereld te beschrijven. Het is een complexe wiskundige theorie die alle ontdekkingen van nieuwe elementaire deeltjes omvat, beginnend met de ontdekking van het elektron in 1897, tot het higgsboson (H), waarvan de ontdekking bijna 10 jaar geleden werd geclaimd. Het higgsboson was niet alleen het laatste ontbrekende puzzelstukje van het elegante Standard Model of particle physics, maar ook een zeer belangrijk puzzelstukje. De introductie ervan lost namelijk divergenties in het model op die anders zouden leiden tot processen binnen de theorie met een waarschijnlijkheid groter dan één.
De afgelopen 10 jaar zijn er meerdere studies geweest die zich richtten op het higgsboson, maar een van de nog openstaande vragen is of het ontdekte deeltje hetzelfde is als het voorspelde deeltje in het Standard Model of particle physics, of dat het slechts iets is dat erop lijkt. Het doel van deze scriptie is om bij te dragen aan deze inspanning. In het bijzonder wordt onderzocht hoe het higgsboson vervalt in twee W-bosonen, de deeltjes die verantwoordelijk zijn voor radioactief verval. Dit proces wordt meestal aangeduid als $H \to WW^*$, waarbij het sterretje aangeeft dat een van de W-bosonen "off-shell" of "virtueel" is, wat betekent dat de massa ervan afwijkt van de normale W-piek bij ongeveer 80 GeV. Het $H \to WW^*$-proces komt relatief vaak voor: bijna 22% van de tijd vervalt een higgsboson op deze manier, waardoor er voldoende gegevens kunnen worden verzameld om de vervalkenmerken met hoge precisie te onderzoeken.
In dit proefschrift worden twee analyses gepresenteerd die zijn uitgevoerd bij de LHC met behulp van het ATLAS-experiment.

De ***Couplings***-analyse kwantificeert de productie van het higgsboson in de gluon-fusion (ggF) en de vector-boson fusion (VBF) kanalen, waarvan grafische voorstellingen worden gegeven door Feynman-diagrammen in Figuur S.1.
Er zijn meerdere redenen om elk van deze processen belangrijk te vinden: Het ggF-proces, weergegeven met het Feynman-diagram in Figuur S.1(a), is het proces waarbij twee gluonen (g) samensmelten tot een lus van massieve quarks (driehoek van doorgetrokken lijnen) om een higgsboson (witte cirkel) te genereren. Het higgsboson koppelt vervolgens met de twee W vectorbosonen (gestreepte cirkel). Omdat dit het proces met de grootste werkzame doorsnede voor higgsproductie is bij de LHC, levert ggF ons voldoende gegevens voor gevoelige metingen over veel kinematische regio's. Het VBF-proces, waarvan het Feynman-diagram wordt weergegeven

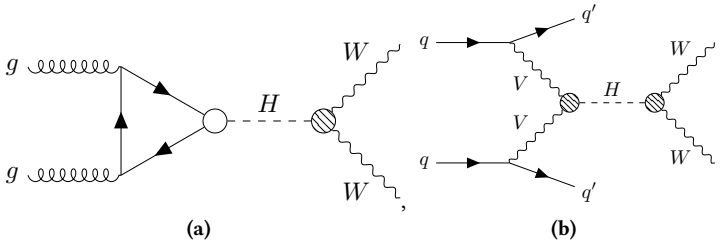

Figure S.1: Feynman-diagrammen voor het ggF-proces (a) en het VBF-proces (b).

in Figuur S.1(b), laat daarentegen twee quarks (q) zien die twee vectorbosonen V uitstralen, die op hun beurt koppelen met het higgsboson (gestreepte cirkel). Dezelfde fysische interactie komt ook voor bij het verval van het higgsboson in de 2 W-bosonen. Het VBF-proces is interessant omdat dit productiekanaal in $H \to WW^*$ tot nu toe niet is waargenomen. Ik ben er trots op dat ik aan deze waarneming heb bijgedragen. Bovendien is dit proces nodig om unitariteitschending in WW-verstrooiing bij hoge energieën te voorkomen. Het VBF-proces omvat twee gevallen van Higgs-vectorboson-interactie (de twee gestreepte cirkels), waardoor het zeer gevoelig is voor de koppeling van het higgsboson aan vectorbosonen.
Het waarnemen van deze processen en het meten van de inclusieve doorsnede vermenigvuldigd met de vervalverhouding (een hoeveelheid die aangeeft hoe vaak dit proces plaatsvindt) onderzoekt de consistentie met het SM. Dezelfde meting kan ook afzonderlijk worden uitgevoerd in onderling uitsluitende kinematische regio's, volgens de voorschriften van de simplified template cross sections (STXS), om extra gevoeligheid te bieden voor regio's waar effecten van fysica die niet in het SM voorkomt mogelijk worden versterkt.

De algehele strategie van deze analyse, waarvan een schets wordt weergegeven in Figuur S.2, is als volgt: Eerst wordt er een voorselectie uitgevoerd waarbij de signaalprocessen worden

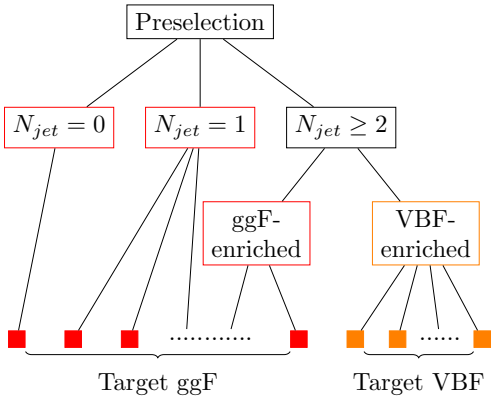

Figure S.2: Schets van de algehele strategie voor de ***Couplings*** analyse.

gericht. Twee leptonen met verschillende smaken worden geselecteerd om achtergrondruis na te bootsen die de signaal-topologie nabootst. Vervolgens worden verschillende kenmerken van

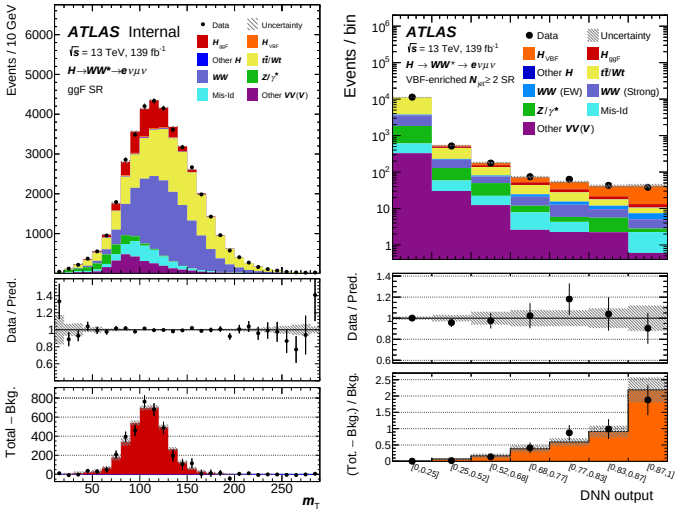

(a) (b)

Figure S.3: Post-fit verdelingen van m_{T} met de bijdragen van het signaal en de achtergrond gemodelleerd in de gecombineerde signaalregio's. Meer details in Figuur 7.12(d) in de tekst (a). Post-fit verdeling van de DNN output in het VBF SR. Meer details in Figuur 7.13 in de tekst (b).

het verval van het higgsboson benut: aangezien een van de W-bosonen de neiging heeft off-shell te zijn, worden asymmetrische lepton-snedes op de transversale impuls (p_{T}) van de leptonen gebruikt om de signaalacceptatie te maximaliseren. De spin-0 aard van het higgsboson en de intrinsieke eigenschap van de interactie (de chiraliteit van de zwakke interactie) zorgen ervoor dat de twee geladen leptonen bij voorkeur met een kleine openingshoek worden uitgezonden, wat wordt benut. Een andere kernfunctie van de analyse is dat de gegevens worden onderverdeeld in kanalen op basis van de jet-multipliciteit, wat wordt gedaan om te profiteren van de variërende achtergrondsamenstelling per jet-bin. We eindigen met $N_{\mathrm{jet}} = 0$, $N_{\mathrm{jet}} = 1$ en $N_{\mathrm{jet}} \geq 2$ multipliciteit bins die zich richten op het ggF proces. Een reeks selectiecriteria en machine learning-technieken worden gebruikt om signaalregio's te creëren in elk van deze kanalen die voldoende zuiver zijn voor de processen van belang om metingen van de doorsnede vermenigvuldigd met de verhouding van vertakkingen te mogelijk te maken voor zowel ggF als VBF.

De ***Couplings*** analyse verschilt van de vorige iteratie door de toevoeging van het ggF $N_{\mathrm{jet}} \geq 2$ kanaal, een meer geavanceerde multivariate analyse techniek (neurale netwerken in plaats van de BDT) en de studie van de doorsnede in STXS bins. Voor het uiteindelijke resultaat wordt er een simultane fit uitgevoerd over de ggF en VBF kanalen, waarbij de uiteindelijke onderscheidende grootheid ofwel m_{T} (voor ggF kanalen) zoals weergegeven in Figuur S.3(a), ofwel de score van de DNN output (voor VBF kanaal) zoals weergegeven in Figuur S.3(b) wordt gebruikt.

De resultaten in termen van signaalsterkte en doorsnedes tonen goede consistentie met het SM. De producten van de totale ggF en VBF doorsnedes vermenigvuldigd met de $H \to WW^*$ vervals-

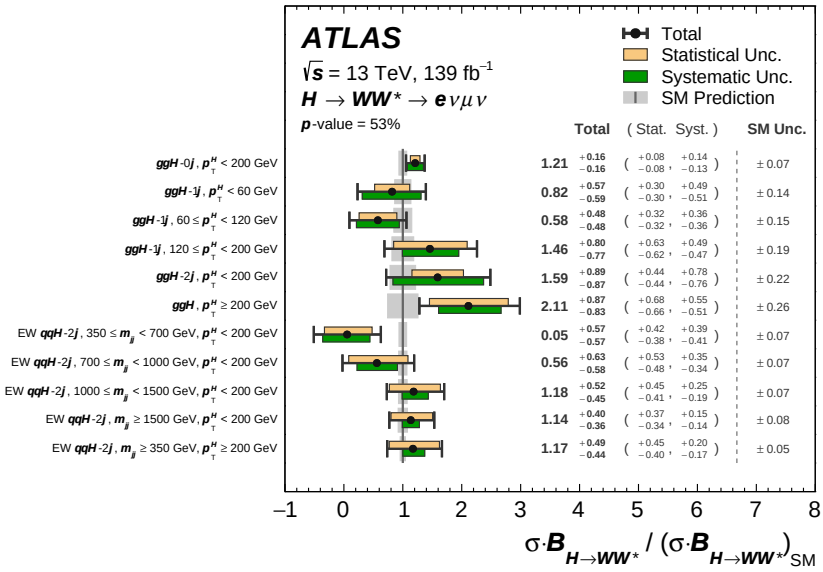

(a)

Figure S.4: Best-fit waarden voor de gemeten STXS, meer details in Figuur 8.5 in de tekst.

fractie worden respectievelijk gemeten als 12.0 ± 1.4 pb en $0.75;^{+0.19}_{-0.16}$ pb, terwijl de doorsnedes vermenigvuldigd met de $H \to WW^*$ vervalsfractie metingen voor de STXS categorieën worden weergegeven in Figuur S.4.

Deze analyse biedt de eerste observatie van VBF $H \to WW^*$ productie met een significantie van $Z_0 = 5.8\sigma$ (6.2 σ verwacht). Een significantie van 5.8σ betekent dat de kans dat het waargenomen signaal het gevolg is van een statistische fluctuatie kleiner is dan 1 op 150 miljoen.

Deze metingen zijn al opgenomen in de meest recente Higgs-combinatie, waar ze aanzienlijk bijdragen aan de precisie ervan.

De ***Properties***-analyse heeft tot doel de CP-eigenschappen van het higgsboson te bepalen, waarbij C staat voor "ladingsconjugatie", een discrete symmetrietransformatie die deeltjes vervangt door de bijbehorende antideeltjes, en P staat voor "pariteit", een discrete symmetrietransformatie die overeenkomt met ruimtelijke inversie door de oorsprong.
Volgens het SM is het higgsboson een CP-even scalair deeltje. Echter, de bewegingsvergelijking die de Higgs-velden representeert, zou ook een CP-oneven scenario toestaan, evenals een CP-gemengd scenario, d.w.z. c_1CP-even + c_2CP-oneven, waarbij $c_1/c_2 = \cos\alpha$ wordt gedefinieerd als de menghoek tussen de twee scenario's.
Dit onderzoek onderzoekt de eigenschappen van de effectieve Higgs-gluoninteractie door higgsbosonen te selecteren die via ggF tegelijkertijd worden geproduceerd met twee jets. De aanwezigheid van deze jets is cruciaal omdat hun onderlinge hoekcorrelatie gevoeligheid uitdrukt voor de CP-eigenschappen van de interactie. De twee uitgaande jets vertonen inderdaad een

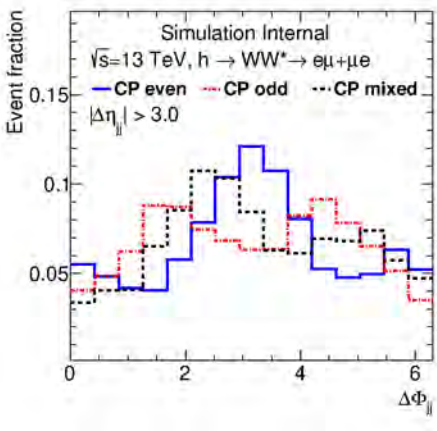

(a)

Figure S.5: Verdelingen van de waarneembare $\Delta\phi_{jj}$ worden getoond voor ggF-geïnduceerde productiemodi van Hjj-gebeurtenissen voor een CP-even, een CP-oneven en een CP-gemengd referentiemodel. Figuur 6.2 in de tekst.

verschillende verdeling in $\Delta\eta_{jj}$ afhankelijk van de CP van het higgsboson, zoals getoond in Figuur S.5.

Vergelijkbaar met de ***Couplings***-analyse wordt er een voorselectie toegepast, gericht op het signaalproces (in dit geval alleen ggF $N_{\text{jet}} \geq 2$): er worden twee leptonen met verschillende smaken geselecteerd, asymmetrische snedes op p_{T}-lepton worden gebruikt, en er wordt een kleine opening tussen de twee geladen leptonen vereist. Verdere selectiecriteria worden gebruikt om geoptimaliseerde signaal- en controlegebieden te definiëren, zodat de waarde van $\tan\alpha$ kan worden bepaald. Ten slotte maakt deze analyse gebruik van een machine learning-algoritme om de signaal-achtergrondverhouding te verbeteren en het onderscheidend vermogen van meerdere waarneembare grootheden te benutten.

Het resultaat is $\tan(\alpha) = 0.0 \pm 0.4(\text{stat.}) \pm 0.3(\text{syst.})$, wat in overeenstemming is met de SM-voorspelling van $\tan(\alpha) = 0$.
Deze meting is uitgevoerd met een verkleinde dataset van 36 fb^{-1}en wordt gedomineerd door de beperkte statistiek van de gegevens, waardoor er ruimte is voor verdere, nauwkeurigere studies met Run-2- en Run-3-gegevens in de komende jaren. Blijf op de hoogte!

S

L

List of Abbreviations

A

CONTROL REGIONS PLOTS IN THE *COUPLINGS* ANALYSIS

In the following plots, the normalization factor derived from the CR has been applied. The hatched band in the upper plot, and the shaded band in the ratio plot, give the statistical uncertainty on the MC.

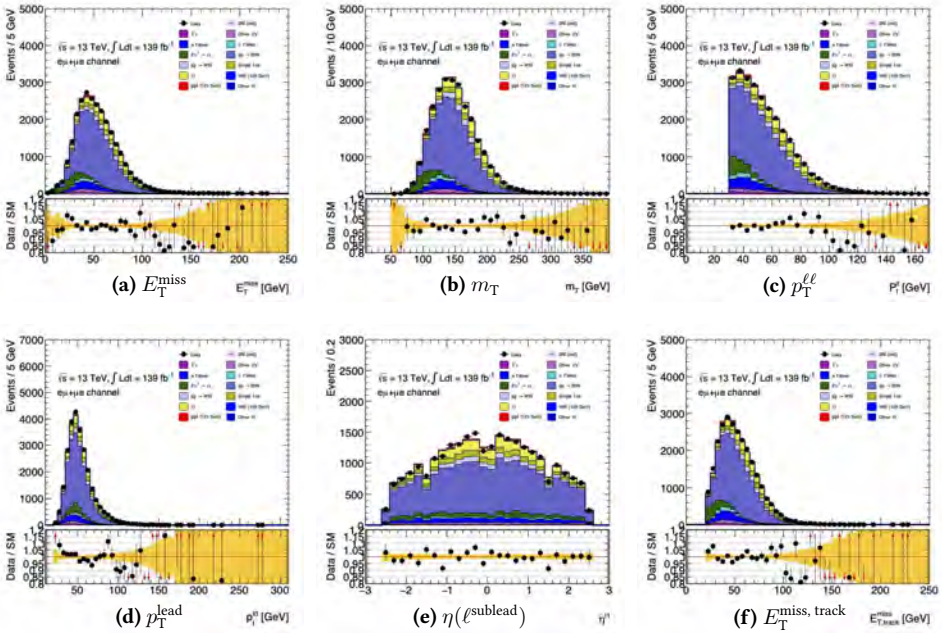

(a) $E_{\mathrm{T}}^{\mathrm{miss}}$ (b) m_{T} (c) $p_{\mathrm{T}}^{\ell\ell}$

(d) $p_{\mathrm{T}}^{\mathrm{lead}}$ (e) $\eta(\ell^{\mathrm{sublead}})$ (f) $E_{\mathrm{T}}^{\mathrm{miss,\,track}}$

Figure A.1: Comparison of data and MC in the WW control region in the $N_{\mathrm{jet}} = 0$ category.

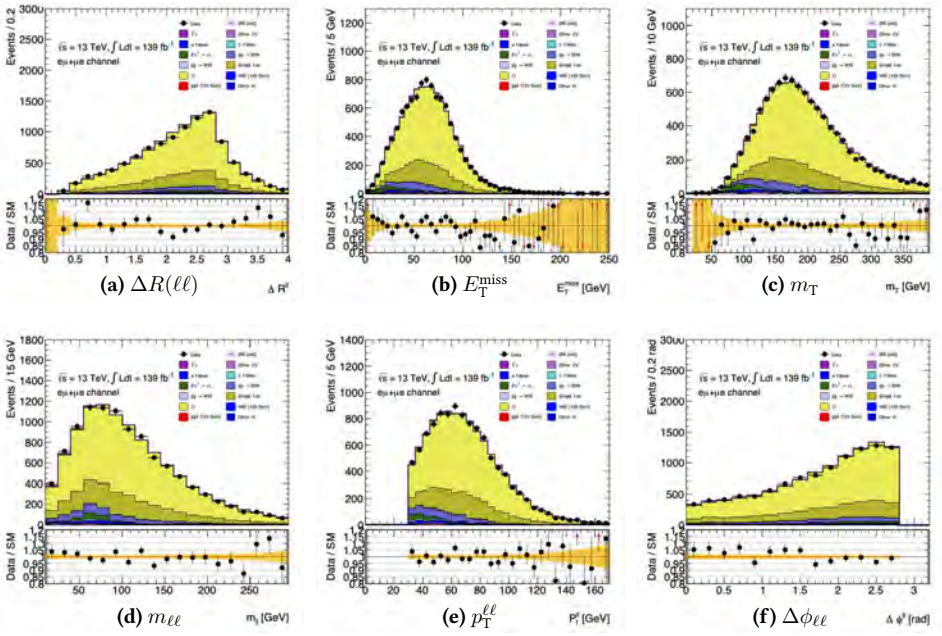

(a) $\Delta R(\ell\ell)$ (b) $E_{\mathrm{T}}^{\mathrm{miss}}$ (c) m_{T}

(d) $m_{\ell\ell}$ (e) $p_{\mathrm{T}}^{\ell\ell}$ (f) $\Delta\phi_{\ell\ell}$

Figure A.2: Comparison of data and MC in the Top region in the $N_{\mathrm{jet}} = 0$ category.

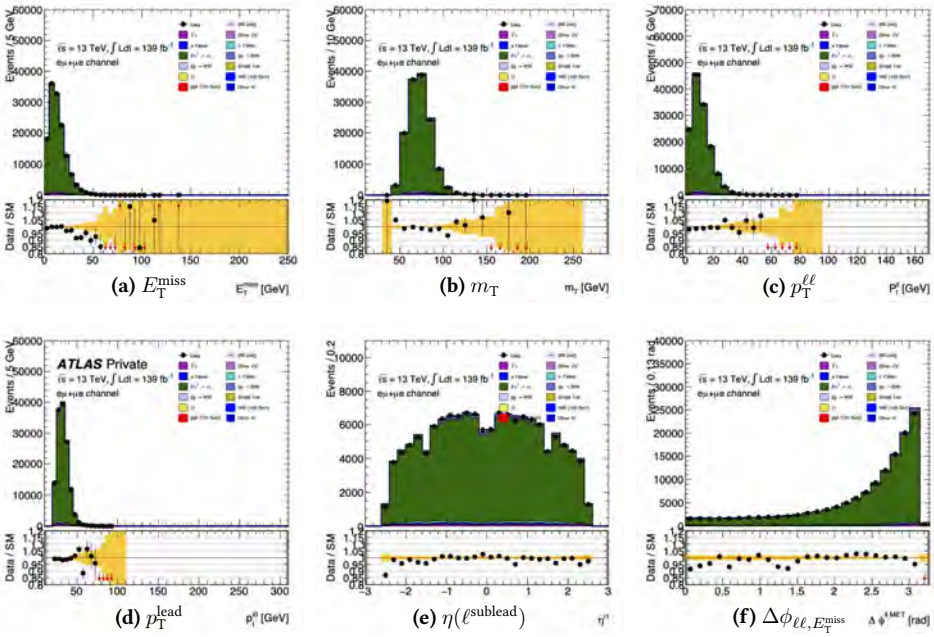

Figure A.3: Comparison of data and MC in the $Z \to \tau\tau$ control region in the $N_{\mathrm{jet}} = 0$ category.

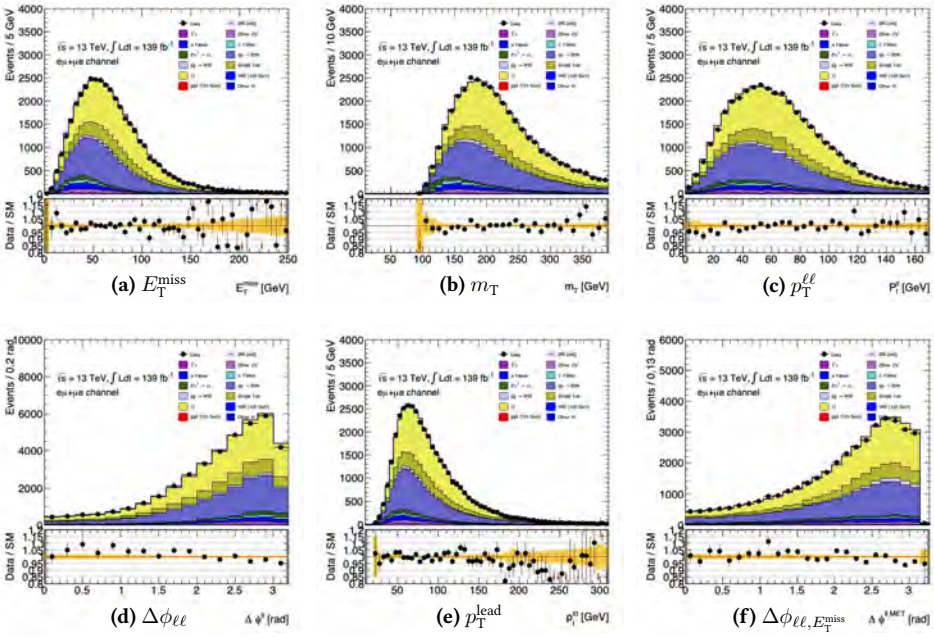

Figure A.4: Comparison of data and MC in the WW control region in the $N_{\mathrm{jet}} = 1$ category.

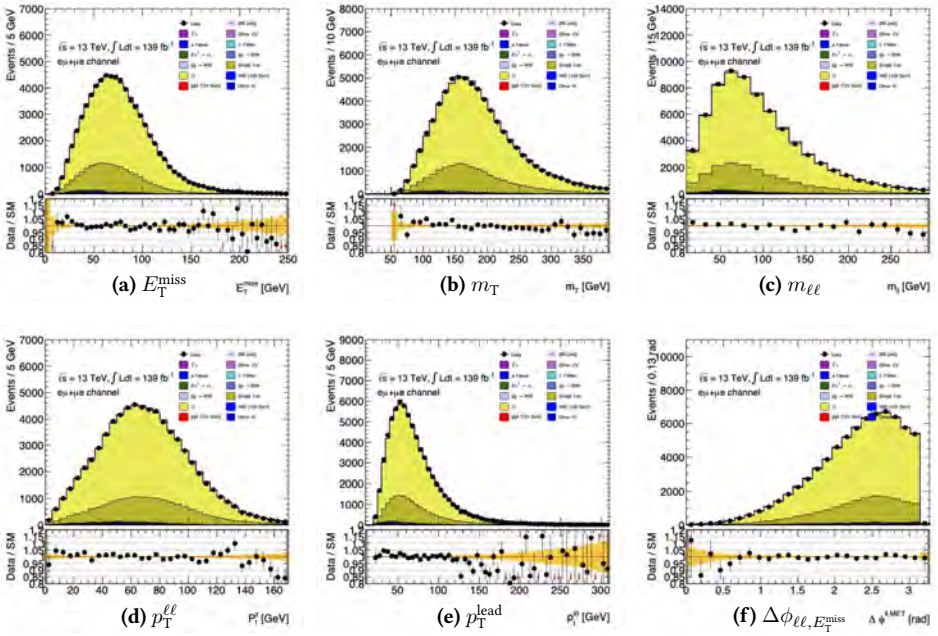

Figure A.5: Comparison of data and MC in the Top control region in the $N_{\mathrm{jet}} = 1$ category.

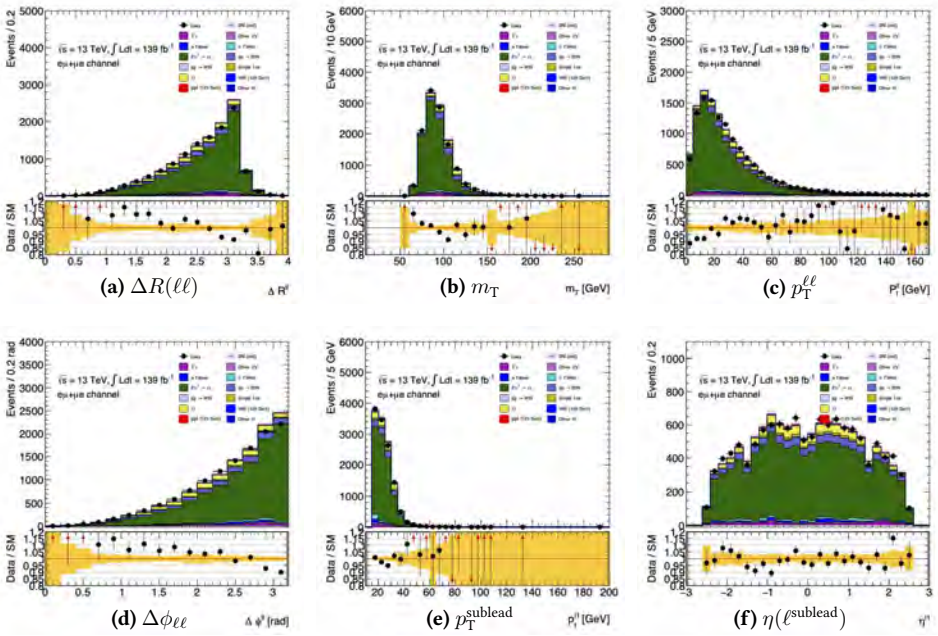

Figure A.6: Comparison of data and MC in the $Z \to \tau\tau$ control region in the $N_{\mathrm{jet}} = 1$ category.

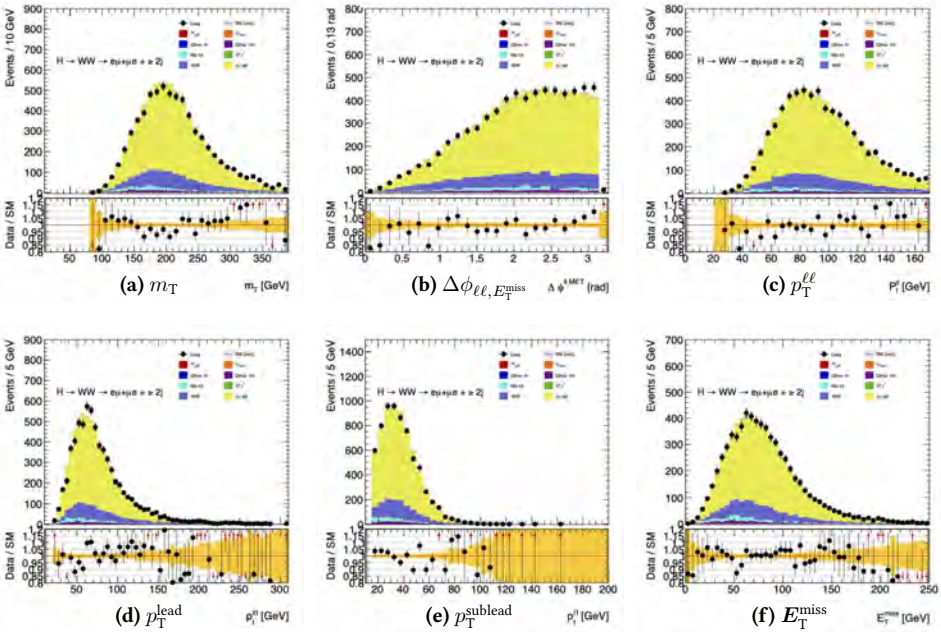

Figure A.7: Comparison of data and MC in the Top CR in the ggF $N_{\mathrm{jet}} \geq 2$ category.

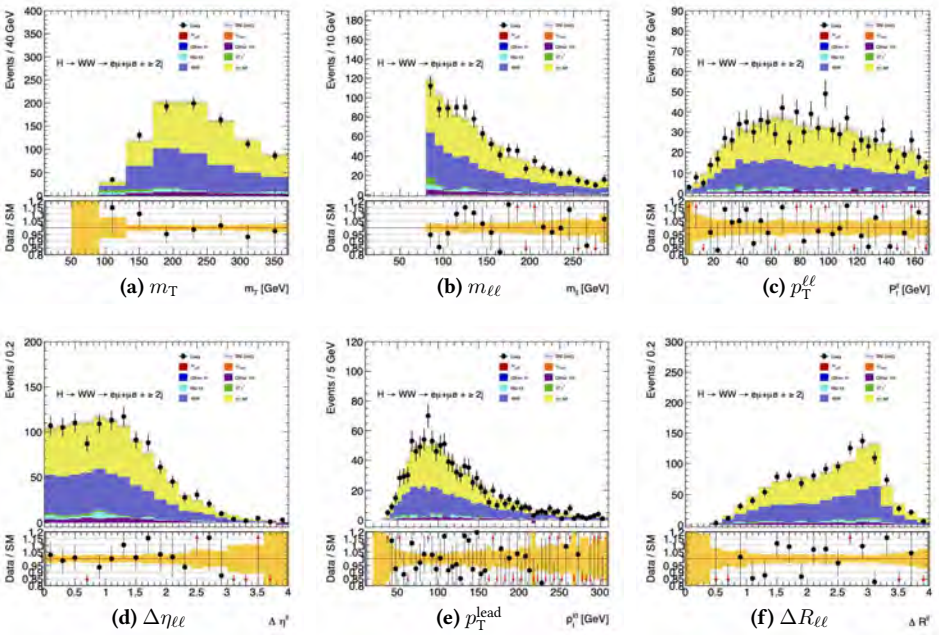

Figure A.8: Comparison of data and MC in the WW region in the $\mathrm{ggF}_{2+\ \mathrm{jet}}$ category.

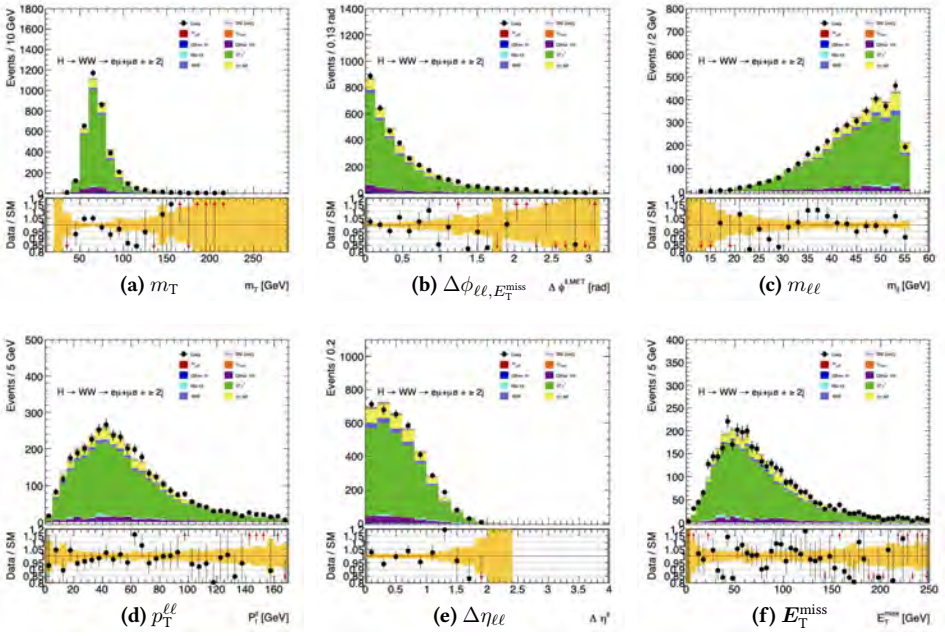

(a) m_{T} (b) $\Delta\phi_{\ell\ell,E_{\mathrm{T}}^{\mathrm{miss}}}$ (c) $m_{\ell\ell}$

(d) $p_{\mathrm{T}}^{\ell\ell}$ (e) $\Delta\eta_{\ell\ell}$ (f) $E_{\mathrm{T}}^{\mathrm{miss}}$

Figure A.9: Comparison of data and MC in the $Z \to \tau\tau$ CR in the $\mathrm{ggF}_{2+\text{ jet}}$ category.

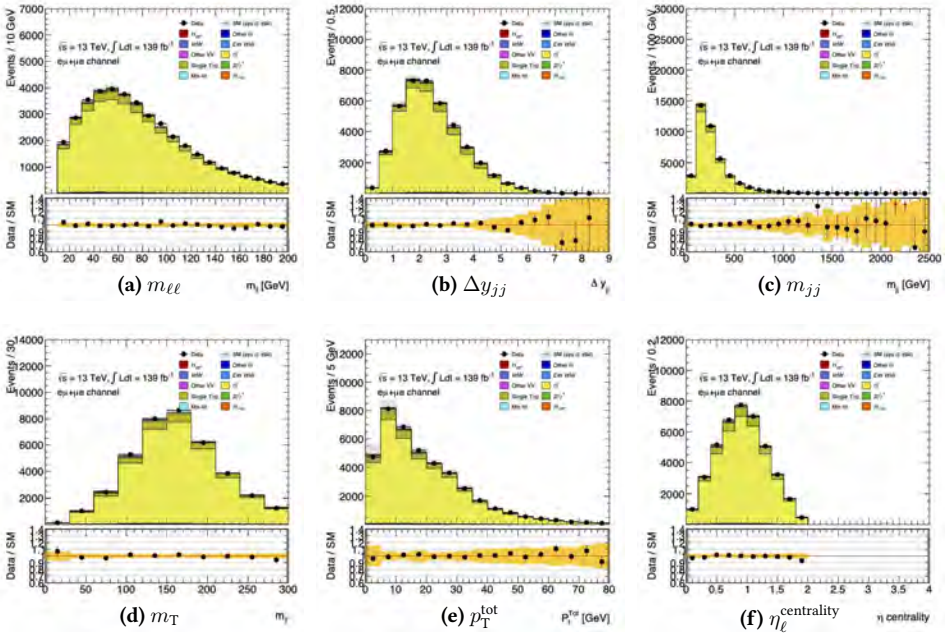

(a) $m_{\ell\ell}$ (b) Δy_{jj} (c) m_{jj}

(d) m_{T} (e) $p_{\mathrm{T}}^{\mathrm{tot}}$ (f) $\eta_{\ell}^{\mathrm{centrality}}$

Figure A.10: Comparison of data and MC in the Top CR in the VBF $N_{\mathrm{jet}} \geq 2$ category.

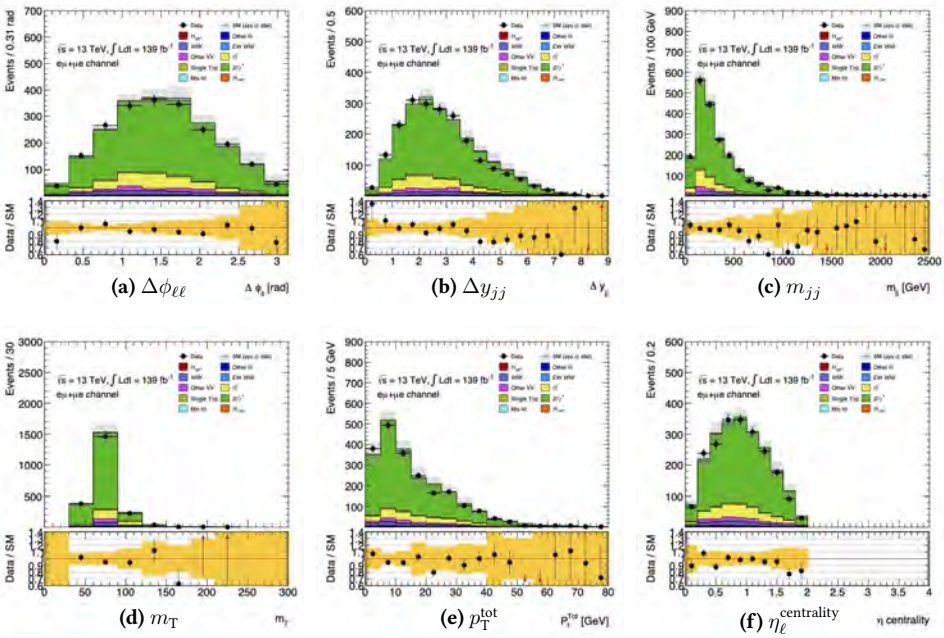

(a) $\Delta\phi_{\ell\ell}$ (b) Δy_{jj} (c) m_{jj}

(d) m_{T} (e) $p_{\mathrm{T}}^{\mathrm{tot}}$ (f) $\eta_{\ell}^{\mathrm{centrality}}$

Figure A.11: Comparison of data and MC in the $Z \to \tau\tau$ CR in the VBF $N_{\mathrm{jet}} \geq 2$ category.

L

L

List of Figures

L

L

A

Acknowledgements

This is it, and looking back at the last four years is now inevitable.
During my journey, I tried to learn from the people who shared a part of my path, with the hope of being a better scientist and a better person.

First and foremost I would like to acknowledge my supervisors, without you, this thesis would have not seen the light. I would like to express my deepest gratitude to Wouter for stepping in as my supervisor during a crucial period of my academic journey. Your willingness to take on this responsibility and provide invaluable guidance has been instrumental in the successful completion of my thesis. Pamela, since the first moment we met I have been thinking that you are just *incredibile*, your expertise is invaluable and your enthusiasm is contagious. Thanks for believing in me and guiding me during this journey. Bob, with all your insightful feedback, you pushed me to sharpen my thinking and brought my work to a higher level.
I would also like to thank prof. dr. M. P. Decowski, prof. dr. A. P. Colijn, prof. dr. ir. P. J. de Jong, prof. dr. R. Fleischer and dr. A. Nisati for being part of my doctorate committee and for carefully reading this thesis.

A big thank-you goes to the HWW Properties group: Pamela, Magdalena, Dominik, Carsten and Ralf. This was my first real project, and it was overwhelming. Thanks for bringing me up to speed with patience and kindness, for the help, and for all the useful discussions.
Speaking of patience, a big acknowledgment is for my officemates Alice, Ann-Kathrin, Carsten, Lydia, and Stefano. I am rich in good memories of laughs, fun, and nice in-between-work conversations.

My time as part of the big HWW family is one of the most fruitful of my life. Benny, Hayden, Konstantin and Robin you are the best *task force* I could have ever imagined. Working with you in the same office or nine time zones apart has been incredibly easy and satisfactory. Benedict, David, Kristin, Yun-Ju thanks for coordinating us so efficiently and pulling us through all analysis approval processes in such a smooth way.

A big acknowledgment goes to all the Nikhef people, for the fruitful discussions, coffee breaks and amazing outings.

Alice, you were the first person I met at Nikhef, and I am so grateful that after all these years you are still a big part of my life. Ralf, thanks for your endless help, you saved me from so many sleepless nights, and for the fun playing together. And now, I like to believe to have inherited some of your *magic*.
Carsten, I was happy for your presence during my PhD, not only for the uncountable advices you

gave me on debugging and more but mostly for the laughs (actually also for avoiding nasty speed tickets on the highway :p). *Ich habe wirklich die Sau rausgelassen.*
Ann-Kathrin, I am really grateful for our friendship! Despite the fact that we are different like the Sun and the Moon, you understand me way more than myself sometimes.
Benedict, you are a great person, a good friend, and an amazing mentor. Thanks for always having my back, also on this occasion.
Matteo, thank you not only for having *saved* my life -in multiple occasions- but also for Tom and Giovanni.

Grazie a mia madre e a tutti i suoi sacrifici, e a mio padre che sapeva che questo momento sarebbe arrivato.

For you, Konstantin, *Ich lass für Dich das Licht an*, like you did with me for all these years.